Advanced Space Concepts Laboratory

Department of Mechanical and Aerospace Engineering

Faculty of Engineering

University of Strathclyde

Non-Keplerian orbits using hybrid solar sail propulsion for Earth applications

Jeannette Heiligers

Submitted in fulfilment of the requirements for
the degree of Doctor of Philosophy

2012

Jeannette Heiligers

Glasgow, Scotland, September 2012

Supervisors

First supervisor:

Professor Colin R. McInnes
Advanced Space Concepts Laboratory, University of Strathclyde
Glasgow, United Kingdom

Second supervisor:

Dr. James D. Biggs
Advanced Space Concepts Laboratory, University of Strathclyde
Glasgow, United Kingdom

Third supervisor:

Dr. Matteo Ceriotti
Advanced Space Concepts Laboratory, University of Strathclyde
Glasgow, United Kingdom

Examiners

External examiner:

Mr. Stephen Kemble
EADS Astrium
Stevenage, United Kingdom

Internal examiner:

Dr. Eur Ing Malcolm Macdonald
Advanced Space Concepts Laboratory, University of Strathclyde
Glasgow, United Kingdom

"Logic will get you from A to B. Imagination will take you everywhere."

Albert Einstein

Acknowledgements

I came across Einstein's quote *"Logic will get you from A to B. Imagination will take you everywhere."* on a wedding invitation of a good friend of mine about a year ago. It didn't take me long to decide that this quote would get a special mentioning in my PhD thesis, because no other quote could have characterised my PhD better. Not only does it perfectly reflect my PhD in terms of the actual contents, which shows that out of the box thinking and visionary concepts can literally take a spacecraft everywhere, but also the process in general: just over three years ago, moving to Scotland, starting a PhD and successfully finishing it seemed a world away. But divergence of the usual path and my imagination did take me here and it truly has been the experience of a lifetime.

Clearly, this fantastic journey could not have been possible without the help and support of many people. Firstly, I would like to express my gratitude to my supervisor, Professor Colin McInnes, for giving me the opportunity to do a PhD within a truly outstanding and inspiring research group. Colin, your vision and guidance throughout have been invaluable to the successful completion of my PhD and your imaginative thinking has been a great inspiration. My thanks also go to Dr. James Biggs, my second supervisor. Thank you so much for your input, suggestions and ideas over the last three years. Additionally, I would like to express my gratitude to my third supervisor, Dr. Matteo Ceriotti. Matteo, your insights, ideas and input have been extremely valuable to my PhD and it truly has been a great pleasure working with you. Hopefully, one day, we will see a tiny bright dot appearing in the night sky, very close to Polaris, bringing the pole-sitter to reality. Furthermore, I would like to thank everybody else in the Advanced Space Concept Laboratory for discussions and technical advice. In particular, I would like to thank Dr. Massimiliano Vasile for his valuable input on the expo-elliptic shaped based method. Finally, a special thank you goes to my ERC-companions, Camilla, Matteo (again), Pau, Charlotte, Russell, Andreas, Daniel and Garrie,

as well as to Marta, for sharing ups and downs and for loads of fun both during and after working hours.

There are many more people to thank. First and foremost my parents. Thank you so much for teaching me the values and virtues that have brought me where I am now and for your everlasting support in everything I do. As always, I worked throughout my PhD the way you taught us, "to always do your best", and I hope I did you proud. A big thank you also goes to my sisters, who are my great examples and who I can always rely on, their husbands and my wonderful niece and nephew for bringing so much joy. Furthermore, I would like to thank Sander's parents, who had to see their son follow his girlfriend's dreams abroad, for moving our entire household across the Channel and their never-ending support. And last, but definitely not least, Sander. Words cannot express how grateful I am that you followed me to Glasgow, making this wonderful experience possible. Your support, help and advice throughout my PhD have been priceless. I will treasure our time in beautiful Scotland forever; it has been an adventure I could only have hoped for and I cannot wait to start the next one with you.

Abstract

Half a century of space technology development has provided a wealth of new space applications. However, many still remain to be explored. Examples include increased geostationary coverage and new opportunities to enhance polar observation. This thesis investigates both of these opportunities using families of non-Keplerian orbits, while demonstrating the potential of hybridised solar sail and solar electric propulsion (SEP) to enable these orbits.

Due to an increased number of geostationary spacecraft and limits imposed by east-west spacing requirements, GEO is starting to get congested. As a solution, this thesis creates new geostationary slots by displacing the geostationary orbit out of the equatorial plane by means of low-thrust propulsion. A full mission analysis and systems design is presented as well as an investigation of a range of transfers that can improve the performance of the displaced GEO and establish its accessibility. The analyses demonstrate that only hybrid propulsion can enable payloads to be maintained in a true geostationary orbit beyond the geostationary station-keeping box for lifetimes comparable to current GEO spacecraft.

The second opportunity, enhancing polar observations, is investigated by designing optimal transfers from low Earth orbit (LEO) to an Earth pole-sitter orbit that allows the spacecraft to hover above the polar regions. Both high-thrust (upper-stage) and low-thrust (spiral) transfers are considered and show that hybrid propulsion increases the mass delivered to the pole-sitter orbit compared to a pure SEP case, enabling an extension of the mission. In addition, transfers between north and south pole-sitter orbits are investigated to overcome limitations in observations during the polar winters. Again, hybrid propulsion reduces the propellant consumption compared to pure SEP, while increasing the polar observation time.

Overall, hybrid propulsion is proven an enabling propulsion method that can enable missions that are not feasible using only a solar sail and can extend the mission lifetime and/or payload capacity with respect to an SEP only mission.

Table of contents

List of symbols and acronyms

Acronyms

AD^2	Advancement Degree of Difficulty
ADCS	Attitude Determination and Control System
AEP	Artificial Equilibrium Point
ADOL-C	Automatic Differentiation by OverLoading in C++
AU	Astronomical Unit
CR3BP	Circular Restricted Three Body Problem
ESA	European Space Agency
FCC	Federal Communications Commission
FEEP	Field-Emission Electric Propulsion
GEO	Geostationary Orbit
GOCE	Gravity Field and Steady-State Ocean Circulation Explorer
GPOPS	General Pseudospectral Optimal Control Software
GTO	Geostationary Transfer Orbit
HBVP	Hamiltonian Boundary Value Problem
IADC	Inter-Agency Space Debris Coordination Committee
IKAROS	Interplanetary Kite-craft Accelerated by Radiation Of the Sun
IPOPT	Interior Point Optimizer
ITU	International Telecommunication Union
JAXA	Japanese Aerospace Exploration Agency
KKT	Karush-Kuhn-Tucker
LEO	Low Earth Orbit
LG	Legendre-Gauss
LGL	Legendre-Gauss-Lobatto
NASA	National Aeronautics and Space Administration
NEXT	NASA's Evolutionary Xenon Thruster
NKO	Non-Keplerian Orbit

NLP	Non-Linear Programming
NOAA	National Oceanic and Atmospheric Administration
NSTAR	NASA Solar Technology Application Readiness
OBDH	Onboard Data Handling
ROGER	Robotic Geostationary Orbit Restorer
SEP	Solar Electric Propulsion
SERT	Space Electric Propulsion Test
SMART-1	First Small Mission for Advanced Research in Technology
SNOPT	Sparse Nonlinear OPTimizer
SQP	Sequential Quadratic Programming
TFSC	Thin Film Solar Cells
TRL	Technology Readiness Level
UN COPUOS	United Nations Committee on the Peaceful Uses of Outer Space

Variables

a	Semi-major axis
a_H	Parameter of the smooth Heaviside function
$\mathbf{a}$	Thrust-induced acceleration
A	Area
a_1, a_2, a_3, a_4	Constants
$\mathbf{a}_1, \mathbf{a}_2, \mathbf{a}_3, \mathbf{a}_4$	Vectors of constants
a_c	Solar sail characteristic acceleration
B	Non-Lambertian coefficient
b_1, b_2, b_3	Coefficients of solar sail parametric force model
c	Speed of light
c	Short notation for $\cos(k_2\theta + \phi)$
$\mathbf{c}$	Vector of path constraints
$\mathbf{C}$	Approximated vector of path constraints
c_1, c_2, c_3	Constants
cn	Short notation for $\text{cn}(k_2\theta + \phi, k)$

d	Earth to pole-sitter distance
$\tilde{d}$	Degradation factor
D	Differentiation matrix
dn	Short notation for $\mathrm{dn}\left(k_2\theta + \phi, k\right)$
e	Eccentricity
E	Eccentric anomaly
e_{trans}	Transformed eccentricity
f	Acceleration
$\mathbf{F}$	Force vector
$f_{\Delta i}$	Fraction of inclination change performed at periapsis
f_{other}	Fraction of dry mass for other spacecraft subsystems
$f_{penalty}$	Penalty on objective function
$\mathbf{g}$	General constraint vector
$\tilde{g}$	Solar sail reflectively coefficient
G	Universal constant of gravitation, 6.6738×10^{-11} m^3/(kg·s^2)
g_0	Earth standard gravitational acceleration at surface, 9.80665 m/s^2
h	Out-of-plane displacement
$\tilde{h}$	Solar sail reflectivity coefficient
H	Hamiltonian
H_1	Smooth Heaviside function
i	Inclination
i	Node number
i_{obl}	Obliquity of the ecliptic
I_{sp}	Specific impulse
J	Cost function
$\tilde{J}$	Expanded cost function

J_2	Oblateness coefficients of the Earth's gravitational field
$J_{2,2}$	Equatorial ellipticity coefficient of the Earth's gravitational field
k	Modulus of Jacobi elliptic function
k_{SA}	Solar array specific performance
k_{SEP}	SEP thruster specific performance
K	Periodicity of Jacobi elliptic function
k_0, k_1, k_2	Shape parameters of exponential sinusoids and expo-elliptic shape functions
L	Mission lifetime
L_g	Lagrangian
l_s	Solar sail side-length
L_N	Legendre polynomial of degree N
$L_\odot$	Solar luminosity
m	Mass
M	Mayer cost function
m_{gimbal}	Gimbal mass
$m_{mission,0}$	Spacecraft mass upon pole-sitter orbit injection
m_P	Power source mass
m_{pay}	Payload mass
m_{prop}	Propellant mass
m_{tank}	Propellant tank mass
n	Integer
n	Mean motion
N	Number of discretisation nodes
N	Number of orbital revolutions
N_i	Number of impulses per orbit
$\hat{\mathbf{n}}$	Solar sail normal vector

$\mathbf{p}$	Vector of parameters
P	Solar radiation pressure
P_o	Orbital period
p_e	Part of low-thrust spiral where inertial steering is applied
p_i	Part of low-thrust spiral where out-of-plane steering is applied
p_s	Part of low-thrust spiral where tangential steering is applied
$P_{SEP,\max}$	Maximum power required by SEP system
q	Constant
$\mathbf{r}$	Position vector
$\tilde{r}$	Portion of reflected photons
$\tilde{r}_s$	Portion of specularly reflected photons
$\hat{\mathbf{r}}_s$	Sun-sail unit vector
$\tilde{r}_{ns}$	Portion of non-specularly reflected photons
$R_\oplus$	Radius of the Earth
s	Short notation for $\sin(k_2\theta+\phi)$
sn	Short notation for $\mathrm{sn}(k_2\theta+\phi,k)$
t	Time
T	Time of flight
$\mathbf{T}$	Thrust vector
$\hat{\mathbf{t}}$	Tangential unit vector
t_L	Launch date
t_{obs}	Polar observation time
t_p	Time in between impulses
t_t	Time spent in transfer phase
$\mathbf{u}$	Control vector
U	Effective potential

$\mathbf{U}$	Approximated control vector
V	Gravitational potential
V	Velocity
w	Objective function weight
W	Solar energy flux
w_k	Gauss quadrature weights
x	X coordinate
$\mathbf{x}$	State vector
$\mathbf{X}$	Approximated state vector
$\mathbf{x}_{oe}$	State vector of orbital elements
y	Y coordinate
$\mathbf{y}$	Decision vector
z	Z coordinate
α	Pitch angle
α_c	Solar sail cone angle
β	Solar sail lightness number
γ	Flight path angle
$\gamma_{SEP,\max}$	Angle between Sun-sail line and solar sail normal vector when $T = T_{\max}$
δ	Yaw angle
Δd	Allowed approach distance to GEO
ΔL	Loss in mission lifetime
Δr	In-plane displacement
Δr_f	Error on final radius
ΔV_c	Velocity change for orbit circularisation
ΔV_i	Velocity change for inclination change
ΔV_{traj}	Velocity change in transfer trajectory

$\Delta\lambda$		Width of geostationary station keeping box
ε		Emissivity
ε_{new}		Margin for new technologies
ε_{old}		Margin for well-proven technologies
ζ		Vector of differential defects
η		Efficiency
θ		In-plane angle
θ		True anomaly
λ		Degradation constant
λ		Longitude
$\boldsymbol{\lambda}$		Vector of adjoint variables
$\lambda_{2,2}$		Coefficient related to the $J_{2,2}$ term of the Earth's gravitational field
$\tilde{\lambda}_k$		Karush-Kuhn-Tucker (KKT) multipliers
μ		Mass ratio
μ		Gravitational parameter of central body
$\boldsymbol{\mu}$		Vector of Lagrange multipliers associated with path constraints
$\boldsymbol{\nu}$		Lagrange multipliers associated with boundary conditions
ξ		Angle in pole-sitter orbit measuring from the summer solstice
ρ		Projected radius
σ		Mass to area ratio
Σ		Solar radiation dose
$\bar{\Sigma}$		Dimensionless solar radiation dose
$\hat{\Sigma}$		Half life solar radiation dose
σ^*		Critical sail loading, 1.53 g/m^2
τ		Fraction of maximum thrust magnitude
ϕ		Latitude
ϕ		Out-of-plane angle

ϕ	Shape parameter of exponential sinusoids and expo-elliptic shape functions
$\boldsymbol{\phi}$	Vector of boundary conditions
Φ	Scalar potential function
$\boldsymbol{\Phi}$	Approximated boundary conditions vector
φ_k	Lagrange interpolating polynomial
χ	Position of Earth on its orbit around the Sun measured from the winter solstice
ψ	Angle between Sun-Earth line and equatorial plane
ψ_t	Transfer angle
ω	Argument of perigee
$\boldsymbol{\omega}$	Angular velocity vector
Ω	Right ascension of the ascending node
ω_*	Angular velocity of Keplerian orbit with radius equal to non-Keplerian orbit radius

Subscripts, superscripts and other notations

Subscripts

a	Absorbed photons
A	Ascending node
$adapter$	Adapter
apo	At apoapsis
AU	At 1 Astronomical Unit (AU)
b	Back side of solar sail
C	Central body
D	Descending node
e	Re-emitted absorbed photons
E	In Earth fixed equatorial rotating reference frame
EC	In Earth fixed ecliptic inertial reference frame

EQ	In Earth fixed equatorial inertial reference frame
f	At final time
F	Fregat upper-stage
fr	Front side of solar sail
GEO	Geostationary orbit
GTO	Geostationary transfer orbit
h	Hybrid sail propulsion
i	Impinging photons
in	In-plane
int	Intermediate orbit
J	Due to combined J_2 and $J_{2,2}$ effects
J_2	Due to oblateness of Earth's gravitational field
$J_{2,2}$	Due to equatorial ellipticity of Earth's gravitational field
k	k^{th} discretisation node
I	In inertial reference frame
l	Lower bound
L	Value defined by Lambert problem
max	Maximum value
min	Minimum value
n	Normal to solar sail
N	North pole-sitter orbit
out	Out-of-plane
park	Parking orbit
peri	Periapsis
PS	Pole-sitter
r	Reflected photons
R	In rotating reference frame

$\tilde{r}$	Reflection coefficient
r, λ, ϕ	In radial, longitudal and latitudal direction
r, θ, ϕ	In radial direction, along the in-plane angle and along the out-of-plane angle
r, t, n	In radial, transverse and normal direction
s	Solar sail
S	South pole-sitter orbit
s, e, n	Referring to tangential, inertial and out-of-plane steering laws
SA	Solar array
SEP	SEP thruster
sp	In low-thrust spiral
t	Tangential to solar sail
t	In transfer phase
$target$	Target orbit
TF	Thin film solar cells
$tilted$	Tilted pole-sitter orbit
u	Upper bound
$upper\text{-}stage$	Upper-stage
x, y, z	In x, y and z direction
$year$	Duration of one year
0	At initial time
$1, 2$	Referring to smaller and larger body
∞	At infinite time
$\oplus$	Earth
$\odot$	Sun

Superscripts

$-$	Prior to impulse
$+$	After impulse
$*$	Optimal

Other notations

$\dot{\square}$	First order derivative
$\ddot{\square}$	Second order derivative
$\hat{\square}$	Unit vector
$\bar{\square}$	Averaged value
$\Delta\square$	Indicating change in variable

List of figures

List of tables

Chapter 1

Introduction

In this first chapter, the research objectives of the thesis will be defined. To this end, the limitations of Keplerian orbits for particular space applications will be discussed in Section 1.1, in particular for geostationary orbit and polar observation. This discussion is used to define the research objectives in Section 1.2. Section 1.3 will subsequently highlight the contributions of this thesis, while Section 1.4 will provide an overview of the journal and conference papers in which these contributions have been published. Finally, in Section 1.5 an outline of the thesis will be presented.

1.1   Limitations of Keplerian orbits

Only a century ago, the wealth of space applications that are at our disposal today was unthinkable. However, the foundations were laid at that time by the Soviet pioneer of astronautics, Konstantin Eduardovich Tsiolkovsky. In 1897 he developed the *rocket equation* which describes the motion of a body of variable mass, and later used this in his most important work, *The exploration of cosmic space by means of reaction devices*,[1] to show that an orbit around the Earth could be achieved by means of a multi-stage rocket, fuelled by liquid oxygen and liquid hydrogen. The work of Tsiolkovsky and his followers, Hermann Oberth (*Wege zur Raumschiffahrt* (Ways to Spaceflight)) and Robert H. Goddard (*Method of Reaching Extreme Altitudes*),[2] resulted in an international space exploration movement. They are therefore rightfully considered the founding fathers of modern rocketry. However, it would take until 1942, during World War II, for the first human-made object, a German V2 rocket, to reach space,[3] and it would take another 15 years, until 1957, before the first satellite, Sputnik 1, was delivered into orbit around the Earth. From then, the American and

Soviet space programs escalated, resulting in a range of experimental missions, followed by the first successful Soviet human spaceflight in 1961, the first flyby of another planet (Venus) in 1962 and the American Moon landing in 1969.[4]

Besides these historic milestones, the 1960s also saw the launch of a set of Earth orbiting satellites that, for the first time, provided satellite applications of wide public benefit. For example, 1960 brought the first successful navigation satellite (Transit 1B), the first communication satellite (Echo 1) and the launch of the first meteorological satellite (Tiros 1).[4, 5] Since then, the number of satellites, services and the quality of these services have increased beyond expectation: not only do satellites provide key public and commercial services, they also provide crucial applications to significantly enhance life on Earth. Examples include the use of space data for disaster monitoring, water resource management, air quality assessments, forestry health assessments and climate change investigations.

However, after half a century of space development, the limitations of some space resources such as geostationary orbit, have been reached. And many other limitations are still limitations to overcome, for example in order to significantly enhance polar observations. Both issues will be addressed in more detail in the next two subsections, which then flow into the research objectives of this thesis.

1.1.1 Displaced geostationary orbits

The concept of geostationary orbit (GEO) was first noted in the literature in 1929 by Hermann Noordung (pseudonym for Hermann Potočnik) in his book *Das Problem der Befahrung des Weltraums - der Raketen-Motor* (The problem of space travel – the rocket motor).[6] He describes a satellite in this unique stationary orbit as "the pinnacle of a enormously high tower that would not even exist but whose bearing capacity would be replaced by the effect of centrifugal force". It would eventually take another 35 years to make this pinnacle reality.

In 1964, Syncom-3 became the first geostationary satellite,[7] and since then many communication and weather satellites have exploited the unique properties of geostationary orbit. With an orbit period equal to the Earth's rotational period, spacecraft in GEO are stationary with respect to an observer on the Earth, allowing for a continuous downlink to terrestrial communications users. This makes GEO ideal to host satellites for telecommunication and Earth observation applications and is therefore one of the most important and valuable regions in space.[8]

However, with only one such unique orbit and the high demand for geostationary slots, GEO is starting to become congested. Jehn et al.[9] report the status of geostationary orbit in January 2009 and provide the distribution of the 335 actively controlled satellites (for which the orbital position is known) on geostationary orbit, see Fig. 1.1. The figure shows concentrations of satellites over Europe, Asia and the United States, and clearly illustrates the congestions of geostationary orbit, except for a small unoccupied band above the Pacific. Despite this, the population of geostationary spacecraft is still growing. As an example, in 2008, 29 geostationary mission were launched, while only 12 reached their end-of-life.[9]

Guidelines drawn up by organisations such as the Inter-Agency Space Debris Coordination Committee (IADC),[10] the United Nations Committee on the Peaceful Uses of Outer Space (UN COPUOS)[11] and the International Telecommunication Union (ITU)[12] request that spacecraft are removed from densely populated orbital regions (such as GEO) once they have reached their end-of-life to prevent further congestion of the geostationary zone. For this, and because no effective natural removal mechanism (such as atmospheric drag) exists in GEO, satellites have to be actively transferred away from the geostationary ring, which is the reason that many operators do not or cannot comply with these regulations.[13] Again, taking the example of the 12 satellites that reached their end-of-life in 2008, only 7 were disposed of in accordance with IADC guidelines.[9] Fig. 1.2, which is also taken from Reference 9, shows the resulting number of uncontrolled GEO satellites in January 2009. In total, 1186 objects occupied the geostationary zone. The situation becomes even worse when considering the fact that, besides these (un)controlled satellites, geostationary orbit also contains fragmentation debris, expended upper-stages and other mission-related objects.
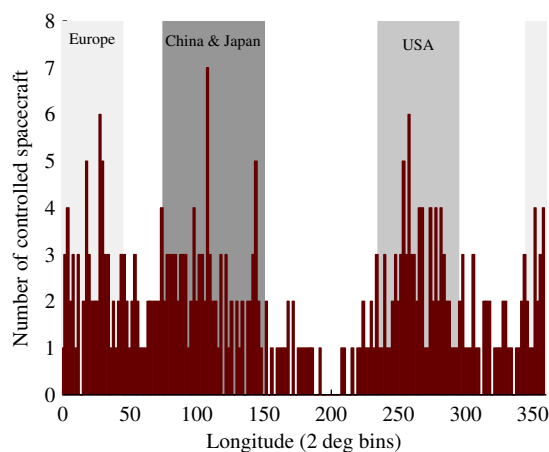
Fig. 1.1 Distribution of longitude of actively controlled GEO satellites in January 2009.[9]
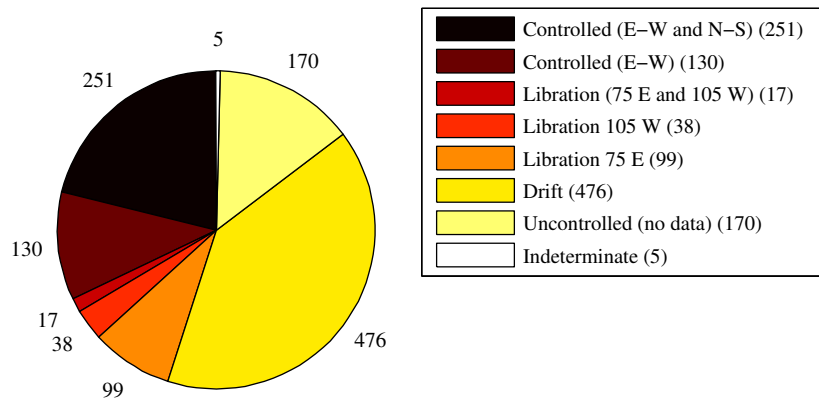
Fig. 1.2 Number of controlled and uncontrolled satellites in GEO in January 2009.[9]

In order to cope with this congestion of GEO, studies have been undertaken to investigate the possibility of debris removal missions such as the Robotic Geostationary Orbit Restorer (ROGER) concept of the European Space Agency (ESA).[14] In addition to such studies and missions, the aim of this thesis is to investigate other solutions in order to comply with the ever growing demand for new geostationary slots: in particular, the possibility of using displaced non-Keplerian orbits to displace spacecraft either above/below GEO or in the equatorial plane is investigated to generate new geostationary slots.

The concept of displaced geostationary orbits was first noted by Forward,[15] who proposed the use of a solar sail (see Section 2.2.2) to levitate a spacecraft above or below the equatorial plane. However, in his analysis, Forward neglects the solar sail acceleration component parallel to the equatorial plane, causing claims that levitated geostationary orbits are not feasible.[16, 17] In more recent work by Baig and McInnes[18] this in-plane component is used to generate a periodic orbit. Still, a residual in-plane sail acceleration causes the spacecraft to move with respect to an observer on the Earth. Furthermore, for near-future solar sails, only small displacements, still well inside the geostationary station-keeping box appear feasible. Improvements in the concept of displaced geostationary orbits are thus still to be made.

1.1.2   Pole-sitter orbits

The polar regions of the Earth play a critical role in shaping the Earth's climate system and can therefore provide answers to key questions concerning global climate change. Observations of the poles are therefore crucial: continuous data are essential to identify

changes in the polar environment in terms of sea-ice coverage and thickness, to analyse long-term climate trends and to be able to model and predict future cryospheric processes.

Due to the remoteness of the polar regions, obtaining such data in situ is difficult and observations of the poles have therefore long been impossible until the launch of the first polar orbiting satellite, Discoverer 1, in 1959.[19] Since then, a range of satellites for general atmospheric and environmental research have been launched into low-altitude polar orbits, as well as satellites devoted to glaciology and ice-pack monitoring, such as NASA's ICESat-1 mission (2003 – 2010)[20] and ESA's Cryosat-2 mission (2010 – ongoing).[21] Although enabling high spatial resolution observations, the low-altitude of the polar orbits restricts spacecraft to observe only narrow swaths of the polar regions during each passage. Therefore, to obtain a full view of the polar regions, images from different passages have to be patched together to form so-called composite images or mosaics,[22] see Fig. 1.3a, which have poor temporal resolution. As an example, ESA's CryoSat mission orbits the Earth with repeated ground tracks of 369 days, with a sub-cycle of 33 days, only after which uniform coverage of the polar regions is obtained.

a)   b)
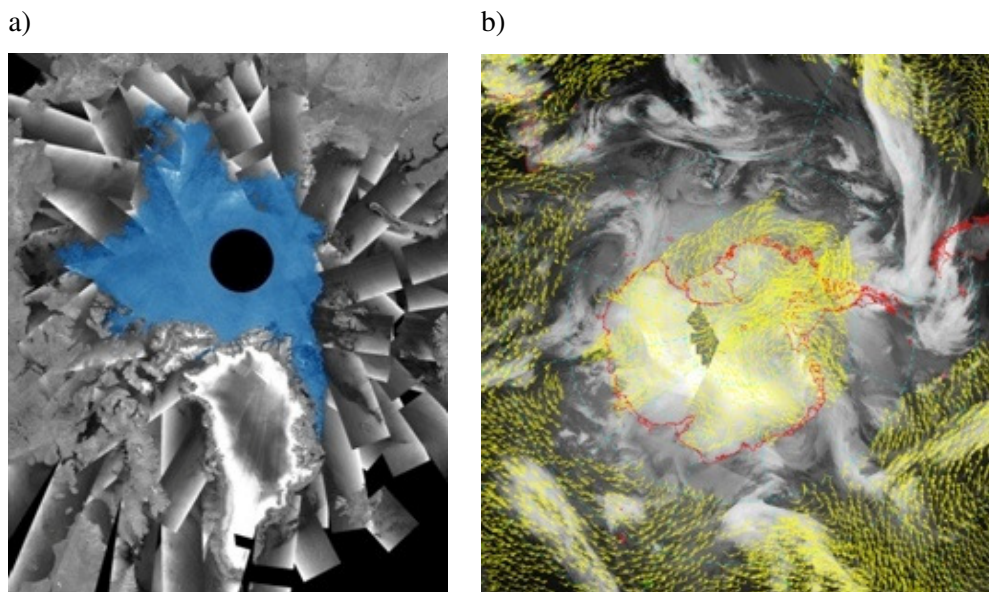
Fig. 1.3 a) Mosaic of Envisat ASAR radar images of arctic ice.[22] b) Atmospheric motion vectors (AMV) from geostationary satellite observations on the periphery and from polar-orbiting satellite observations over the Antarctic continent.[23]

Besides their key role in understanding global climate change, the polar regions are also of importance from a geo-political point of view. It is expected that 30 percent of the world's undiscovered gas and 13 percent of the world's undiscovered oil are located in the Arctic.[24] Therefore, exploration of these areas will occur in the coming decades and means have to be

put in place to ensure management of these regions and to support telecommunications, weather forecasting and ship navigation. An increase in shipping activity can also be expected from the fact that the northern sea routes are opening up due to climate change, thereby providing a fast and economic passage between the Atlantic Ocean and Pacific Ocean.[25]

Normally, applications such as telecommunications and weather forecasting are provided by satellites in GEO that provide high temporal resolution. However, GEO platforms can only provide these services in the equatorial and temperate zones, where elevation angles are sufficiently high.[8] Even augmenting GEO coverage with polar satellite coverage results in incomplete data, as is illustrated in Fig. 1.3b for the detection of atmospheric motion vectors over the Antarctic continent.[23]

A compromise between polar and geostationary satellites is the Molniya orbit,[8] which is an eccentric orbit with apocenter at a distance that is comparable to GEO, thereby providing a much higher temporal resolution than polar satellites. It has the unique property that the argument of perigee remains fixed under the influence of the Earth's oblateness, which restricts the inclination to a critical value of 63.4° or 116.6°. Depending on the application (i.e. remote sensing or telecommunications), and therefore on the required field of view, satisfactory coverage of the polar caps or high-latitude regions cannot always be achieved. Furthermore, using one spacecraft, continuous coverage can also not be obtained. Recent research[26] has attempted to improve some of the limitations of the Molniya orbit by changing its critical inclination to 90° by applying a continuous acceleration provided by a solar electric propulsion system (see Section 2.2.1). Analyses showed that these polar Molniya orbits allow continous, high elevation observation above 55 deg latitude using three spacecraft, while a conventional Molniya orbit would require in excess of fifteen spacecraft.[27]

In addition to the traditional polar orbiting, GEO and Molniya spacecraft, the literature shows several other concepts for polar observations that rely on artificial displaced equilibria,[28] non-Keplerian orbits[29] and vertical Lyapunov orbits or so-called eight-shaped orbits.[30, 31] A thorough comparison of all these concepts is provided in Reference 30, which shows that none of the mission concepts achieve satisfactory conditions for continuous coverage of the high-latitude regions using one single spacecraft.

The only platform that would be able to generate these conditions is one that is constantly above one of the poles, stationary with respect to the Earth, in the same way as a GEO spacecraft is stationary above one point on the equator. This spacecraft is known in the

literature as a *pole-sitter*,[32] which uses low-thrust propulsion to maintain a position along the polar axis, counterbalancing mainly the gravitational attraction of the Earth and Sun. The key advantages of the pole-sitter concept are, firstly, the fact that it requires only a *single spacecraft* for continuous polar coverage. Second, since the minimum latitude observed is only limited by the minimum elevation angle required, the pole-sitter platform provides *continuous* coverage at much lower latitudes than concepts such as the Molniya and polar Molniya orbits. And finally, the pole-sitter spacecraft is *stationary* with respect to ground stations on Earth, removing the need for active tracking of the satellite. It is these advantages that make the pole-sitter concept highly promising and worth investigating further.

However, the ability of continuous, stationary coverage of nearly the entire hemisphere comes at the cost of a decrease in spatial resolution. In order to limit the acceleration required for maintaining the pole-sitter position, the Earth-spacecraft distance is in the order of 1.5 million km. At such large distances, the available spatial resolution is limited. However, within the UV to near-IR range, the resolution should be in the order of a few kilometres.[30] According to Lazzara et al.,[23] this would significantly enhance polar environmental remote sensing for meteorological forecasting, to identify and track storm systems and to close the gap in atmospheric motion vectors as shown in Fig. 1.3b. Clearly, glaciology and ice-pack monitoring would also significantly benefit. Furthermore, the pole-sitter could contribute to space weather monitoring for which auroral conditions need to be monitored continuously, since they can change rapidly and as such have major impacts on radar operations and communications. Moreover, it could establish a critical communication link and navigation services for the expected increase in Arctic shipping activity as noted earlier. Finally, a pole-sitter can serve as a data relay with polar regions, for example for Antarctic research activities that also require links to automated weather stations, emergency airfields and for telemedicine.

The pole-sitter concept was first proposed in the literature by Driver[33] and later by Forward.[28] However, an extensive investigation of optimal pole-sitter orbits and their control has only recently been performed by Ceriotti and McInnes[32] for the use of both pure solar electric propulsion and hybrid sail propulsion (see Section 2.2.3). They established optimal pole-sitter orbits that follow the polar axis during the year, but allow the distance between the Earth and spacecraft to change for fuel efficiency, as well as a feedback control system to show that the orbit is controllable under unexpected conditions such as injection errors and temporary failure of the thruster.[34]

Although the in-orbit phase of the pole-sitter mission has been studied in detail, the transfer from Earth to access the pole-sitter orbit is largely unexplored. Golan and Breakwell[35] investigated locally optimal transfers from a circular low Earth orbit (LEO) to a so-called 'pole-squatter', which is a highly elliptic orbit with apogee in the order of 100 Earth radii, and thus not a true pole-sitter. Also Hughes[36] investigated transfers to an orbit for polar observation. However, again, this so-called 'polar observer orbit' is not a true pole-sitter: it is synchronous with the orbit of the Earth around the Sun, but does not follow the polar axis throughout the year. This thesis therefore aims to provide a new approach to investigate optimal transfers from LEO to the true pole-sitter orbits found by Ceriotti and McInnes. Note that the transfer will start from LEO in order to allow for realistic launch vehicle performances to be included in the transfer design. Also, while Golan and Breakwell only considered solar electric propulsion (SEP) to enable the transfers and Hughes investigated the use of a solar sail, this thesis will consider a novel propulsion concept where SEP is hybridised with a solar sail.

Another issue addressed in this thesis is related to limitations in polar observations introduced by the tilt of the polar axis. Due to this tilt, the polar regions are alternately situated in darkness for long periods during the year. Clearly, for observations in the visible spectrum, this significantly constrains observation and limits the scientific return of the mission. The final aim of this thesis is therefore to investigate ways to transfer between pole-sitter orbits above the north and south poles before the start of their respective winters, such that unfavourable conditions above one of the poles are exchanged for favourable conditions above the opposite pole.

Besides the increased scientific return that these transfers can deliver, they can serve an additional purpose. Although polar observations from LEO cannot provide the continuous coverage required for a range of applications, they do have the advantage of visiting both the north and south poles with one single spacecraft. A similar mission objective can be achieved for the pole-sitter spacecraft by dividing the mission into segments where each segment is devoted to the observation of one of the Earth's poles.

1.2   Thesis research objectives

From the discussion of geostationary orbits in Section 1.1.1 and the requirement for polar coverage in Section 1.1.2, the following research objectives can be defined:

Displaced geostationary orbits
- Investigate the use of displaced non-Keplerian orbits to provide a solution to the congested geostationary orbit that provides true geostationary conditions, outside the geostationary station-keeping box.
- In order to enable these orbits, investigate and compare the use of different propulsion strategies with particular focus on hybridised SEP and solar sail propulsion, and (where applicable) optimise their performance.
- Investigate optimal transfers to these orbits in order to assess their accessibility.

Pole-sitter orbits
- Investigate optimal transfers from LEO to true pole-sitter orbits in order to evaluate their accessibility and to allow for a determination of mission performance in terms of payload capacity and/or mission lifetime.
- To overcome limitations in the observations from pole-sitter orbits during the Arctic and Antarctic winters, investigate optimal transfers between orbits positioned above the north and south poles to only observe the pole that is illuminated.
- In order to enable both types of transfers, investigate and compare the use of different propulsion strategies with particular focus on hybridised SEP and solar sail propulsion.

1.3   Contributions of thesis

In this thesis, the potential of non-Keplerian orbits to overcome limitations of Keplerian orbits for future geostationary coverage and improved polar observations is demonstrated and transfers to these orbits are designed to prove the feasibility of the different concepts and to improve their performances. In particular, displaced geostationary orbits and pole-sitter orbits are investigated. In all the analyses, the use of a highly-novel type of propulsion (i.e. hybrid sail propulsion) is proposed and its potential demonstrated through a thorough comparison of its performance with conventional types of propulsion.

Displaced geostationary orbits
The literature has already proposed displaced geostationary orbits as solution to the congestion of geostationary orbit. However, in all cases, only solar sailing is considered as a

method to generate the required acceleration for maintaining the displaced GEO, which cannot achieve true geostationary conditions and cannot levitate the orbit outside the geostationary station keeping box when using near-term solar sails. By using or adding an unconstrained type of propulsion system such as pulsed (i.e. chemical) propulsion or solar electric propulsion, this thesis shows that true geostationary conditions outside the geostationary station-keeping box can be achieved. This is demonstrated for a range of displaced geostationary orbits (i.e. out-of-plane and in-plane displaced GEOs and for a range of displacement distances). A mission analysis and systems design approach is developed to provide, for the first time, an end-to-end investigation of displaced GEO by investigating the performance of different types of propulsion system in terms of mission lifetime versus the initial-to-final mass fraction, specific impulse and payload mass. In all analyses, the potential of hybrid sail propulsion for a displaced GEO mission is proven and by considering a range of solar sail lightness numbers, both near-term and far-term solutions are presented.

Within the analyses, a set of novel transfers are identified that can significantly improve the performance of a displaced GEO mission and can ensure accessibility of displaced GEO. These transfers include transfers between non-Keplerian orbits and between Keplerian and non-Keplerian orbits for which the optimal control problem is solved and the promising performance of hybrid sail propulsion is once more demonstrated.

Pole-sitter orbits

Recent studies have shown the feasibility of an Earth pole-sitter mission where a spacecraft follows the Earth's polar axis to provide a continuous, hemispherical view of one of the Earth's poles. The transfer to this pole-sitter orbit, which is required in order to determine the mass that can be delivered to such a novel orbit, has not been investigated. Only transfers to highly elliptic orbits and Earth synchronous orbits, as approximation to a pole-sitter orbit, have been considered. This thesis therefore provides, for the first time, the design of low-thrust transfers to true pole-sitter orbits. A novel approach is developed that, firstly, divides the transfer into a launch phase and a transfer phase. Subsequently, for the launch phase, realistic launch vehicle performances are derived and the two phases are rejoined in the optimal control problem. This allows to design trajectories that are optimal from LEO to the pole-sitter. A large design space is considered by investigating different pole-sitter orbits and different launch strategies. For the latter, both high-thrust and low-thrust approaches are investigated using either a launch vehicle upper-stage or a low-thrust spiral. Furthermore, different performance indices are considered, including minimising the mass required in

LEO to deliver a predetermined mass into the pole-sitter orbit and maximising the mass injected into the pole-sitter orbit by fully exploiting the performance of the launch vehicle.

To optimise the transfer for these objective functions, a new shape-based approach is developed for generating the initial guess. This shape is a generalisation of the existing exponential sinusoidal (exposin) shape and is proven to outperform the exposins for a range of test cases, including the transfer to the pole-sitter.

The results are generated for different types of propulsion system to highlight the benefits of hybrid sail propulsion. They can be used for an end-to-end mission analysis and systems design of both a near-term and far-term pole-sitter mission, depending on the sail technology chosen.

Finally, another novel transfer is introduced in this thesis that transfers the pole-sitter spacecraft between pole-sitter orbits above the north and south poles to only hover above the pole that is illuminated at that time. The feasibility of such a transfer is demonstrated and the improved performance of hybrid sail propulsion over conventional types of propulsion is once again demonstrated. A set of transfers, trading off propellant consumption and observational time, is generated that can be substituted into the pole-sitter mission at appropriate locations and will be shown to enable an extension of the pole-sitter mission due to their limited propellant consumption.

1.4   Published work

The contributions mentioned in the previous section have been published in the following journal and conference papers.

Journal papers
- Heiligers, J., Ceriotti, M., McInnes, C.R., and Biggs, J.D., *Displaced Geostationary Orbit Design Using Hybrid Sail Propulsion*, Journal of Guidance, Control, and Dynamics, 2011 Volume 34, No. 6, Pages 1852-1866, DOI 10.2514/1.53807.
- McInnes, C., Ceriotti, M., Colombo, C., Sanchez Cuartielles, J., Bewick, R., Heiligers, J., and Lucking, C., *Micro-to-Macro: Astrodynamics at Extremes of Length-scale*, Acta Futura, 2011, Volume 4, Pages 81-97, DOI 10.2420/AF04.2011.81.
- Heiligers, J., Ceriotti, M., McInnes, C.R., and Biggs, J.D., *Displaced Geostationary Orbits Using Hybrid Low-thrust Propulsion*, Acta Astronautica, 2012, Volume 71, Pages 51-67, DOI 10.1016/j.actaastro.2011.08.012.

- Heiligers, J., Ceriotti, M., McInnes, C.R., and Biggs, J.D., *Design of Optimal Earth Pole-sitter Transfers Using Low-thrust Propulsion*, Acta Astronautica, 2012, Volume 79, Pages 253-268, DOI 10.1016/j.actaastro.2012.04.025.
- Ceriotti, M., Heiligers, J., and McInnes, C.R., *Trajectory and Spacecraft Design for a Pole-Sitter Mission*, Journal of Spacecraft and Rockets, 2012, accepted subject to minor corrections.
- Heiligers, J., Ceriotti, M., McInnes, C.R., and Biggs, J.D., *Mission Analysis and Systems Design of a Near-term and Far-term Pole-sitter Mission*, Acta Astronautica, 2012, in press.

Conference papers

- Heiligers, J., *Displaced Geostationary Orbits Using Hybrid Low-thrust Propulsion*, 61st International Astronautical Congress, 2010, Prague, Czech Republic.
- Heiligers, J., Ceriotti, M., McInnes, C.R., and Biggs, J.D., *Design of Optimal Earth Pole-sitter Transfers Using Low-thrust Propulsion*, 62nd International Astronautical Congress, 2011, Cape Town, South Africa.
- Heiligers, J., Ceriotti, M., McInnes, C.R., and Biggs, J.D., *Design of Optimal Transfers Between North and South Pole-sitter Orbits*, 22nd AAS/AIAA Spaceflight Mechanics Meeting, 2012, Charleston, South Carolina, USA.
- Heiligers, J., Ceriotti, M., McInnes, C.R., and Biggs, J.D., *Mission Analysis and Systems Design of a Near-term and Far-term Pole-sitter Mission*, 1st IAA Conference on Dynamics and Control of Space Systems, 2012, Porto, Portugal.
- Ceriotti, M., Heiligers, J., and McInnes, C.R., *Novel Pole-sitter Mission Concepts for Continuous Polar Remote Sensing*, SPIE Remote Sensing, 2012, Edinburgh, United Kingdom.

1.5   Thesis structure

In order to investigate the thesis research objectives defined in Section 1.2, Chapter 2 will provide necessary background information, including a discussion on the theory and applications of non-Keplerian orbits, an overview of different types of low-thrust propulsion to enable these non-Keplerian orbits and an outline of the optimal control problem that needs to be solved in order to optimise the use of low-thrust propulsion.

Building upon this background information, the remainder of this thesis can be divided into two main parts: the first part covers Chapter 3 and Chapter 4 and focuses on the design of displaced geostationary orbits and the transfers involved with this concept. The second part spans Chapter 5 to Chapter 7 and investigates optimal transfers to and between Earth pole-sitter orbits.

In Chapter 3, the concept of the displaced geostationary orbit will be discussed and both out-of-plane and in-plane displaced GEOs will be defined. For comparison purposes, the performance of both types of orbit will be assessed for the use of conventional types of propulsion, including impulsive and pure solar electric propulsion, and hybrid sail propulsion. This performance will be investigated in terms of mission lifetime and a mass budget analysis allows the calculation of the payload mass capacity. Finally, the performance in displaced GEO is assessed under the influence of perturbations such as the non-uniformity of the Earth's gravitational field and non-ideal properties of the solar sail.

In Chapter 4, the transfer to the displaced geostationary orbits designed in Chapter 3 will be considered in order to investigate their accessibility. In addition, two other transfers will be investigated that can improve the performance of hybrid sail propulsion and the performance of higher displaced orbits. Initially, the use of pure SEP will be considered, but this is later extended to the use of hybrid sail propulsion. For all three types of transfers the optimal control problem is defined and a suitable initial guess is derived to eventually solve the optimal control problem using both a direct and indirect optimisation method for validation purposes.

Chapter 5 marks the start of the second part of this thesis and presents the design of optimal Earth to pole-sitter transfers. The chapter starts by introducing the pole-sitter mission concept and defines a set of pole-sitter orbits that will be considered in this thesis, including constant altitude, tilted and optimal-fuel pole-sitter orbits. Subsequently, the design approach is presented, dividing the transfer into two phases, a high-thrust launch phase and a low-thrust transfer phase. The optimal control problem in the transfer phase is solved for two different types of objective functions to either minimise launch mass or maximise injected mass. To solve the optimal control problem, a novel shape-based approach will be presented and its applicability demonstrated. Both pure SEP and hybrid sail transfers will be considered to outline the potential of hybrid sail propulsion and the results will be validated.

In Chapter 6 the high-thrust launch phase will be replaced by a low-thrust, minimum-time, multi-revolution spiral. The design approach, that includes the use of locally optimal steering laws and orbital averaging, will be outlined and the optimal control problem to be solved in the spiral will be derived. Using pure SEP, the results in terms of launch mass savings and gains in injected mass will be presented. The orbital averaging technique will be critically reviewed and additional optimisations to refine the low-thrust spiral will be performed.

Finally, in Chapter 7, the transfer to overcome limitations in the observations from the pole-sitter orbit during the polar winters will be investigated. First, two types of transfers, i.e. a

short duration and long duration transfer, will be defined for which the optimal control problem and suitable initial guesses will be derived. First, minimum SEP propellant transfers will be sought and will be presented for both the use of SEP and hybrid propulsion. Then, additional transfers, that trade-off propellant consumption and useful observation time per pole, will be investigated and all results will be validated.

Each separate chapter finishes with conclusions, which come together in the overall conclusions at the end of this thesis as well as a discussion on future work.

Chapter 2
Non-Keplerian orbits

In order to investigate the research objectives defined in the previous chapter, this chapter introduces the theoretical background that will be used throughout this thesis. In particular, the theory on non-Keplerian orbits (NKOs) will be discussed in Section 2.1. A discussion of various types of low-thrust propulsion that can be employed to enable these NKOs is provided in Section 2.2. Finally, the definition of and ways to solve optimal control problems to optimise the use of low-thrust propulsion are described in Section 2.3.

2.1   Non-Keplerian orbits

In order to properly introduce the concept of non-Keplerian orbits, this section will begin with a discussion on the natural motion of spacecraft in both the two- and three-body problems. Subsequently, the use of low-thrust propulsion will be considered to perturb the two- and three-body problems and generate the sought for non-Keplerian orbits.

2.1.1   Natural motion

Two-body problem
The natural motion of a smaller body around a larger, central, body were first described when Johannes Kepler published two empirical laws about the orbits of planets around the Sun in his 1609 work *Astronomia Nova De Motibus Stellae Martis*.[37] He based his laws on long-term and precise observations of planetary motion taken by Tycho Brahe.[38] Later, in 1619, Kepler added a third empirical law to these, resulting in the following well-known laws:[38]

- Kepler's first law: The orbit of a planet is an ellipse with the Sun at one of the foci
- Kepler's second law: The radius vector of a planet sweeps out equal areas in equal intervals of time
- Kepler's third law: The ratio between the square of the period and the cube of the major axis of the elliptic orbit is equal for all planets

These laws were validated in 1686 when Isaac Newton published his *Philosophiæ Naturalis Principia Mathematica*,[39] which includes Newton's laws of motion and Newton's law of gravitation. The latter states that two point masses, m_1 and m_2, attract one another with a force that is directly proportional to the product of their masses and inversely proportional to the square of the distance between them. In terms of acceleration and in vectorial form, this results in:

$$\ddot{\mathbf{r}} = -\frac{\mu_C}{r^3}\mathbf{r} \tag{2.1}$$

with $\mathbf{r}$ the vector pointing from the larger, central body (body 1) to the smaller body (body 2), see Fig. 2.1, and $\mu_C = G(m_1 + m_2)$ with $G = 6.67384 \times 10^{-11}$ m^{3}kg^{-1}s^{-2} the gravitational constant. However, since for many practical applications $m_2 \ll m_1$, the parameter μ_C can be reduced to $\mu_C = Gm_1$ and is called the gravitational parameter of the central body.
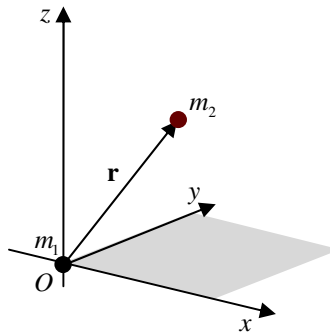
Fig. 2.1 Schematic of two-body problem.

The analytical solution to Eq. (2.1) is referred to as a Keplerian orbit and is a conic section, which was derived in detail by Leonhard Euler in 1744.[40] The most common notation of the orbit is through the use of the six traditional Keplerian elements: the semi-major axis, a, the eccentricity, e, the inclination, i, the right ascension of the ascending node, Ω, the argument of periapsis, ω, and the true anomaly, θ, as illustrated in Fig. 2.2. The type of

conic section described by the smaller body depends solely on the value for the eccentricity: $e = 0$ (circle), $0 < e < 1$ (ellipse), $e = 1$ (parabola) and $e > 1$ (hyperbola).[38]
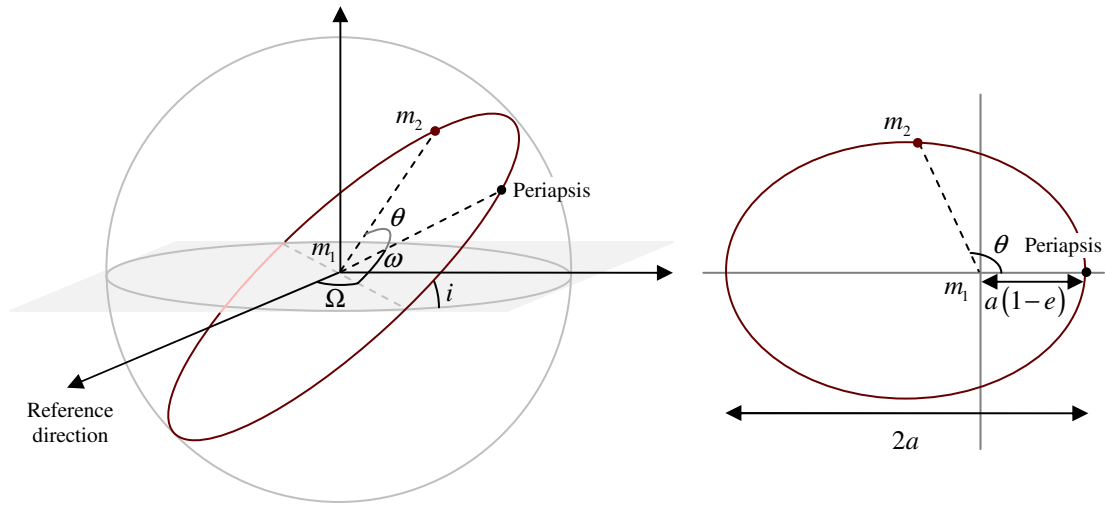
Fig. 2.2 Schematic of Keplerian elements. a) Three dimensional representation. b) Projection on the orbital plane.

Circular restricted three-body problem

Despite Kepler's and Newton's contributions to astrodynamics, the two-body problem can not accurately determine the motion of the planets around the Sun since it does not account for the masses of the other planets. Because for many applications the influence of a second large body cannot be neglected, another commonly used model is the circular restricted three-body problem (CR3BP).[38] Although, due to the introduction of the influence of the second large body, the problem is not Keplerian anymore, it is still considered to be "natural motion".

In the CR3BP the natural motion of an infinitely small mass, m, (i.e. the spacecraft), is described under the influence of the gravitational attraction of two much larger primary masses, m_1 and m_2. The gravitational influence of the small mass on the larger masses is neglected and the larger masses are assumed to move in circular orbits about their common centre-of-mass. Examples of CR3BPs are the Sun-Earth CR3BP, where the Sun represents m_1 and the Earth m_2, and the Earth-Moon CR3BP, where the Earth represents m_1 and the Moon m_2.

Fig. 2.3 shows the reference frame that is employed in the CR3BP: the origin coincides with the centre-of-mass of the system, the x-axis connects the larger masses and points in the direction of the smaller of the two, m_2, while the z-axis is directed perpendicular to the

plane in which the two larger masses move. The y-axis completes the right handed reference frame. Finally, the frame rotates at constant angular velocity, ω, about the z-axis, $\boldsymbol{\omega} = \omega \hat{\mathbf{z}}$.

New units are introduced: the sum of the two larger masses is taken as the unit of mass, i.e. $m_1 + m_2 = 1$. Then, with the mass ratio $\mu = m_2 / (m_1 + m_2)$, the masses of the large bodies become $m_1 = 1 - \mu$ and $m_2 = \mu$. As unit of length, the distance between the main bodies is selected, and $1/\omega$ is chosen as unit of time, yielding $\omega = 1$, and so one year is represented by 2π. In this reference system, the motion of the spacecraft is described by:

$$\ddot{\mathbf{r}} + 2\boldsymbol{\omega} \times \dot{\mathbf{r}} + \boldsymbol{\omega} \times (\boldsymbol{\omega} \times \mathbf{r}) = -\nabla V \tag{2.2}$$

with $\mathbf{r} = \begin{bmatrix} x & y & z \end{bmatrix}^T$ the position vector of m. The terms on the left hand side are the kinematic, coriolis and centripetal accelerations, respectively, while the term on the right hand side is the gravitational acceleration exerted by the primary masses. The latter is given by the gradient of the gravitational potential, V:

$$V = -\left(\frac{1-\mu}{r_1} + \frac{\mu}{r_2} \right) \tag{2.3}$$

Since the centripetal acceleration in Eq. (2.2) is conservative, it can be written as the gradient of a scalar potential function, $\Phi = -\frac{1}{2} \| \boldsymbol{\omega} \times \mathbf{r} \|^2$, and can be combined with the gravitational potential into a new, effective potential, U:

$$U = -\frac{x^2 + y^2}{2} - \left(\frac{1-\mu}{r_1} + \frac{\mu}{r_2} \right) \tag{2.4}$$

with $\mathbf{r}_1 = \begin{bmatrix} x + \mu & y & z \end{bmatrix}^T$ and $\mathbf{r}_2 = \begin{bmatrix} x - (1-\mu) & y & z \end{bmatrix}^T$. The new set of equations of motion then become:

$$\ddot{\mathbf{r}} + 2\boldsymbol{\omega} \times \dot{\mathbf{r}} + \nabla U = 0 \tag{2.5}$$

These equations do not have a closed form solution, but yield five equilibrium solutions (Lagrange points) when $\nabla U = 0$.[38]
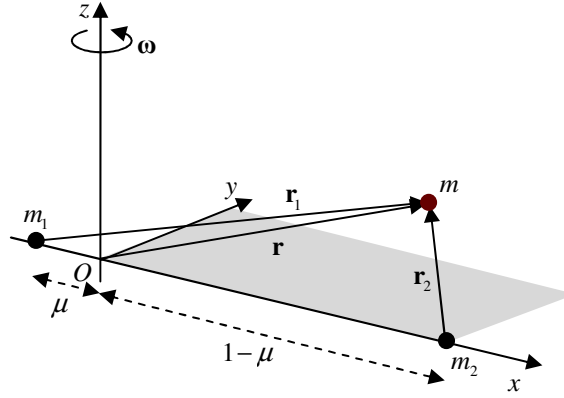
Fig. 2.3 Schematic of circular restricted three-body problem.

2.1.2   Non-Keplerian motion

In reality, the actual motion of a satellite will slightly deviate from natural motion due to perturbations such as non-spherical properties of the central body, atmospheric drag, and solar radiation pressure.[8] In addition, using a propulsive force, the satellite can deliberately be forced to deviate from a natural path, opening up a wealth of new orbits for the spacecraft motion about the central body. In that case the orbit is referred to as non-Keplerian. A particular subset of non-Keplerian orbits are displaced NKOs where a continuous acceleration is applied perpendicular to or in the orbit plane to displace the orbit from the natural Keplerian orbit in the two-body problem.[41]

The dynamics of such two-body displaced NKOs can be investigated by considering the equations of motion of the spacecraft in a rotating frame of reference. Equilibrium solutions of these equations of motion will then provide the sought for displaced NKOs and a transformation to an inertial frame will subsequently show that the spacecraft executes a circular orbit displaced away from the natural Keplerian orbit.[42] Fig. 2.4 shows these reference frames where $R(x_R, y_R, z_R)$ is a frame of reference that rotates with constant angular velocity $\boldsymbol{\omega} = \omega \hat{\mathbf{z}}_R$ with respect to an inertial frame $I(x_I, y_I, z_I)$, where the z_R-axis and z_I-axis coincide. Furthermore, to maintain the displaced NKO a thrust-induced acceleration, $\mathbf{a}$, is assumed.

The equations of motion of the spacecraft in the rotating reference frame are then given by the following equation:

$$\ddot{\mathbf{r}} + 2\boldsymbol{\omega} \times \dot{\mathbf{r}} + \nabla U = \mathbf{a} \qquad (2.6)$$
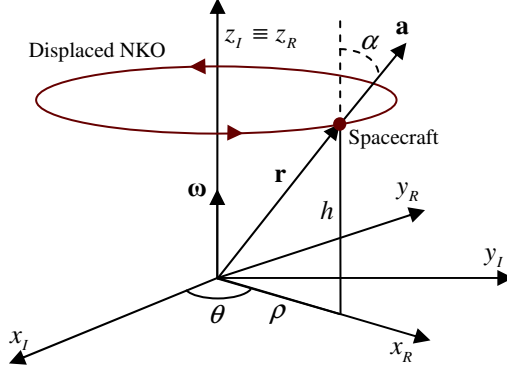
Fig. 2.4 Displaced non-Keplerian orbit reference frames.

Note that Eq. (2.6) is similar to Eq. (2.5) for $\mathbf{a} = 0$, but is defined here in the two-body problem. The radius vector $\mathbf{r}$ thus equals the vector between the central body and the spacecraft, see Fig. 2.4, rather than the vector from the three-body barycentre to the spacecraft as illustrated in Fig. 2.3. Furthermore, the potential U can be written using a set of cylindrical polar coordinates (ρ, θ, h) as shown in Fig. 2.4:

$$U = -\left(\frac{1}{2}(\omega \rho)^2 + \frac{\mu_C}{r} \right) \tag{2.7}$$

Following the analysis in Reference 41, equilibrium solutions can subsequently be found by setting $\dot{\mathbf{r}} = \ddot{\mathbf{r}} = 0$ in Eq. (2.6), which eliminates the first two terms on the left hand side:

$$\nabla U = \mathbf{a} \tag{2.8}$$

Equation (2.8) directly gives the magnitude and direction of the thrust acceleration required to maintain the displaced NKO.[42]

Because $\boldsymbol{\omega}$ is constant, no transverse component of the thrust can exist, requiring the thrust vector to lie in the plane spanned by the radius vector and the z_R-axis. The thrust direction is therefore defined by the pitch angle α only:

$$\tan \alpha = \frac{\left| \hat{\mathbf{z}}_R \times \nabla U \right|}{\hat{\mathbf{z}}_R \cdot \nabla U} \tag{2.9}$$

Substituting Eq. (2.7) into Eqs. (2.9) and (2.8) results in the following required thrust direction and magnitude to maintain the displaced NKO:

$$\tan\alpha\left(\rho,h;\omega\right)=\frac{\rho}{h}\left(1-\left(\frac{\omega}{\omega_*}\right)^2\right) \tag{2.10}$$

$$a\left(\rho,h;\omega\right)=\sqrt{\rho^2\left(\omega^2-\omega_*^2\right)^2+h^2\omega_*^4} \tag{2.11}$$

with ω_* the orbit angular velocity of a circular Keplerian orbit with a radius equal to the radius of the NKO:

$$\omega_*=\sqrt{\frac{\mu_C}{\left(\rho^2+h^2\right)^{3/2}}} \tag{2.12}$$

While Eqs. (2.10) and (2.11) provide the general conditions to maintain a displaced NKO, three particular families of displaced NKOs are defined in the literature,[41, 42] depending on the choice of the orbit angular velocity of the NKO:

- Type I: $\omega=\omega_*$: the orbit period of the displaced NKO is equal to the orbit period of a Keplerian orbit with radius equal to the radius of the NKO.

- Type II: $\omega=\sqrt{\mu_C/\rho^3}$: the orbit period of the displaced NKO is equal to the orbit period of a Keplerian orbit with radius equal to the projected radius of the NKO.

- Type III: $\omega=\omega_0$: the orbit period is constant for any combination of $\left(\rho,h\right)$.

For each family, the required thrust direction and acceleration can be derived from Eqs. (2.10) and (2.11), by substituting the correct condition for ω. Furthermore, the acceleration contours for each of the families can be obtained as shown in Fig. 2.5, which provide insight in the relative effort required to maintain particular NKOs. These contours are provided in a non-dimensional form, with the axes made dimensionless with respect to the radius of the central body and the acceleration made dimensionless with respect to the gravitation acceleration at unit radius.

From an extensive literature survey on non-Keplerian orbits by McKay et al.,[43] it appears that Oberth was the first to mention the existence of a displaced orbit when discussing Earth orbiting reflectors for surface illumination in his *Wege zur Raumschiffarht*.[44] He noted that due to solar radiation pressure, reflectors in a polar orbit will be displaced in the anti-Sun direction. However, it was apparently Dusek in 1966 who was the first to formally mention the concept of counter-acting gravity through the use of a propulsive thrust.[45]

a)   b)

c)
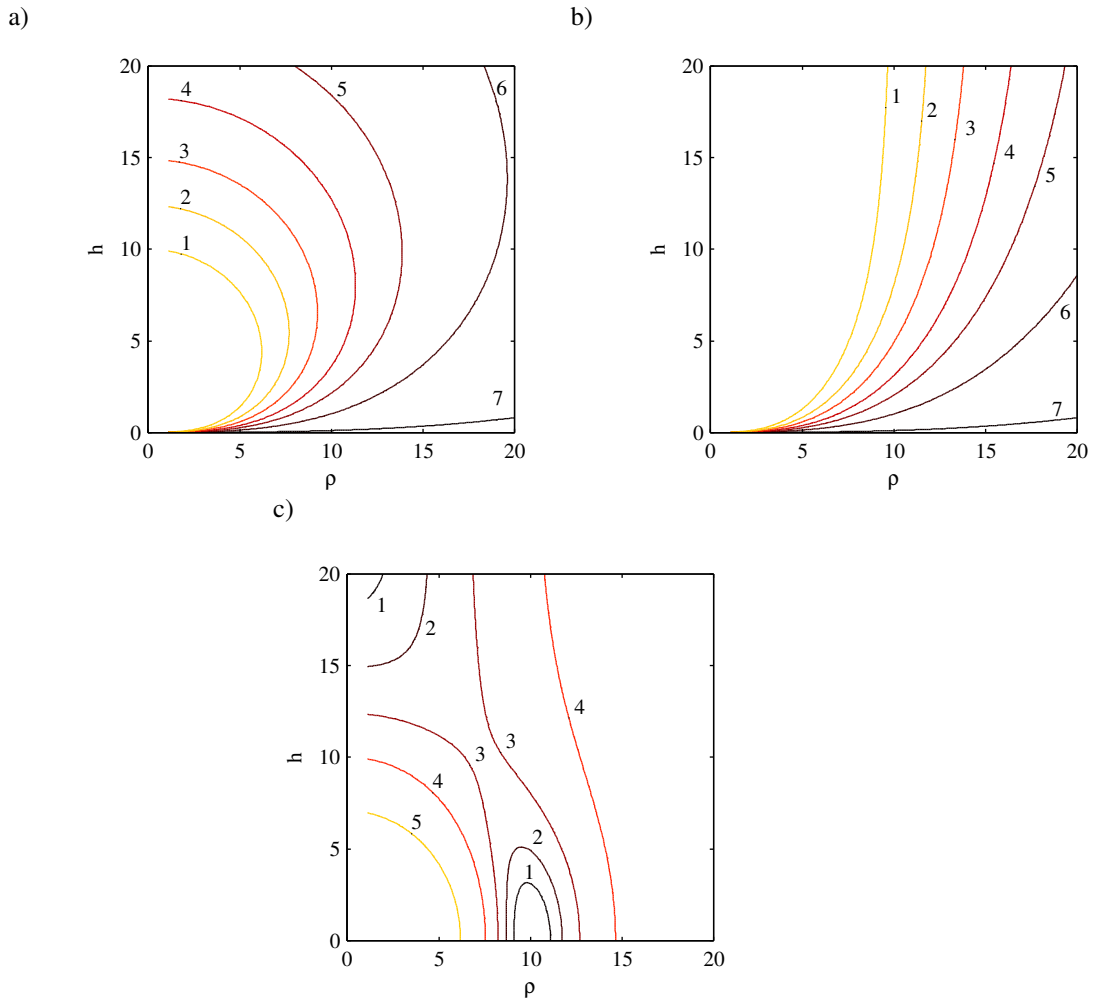
Fig. 2.5 Acceleration contour plots for displaced NKOs. a) Type I. b) Type II. c) Type III that is synchronous with a Keplerian orbit with radius $\rho = 10$. The projected radius, ρ, and displacement, h, are dimensionless with respect to the central body radius and the acceleration is dimensionless with respect to the acceleration at unit body radius. The labels represent the following accelerations: (a-b) 1: 10^{-2}, 2: 6.5×10^{-3}, 3: 4.5×10^{-3}, 4: 3×10^{-3}, 5: 2×10^{-3}, 6: 10^{-3}, 7: 10^{-4}. (c) 1: 3×10^{-3}, 2: 4.5×10^{-3}, 3: 6.5×10^{-3}, 4: 10^{-2}, 5: 2×10^{-2}.[42]

Since then, the most extensive investigation of NKOs has been conducted by McInnes and co-workers. McInnes was the first to categorise displaced orbits according to their orbital period and to consider their stability and control issues.[42, 46, 47] Often, the use of solar sails (see Section 2.2.2) are used to generate the displaced NKOs.[18, 29, 41, 48] Therefore, many of the applications are Sun-centred, such as NKOs for solar physics and one year orbits synchronous with the Earth for space weather monitoring.[46] However, an extension to planet-centred orbits has also been made[49] by considering, for example, NKOs displaced behind the Earth to observe the structure of the geomagnetic tail[50] and orbits displaced above and synchronous with Saturn's rings for high-resolution imaging.[51]

22

Other authors have also investigated displaced NKOs. For example, the displaced geostationary orbit as investigated by Forward[15] and Baig[18] was already mentioned in Section 1.1.1. Furthermore, Nock[52] and Spilker[53] also investigated the potential of displaced NKOs to investigate Saturn rings. Finally, Lu and Love[54] and Wie[55] proposed the use of NKOs to hover over an asteroid.

Although many of the works listed above consider displaced NKOs in the two-body problem, a thrust-induced acceleration can also be added to the equations of motion of the three-body problem in Eq. (2.5):

$$\ddot{\mathbf{r}} + 2\boldsymbol{\omega} \times \dot{\mathbf{r}} + \nabla U = \mathbf{a} \tag{2.13}$$

This allows complementing the five Lagrange points (see below Eq. (2.5)) with artificial equilibrium points (AEPs), as is shown by the acceleration contour plot in Fig. 2.6 for the Earth-Moon CR3BP, as well as orbits around these AEPs. Again, the first complete analysis of this problem and many subsequent investigations have been conducted by McInnes and co-workers[29, 56, 57] and the applications are as numerous as for the two-body problem: Forward's concept of the 'statite' spacecraft was already previously noted for polar observations.[28] Other uses of NKOs for polar observations and communications have been proposed by Biggs[48] and Ceriotti and McInnes.[58] Additional applications include solar sail equilibria in the ecliptic plane sunward of the L_1-point for the NASA/NOAA Geostorm mission to enhance space weather warning times[59] and applications in the Earth-Moon three-body problem include lunar south pole coverage by Grebow et al.[60] and lunar far side communications with the Earth by Simo and McInnes.[61]
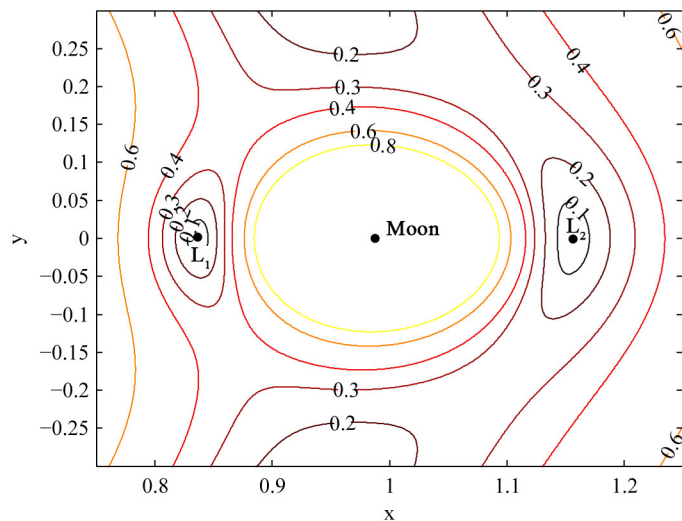
Fig. 2.6 Acceleration contour plot for the Earth-Moon CR3BP. The coordinates and acceleration are made dimensionless according to the CR3BP-convention.

23

2.2   Low-thrust propulsion

In order to enable the non-Keplerian orbits discussed in the previous section, a continuous acceleration is required, which can be provided by a range of different propulsion technologies. It is well-known that generally all types of space propulsion can be categorised into either 'high-thrust' (i.e. impulsive) or 'low-thrust'.

Traditional, chemical rockets fall into the category of 'high-thrust' and, as the name suggests, produce a high thrust, but at very low specific impulse. The latter is a way to describe the efficiency of a rocket: the higher the specific impulse, the higher the speed of the rocket exhaust, the lower the propellant flow rate required for a given thrust and thus the less propellant needed. Low-thrust systems only generate a fraction of the thrust generated by high-thrust systems. However, since the propellant is accelerated to much higher exhaust velocities, they achieve a much higher specific impulse and are thus much more fuel efficient.[62]

Since the non-Keplerian orbits discussed in the previous section require a *continuous* thrust throughout the mission lifetime, it can be expected that low-thrust systems will be much more efficient for this purpose than high-thrust systems. Therefore, in this section, a variety of low-thrust propulsion systems will be discussed, starting with solar electric propulsion in Section 2.2.1, solar sailing in Section 2.2.2 and finally hybrid sail propulsion in Section 2.2.3.

2.2.1   Solar electric propulsion

The first notion of electric propulsion was provided by Konstatin Tsiolkovsky in 1911.[63] However, Robert H. Goddard would be the first to conduct experiments with an actual low-thrust engine in 1916-1917. Still, it would take until 1964 for the first successful tests of electric propulsion in space to occur with NASA's Space Electric Rocket Test 1 (SERT 1).[64] From then on, electric engines began to be used more regularly, but only for satellite station-keeping in GEO.

Only later, in 1998, with the launch of NASA's NSTAR (NASA Solar Technology Application Readiness) thruster onboard the Deep Space 1 mission, would electric propulsion become the main propulsion technology for a deep space mission.[65] After its successful demonstration, electric propulsion flew on multiple other missions, including ESA's first Small Mission for Advanced Research in Technology (SMART-1; 2003),[66] JAXA's Hayabusa (2003),[67] NASA's Dawn mission (2007)[68] and ESA's Gravity Field and

Steady-State Ocean Circulation Explorer (GOCE; 2009),[69] and is expected to be utilised in a number of future missions such as ESA's BepiColombo mission[70] and the joint NASA/ESA LISA Pathfinder mission.[71]

All missions noted above used a particular form of electric propulsion, namely solar electric propulsion (SEP), which uses electric power generated by solar panels, to accelerate an ionised gas to high velocities. Xenon is commonly used as propellant, which is a neutral gas but is ionised by impacting it with electrons. Depending on the type of thruster used, different ways of accelerating the positively charged Xenon ions are employed. For the NSTAR thruster of the Deep Space 1 mission and the majority of other engines that have flown, the Xenon ions are accelerated electrostatically due to a potential difference over a positive and negative grid. Finally, by injecting a separate beam of electrons into the exhaust, the positively charged ions are neutralised.[72]

The acceleration that the SEP thruster can generate is given by:

$$\mathbf{a}_{SEP} = \frac{\mathbf{T}}{m} \tag{2.14}$$

with $\mathbf{T}$ the SEP thrust vector and m the instantaneous mass of the spacecraft. Due to the consumption of propellant during the mission lifetime, the mass of the spacecraft will decrease. The rate at which this occurs is given by the following differential equation that has to be added to the equations of motion in Eqs. (2.6) (two-body problem) and (2.13) (three-body problem):

$$\dot{m} = -\frac{|\mathbf{T}|}{I_{sp} g_0} \tag{2.15}$$

with I_{sp} the specific impulse and g_0 the Earth standard gravitational acceleration.

Based on previous, current and future ion engine technology, see Table 2.1, a fixed specific impulse of $I_{sp} = 3200$ s is assumed throughout this thesis. It is foreseen that this impulse allows levels of thrust of approximately 0.2 N, which is considered suitable for the spacecraft and applications under consideration. Note that higher values of specific impulse can be achieved with current SEP technology (e.g. the ARC/Astrium FEEP (Field-Emission Electric Propulsion) thruster can provide a specific impulse of up to 8,000 s), but the corresponding achievable thrust levels are expected to be too low to enable the NKOs considered in this thesis.[73]

In case larger thrust magnitudes than 0.2 N are required, the option of clustering multiple engines will be investigated, and where applicable limitations on propellant throughput will be considered. Finally, note that, although a *fixed* specific impulse is adopted, it is assumed that the engine is still able to throttle between zero-thrust and maximum thrust without penalising the specific impulse.

Table 2.1 SEP thruster specifications with T_{max} the maximum thrust magnitude and I_{sp} the specific impulse.

Thruster	Developer	$T_{\max}$, N	I_{sp} , s
NSTAR[72, 74]	NASA	0.092	3,120
RIT-XT[75]	EADS/Astrium	0.210	2,500-5,500
NEXT[72, 76]	NASA	0.236	4,190
QinetiQ T6[77]	QinetiQ	0.03-0.210	4,700 (@0.2 N)
FEEP[73]	ARC/Astrium	$0.1\text{-}15 \times 10^{-6}$	4,000-8,000

2.2.2 Solar sailing

It was again Konstantin Tsiolkovsky who, in 1921, was the first to suggest that spacecraft could be propelled through space by using sunlight,[78] although Tsander published the first practical paper on solar sailing in 1924.[79] However, once again, it would take almost a century before the technology had become available to deploy a solar sail in space and successfully demonstrate its use as a propulsion system: in 2010 the Japanese space agency launched its Interplanetary Kite-craft Accelerated by Radiation Of the Sun (IKAROS) mission[80] and NASA followed a few months later with the NanoSail-D2 nanosatellite,[81] although it did not demonstrate solar sailing.

Research in the field of solar sailing is flourishing, driven by the huge potential of solar sail missions that are not constrained by propellant mass: solar sailing exploits the radiation pressure generated by solar photons reflecting off a large, highly reflecting sail to produce a continuous thrust. With the Sun as 'propellant' source, solar sail missions have in principle infinite lifetime.[41]

Three parameters are often used to indicate the performance of a solar sail:

1. Sail lightness number, β :

    The solar sail lightness number can be defined as the ratio of the solar radiation pressure acceleration and the solar gravitational acceleration. Equivalently, it can be defined as the

ratio of the system loading (i.e. the ratio of the spacecraft mass to the solar sail area, $\sigma = m / A_s$) and the critical sail loading, σ^*:[41]

$$\beta = \frac{\sigma^*}{\sigma} \qquad (2.16)$$

The critical sail loading is a unique constant which is defined by the solar luminosity, $L_\odot$, the speed of light, c, and the gravitational parameter of the Sun, $\mu_\odot$:[41]

$$\sigma^* = \frac{L_\odot}{2\pi c \mu_\odot} = 1.53 \text{ g/m}^2 \qquad (2.17)$$

Eq. (2.16) shows that for a sail loading equal to the critical sail loading, the lightness number is unity, indicating that the solar radiation pressure acceleration is exactly equal to the solar gravitational acceleration. However, for a near-term solar sail, values of β up to 0.05 can be assumed.[82] Recent solar sail demonstrators, however, have even lower lightness numbers: JAXA's IKAROS has a 20-m-diagonal square sail and weighs 307 kg ($\beta = 0.001$),[80] while NASA's NanoSail-D2 weighs 4 kg and has a sail area of 10 m^2 ($\beta = 0.003$).[81]

2. Sail loading, σ_s:

The sail loading is the mass of the sail per unit surface area, $\sigma_s = m_s / A_s$. It is expected that technological developments should enable sails of 10 g/m^2 in the near future. Ultra-thin sails (around 2 μm of thickness) are expected in the mid- to far-term timeframe and can lead, for large sails, to sail loadings of the order of 5 g/m^2.[83, 84]

3. Characteristic acceleration, a_c:

The characteristic acceleration is the acceleration that the solar sail can generate at 1 Astronomical Unit (AU), r_{AU}, and when it is flat, facing the Sun:

$$a_c = \beta \frac{\mu_\odot}{r_{AU}^2} \qquad (2.18)$$

This equation also clearly shows the definition of the sail lightness number as for $\beta = 1$ the acceleration produced by the solar sail is equal to the solar gravitational acceleration.[41]

The three performance parameters are closely linked: the larger the sail lightness number, the larger the characteristic acceleration. A larger value for β can be achieved by a lower system loading, which in its turn is achieved by a larger sail area or a smaller sail mass (and thus by a smaller sail loading) or a smaller spacecraft mass.

Once the performance of the solar sail in terms of one of these parameters is known, the actual acceleration produced by the solar sail can be computed. Throughout this thesis, different sail models are used to obtain this acceleration, depending on which one is most applicable and the accuracy required. These sail models are listed below in increasing order of accuracy.

Ideal solar sail

An ideal solar sail is a sail that is perfectly reflecting. The incoming solar photons are therefore specularly reflected and the solar radiation pressure force (in direction $\hat{\mathbf{n}}$) is perpendicular to the sail surface, see Fig. 2.7. The derivation of the resulting sail acceleration is given in Reference 41 and starts from the force produced by the photons impinging on the solar sail:

$$\mathbf{F}_i = PA_s \left(\hat{\mathbf{n}} \cdot \hat{\mathbf{r}}_s \right) \hat{\mathbf{r}}_s \tag{2.19}$$

with P the solar radiation pressure exerted on the sail and $A_s \left(\hat{\mathbf{n}} \cdot \hat{\mathbf{r}}_s \right)$ the area of the solar sail projected onto the direction of the incoming photons. The reflected photons produce a force that is equal in magnitude but directed in the specular reflected direction, $-\hat{\mathbf{r}}_r$:

$$\mathbf{F}_r = -PA_s \left(\hat{\mathbf{n}} \cdot \hat{\mathbf{r}}_s \right) \hat{\mathbf{r}}_r \tag{2.20}$$

Adding Eqs. (2.19) and (2.20) and using the relation $\hat{\mathbf{r}}_s - \hat{\mathbf{r}}_r = 2 \left(\hat{\mathbf{n}} \cdot \hat{\mathbf{r}}_s \right) \mathbf{n}$ gives the total force exerted on the solar sail:

$$\mathbf{F} = 2PA_s \left(\hat{\mathbf{n}} \cdot \hat{\mathbf{r}}_s \right)^2 \hat{\mathbf{n}} \tag{2.21}$$

Furthermore, the solar radiation pressure can be found from the solar energy flux, W, at a distance r_s from the Sun, i.e. the energy crossing a unit sail area in unit time:

$$P = \frac{W}{c} = \frac{L_\odot}{4\pi c r_s^2} \tag{2.22}$$

Substituting Eq. (2.22) into Eq. (2.21) and dividing by the spacecraft mass to obtain the solar sail acceleration gives:

$$\mathbf{a}_s = \frac{L_\odot}{2\pi c} \frac{1}{r_s^2} \frac{A_s}{m} \left(\hat{\mathbf{n}} \cdot \hat{\mathbf{r}}_s \right)^2 \hat{\mathbf{n}} \tag{2.23}$$

Finally, substituting Eq. (2.16) and (2.17) provides:

$$\mathbf{a}_s = \beta \frac{\mu_\odot}{r_s^2} \left(\hat{\mathbf{n}} \cdot \hat{\mathbf{r}}_s \right)^2 \hat{\mathbf{n}} \tag{2.24}$$

The cone angle of the sail, α_c, see Fig. 2.7, is measured between the normal of the sail (which for the ideal sail coincides with the solar radiation pressure force) and the Sun-sail vector, $\hat{\mathbf{r}}_s$. The scalar product $\left(\hat{\mathbf{n}} \cdot \hat{\mathbf{r}}_s \right)$ in Eq. (2.24) could therefore also be written as $\cos \alpha_c$. Finally, note that the solar sail is unable to generate a thrust component in the direction of the Sun and therefore $\alpha_c \in \left[0, 90^\circ \right]$.[41]
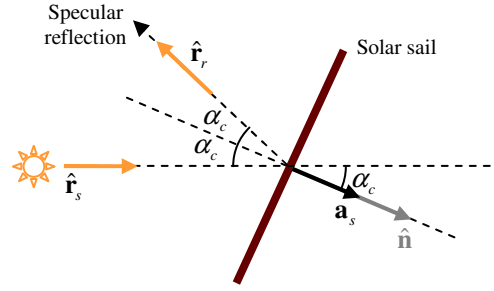
Fig. 2.7 Ideal solar sail model (specular reflection)

Optical solar sail

Although the ideal model is appropriate for initial investigations of the performance of the solar sail, the assumption of pure specular reflection does not hold in reality. A better approximation is to include the absorption of photons in the sail model, resulting in the so-called optical sail model.[85] This will result in a solar radiation pressure force that is no longer perpendicular to the solar sail, but instead also generates a component parallel to sail, along the unit vector $\hat{\mathbf{t}}$, see Fig. 2.8.

The acceleration produced by the solar sail can be derived by starting from the force generated due to absorption of the incident sunlight:

$$\mathbf{F}_a = P A_s \cos \alpha_c \hat{\mathbf{r}}_s \tag{2.25}$$

Using the transformation $\hat{\mathbf{r}}_s = \cos \alpha_c \hat{\mathbf{n}} + \sin \alpha_c \hat{\mathbf{t}}$, Eq. (2.25) can be written as:

$$\mathbf{F}_a = P A_s \cos \alpha_c \left(\cos \alpha_c \hat{\mathbf{n}} + \sin \alpha_c \hat{\mathbf{t}} \right) \tag{2.26}$$

Part of the photons will be specularly reflected in direction $\hat{\mathbf{r}}_r = -\cos \alpha_c \hat{\mathbf{n}} + \sin \alpha_c \hat{\mathbf{t}}$. This portion is indicated by the parameter $\tilde{r}_s$ and produces the following force:

$$\mathbf{F}_s = -PA_s\tilde{r}_s\cos\alpha_c\left(-\cos\alpha_c\hat{\mathbf{n}}+\sin\alpha_c\hat{\mathbf{t}}\right) \tag{2.27}$$

The force generated by the incoming photons is still described by Eq. (2.19) and the total force produced is therefore given by adding Eqs. (2.19) and (2.27). Rewriting that result in a similar way as done to obtain Eq. (2.24) for an ideal solar sail, provides the following acceleration produced by an optical sail:

$$\mathbf{a}_s = \frac{1}{2}\beta\frac{\mu_\odot}{r_s^2}\left[\tilde{g}\cos\alpha_c\hat{\mathbf{n}}+\tilde{h}\sin\alpha_c\hat{\mathbf{t}}\right]\cos\alpha_c \tag{2.28}$$

with $\tilde{g}$ and $\tilde{h}$ coefficients that are a function of the reflectively of the solar sail, $\tilde{r}_s$, as follows:

$$\tilde{g} = 1+\tilde{r}_s, \quad \tilde{h} = 1-\tilde{r}_s \tag{2.29}$$

In this thesis, a reflectivity of $\tilde{r}_s = 0.9$ is assumed,[85] but note that, for an ideal solar sail with $\tilde{r}_s = 1$, Eq. (2.28) reduces to Eq. (2.24).
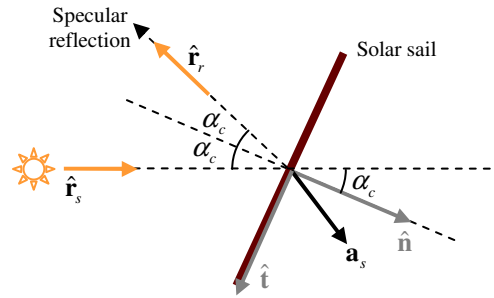
Fig. 2.8 Optical solar sail model (specular reflection + absorption)

Parametric, degrading solar sail

The most high-fidelity model used in this thesis is a parametric solar sail model that takes into account that the sail's optical properties will degrade during the mission lifetime.[82] This model considers reflection, absorption and emission of solar radiation by the solar sail and is illustrated in Fig. 2.9. The derivation of the acceleration generated by such a solar sail starts from Eq. (2.25). Subsequently, it is assumed that part of the absorbed photons will be reflected, indicated by the parameter $\tilde{r}$, of which part will be specularly reflected (parameter $\tilde{r}_s$) and part will be non-specularly reflected, $1-\tilde{r}_s$. The resulting forces are:

$$\mathbf{F}_s = -PA_s \tilde{r}\tilde{r}_s \left(-\cos^2 \alpha_c \hat{\mathbf{n}} + \cos \alpha_c \sin \alpha_c \hat{\mathbf{t}}\right)$$

$$\mathbf{F}_{ns} = B_{fr} PA_s \tilde{r}\left(1-\tilde{r}_s\right)\cos \alpha_c \hat{\mathbf{n}} \tag{2.30}$$

where B_{fr} is the non-Lambertian coefficient of the front side of the solar sail to account for the fact that the sail does not appear equally bright when viewed from different angles.[82]

Finally, the photons that are not reflected, i.e. $\left(1-\tilde{r}\right)$, are re-emitted as thermal radiation on both the front and back side of the solar sail and generate the following force:[41]

$$\mathbf{F}_e = PA_s \left(1-\tilde{r}\right)\frac{\varepsilon_{fr}B_{fr} - \varepsilon_b B_b}{\varepsilon_{fr} + \varepsilon_b}\cos \alpha_c \hat{\mathbf{n}} \tag{2.31}$$

with ε the emissivity and the subscripts 'fr' and 'b' indicating the front and back sides of the solar sail. Adding the separate force components in Eqs. (2.19), (2.26), (2.30) and (2.31) results in the following forces normal and tangential to the solar sail:

$$\mathbf{F}_n = PA_s \left(\left(1+\tilde{r}\tilde{r}_s\right)\cos^2 \alpha_c + B_{fr}\left(1-\tilde{r}_s\right)\tilde{r}\cos \alpha_c + \left(1-\tilde{r}\right)\frac{\varepsilon_{fr}B_{fr} - \varepsilon_b B_b}{\varepsilon_{fr} + \varepsilon_b}\cos \alpha_c\right)\hat{\mathbf{n}}$$

$$\mathbf{F}_t = PA_s \left(1-\tilde{r}\tilde{r}_s\right)\cos \alpha_c \sin \alpha_c \hat{\mathbf{t}} \tag{2.32}$$

More convenient is to obtain the force components in the normal direction and the direction of the sunlight, $\hat{\mathbf{r}}_s$. Once again using the transformation $\hat{\mathbf{r}}_s = \cos \alpha_c \hat{\mathbf{n}} + \sin \alpha_c \hat{\mathbf{t}}$ results in:

$$\mathbf{F} = PA_s \left(\left(1-\tilde{r}\tilde{r}_s\right)\cos \alpha_c \hat{\mathbf{r}}_s + \left(2\tilde{r}\tilde{r}_s \cos^2 \alpha_c + B_{fr}\left(1-\tilde{r}_s\right)\tilde{r}\cos \alpha_c + \left(1-\tilde{r}\right)\frac{\varepsilon_{fr}B_{fr} - \varepsilon_b B_b}{\varepsilon_{fr} + \varepsilon_b}\cos \alpha_c\right)\hat{\mathbf{n}}\right) \tag{2.33}$$

Using the notations

$$b_1 = \left(1-\tilde{r}\tilde{r}_s\right), \quad b_2 = 2\tilde{r}\tilde{r}_s, \quad b_3 = B_{fr}\left(1-\tilde{r}_s\right)\tilde{r} + \left(1-\tilde{r}\right)\frac{\varepsilon_{fr}B_{fr} - \varepsilon_b B_b}{\varepsilon_{fr} + \varepsilon_b} \tag{2.34}$$

provides the following form of the parametric force model:[82, 86]

$$\mathbf{F} = PA_s \left(b_1 \cos \alpha_c \hat{\mathbf{r}}_s + \left(b_2 \cos^2 \alpha_c + b_3 \cos \alpha_c\right)\hat{\mathbf{n}}\right) \tag{2.35}$$

Dividing Eq. (2.35) by the spacecraft mass gives the solar sail acceleration and further rewriting using Section 2.2.2 finally provides:

$$\mathbf{a}_s = \frac{1}{2}\beta\frac{\mu_\odot}{r_s^2}\cos \alpha_c \left(b_1 \hat{\mathbf{r}}_s + \left(b_2 \cos \alpha_c + b_3\right)\hat{\mathbf{n}}\right) \tag{2.36}$$

This new solar sail acceleration thus takes into account the optical characteristics of the solar sail which is defined by a set of six optical coefficients: $\tilde{r}$, $\tilde{r}_s$, ε_{fr}, ε_b, B_{fr} and B_b. Assuming that the front of the solar sail has a highly reflective aluminium coating and the back side a highly emissive chromium coating, the following values can be adopted for each of the coefficients: $\tilde{r} = 0.88$, $\tilde{r}_s = 0.94$, $\varepsilon_{fr} = 0.05$, $\varepsilon_b = 0.55$, $B_{fr} = 0.79$ and $B_b = 0.55$.[82]
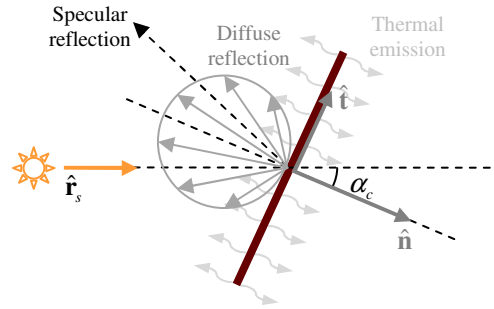
Fig. 2.9 Parametric solar sail model (specular reflection + absorption + diffuse reflection + thermal emission)

An even more refined model of the solar sail can be obtained when considering that the sail's optical properties will degrade during the mission lifetime and that the optical coefficients vary over time. To model this variation, the environmental history of the solar sail (i.e. the radiation dose) has to be known. Reference 82 provides an estimate for this radiation dose, Σ, by assuming that it is dependent on the distance from the Sun and the attitude history of the sail:

$$\Sigma(t) = W_{AU} r_{AU}^2 \int_{t_0}^{t} \frac{\cos\alpha_c}{r^2} dt \tag{2.37}$$

The dimensionless radiation dose, $\overline{\Sigma}$, can be obtained by dividing Eq. (2.37) with the radiation dose received by a solar sail at 1 AU during one year while having its surface perpendicular to the Sun. This radiation dose equals $W_{AU} \cdot t_{year} = 43.1 \text{ GJ/m}^2$.

Reference 82 shows that the variation of the coefficients ε_b, B_{fr} and B_b is negligible. However, for the other three coefficients it is assumed that they vary exponentially between their initial value and the value at infinite time. For example, for the reflection coefficient (but similarly for the other two remaining coefficients):

$$\tilde{r}(t) = \tilde{r}_\infty + (\tilde{r}_0 - \tilde{r}_\infty)\exp\left[-\lambda_{\tilde{r}}\overline{\Sigma}(t)\right] \tag{2.38}$$

with $\lambda_{\tilde{r}}$ the degradation constant associated with the reflection coefficient. This constant is related to the half-life solar radiation dose, $\hat{\Sigma}_{\tilde{r}}$, which is the dimensionless solar radiation dose at which the reflection coefficient reaches its midway value, i.e. $\tilde{r}_{\infty} + (\tilde{r}_0 - \tilde{r}_{\infty})/2$. A value for $\hat{\Sigma}_{\tilde{r}}$ can only be assumed on empirical basis (a common value is 0.5),[82] but once it is known, the degradation constant is given by

$$\lambda_{\tilde{r}} = \frac{\ln 2}{\hat{\Sigma}_{\tilde{r}}} \tag{2.39}$$

With a half-life solar radiation dose assigned to each optical coefficient, the number of parameters in the sail model grows considerably. Therefore, in order to limit the number of parameters, Reference 82 proposes to define one single half-life radiation dose, $\hat{\Sigma}$, (and thus one single degradation constant, λ) and instead introduce a degradation factor, $\tilde{d}$, such that:

$$
\begin{aligned}
\tilde{r}_{\infty} &= \tilde{r}_0 / (1 + \tilde{d}) \\
\tilde{r}_{s,\infty} &= \tilde{r}_{s,0} / (1 + \tilde{d}) \\
\varepsilon_{fr,\infty} &= (1 + \tilde{d})\varepsilon_{fr,0}
\end{aligned}
\tag{2.40}
$$

A common value for the degradation factor is 0.05.[82] Substituting Eq. (2.40) and all assumptions into Eq. (2.38) gives:

$$
\begin{aligned}
\tilde{r}(t) &= \tilde{r}_0 \left(1 + \tilde{d}\exp\left[-\lambda\overline{\Sigma}(t)\right]\right) / (1 + \tilde{d}) \\
\tilde{r}_s(t) &= \tilde{r}_{s,0} \left(1 + \tilde{d}\exp\left[-\lambda\overline{\Sigma}(t)\right]\right) / (1 + \tilde{d}) \\
\varepsilon_{fr}(t) &= \varepsilon_{fr,0} \left(1 + \tilde{d}\left(1 - \exp\left[-\lambda\overline{\Sigma}(t)\right]\right)\right)
\end{aligned}
\tag{2.41}
$$

which is to be used when computing b_1, b_2 and b_3 in Eq. (2.36).

2.2.3   Hybrid sail propulsion

In the two previous sections, solar electric propulsion and solar sailing have been considered as low-thrust propulsion technologies to enable the non-Keplerian orbits discussed in Section 2.1. However, both types of propulsion system have their advantages and disadvantages. For example, solar electric propulsion has significant flight heritage, which has resulted in a high technology readiness level (TRL) and a low advancement degree of difficulty (AD^2), which is an indication of the difficulty to mature a technology on the TRL scale.[87] However, since it relies on propellant to generate an acceleration, its mission lifetime

and therefore its applications are limited. Solar sailing is not constrained by propellant, causing the mission lifetime to be infinite, in principle. However, solar sailing has its own disadvantages, the main one being the fact that despite recent advances in solar sailing, the TRL of solar sailing as primary propulsion system on a reasonable sized mission is still rather low and its AD^2 is high.[87] In addition, a solar sail cannot generate a thrust component in the direction of the Sun, which limits its applications.

Considering the disadvantages and limitations of solar sails and SEP, Leipold and Götz[88] proposed a hybridisation of the two systems on the same spacecraft. Because, at the cost of increased spacecraft and mission design complexity, the separate systems complement each other, cancelling their disadvantages and limitations: since only small solar sails will be required, the hybridisation lowers the solar sail AD^2. The hybrid spacecraft can therefore be seen as a way to gradually introduce solar sails for space applications. Furthermore, while the solar sail lowers the demand on the SEP propellant mass, the SEP system can provide a thrust component in the direction of the Sun (which the solar sail is unable to generate). This is under the assumption that the SEP system is mounted on a gimbal such that the two propulsion systems can steer independently of each other. However, the direction of the SEP thrust force cannot be such that it lies in the plane of the solar sail. This would cause contamination of the sail and the total amount of net thrust available from the SEP thruster would be reduced compared to the case where the exhaust can escape in an undisturbed way.

Such hybrid systems, coined hybrid sail propulsion, have already been suggested to enable interplanetary transfers,[89, 90] to allow for periodic orbits in the vicinity of the Lagrange points in the Earth-Moon system for lunar communication purposes[91] and to generate artificial equilibria in the Earth-Sun three-body problem.[85] All studies show to some extent an improvement for hybrid sails over the use of pure SEP or pure solar sailing in terms of propellant mass consumption, required thrust magnitude levels and/or initial spacecraft mass.

The acceleration produced by a hybrid sail is obtained by adding the accelerations produced by the SEP thruster, see Eq.(2.14), and the solar sail, see Eqs. (2.24), (2.28) or (2.36):

$$\mathbf{a}_h = \mathbf{a}_{SEP} + \mathbf{a}_s \tag{2.42}$$

However, in doing so, the following two issues need to be taken into account.

First, from the definition of the sail lightness number in Eq. (2.16) it becomes clear that the sail lightness number is a function of the spacecraft mass.[85] Since the mass of the hybrid sail spacecraft decreases due to the consumption of propellant by the SEP system, the parameter β increases according to:

$$\beta = \beta_0 \frac{m_0}{m} \qquad (2.43)$$

where β_0 indicates the sail lightness number at the start of the mission, corresponding to the initial mass of the spacecraft. This expression has to be substituted into the solar sail accelerations defined in Eq . (2.24), (2.28) or (2.36).

Second, in conventional spacecraft, the power required to operate the SEP thruster is generated by solar panels. However, in the case of a hybrid sail spacecraft, such an architecture might prove difficult due to the presence of the sail. Therefore, as was proposed by Leipold and Götz[88] and as used for the IKAROS spacecraft,[92] it is assumed that part of the solar sail surface is covered with thin film solar cells (TFSC) to generate power. Clearly, the thin film solar cells will have a reflectively different from the reflectivity of the solar sail (their reflectivity is lower, as part of the light is absorbed and converted into electric power). For the optical sail model this is taken into account by adapting Eq. (2.29) as follows:

$$\tilde{g} = 1 + \tilde{r}_s + \frac{A_{TF}}{A_s} \left(\tilde{r}_{TF} - \tilde{r}_s \right), \quad \tilde{h} = 1 - \tilde{r}_s - \frac{A_{TF}}{A_s} \left(\tilde{r}_{TF} - \tilde{r}_s \right) \qquad (2.44)$$

with $A_{TF} = 0.05 A_s$ the TFSC area as a function of the total sail area, where the 5 percent TFSC coverage is based on previous studies[85] and the IKAROS mission,[93] and $\tilde{r}_{TF} = 0.4$ the reflectivity of the TFSC.[85]

2.3   Optimal control problems

In order to optimise the use of low-thrust propulsion for enabling the non-Keplerian orbits and transfers defined in the research objectives of Section 1.2, the accompanying optimal control problem needs to be solved. In this section, the definition of an optimal control problem is given. The methods used to solve the optimal control problem are usually classified into indirect and direct methods, which will be discussed in Sections 2.3.2 and 2.3.3, respectively. Finally, in Section 2.3.4 more details of the particular direct method used throughout this thesis will be given, while Section 2.3.5 discusses the generation of initial guesses.

2.3.1   Definition

In general, an optimal control problem[94] is to find a state history $\mathbf{x}(t) \in \mathbb{R}^{n_x}$ and a control history $\mathbf{u}(t) \in \mathbb{R}^{n_u}$, with $t \in [t_0, t_f]$ the independent variable, that minimises the cost function:

$$J = M\left(\mathbf{x}_0, \mathbf{x}_f, \mathbf{p}, t_0, t_f\right) + \int_{t_0}^{t_f} L_g\left(\mathbf{x}(t), \mathbf{u}(t), \mathbf{p}, t\right) dt \tag{2.45}$$

Equation (2.45) shows that a set of parameters, $\mathbf{p} \in \mathbb{R}^{n_p}$, may be incorporated that are not dependent on the independent variable. Usually, the independent variable is time, but this can vary depending on the problem under consideration. The first term on the right hand side of Eq. (2.45) is the endpoint (Mayer form) cost function, which is only a function of the initial (subscript '0') and final (subscript 'f') states and time, while the second term is the Lagrange cost function and is a function of time. If both cost functions are present, the problem is referred to as a problem of Bolza.[95]

While minimising the objective function in Eq. (2.45), the dynamics of the system have to be satisfied, which are defined by a set of ordinary differential equations:

$$\dot{\mathbf{x}}(t) = \mathbf{f}\left(\mathbf{x}(t), \mathbf{u}(t), \mathbf{p}, t\right) \tag{2.46}$$

In addition, constraints at the initial time, $\boldsymbol{\phi}_0 \in \mathbb{R}^{n_{\phi_0}}$, and final time, $\boldsymbol{\phi}_f \in \mathbb{R}^{n_{\phi_f}}$, can be defined, which are referred to as event constraints:

$$\begin{aligned}
\boldsymbol{\phi}_0\left(\mathbf{x}(t_0), \mathbf{u}(t_0), \mathbf{p}, t_0\right) &\geq 0 \\
\boldsymbol{\phi}_f\left(\mathbf{x}(t_f), \mathbf{u}(t_f), \mathbf{p}, t_f\right) &\geq 0
\end{aligned} \tag{2.47}$$

Furthermore, algebraic path constraints, $\mathbf{c} \in \mathbb{R}^{n_c}$, might have to be enforced onto the system:

$$\mathbf{c}\left(\mathbf{x}(t), \mathbf{u}(t), \mathbf{p}, t\right) \leq 0 \tag{2.48}$$

Finally, bounds on the state and control variables and parameters can be defined as:

$$\mathbf{x}_l \leq \mathbf{x}(t) \leq \mathbf{x}_u ; \quad \mathbf{u}_l \leq \mathbf{u}(t) \leq \mathbf{u}_u ; \quad \mathbf{p}_l \leq \mathbf{p} \leq \mathbf{p}_u \tag{2.49}$$

2.3.2   Indirect methods

The traditional way of solving the optimal control problem defined in the previous section is by using calculus of variations, which provides a set of first-order necessary conditions for

optimality. The result is a Hamiltonian (or two-point) boundary-value problem (HBVP) that needs to be solved. Since it is the HBVP that is solved rather than the original problem, this approach is referred to as 'indirect'.

To derive the optimality conditions, the cost function in Eq. (2.45) is expanded to include the dynamics and constraints:[96]

$$
\tilde{J} = M\left(\mathbf{x}_0, \mathbf{x}_f, \mathbf{p}, t_0, t_f\right) - \mathbf{v}_0^T \boldsymbol{\phi}_0\left(\mathbf{x}(t_0), \mathbf{u}(t_0), \mathbf{p}, t_0\right) - \mathbf{v}_f^T \boldsymbol{\phi}_f\left(\mathbf{x}(t_f), \mathbf{u}(t_f), \mathbf{p}, t_f\right)
$$
$$
+ \int_{t_0}^{t_f} \left[L_g\left(\mathbf{x}(t), \mathbf{u}(t), \mathbf{p}, t\right) - \boldsymbol{\lambda}^T(t)\left(\dot{\mathbf{x}}(t) - \mathbf{f}(\mathbf{x}(t), \mathbf{u}(t), \mathbf{p}, t)\right) - \boldsymbol{\mu}^T(t)\mathbf{c}\left(\mathbf{x}(t), \mathbf{u}(t), \mathbf{p}, t\right) \right] dt \tag{2.50}
$$

where $\boldsymbol{\lambda}(t) \in \mathbb{R}^{n_x}$ are the adjoint variables, or costates, $\mathbf{v}_0 \in \mathbb{R}^{n_{\phi_0}}$ and $\mathbf{v}_f \in \mathbb{R}^{n_{\phi_f}}$ the Lagrange multipliers associated with the initial and final boundary conditions and $\boldsymbol{\mu}(t) \in \mathbb{R}^{n_c}$ the Lagrange multiplier function associated with the path constraints. Subsequently, the variation of this augmented cost function with respect to each variable is set to zero, which provides the previously mentioned set of optimality conditions. For this, it is convenient to define the augmented Hamiltonian:[96]

$$
H\left(\mathbf{x}(t), \boldsymbol{\lambda}(t), \mathbf{u}(t), \boldsymbol{\mu}(t), \mathbf{p}, t\right) = L_g\left(\mathbf{x}(t), \mathbf{u}(t), \mathbf{p}, t\right) + \boldsymbol{\lambda}^T(t)\mathbf{f}(\mathbf{x}(t), \mathbf{u}(t), \mathbf{p}, t) - \boldsymbol{\mu}^T(t)\mathbf{c}\left(\mathbf{x}(t), \mathbf{u}(t), \mathbf{p}, t\right) \tag{2.51}
$$

from which the following conditions (i.e. HBVP) can be derived:[94, 96, 97]

$$
\dot{\mathbf{x}}^T = \mathbf{f}^T = \frac{\partial H}{\partial \boldsymbol{\lambda}}
$$
$$
\dot{\boldsymbol{\lambda}}^T = -\frac{\partial H}{\partial \mathbf{x}} \quad \text{(adjoint equations)}
$$
$$
\frac{\partial H}{\partial \mathbf{u}} = \mathbf{0}^T \quad \text{(control equations)}
$$
$$
\boldsymbol{\phi}_0 \geq \mathbf{0}; \quad \boldsymbol{\phi}_f \geq \mathbf{0} \tag{2.52}
$$
$$
\left.\begin{array}{l}
\boldsymbol{\lambda}(t_0) = -\dfrac{\partial M}{\partial \mathbf{x}(t_0)} + \mathbf{v}_0^T \dfrac{\partial \boldsymbol{\phi}_0}{\partial \mathbf{x}(t_0)}; \quad \boldsymbol{\lambda}(t_f) = \dfrac{\partial M}{\partial \mathbf{x}(t_f)} - \mathbf{v}_f^T \dfrac{\partial \boldsymbol{\phi}_f}{\partial \mathbf{x}(t_f)} \\[3mm]
H(t_0) = \dfrac{\partial M}{\partial t_0} - \mathbf{v}^T \dfrac{\partial \boldsymbol{\phi}_0}{\partial t_0}; \quad H(t_f) = -\dfrac{\partial M}{\partial t_f} + \mathbf{v}^T \dfrac{\partial \boldsymbol{\phi}_f}{\partial t_f}
\end{array}\right\} \text{Transversality conditions}
$$
$$
\boldsymbol{\mu}^T \mathbf{c} = 0, \quad \boldsymbol{\mu} \leq \mathbf{0}
$$

The control equations provide the optimal control law through Pontryagin's minimum principle,[98] which states that the optimal control law is the one that minimises the portion of the Hamiltonian that explicitly depends on the control vector $\mathbf{u}$.

The advantages of the indirect approach are its high accuracy and the assurance that the solution satisfies the optimality conditions. However, deriving the HBVP may not always be straightforward and convergence to a solution depends on the quality of the initial guess.[96] This is especially true for the profile of the costates, which is often non-intuitive and difficult to obtain.

2.3.3 Direct methods

In order to overcome some of the limitations noted for the indirect methods described in the previous section, direct methods have been developed.[94] Rather than formulating the HBVP as an alternative to the optimal control problem, the direct approach converts the infinite dimensional optimal control problem into a finite dimension non-linear programming (NLP) problem. In most direct methods this is achieved by discretising the domain of the independent variable into a prescribed, finite number of subintervals whose endpoints are called nodes.[96] In that case, the method is referred to as a transcription method. The NLP problem is subsequently numerically solved by non-linear programming methods.[94]

As such, the direct method does not require the analytical derivation of a set of optimality conditions and in general reaches convergence with a much less accurate initial guess than required for an indirect method. Moreover, it does not require an initial guess for the costates, of which it was said that it is non-intuitive and difficult to obtain. This makes direct methods especially attractive for complicated problems. However, for some direct methods the costate information is not available, which makes it difficult to check whether the solution found by the NLP solver is truly the optimal solution.[99]

Many different types of direct methods exist, depending on which time dependent variables are discretised and which type of function is used to approximate and interpolate these time dependent variables at the nodes. Some techniques only discretise the control variables and are therefore called control parameterisation methods. Using the control and starting from the initial state vector, the dynamics are integrated numerically over the interval of the independent variable, after which the constraints and objective function are checked and used to determine the search direction for the NLP solver. Examples of this method are shooting methods and multiple shooting methods. Alternatively, both the control and the state variables can be discretised, in which case the dynamics can be converted into algebraic constraints rather than integrating them numerically.[96, 99]

Considering the interpolating function, many different schemes have been proposed in the literature, ranging from linear and cubic splines[100] to global orthogonal polynomials in which case the direct method is referred to as a pseudospectral method.

Pseudospectral methods were originally developed to solve partial differential equations, but have become increasingly of interest for solving optimal control problems.[101, 102] The reason underlying this increased interest is the fact that the characteristics of the orthogonal polynomials are very well suited to the mathematical operations required to solve the optimal control problem: functions can be very accurately approximated, derivatives of the state functions at the nodes are computed by matrix multiplication only and any integral associated with the problem is approximated using well-known Gauss quadrature rules. This, together with the fact that pseudospectral methods have a rapid rate of convergence (i.e. convergence to a very accurate solution with few number of nodes),[103] is the reason for using pseudospectral methods in this thesis. More details on pseudospectral methods will be given below.

First, it must be noted that pseudospectral methods are a collection of different methodologies that differ from each other in the interpolating function used (often Legendre[101] or Chebyshev[104] polynomials), but also in the choice for the discretisation. For example, the Gauss pseudospectral method[103] uses N Legendre-Gauss (LG) nodes which correspond to the roots of the Nth degree Legendre polynomial, L_N. Alternatively, the Legendre pseudospectral method uses N Legendre-Gauss-Lobatto (LGL) nodes which are the roots of $\dot{L}_N$. Note that all pseudospectral methods use a non-uniform distribution of the nodes (i.e. a denser distribution towards the edges of the interval) to prevent the Runge-phenomenon, which causes the approximation near the edges of the interval to be very poor for high-degree polynomial interpolation.[105] Since the optimal control solver used throughout this thesis makes use of the Legendre pseudospectral method, some more details will be given for that particular technique following References 96, 102 and 106.

The Legendre polynomial of order N is given by

$$L_N(\tau) = \frac{1}{2^N N!} \frac{d^N}{d\tau^N} \left(\tau^2 - 1 \right)^N \tag{2.53}$$

with τ_k and $k = 0, ..., N$, $\tau_0 = -1$ and $\tau_N = 1$ the LGL nodes which are the roots of $\dot{L}_N(\tau)$ as previously noted. Let $f(\tau)$ be the smooth function representing the state or control profile on the interval $[-1, 1]$. Then, $F(\tau)$ is an approximation of that function through

$$f(\tau) \approx F(\tau) = \sum_{k=0}^{N} f(\tau_k)\varphi_k(\tau) \tag{2.54}$$

with $\varphi_k(\tau)$ the Lagrange interpolating polynomial defined as

$$\varphi_k(\tau) = \frac{1}{N(N+1)L_N(\tau_k)} \frac{(\tau^2 - 1)\dot{L}_N(\tau)}{\tau - \tau_k} \tag{2.55}$$

The derivative of the function $f(\tau)$ can subsequently be approximated using a differentiation matrix, $D_{ki} \in \mathbb{R}^{(N+1)\times(N+1)}$, as follows:

$$\dot{f}(\tau_k) \approx \dot{F}(\tau_k) = \sum_{i=0}^{N} D_{ki} f(\tau_i) \tag{2.56}$$

with

$$D_{ki} = \begin{cases} \dfrac{L_N(\tau_k)}{L_N(\tau_i)} \dfrac{1}{\tau_k - \tau_i} & \text{if } k \neq i \\[2mm] -\dfrac{N(N+1)}{4} & \text{if } k = i = 0 \\[2mm] \dfrac{N(N+1)}{4} & \text{if } k = i = N \\[2mm] 0 & \text{otherwise} \end{cases} \tag{2.57}$$

Finally, using the Legendre polynomial, the integral of a function $h(\tau)$ can be approximated through Gauss quadrature, consisting of a weighted sum of the function values at the discretisation nodes:

$$\int_{-1}^{1} h(\tau)d\tau \approx \sum_{k=0}^{N} h(\tau_k) w_k \tag{2.58}$$

with the weights w_k given by

$$w_k = \frac{2}{N(N+1)} \frac{1}{\left[L_N(\tau_k)\right]^2} \tag{2.59}$$

In order to apply Eqs. (2.54) to (2.59) to the optimal control problem defined in Section 2.3.1, the problem needs to be transformed to a new independent variable as $t \in \left[t_0, t_f\right] \rightarrow \tau \in [-1,1]$ through

$$\tau = \frac{2t}{t_f - t_0} - \frac{t_f + t_0}{t_f - t_0} \tag{2.60}$$

This results into the following new definition of the optimal control problem: find a state history $\mathbf{x}(\tau) \in \mathbb{R}^{n_x}$ and a control history $\mathbf{u}(\tau) \in \mathbb{R}^{n_u}$, with $\tau \in [\tau_0, \tau_f]$ the independent variable, that minimises the cost function:

$$J = M\left(\mathbf{x}(\tau_0), \mathbf{x}(\tau_f), \mathbf{p}, t_0, t_f\right) + \frac{t_f - t_0}{2} \int_{\tau_0}^{\tau_f} L_g\left(\mathbf{x}(\tau), \mathbf{u}(\tau), \mathbf{p}, \tau\right) d\tau \tag{2.61}$$

subject to the following dynamics, event constraints, path constraints and bounds on the state and control variables:

$$\dot{\mathbf{x}}(\tau) = \frac{t_f - t_0}{2} \mathbf{f}(\mathbf{x}(\tau), \mathbf{u}(\tau), \mathbf{p}, \tau) \tag{2.62}$$

$$\begin{aligned} \boldsymbol{\phi}_0\left(\mathbf{x}(\tau_0), \mathbf{u}(\tau_0), \mathbf{p}, t_0\right) \geq 0 \\ \boldsymbol{\phi}_f\left(\mathbf{x}(\tau_f), \mathbf{u}(\tau_f), \mathbf{p}, t_f\right) \geq 0 \end{aligned} \tag{2.63}$$

$$\mathbf{c}\left(\mathbf{x}(\tau), \mathbf{u}(\tau), \mathbf{p}, \tau\right) \leq 0 \tag{2.64}$$

$$\mathbf{x}_l \leq \mathbf{x}(\tau) \leq \mathbf{x}_u; \quad \mathbf{u}_l \leq \mathbf{u}(\tau) \leq \mathbf{u}_u; \quad \mathbf{p}_l \leq \mathbf{p} \leq \mathbf{p}_u \tag{2.65}$$

Subsequently using an Nth-order Lagrange polynomial based on interpolation at the LGL nodes, the optimal control problem defined in Eqs. (2.61) to (2.65) can be discretised. The state and control profiles then become:

$$\mathbf{x}(\tau) \approx \mathbf{X}(\tau) = \sum_{k=0}^{N} \mathbf{x}(\tau_k) \varphi_k(\tau) \qquad \mathbf{X} \in \mathbb{R}^{n_x \times (N+1)} \tag{2.66}$$

$$\mathbf{u}(\tau) \approx \mathbf{U}(\tau) = \sum_{k=0}^{N} \mathbf{u}(\tau_k) \varphi_k(\tau) \qquad \mathbf{U} \in \mathbb{R}^{n_u \times (N+1)} \tag{2.67}$$

Furthermore, using the differentiation matrix in Eq. (2.57) the dynamics are given by:

$$\dot{\mathbf{x}}(\tau_k) \approx \dot{\mathbf{X}}(\tau_k) = \sum_{i=0}^{N} D_{ki} \mathbf{X}(\tau_i) \qquad \dot{\mathbf{X}} \in \mathbb{R}^{n_x \times (N+1)} \tag{2.68}$$

The following step is the key step of all collocation methods to which the Legendre pseudospectral method belongs. A collocation method requires the approximation of the dynamics to be equal to the evaluation of the dynamics at the discretisation nodes, or collocation points, which is given through the differential defects. Note that for the Legendre pseudospectral method, the number of discretisation nodes is equal to the collocation points, while this is not true for all pseudospectral methods. For example, the gauss pseudospectral method only collocates at the interior points (not at the initial and final discretisation nodes), and therefore there are two more discretisation nodes than collocation points. The differential defects are given through:

$$\zeta(\tau_k) = \dot{\mathbf{X}}(\tau_k) - \frac{t_0 - t_f}{2} \mathbf{f}(\mathbf{X}(\tau_k), \mathbf{U}(\tau_k), \mathbf{p}, \tau_k) \qquad \zeta \in \mathbb{R}^{n_x \times (N+1)} \tag{2.69}$$

Note that, through Eq. (2.69) the dynamics of the system are replaced by a set of algebraic conditions at the discretisation nodes.

Finally, the objective function, event constraints, path constraints and bounds are discretised as well according to

$$J = M\left(\mathbf{X}(\tau_0), \mathbf{X}(\tau_f), \mathbf{p}, t_0, t_f\right) + \frac{t_f - t_0}{2} \sum_{k=0}^{N} L_g\left(\mathbf{X}(\tau_k), \mathbf{U}(\tau_k), \mathbf{p}, \tau_k\right) w_k \tag{2.70}$$

$$\begin{aligned}
\boldsymbol{\Phi}_0\left(\mathbf{X}(\tau_0), \mathbf{U}(\tau_0), \mathbf{p}, t_0\right) \geq 0 & \qquad \boldsymbol{\Phi}_0 \in \mathbb{R}^{n_{\phi_0}} \\
\boldsymbol{\Phi}_f\left(\mathbf{X}(\tau_f), \mathbf{U}(\tau_f), \mathbf{p}, t_f\right) \geq 0 & \qquad \boldsymbol{\Phi}_f \in \mathbb{R}^{n_{\phi_f}}
\end{aligned} \tag{2.71}$$

$$\mathbf{C}\left(\mathbf{X}(\tau_k), \mathbf{U}(\tau_k), \mathbf{p}, \tau_k\right) \leq 0 \qquad \mathbf{C} \in \mathbb{R}^{n_c \times (N+1)} \tag{2.72}$$

$$\mathbf{x}_l \leq \mathbf{X}(\tau_k) \leq \mathbf{x}_u \ ; \ \mathbf{u}_l \leq \mathbf{U}(\tau_k) \leq \mathbf{u}_u \ ; \ \mathbf{p}_l \leq \mathbf{p} \leq \mathbf{p}_u \tag{2.73}$$

with the weights, w_k, in Eq. (2.70) defined in Eq. (2.59). The final step is now to express the discretised optimal control problem as a nonlinear programming problem, which in general is defined as finding the decision vector $\mathbf{y}$ to the following minimisation problem:[94]

$$\min_{\mathbf{y}} F(\mathbf{y}) \tag{2.74}$$

subject to the constraints

$$\mathbf{g}_l \leq \mathbf{g}(\mathbf{y}) \leq \mathbf{g}_u \tag{2.75}$$

and bounds

$$\mathbf{y}_l \leq \mathbf{y} \leq \mathbf{y}_u \tag{2.76}$$

The decision vector for the problem defined in Eqs. (2.66) to (2.73) is:

$$\mathbf{y} = \begin{bmatrix} \text{vec}(\mathbf{X}) \\ \text{vec}(\mathbf{U}) \\ \mathbf{p} \end{bmatrix} \qquad \mathbf{y} \in \mathbb{R}^{n_x(N+1)+n_u(N+1)+n_p} \tag{2.77}$$

with bounds defined as

$$\mathbf{y}_l = \begin{bmatrix} \text{stack}(\mathbf{x}_l, N+1) \\ \text{stack}(\mathbf{u}_l, N+1) \\ \mathbf{p}_l \end{bmatrix}, \qquad \mathbf{y}_u = \begin{bmatrix} \text{stack}(\mathbf{x}_u, N+1) \\ \text{stack}(\mathbf{u}_u, N+1) \\ \mathbf{p}_u \end{bmatrix} \tag{2.78}$$

where the notation 'vec' is used to indicate that the columns of the matrices $\mathbf{X}$ and $\mathbf{U}$ are stacked to create one long vector and the notation 'stack' is used to indicate that the vectors $\mathbf{x}_l$ and $\mathbf{u}_l$ are repeatedly stacked such that the same bounds hold for every discretisation node in $\text{vec}(\mathbf{X})$ and $\text{vec}(\mathbf{U})$.

The objective function $F(\mathbf{y})$ is given by Eq. (2.70), while the constraints vector is constructed as follows:

$$\mathbf{g} = \begin{bmatrix} \text{vec}(\zeta) \\ \text{vec}(\mathbf{C}) \\ \mathbf{\Phi}_0 \\ \mathbf{\Phi}_f \end{bmatrix} \qquad \mathbf{g} \in \mathbb{R}^{n_x(N+1)+n_c(N+1)+n_{\phi_0}+n_{\phi_f}} \tag{2.79}$$

with bounds defined as

$$\mathbf{g}_l = \begin{bmatrix} \mathbf{0}_{n_x(N+1)} \\ \text{stack}(\mathbf{c}_l, N+1) \\ \phi_{0,l} \\ \phi_{f,l} \end{bmatrix}, \qquad \mathbf{g}_u = \begin{bmatrix} \mathbf{0}_{n_x(N+1)} \\ \text{stack}(\mathbf{c}_u, N+1) \\ \phi_{0,u} \\ \phi_{f,u} \end{bmatrix} \tag{2.80}$$

The NLP problem defined in Eqs. (2.74) to (2.80) can now be presented to an NLP solver to solve the optimal control problem originally defined in Section 2.3.1.

A final note in this section can be devoted to the theorem of costate mapping.[103, 107] It was already stated previously that one of the advantages of the direct methods is the fact that it does not need an initial guess for the costates and there is also no need to discretise and

approximate the costates. However, if it would be feasible to still extract an approximation of the costates from the direct method, this could help both in terms of validating the optimality of the solution of the direct method and in terms of use as an initial guess to solve the optimal control problem through the indirect method. The way to obtain the profile of the costates is through the costate mapping theory, which is illustrated in Fig. 2.10.

The figure shows that from the discretised NLP a set of first-order optimality conditions, referred to as the Karush-Kuhn-Tucker (KKT) conditions, can be developed similarly to the optimality conditions defined for the indirect method. Moreover, these KKT conditions include a set of Lagrange multipliers which can be shown to directly map onto the costates of the indirect method after the continuous HBVP is discretised using the same pseudospectral discretisation that was used in the direct method. Once these KKT multipliers, $\tilde{\lambda}_k$ are obtained, the costates at the LGL points can easily be computed from:

$$\lambda(\tau_k) = \frac{\tilde{\lambda}_k}{w_k} \tag{2.81}$$

with w_k the weights defined in Eq. (2.59).
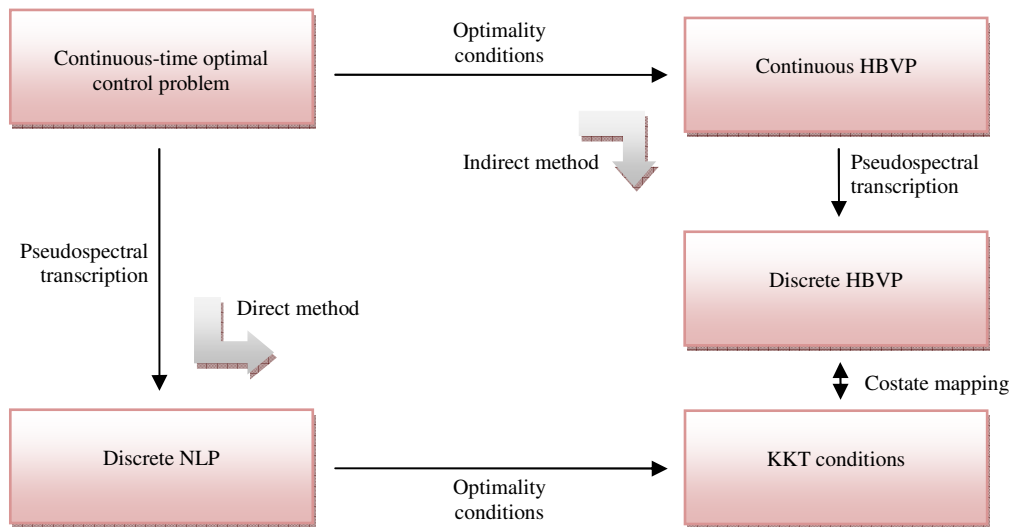
Fig. 2.10 Flow diagram of the indirect and direct pseudospectral methods.[103]

2.3.4 PSOPT

A range of software packages exist that implement the direct pseudospectral method discussed in the previous section. This thesis mainly uses the optimal control solver PSOPT (release 2).[106, 108] PSOPT is an open source tool developed by Victor M. Becerra of the University of Reading and is written in C++. It can use both Legendre and Chebyshev

polynomials to approximate and interpolate the dependent variables at the nodes and has interfaces to two NLP solvers: IPOPT (Interior Point OPTimizer),[109] an open source C++ implementation of an interior point method for large scale problems and SNOPT (Sparse Nonlinear OPTimizer),[110] a well-known and widely used proprietary large scale NLP solver. However, in this thesis only the Legendre pseudospectral method and IPOPT will be used.

PSOPT is a very versatile and user-friendly software package that can deal with Mayer and Lagrange cost functions, nonlinear dynamics, event constraints, nonlinear path constraints and bounds on the state and control variables and the parameters. In addition, PSOPT can deal with interior point constraints, bounds on the initial and final times, dynamics with delayed variables and includes options for mesh refinements, automatic scaling and the use of multiple phases. For the latter, the domain of the independent variable is divided into smaller intervals, referred to as phases, and the different phases are connected together through additional linkage constraints. Multiple phases allow the implementation of different dynamics and constraints in each phase and it also allows accommodating any discontinuities in the state and/or control profile which are difficult to capture with smooth polynomials.

Another key characteristic of PSOPT is the fact that it employs the ADOL-C (Automatic Differentiation by OverLoading in C++) library[111] for the automatic differentiation of the objective, dynamics and constraint functions. Automatic derivatives are more accurate than numerical derivatives as they are free of truncation errors and shorten the computational time. However, in case that automatic differentiation is not suitable for the problem under consideration, PSOPT also offers the possibility of numerical differentiation by using sparse finite differences.

A final key attribute of PSOPT is the fact that it can obtain the KKT multipliers from the NLP solver and can therefore provide an approximation of the costate profile at the LGL nodes through the use of Eq. (2.81).

Note that a benchmark of PSOPT for the problems considered in this thesis work is provided in Section 4.6 by comparing its results with the solution obtained using an indirect approach where the initial guess for the costate variables is obtained through the costate mapping theorem. Another approach to validate PSOPT is provided in Section 5.7, where the results are compared with those generated using another pseudospectral optimal control solver, GPOPS (General Pseudospectral OPtimal Control Software) (version 2.3).[112]

2.3.5 Initial guess generation

As stated in the previous section, optimal, low-thrust trajectories can be found by solving the accompanying optimal control problem using either an indirect or direct method. In both cases, a suitable initial guess is required, which is not always straightforward to obtain. Many papers appearing in the literature address this problem by providing analytical solutions for low-thrust trajectories,[38, 113-117] but all are based to some extent on problem-dependent approximations and simplifications, for example pure radial or tangential thrust. A solution for more general cases was introduced by Petropoulos and Longuski[118] in the form of a shape-based approach. Shape-based approaches use an inverse method by first assuming a particular shape for the trajectory and subsequently analytically computing the thrust magnitude and thrust angle profiles required to follow that shape, while satisfying the equations of motion and boundary conditions. As such, they can quickly and efficiently generate the required first guesses and perform the search across the large design space.

The particular shape proposed by Petropoulos and Longuski[118-120] is the exponential sinusoid, which is defined in polar coordinates (r, θ) and is therefore suitable for planar motion:

$$r = k_0 \exp\left[k_1 \sin\left(k_2\theta + \phi\right)\right] \tag{2.82}$$

where k_0, k_1, k_2 and ϕ are constants or shape parameters. The parameter k_0 is a scaling factor, k_1 is the dynamic range parameter that determines the ratio of the apoapsis distance to periapsis distance, k_2 is the winding parameter (the smaller k_2 the narrower the windings) and ϕ determines the orientation of the trajectory in the plane.[120] Starting from the two-body dynamics in polar coordinates:

$$\ddot{r} - r\dot{\theta}^2 + \frac{\mu_C}{r^2} = F \sin\alpha$$
$$\ddot{\theta}r + 2\dot{\theta}\dot{r} = F \cos\alpha \tag{2.83}$$

and assuming a tangential thrust profile (i.e. the thrust angle α equals the flight path angle γ), the following expressions for the angular rate, the normalised thrust acceleration and flight path angle can be derived analytically:

$$\dot{\theta}^2 = \left(\frac{\mu_C}{r^3}\right)\frac{1}{\tan^2\gamma + k_1 k_2^2 s + 1} \tag{2.84}$$

$$a = \frac{\tan\gamma}{2\cos\gamma}\left(\frac{1}{\tan^2\gamma + k_1 k_2{}^2 s + 1} - \frac{k_2{}^2(1 - 2k_1 s)}{\left(\tan^2\gamma + k_1 k_2{}^2 s + 1\right)^2}\right) \quad (2.85)$$

$$\tan\gamma = k_1 k_2 c \quad (2.86)$$

with $a = F/\left(\mu_C/r^2\right)$, $s = \sin(k_2\theta + \phi)$ and $c = \cos(k_2\theta + \phi)$. Finally, a condition on the feasibility of the exponential sinusoids can be introduced, since it can be shown that at apoapsis and periapsis, where $\gamma = 0$ and $s = \pm 1$, the exponential sinusoids are only feasible if

$$\left|k_1 k_2^2\right| < 1 \quad (2.87)$$

otherwise $\dot{\theta}^2 < 0$.

The exponential sinusoids are easy to implement and can quickly generate trajectories. Because they only contain four shaping parameters, they cannot satisfy both boundary constraints on position and velocity and constraints on, for example, the time of flight and thrust magnitude. The boundary conditions on the velocity are therefore often translated into additional impulses to be given at the start and end of the transfer. As these impulses can be optimised, this is not an immediate problem, although the exponential sinusoids often lead to rather large impulses which can result in poor convergence properties when used as initial guess in an optimal control solver. More recent shapes such as a shape consisting of parameterised pseudoequinoctial elements by De Pascale and Vasile,[121] an inverse polynomial shape by Wall and Conway[122, 123] and a spherical shape by Novak and Vasile,[124] do allow for all boundary conditions to be satisfied, even in a three-dimensional case. Also, besides satisfying the boundary constraints, the shapes by De Pascale and Vasile[121] and Novak and Vasile[124] can also satisfy a constraint on the thrust magnitude.

Chapter 3

Design of displaced geostationary

orbits

This chapter considers the design of displaced geostationary orbits as a solution to the congestion of geostationary orbit as detailed in Section 1.1.1. The first section will define out-of-plane and in-plane displaced GEOs as investigated in this work. Using these definitions, Sections 3.2 and 3.3 will derive the performance of impulsive and pure SEP control for maintaining the displaced GEO in terms of propellant consumption and mission lifetime. Similar results will be obtained for the hybrid sail case in Section 3.4. Since the out-of-plane case outperforms the in-plane case, the out-of-plane case will be used for a detailed mass budget analysis in Section 3.5 to assess the performance in terms of payload mass capacity. Finally, in Section 3.6, the control of the displaced GEO under the influence of both the J_2 and $J_{2,2}$ terms of the Earth's gravitational potential and non-ideal solar sail properties will be provided. The chapter finishes with conclusions.

3.1   Displaced geostationary orbit definition

This thesis considers two types of displaced geostationary orbits: out-of-plane displaced GEOs where the geostationary orbit is levitated *out of* the equatorial plane and in-plane displaced GEOs where the geostationary orbit is displaced *in* the equatorial plane. Both types of orbits will be defined in Sections 3.1.1 and 3.1.2, respectively.

3.1.1 Out-of-plane displaced geostationary orbit

In Section 2.1.2 the expressions for the required acceleration and thrust direction for a general two-body displaced NKO were derived, see Eqs. (2.10) and (2.11). However, for the displaced GEO it is given that the angular velocity equals $\omega = \omega_{GEO} = \sqrt{\mu_\oplus / r_{GEO}^3}$, with $\mu_\oplus$ the gravitational parameter of the Earth and r_{GEO} = 42164.1696 km, where the value for the GEO radius is obtained from the fact that GEO has an orbital period of one sidereal day (23 hours, 56 min and 4.091 s). Furthermore, assuming a displacement, h, to create an out-of-plane displaced GEO, Eq. (2.11) can be used to find the corresponding projected radius ρ that minimises the required acceleration. Taking the first derivative of Eq. (2.11) with respect to ρ and setting it equal to zero yields the following condition:

$$r^6 + \frac{\mu_C}{\omega^2} r^3 - 3 \frac{\mu_C}{\omega^2} h^2 r - 2 \left(\frac{\mu_C}{\omega^2} \right)^2 = 0 \qquad (3.1)$$

The complex and negative real roots of this sixth order polynomial are ignored and Descartes' Rule of Signs is applied to find that Eq. (3.1) has one sign change and therefore one positive real root.[125] An analytical solution to Eq. (3.1) was not found, therefore a numerical method in the form of Newton's method was applied to find the optimal projected radius.[126] The results for a large range of out-of-plane displacements are illustrated in Fig. 3.1, which shows the Type III NKO acceleration contour plots for ω_{GEO} (similar to Fig. 2.5c) and includes the solution to Eq. (3.1). The figure shows the correctness of the approach as the solution connects the extrema of the separate contour lines, i.e. the minimum acceleration required to provide a particular out-of-plane displacement.

The figure furthermore shows that, clearly, the smaller the out-of-plane displacement, the smaller the required acceleration. However, for the displaced GEO, the minimum displacement is predefined by the geostationary station-keeping box to prevent the spacecraft from interfering with other satellites in GEO. Considering International Telecommunications Union (ITU) regulations and regulations drawn up by individual countries, such as those of the US Federal Communications Commission (FCC), a geostationary longitude station-keeping box width, $\Delta\lambda$, of $2\Delta\lambda = 0.1° - 0.2°$ can be defined, equalling a box size of 73.6 - 147.2 km centred around a geostationary satellite.[11, 127] This leads to a range of minimum displacement distances of 36.8 – 147.2 km, where 36.8 km represents the case that the spacecraft just hovers above the GEO station-keeping box, while the higher displacements also take a station-keeping box for the displaced spacecraft into account, see Fig. 3.2 .
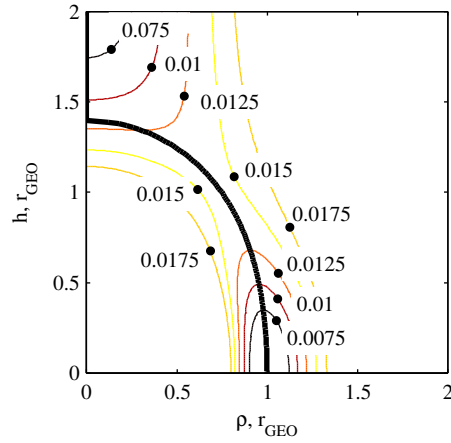
Fig. 3.1 Type III NKO acceleration contour plots for ω_{GEO} including the minimised acceleration for a given out-of-plane displacement, h (denoted by solid black line). The acceleration is dimensionless with respect to the gravitational acceleration at unit planet radius and is marked on the contours.
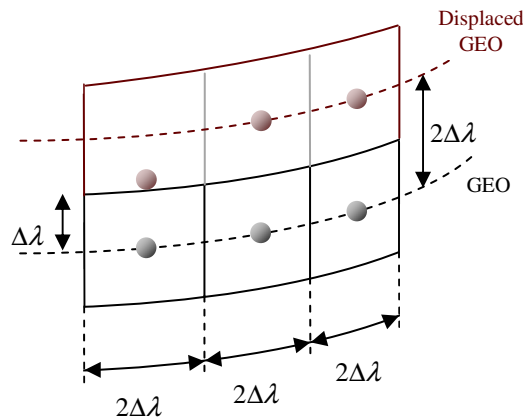
Fig. 3.2 Definition of geostationary station-keeping box.

Three displacement distances will therefore be considered in this thesis, namely 35, 75 and 150 km, which are the rounded values of 36.8 km, 2×36.8 km and 147.2 km. Solving Eq. (3.1) for these three displacements and subsequently using Eq. (2.10) to find the required thrust pitch angle, provides the optimal displaced GEOs as defined in Table 3.1.

Table 3.1 Definition of minimum acceleration out-of-plane displaced GEOs.

h, km	ρ, km	α, deg	a, mm/s^2
±35	42164.165	0.0476	0.1861
±75	42164.147	0.1019	0.3988
±150	42164.080	0.2038	0.7976

50

From the pitch angle it becomes clear that an almost pure out-of-plane acceleration (i.e. $\alpha = 0$) is required. Equation (2.10) subsequently shows that, to obtain $\alpha = 0$, the condition $\omega = \omega_*$ should be satisfied, which corresponds to a Type I NKO, which in its turn requires $r = r_{GEO}$. Substituting this into Eq. (2.11), gives the required thrust magnitude to maintain such a Type I displaced GEO:

$$a = h\omega_*^2 = \frac{\mu_\oplus h}{r_{GEO}^3} \tag{3.2}$$

A schematic of this type of out-of-plane displaced GEO is provided in Fig. 3.3. Contrary to the cases in Table 3.1, the Type I displaced GEO allows for an analytical derivation of the performance of hybrid sail control, and will therefore be used later for the out-of-plane case. Since the difference in acceleration between the minimised accelerations given in Table 3.1 and the Type I NKO is only 6.3×10^{-4} percent at maximum (i.e. for $h = 150$ km), using a Type I orbit, rather than the optimised displaced GEO, will only result in a slightly conservative estimate of the required performance.
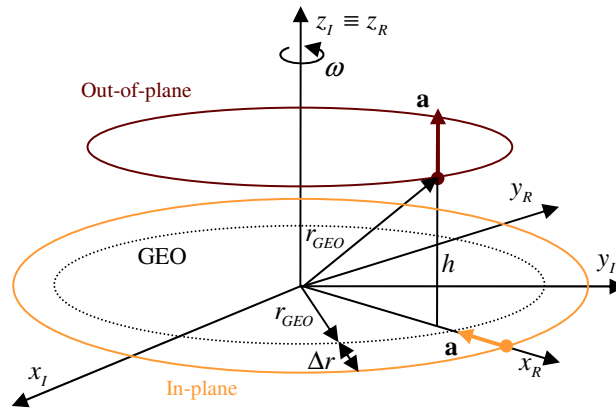
Fig. 3.3 Definition of out-of-plane and in-plane displaced GEOs.

3.1.2   In-plane displaced geostationary orbit

Rather than displacing the GEO out-of-plane, another option would be to displace the GEO in-plane, i.e. in the equatorial plane, see also Fig. 3.3. Substituting $h = 0$ into Eq. (2.10) and (2.11) provides the thrust direction and magnitude required to maintain such an in-plane displaced GEO:

$$\alpha = \pm\frac{1}{2}\pi \tag{3.3}$$

$$a = \left| \rho \left(\omega_{GEO}^2 - \omega_*^2 \right) \right| \qquad (3.4)$$

with $\omega_* = \sqrt{\mu_\oplus / \rho^3}$ and $\rho = r_{GEO} + \Delta r$, where the radial displacement $\Delta r > 0$ and $\Delta r < 0$ for orbits displaced outside or inside GEO, respectively. Equation (3.3) furthermore shows that a pure radial thrust is required, directed either inward ($\alpha < 0$) or outward ($\alpha > 0$), depending on the sign of Δr, to increase or decrease the angular velocity of a Keplerian orbit with radius ρ to the angular velocity of GEO.

An initial assessment of the relative performance of the out-of-plane and in-plane displaced orbits can be derived from the contour plot in Fig. 3.1. The figure shows that for *small* and *equal* displacements in out-of-plane (along the vertical axis) and in-plane (along the horizontal axis) direction, the ratio of the required accelerations is approximately 3, as can also be shown from Hill's equations.[126] The in-plane displacement thus requires an acceleration three times higher than an equally displaced out-of-plane orbit. The acceleration contours furthermore show that it is slightly more advantageous to displace the orbit outside ($\Delta r > 0$) the GEO than inside: for the same acceleration a larger displacement outside than inside the GEO can be achieved. This thesis therefore always considers the $\Delta r > 0$ case (as depicted in Fig. 3.3) for the in-plane displaced GEO.

3.2   Impulsive propulsion

Although a continuous acceleration is required to achieve a displaced NKO, impulsive control using a chemical propulsion system can be employed to maintain a minimum displacement from a Keplerian orbit. By providing multiple impulsive velocity changes along the displaced GEO, the spacecraft can 'bounce' on the displaced orbit. Then, at time $t = 0$ the spacecraft is located at the displaced GEO and an instantaneous change in velocity, or impulse, ΔV, is given. This will cause the spacecraft to slightly move away from the displaced GEO. However, since no thrust is applied between pulses, the spacecraft follows a natural Keplerian orbit after the impulse, causing the spacecraft to cross the displaced GEO after some time. Upon this crossing, another impulse is given to reverse the spacecraft velocity and start the cycle again. This concept is illustrated in Fig. 3.4 for an out-of-plane displaced GEO. The use of impulsive control to maintain displaced NKOs has been investigated before and has among others been suggested to hover above Saturn's rings[42, 53] and to maintain a local cluster of spacecraft for high resolution imaging of terrestrial or astronomical targets using interferometry techniques.[128]
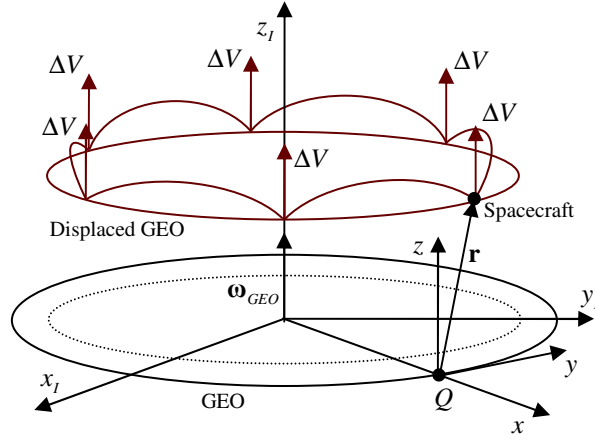
Fig. 3.4 Illustration of impulsive control for an out-of-plane displaced GEO and definition of reference frame for Hill's equations.

For small displacements, the required magnitude of the impulses can be computed using the linearised Hill's equations that represent the dynamics of a spacecraft in the vicinity of a point Q on a circular Keplerian reference orbit, see Fig. 3.4.[42, 126] A detailed derivation is given by McInnes[42] and is therefore not repeated here. Only the results are provided. For the first impulse the following holds:

$$\Delta V_{x,0} = \dot{x}_0 = \frac{3\omega_{GEO}^2 x_0 t_p \tan\left(\omega_{GEO} t_p / 2\right)}{3\omega_{GEO} t_p - 8\tan\left(\omega_{GEO} t_p / 2\right)} \tag{3.5}$$

$$\Delta V_{y,0} = \dot{y}_0 = 6 x_0 \omega_{GEO} \frac{\omega_{GEO} t_p - 2\tan\left(\omega_{GEO} t_p / 2\right)}{8\tan\left(\omega_{GEO} t_p / 2\right) - 3\omega_{GEO} t_p} \tag{3.6}$$

$$\Delta V_{z,0} = \dot{z}_0 = \omega_{GEO} z_0 \tan\left(\omega_{GEO} t_p / 2\right) \tag{3.7}$$

with x_0 and z_0 defined in the rotating reference frame shown in Fig. 3.4 with the subscript '0' indicating the initial conditions and $t_p = P_o / N_i$ where P_o is the orbital period and N_i the number of impulses per orbit. For the out-of-plane displaced GEO $\dot{x}(t_p) = -\dot{x}(0)$, $\dot{y}(t_p) = \dot{y}(0)$ and $\dot{z}(t_p) = -\dot{z}(0)$ and therefore only repeated impulses in x and z direction have to be provided, but with double the required ΔV to reverse the direction of the velocity vector. For an in-plane displaced GEO $\dot{x}(t_p) = -\dot{x}(0)$, $\dot{y}(t_p) = \dot{y}(0)$ and $\dot{z}(t_p) = \dot{z}(0) = 0$, which requires only repeated, double magnitude impulses in the x direction.
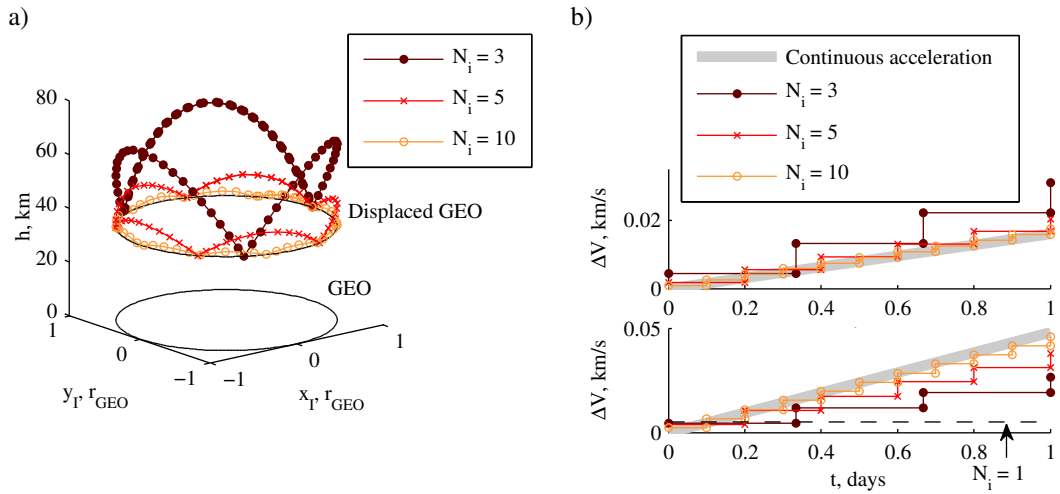
Fig. 3.5 a) 35 km out-of-plane displaced GEO with impulsive control. b) Required *ΔV* for a 35 km out-of-plane (top) and in-plane (bottom) displaced GEO for different numbers of impulses per orbit, N_i.

Figure 3.5a shows the results for an out-of-plane displaced GEO levitated 35 km above the equatorial plane for one orbital revolution and for different numbers of impulses along the orbit. The top plot in Fig. 3.5b furthermore shows the ΔV required to maintain such an orbit, while the bottom plot provides similar information for a 35 km in-plane displaced orbit. The figure clearly shows the larger ΔV required for the in-plane case than for the out-of-plane case, as expected from the analysis in Section 3.1.2. It also shows that a higher number of pulses is advantageous when displacing the orbit out-of-plane, i.e. the penalty on the ΔV due to pulsed rather than continuous control becomes less. Contrary, for the in-plane displaced GEO, a higher number of impulses is disadvantageous, because, although the amount of ΔV *per impulse* decreases, the decrease is not sufficient to compensate for the larger *number of impulses* that needs to be provided. This implies that the impulsive control case requires less ΔV than the continuous control case for the in-plane displaced GEO. The reason for this can be explained when considering the limit case, when $N_i = 1$ and $t_p = t_o$. Then, from Eq. (3.5) it follows that $\Delta V_{x,0} = 0$ and therefore no additional impulses are required after the initial impulse, which only consists of a ΔV in y direction (i.e. along track), $\Delta V_y = $ -0.0051 km/s. The result is that the spacecraft is injected into a slightly elliptic orbit with apogee coinciding with the displaced GEO and perigee inside the geostationary orbit (i.e. for the case where the displaced GEO is located outside the geostationary orbit, as decided in the previous section). The total ΔV throughout the mission thus equals 0.0051 km/s, which easily outweighs the ΔV built up during the mission when using continuous control. It even outweighs the impulsive, out-of-plane case. However, as

indicated, the orbit crosses the geostationary orbit, which introduces a significant collision risk and is therefore not of practical use. At least three impulses are required in order not to cross the geostationary orbit, but then, the total ΔV per orbit is once again larger than for the continuous, out-of-plane case.

The analysis in Fig. 3.5 can be extended from one orbital revolution to multiple revolutions to obtain the performance of impulsive control for maintaining the displaced GEO in terms of mission lifetime. This lifetime, L, is defined as the epoch at which a particular mass fraction, m_f / m_0 is obtained:

$$\frac{m_f}{m_0} = \frac{m_0 - m_{prop}}{m_0} \tag{3.8}$$

with m_f, m_0 and m_{prop} the final, initial and propellant mass, respectively. The propellant mass can be computed through an iterative approach and using the rocket equation that gives the ratio of the mass prior, m^-, and after, m^+, the impulses providing the combined ΔV:

$$\frac{m^-}{m^+} = e^{\frac{\Delta V}{I_{sp} g_0}} \tag{3.9}$$

Equation (3.9) in combination with the results in Fig. 3.5b immediately shows that the out-of-plane displaced GEO will outperform the in-plane displaced GEO due to the smaller amount of ΔV required. The results, as shown in Fig. 3.6, are therefore only provided for the out-of-plane case. Figure 3.6 holds for an arbitrary initial mass and considers both a range of specific impulses (from current to near term and far-future technology) and a range of mass fractions for the three displacement distances of 35, 75 and 150 km. Furthermore, 10 impulses per orbit are assumed to provide a balance between the complexity of the mission, for which the number of impulses per orbit should be as low as possible, and the penalty on the ΔV for pulsed control and the deviation from the nominal displaced orbit, for which the number of impulses per orbit should be as large as possible. Note that the symmetry of the problem causes the results for GEOs displaced above and below the equatorial plane to be exactly the same.

The graphs in Fig. 3.6 can be interpreted in different ways. For example, for a 35 km displaced GEO, a currently achievable specific impulse of 320 s[62] and a mass fraction of 0.5 a lifetime of 0.36 years can be achieved. Comparing that to lifetimes of 10-15 years for current GEO spacecraft,[127] where the lifetime is mainly limited due to required costly station-keeping manoeuvres, it becomes clear that similar lifetimes cannot be achieved using

impulsive control. Only a maximum of 1.9 years can be obtained for the smallest displacement distance and for extreme values of the specific impulse and the mass fraction. The cause of this poor performance lies in the penalty on the ΔV for pulsed rather than continuous control (i.e. for the out-of-plane case) and the low specific impulse of chemical propulsion systems.

a)   b)   c)

$h = \pm35$ km $h = \pm75$ km $h = \pm150$ km
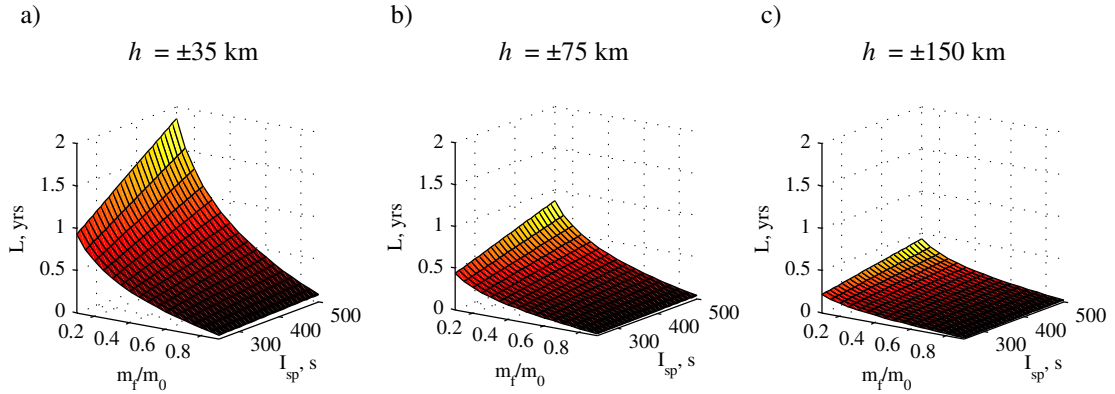
Fig. 3.6 Out-of-plane displaced GEOs maintained with impulsive control ($N_i = 10$): mission time, L, as a function of the specific impulse, I_{sp}, and the mass fraction, m_f/m_0, for different values of the displacement distance, h.

3.3   Solar electric propulsion

This section investigates the use of SEP to maintain the displaced GEO in order to improve the performance of the displaced GEO with respect to the use of impulsive control. The performance of SEP control in terms of mission lifetime for a particular mass fraction can be assessed by considering the differential equation for the mass in Eq. (2.15). Since the required acceleration is constant (see Eq. (3.2)), the lifetime can be derived analytically from Eq. (2.15): substituting $T = a \cdot m$ into Eq. (2.15) and rearranging gives:

$$\int_{m_0}^{m_f} \frac{dm}{m} = -\int_{t_0}^{t_f} \frac{a}{I_{sp} g_0} dt \tag{3.10}$$

Evaluating these integrals and setting $t_0 = 0$ yields the following lifetime:

$$L = t_f = \ln\left(\frac{m_0}{m_f}\right) \frac{I_{sp} g_0}{a} \tag{3.11}$$

Equation (3.11) shows that, clearly, a higher required acceleration reduces the mission lifetime. Considering the fact that the in-plane displaced GEO requires a larger acceleration than an equally displaced out-of-plane orbit (see Section 3.1.2), a shorter lifetime can be expected for the in-plane case. The results, as shown in Fig. 3.7, are therefore again only provided for the out-of-plane case. The figure shows the mission lifetime for an arbitrary initial mass, a wide range of specific impulses and mass fractions and for the three displacement distances of 35, 75 and 150 km. Again, the results hold both for GEOs displaced above the equatorial plane and for those displaced below the equatorial plane, due to the symmetry of the problem.

The graphs can be interpreted similarly to the graphs in Fig. 3.6. Comparing Fig. 3.7 with Fig. 3.6 immediately shows a dramatic improvement of the lifetime for an SEP-controlled spacecraft over an impulsive controlled spacecraft. Again, considering a mass fraction of 0.5 and assuming a currently feasible SEP specific impulse of 3200 s as determined in Section 2.2.1, the lifetime is increased from 4.3, 2.0 and 1.0 months for impulsive control to 3.7, 1.7 and 0.9 years for 35, 75 and 150 km displaced orbits, respectively. And again, considering a lifetime of 10-15 years for current geostationary spacecraft, Fig. 3.7 shows that similar lifetimes can only be achieved for the smallest displacement of 35 km and either for low mass fractions (e.g. $m_f / m_0 = 0.1$ and $I_{sp} = 2600$ s) or for high specific impulses (e.g. $m_f / m_0 = 0.45$ and $I_{sp} = 7500$ s).
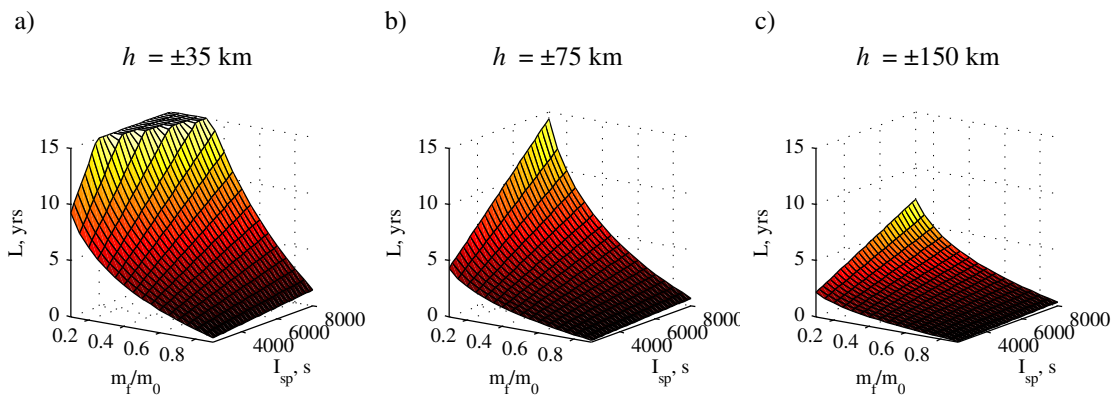
Fig. 3.7 Out-of-plane displaced GEOs maintained with SEP control: mission time, *L*, (a maximum of 15 years is considered) as a function of the specific impulse, *I_{sp}*, and the mass fraction, *m_f/m_0*, for different values of the displacement distance, *h*.

3.4   Hybrid sail propulsion

To improve the performance of the displaced GEO even further, this section will investigate the use of hybrid sail propulsion. For this, the acceleration required to maintain the displaced GEO, $\mathbf{a}$, see Eq. (3.2) for the out-of-plane case and Eqs. (3.3) and (3.4) for the in-plane case, is split between the acceleration generated by the SEP system, $\mathbf{a}_{SEP}$, and the acceleration produced by the solar sail, $\mathbf{a}_s$, equivalently to what was done in Eq. (2.42) in Section 2.2.3:

$$\mathbf{a}_h = \mathbf{a}_{SEP} + \mathbf{a}_s \tag{3.12}$$

To maximise the lifetime of the mission using hybrid sail propulsion, the objective is to minimise the magnitude of the acceleration required from the SEP system:

$$\min\left(a_{SEP}\right) = \min\left(\left|\mathbf{a} - \mathbf{a}_s\right|\right) \tag{3.13}$$

Here, an ideal solar sail model is assumed, so the acceleration provided by the solar sail is given by Eq. (2.24). Later on, in Section 3.6.2, the influence of non-ideal solar sail properties will be investigated. Note that, for the displaced GEO, the Sun-sail distance in Eq. (2.24), r_s, is approximated by a constant Sun-Earth distance of 1 AU. This assumption introduces only a small error with a maximum value of 1.7 percent in the Sun-sail distance, which includes both the variation in the Sun-Earth radius during the year and the change in Earth-spacecraft vector during one orbital revolution.

Furthermore, due to the tilt of the Earth's rotational axis with respect to the ecliptic plane, the direction of the Sun-sail unit vector, $\hat{\mathbf{r}}_s$ changes during the year. To model this variation, an Earth fixed rotating reference frame $E(x_E, y_E, z_E)$ as shown in Fig. 3.8 is used. Centred at the Earth with the (x_E, y_E)-plane in the equatorial plane and the z_E-axis along the rotational axis of the Earth, this reference frame rotates with the same angular velocity as the Earth in its orbit around the Sun, causing the unit vector $\hat{\mathbf{r}}_s$ to always be contained in the (x_E, z_E)-plane. The angle χ describes the position of the Earth along its orbit (with $\chi = 0$ at the winter solstice), while the angle ψ is defined as the angle between $\hat{\mathbf{r}}_s$ and the equatorial plane and is therefore a function of χ. This angle is at its maximum at the winter solstice $(\psi(0) = i_{obl})$ and at its minimum at the summer solstice $(\psi(\pi) = -i_{obl})$ with i_{obl} the obliquity of the ecliptic. The variation of ψ is in magnitude equal to the solar declination, but is opposite in sign:

$$\psi(\chi) = \sin^{-1}\left(\sin i_{obl} \cos \chi\right) \tag{3.14}$$

yielding:

$$\hat{\mathbf{r}}_s = \begin{pmatrix} \cos\psi \\ 0 \\ \sin\psi \end{pmatrix} \tag{3.15}$$
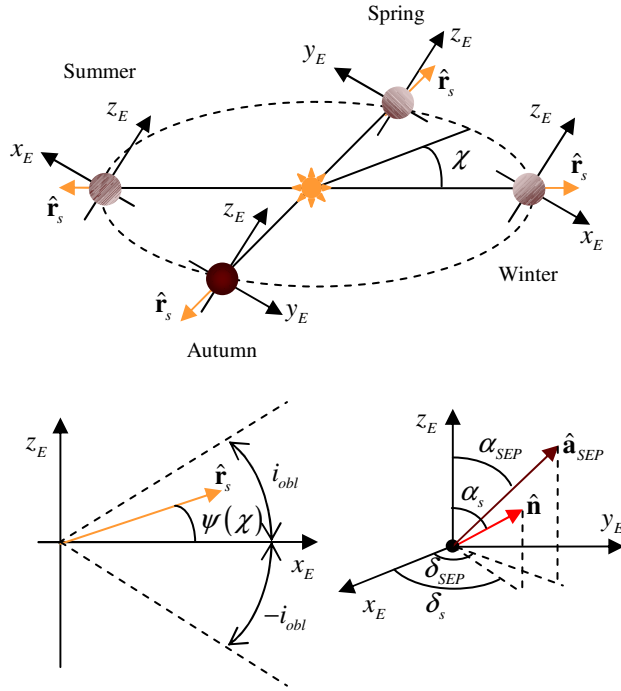
Fig. 3.8 Definition of reference frame and parameters used to model the seasonal variation of the Sun-sail vector and to define the solar sail and SEP pitch, α, and yaw, δ, angles.

The unit vector normal to the sail surface, $\hat{\mathbf{n}}$, can be described using the same frame of reference, see Fig. 3.8. Using the solar sail pitch angle, α_s, and yaw angle, δ_s, the unit vector $\hat{\mathbf{n}}$ is given by:

$$\hat{\mathbf{n}} = \begin{pmatrix} \sin\alpha_s \cos\delta_s \\ \sin\alpha_s \sin\delta_s \\ \cos\alpha_s \end{pmatrix} \tag{3.16}$$

Substituting Eq. (3.16) and the expressions for $\hat{\mathbf{r}}_s$, $\hat{\mathbf{n}}$ and β into Eq. (3.12) and rearranging gives:

$$a_{SEP,x_E} = a_{x_E} - \beta_0 \frac{m_0}{m} \frac{\mu_\odot}{r_s^2} (\cos\psi \sin\alpha_s \cos\delta_s + \sin\psi \cos\alpha_s)^2 \sin\alpha_s \cos\delta_s$$

$$a_{SEP,y_E} = a_{y_E} - \beta_0 \frac{m_0}{m} \frac{\mu_\odot}{r_s^2} (\cos\psi \sin\alpha_s \cos\delta_s + \sin\psi \cos\alpha_s)^2 \sin\alpha_s \sin\delta_s \qquad (3.17)$$

$$a_{SEP,z_E} = a_{z_E} - \beta_0 \frac{m_0}{m} \frac{\mu_\odot}{r_s^2} (\cos\psi \sin\alpha_s \cos\delta_s + \sin\psi \cos\alpha_s)^2 \cos\alpha_s$$

with a_{x_E}, a_{y_E} and a_{z_E} the components of the acceleration required to maintain the displaced GEO as defined in Eq. (3.2) for the out-of-plane case and in Eqs. (3.3) and (3.4) for the in-plane case. For example, for the out-of-plane case, $a_{x_E} = a_{y_E} = 0$ and $a_{z_E} = \mu_\oplus h / r_{GEO}^3$. In that case, the SEP system thus needs to counterbalance the in-plane component of the solar sail acceleration and needs to augment the out-of-plane solar sail acceleration to obtain the required out-of-plane acceleration.

Inspecting Eq. (3.17) shows that for a given value for m and ψ (i.e. for a particular instant of time), the minimisation problem in Eq. (3.13) is merely a function of the solar sail pitch and yaw angles and therefore reduces to finding the optimal solar sail pitch and yaw angles that minimise the acceleration required from the SEP system:

$$\left(\alpha_s^*, \delta_s^*\right) = \underset{\substack{\alpha_s \in \left[\alpha_{s,\min}, \alpha_{s,\max}\right] \\ \delta_s \in [-\pi, \pi]}}{\arg\min} \left(a_{SEP}(\alpha_s, \delta_s)\right) \qquad (3.18)$$

where the domain of α_s is defined later in this section. The next two subsections solve this minimisation problem for the out-of-plane and in-plane cases separately.

3.4.1   Out-of-plane displaced geostationary orbit

For the out-of-plane case, the solution to Eq. (3.18) can be found by setting the partial derivative of the SEP acceleration with respect to the sail pitch and yaw angles equal to zero:

$$\frac{\partial a_{SEP}}{\partial \alpha_s} = \frac{\partial a_{SEP}}{\partial \delta_s} = 0 \qquad (3.19)$$

For this, the SEP acceleration is first written as:

$$a_{SEP} = \sqrt{a_{SEP,x_E}^2 + a_{SEP,y_E}^2 + a_{SEP,z_E}^2} = \sqrt{c_1^2 \left(\hat{\mathbf{n}} \cdot \hat{\mathbf{r}}_s\right)^4 - 2 c_1 c_2 \left(\hat{\mathbf{n}} \cdot \hat{\mathbf{r}}_s\right)^2 \cos\alpha_s + c_2^2} \qquad (3.20)$$

with

$$c_1 = \beta_0 \frac{m_0}{m} \frac{\mu_\odot}{r_s^2}, \quad c_2 = \frac{\mu_\oplus h}{r_{GEO}^3} \tag{3.21}$$

Taking the first derivative of Eq. (3.20) with respect to the yaw angle yields:

$$\frac{\partial a_{SEP}}{\partial \delta_s} = \frac{1}{2a_{SEP}} \frac{\partial}{\partial \delta_s} \left(c_1^2 \left(\hat{\mathbf{n}} \cdot \hat{\mathbf{r}}_s \right)^4 - 2c_1 c_2 \left(\hat{\mathbf{n}} \cdot \hat{\mathbf{r}}_s \right)^2 \cos \alpha_s + c_2^2 \right) = 0 \tag{3.22}$$

from which the following condition can be derived:

$$4c_1 \left(\hat{\mathbf{n}} \cdot \hat{\mathbf{r}}_s \right) \left(c_1 \left(\hat{\mathbf{n}} \cdot \hat{\mathbf{r}}_s \right)^2 - c_2 \cos \alpha_s \right) \cos \psi \sin \alpha_s \sin \delta_s = 0 \tag{3.23}$$

For Eq. (3.22) to hold throughout the year and considering that $c_1 \neq 0$ and $\left(\hat{\mathbf{n}} \cdot \hat{\mathbf{r}}_s \right) > 0$ (to generate a solar sail acceleration) the optimal yaw angle equals:

$$\delta_s^* = n\pi \tag{3.24}$$

with n an integer equalling either 0 or 1. Substituting this value into Eq. (3.17) (with $a_{x_E} = a_{y_E} = 0$ and $a_{z_E} = \mu_\oplus h / r_{GEO}^3$) shows that the y_E-component of the SEP thrust force is zero at all times. Furthermore, considering the fact that the solar sail is unable to generate a thrust component in the direction of the Sun and recalling that the x_E-axis points away from the Sun at all times, Eq. (3.24) can be reduced to:

$$\delta_s^* = 0 \tag{3.25}$$

A similar analysis can be performed for the partial derivative with respect to the sail pitch angle. Substituting $\delta_s = \delta_s^* = 0$ gives the following condition:

$$\sin(\alpha_s + \psi) - \frac{c_2}{c_1} \frac{\cos \alpha_s}{\sin(\alpha_s + \psi)} + \frac{c_2}{2c_1} \frac{\sin \alpha_s}{\cos(\alpha_s + \psi)} = 0 \tag{3.26}$$

An analytical solution for the optimal pitch angle was not found from this expression, therefore Newton's method is applied to find α_s^*. To ensure that the optimal pitch angle does not generate a normal vector $\hat{\mathbf{n}}$ pointing towards the Sun, bounds are imposed on the optimum pitch angle, as depicted in Fig. 3.9 for two epochs during the year. Furthermore, by requiring α_s to be contained in the first two and last two quadrants for orbits displaced

above and below the equatorial plane, respectively, $\partial^2 a_{SEP} / \partial \alpha_s^2 > 0$ is ensured such that the solution corresponds to a minimum rather than a maximum of $a_{SEP}(\alpha_s, \delta_s)$.

Note that Fig. 3.9 clearly illustrates that the out-of-plane displaced GEO cannot be maintained throughout the year using only a solar sail. For example, in summer the shaded area shows that the required thrust direction for a displaced GEO displaced *above* the equatorial plane (i.e. a thrust along the positive z_E-axis) cannot be achieved by the solar sail. A similar reasoning holds for a GEO displaced *below* the equatorial plane in winter. Furthermore, in autumn and spring the required thrust direction for orbits displaced both above and below the equator lies on the edge of the shaded half-circle. The magnitude of the solar sail acceleration along the z_E-axis in that case becomes equal to zero as the Sun shines edge-on to the solar sail.
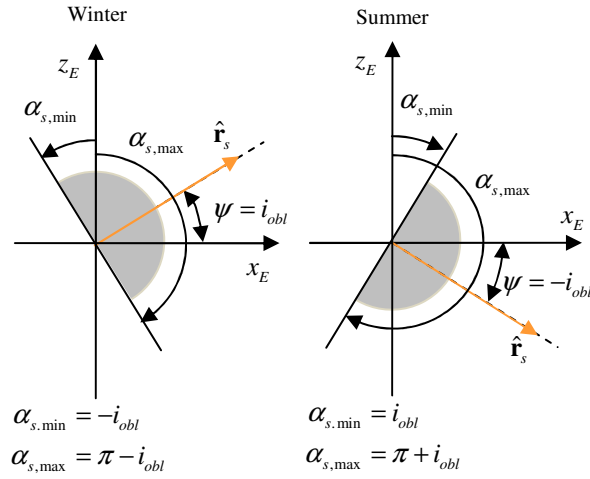
Fig. 3.9 Definition of minimum and maximum solar sail pitch angles during the year.

Once the optimal sail pitch and yaw angles are found, the magnitude and direction of the acceleration required from the SEP system can be obtained. Using Eq. (3.17), the pitch and yaw angles of the SEP thrust force, α_{SEP} and δ_{SEP} respectively, can be computed, see Fig. 3.8:

$$\alpha_{SEP} = \cos^{-1}\left(\frac{a_{SEP,z_E}}{a_{SEP}}\right)$$
$$\delta_{SEP} = \text{atan2}\left(a_{SEP,y_E}, a_{SEP,x_E}\right)$$

(3.27)

as well as the magnitude of the required SEP thrust force:

$$T = m \cdot a_{SEP}$$

(3.28)

Previously it was already stated that $a_{SEP,y_E} = 0$ since $\delta_s^* = 0$. Substituting $a_{SEP,y_E} = 0$ into Eq. (3.27) gives a constant SEP yaw angle of $\delta_{SEP} = n\pi$, again with n an integer equalling either 0 or 1.

As noted before, the above holds for one instant in time, i.e. for a given value for m and ψ. To find the variation of the controls, accelerations, thrust magnitude and mass as a function of time over multiple orbital periods, the displaced GEO is discretised into several nodes. The nodes are equally distributed over the orbit, leading to a constant time interval Δt in between two consecutive nodes. At each node, i, the required SEP thrust magnitude can be approximated using Eq. (3.28) as $T_i = m_i \cdot a_{SEP,i}$. Then, assuming a constant thrust magnitude during the interval Δt, the mass at the end of the ith interval can be approximated through the recurrence relation:

$$m_{i+1} = m_i - \frac{T_i}{I_{sp} g_0} \Delta t \tag{3.29}$$

At each node the optimal solar sail angles (and subsequently the SEP acceleration, thrust angles and thrust magnitude) can be computed. When changing from one node to the successive node, the change in ψ can be computed using Eq. (3.14), while the mass at the start of the new interval can be computed using Eq. (3.29).

The results in terms of optimal steering angles, mass profile and required thrust magnitude during the first year in a GEO displaced 35 km along the positive z_E-axis are shown in Fig. 3.10 and by the solid lines in Fig. 3.11. A time interval of $\Delta t = 0.005$ days is adopted, which is considered to be small enough to allow for a fair comparison later in the chapter with the analytical analysis for SEP control in Section 3.3. Furthermore, an initial mass of 1500 kg (the smaller class of geostationary spacecraft)[129-131] is assumed and the previously specified specific impulse of 3200 s is used. Finally, based on the near-term solar sail lightness number of 0.05 established in Section 2.2.2, four different values for the lightness number are considered, $\beta_0 = 0.01$, 0.05, 0.1 and 0.2. Note that all results neglect the effects of eclipses on the performance of the solar sail, but should be considered in future analyses. For the (displaced) GEO, eclipses occur for a short period per day around the equinoxes.
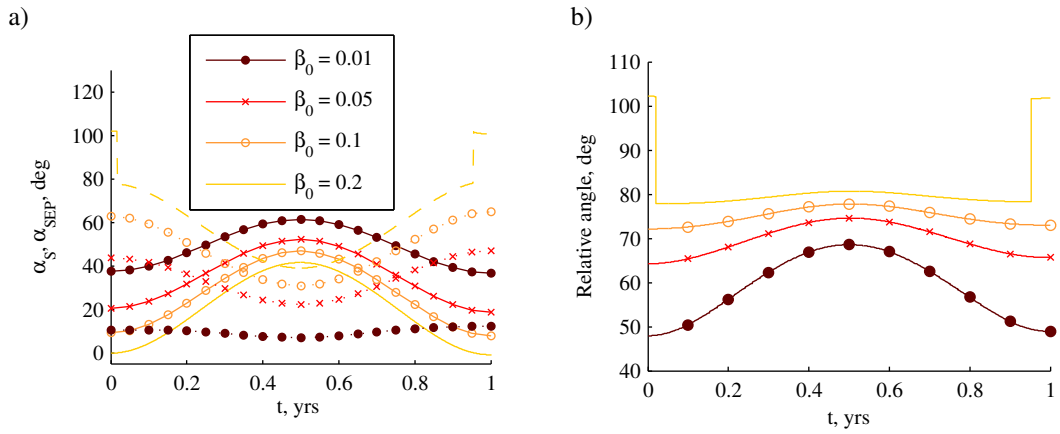
Fig. 3.10 35 km out-of-plane displaced GEO maintained with hybrid sail control for different values of the solar sail lightness number, β_0. a) Optimal solar sail (solid lines) and SEP (dotted lines) pitch angles. b) Relative angle between the solar sail and SEP thrust forces.
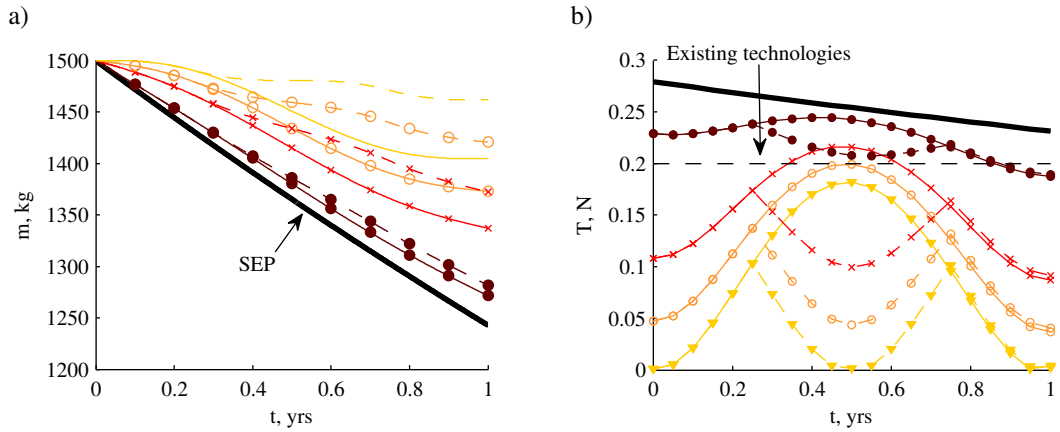
Fig. 3.11 35 km out-of-plane displaced GEO maintained with hybrid sail control for different values of the solar sail lightness number, β_0, assuming an initial mass of 1500 kg. Solid lines indicate a year-long displacement along the positive z_E-axis. Dashed lines include a seasonal transfer between north and south displaced GEOs. a) Spacecraft mass. b) Required SEP thrust magnitude.

Figure 3.10 shows that the optimal pitch angle of the solar sail decreases and the pitch angle of the SEP thruster increases for increasing values of β_0, indicating a larger contribution from the sail to the required out-of-plane acceleration for larger values of β_0. It also indicates a shift in the main task of the SEP thruster from providing the out-of-plane acceleration to compensating the in-plane component of the sail acceleration. Furthermore, some discontinuities can be observed in the profile of the SEP pitch angle for the largest value of β_0. This large value for β_0 causes the component of the solar sail acceleration along the positive z_E-axis to become larger than the required out-of-plane acceleration. This

requires the SEP thruster to thrust along the negative z_E-axis to counterbalance the excess out-of-plane acceleration, hence the switch in the SEP pitch angle from $\alpha_{SEP} < \pi/2$ to $\alpha_{SEP} > \pi/2$. Figure 3.10a furthermore shows that the turn rate of the solar sail, which can often lead to operational difficulties, is very slow and has a maximum of approximately 40 deg per half year for $\beta_0 = 0.2$. Another operational difficulty noted in Section 2.2.3 is the direction of the SEP thrust force with respect to the solar sail, which cannot be such that it lies in the plane of the solar sail. From the relative angle between the solar sail and SEP thrust forces, see Fig. 3.10b, it can be concluded that this is not the case for the displaced GEO.

In general, the larger the value for β_0 the lower the demand on the SEP system, which directly translates into a larger final mass after 1 year in orbit when using hybrid sail control instead of SEP control, see Fig. 3.11a. Already a solar sail with $\beta_0 = 0.01$ provides a gain in propellant mass of 29 kg. Further increasing β_0 results in savings of 94, 130 and 161 kg for $\beta_0 = 0.05$, 0.1 and 0.2, respectively.

Finally, considering the required thrust magnitude in Fig. 3.11b, another advantage of hybrid sails over pure SEP becomes evident. While the thrust level required for a 1500 kg spacecraft with SEP control is larger than currently achievable thrust levels of 0.2 N as determined in Section 2.2.1, thrust levels smaller than 0.2 N throughout the year can be observed for $\beta_0 = 0.1$ and 0.2. Even for $\beta_0 = 0.05$ the thrust level remains well under 0.2 N during winter, but it is higher during summer. However, this performance can be improved by transferring the spacecraft from a GEO displaced above the equatorial plane (north) in winter to an orbit displaced below the equatorial plane (south) in summer. Then, the performance of the sail is no longer limited by the obliquity of the ecliptic and can perform equally well in summer as it does in winter above the equatorial plane.

When this so-called 'seasonal transfer' is introduced in the model, results as presented by the dashed lines in Fig. 3.11 are obtained. Note that the mission is assumed to always start in winter, i.e. above the equatorial plane, and that an instantaneous seasonal transfer is considered. As expected, significant improvements both in terms of propellant consumption and required thrust levels can be observed. The mass savings mentioned before are now increased to 39, 129, 178 and 219 kg for $\beta_0 = 0.01$, 0.05, 0.1 and 0.2, respectively. In Chapter 4 it will be shown that transfers from above to below the equatorial plane and vice versa are possible and come at the cost of a negligible to modest SEP propellant consumption.
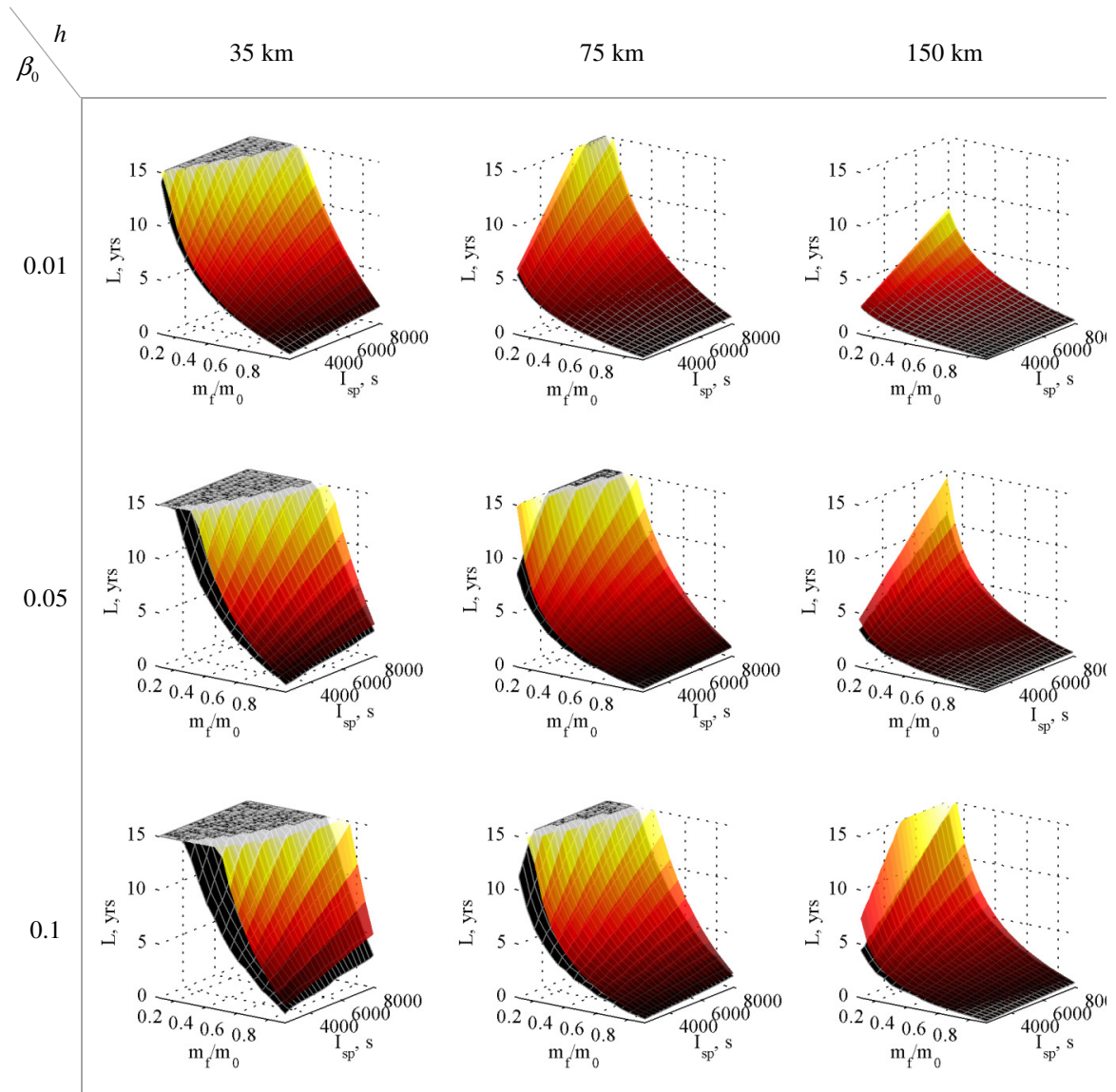
Fig. 3.12 Out-of-plane displaced GEOs maintained with hybrid sail control: mission time, *L*, (a maximum of 15 years is considered) as a function of the specific impulse, *I*$_{sp}$, and the mass fraction, *m$_f$/m$_0$*, for different values of the displacement distance, *h*, and the sail lightness number, *β$_0$*. The solid, black surfaces exclude a seasonal transfer between north and south displaced GEOs. The transparent, coloured surfaces include this transfer.

While the results in Fig. 3.10 and Fig. 3.11 only hold for a mission lifetime of one year, it is interesting to investigate whether hybrid propulsion can enable out-of-plane displaced GEO missions lasting as long as current geostationary missions. Previous sections already showed that impulsive and SEP control are unable to do so. Extending the mission lifetime for hybrid sail control results in the graphs of Fig. 3.12.

Figure 3.12 includes both cases of excluding and including the seasonal transfer and shows that the seasonal transfer can significantly increase the mission lifetime from a few months for the smaller values for β_0 up to a few years for the larger values for β_0. Furthermore, comparing Fig. 3.12 with Fig. 3.6 and Fig. 3.7 shows a dramatic improvement of the lifetime for hybrid sail propulsion compared to both impulsive and SEP propulsion. For small displacement distances even lifetimes of 10 - 15 years come into reach and the lifetime for the larger displacements become reasonable. Again, comparing the lifetimes for a mass fraction of 0.5 and a specific impulse of 3200 s increases the lifetime for a 35 km out-of-plane displaced orbit from 3.7 years for SEP control to 4.4 - 9.2 years (depending on the value chosen for β_0) when the seasonal transfer is not included and to 4.7 - 15 years when the transfer is included. Similarly, the lifetimes for a 150 km out-of-plane displaced orbit are increased from 0.9 years to 0.9 - 1.2 years (excluding transfer) and to 0.9 - 1.4 years (including transfer).

3.4.2 Comparison with in-plane displaced geostationary orbit

Although the analyses performed in Sections 3.2 and 3.3 already showed that the out-of-plane displaced GEO outperforms the in-plane displaced GEO for the use of impulsive and SEP control, it is still of interest to investigate the performance of the in-plane displaced GEO for the use of hybrid sails. The reason for this is the fact that, despite the larger required acceleration to maintain the in-plane displaced GEO, the direction of this acceleration is much more favourable as it is approximately along the Sun-sail line in parts of the orbit.

To investigate the performance of hybrid sails for the in-plane displaced GEO, the minimisation problem in Eq. (3.18) needs to be solved with:

$$
\begin{aligned}
a_{x_E} &= \rho \left(\omega_{GEO}^2 - \omega_*^2 \right) \cos \theta_{GEO} \\
a_{y_E} &= \rho \left(\omega_{GEO}^2 - \omega_*^2 \right) \sin \theta_{GEO} \\
a_{z_E} &= 0
\end{aligned}
\tag{3.30}
$$

where θ_{GEO} is the angular position in the displaced GEO, measured from the positive x_E-axis in counter clockwise direction. Applying the same approach as used in Section 3.4.1 to solve for the optimal solar sail pitch and yaw angles would require a system of nonlinear equations to be solved using Newton's method, rather than the single expression in Eq. (3.26). Therefore, the minimisation problem is solved using a sequential quadratic programming

(SQP) method.[132] This function allows the definition of the bounds for the sail pitch angle α_s as shown in Fig. 3.9 and the inclusion of a constraint to ensure $(\hat{\mathbf{n}} \cdot \hat{\mathbf{r}}_s) \geq 0$. As for the out-of-plane case, the displaced GEO is discretised into nodes, again with a time interval of $\Delta t = 0.005$ days, and at each node the minimisation problem of Eq. (3.18) is solved.

The results for a 35 km displaced orbit are provided in Fig. 3.13 and Fig. 3.14. Figure 3.14 confirms that also for hybrid sail propulsion the in-plane displaced GEO is more demanding than the out-of-plane displaced GEO, because the acceleration required from the SEP thruster is higher throughout (most of) the orbit. Furthermore, Fig. 3.13 clearly illustrates the influence of the changing direction of the Sun-sail line during the year and the sail attitude constraint that prevents the sail from generating an acceleration in the direction of the Sun. The latter requires the sail to be turned 180° every orbit and almost instantaneously during the equinoxes. However, as expected, during parts of the in-plane displaced orbit (around $\theta_{GEO} = 0$) the sail normal is aligned with the required, radial acceleration, which significantly lowers the demand on the SEP thruster, see Fig. 3.14.

After considering all propulsion strategies for the displaced GEO, it can be concluded that the out-of-plane displaced GEO outperforms the in-plane displaced GEO. The remainder of the analyses for the displaced GEO will therefore focus solely on the out-of-plane displaced GEO.
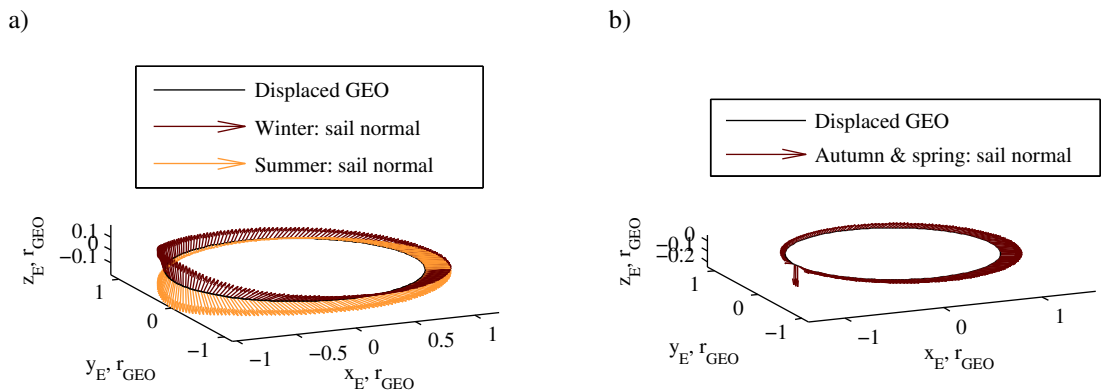
Fig. 3.13 Solar sail normal vector (β_0 = 0.1) for a 35 km in-plane displaced GEO. a) Solstices.
b) Equinoxes.

a)

b)
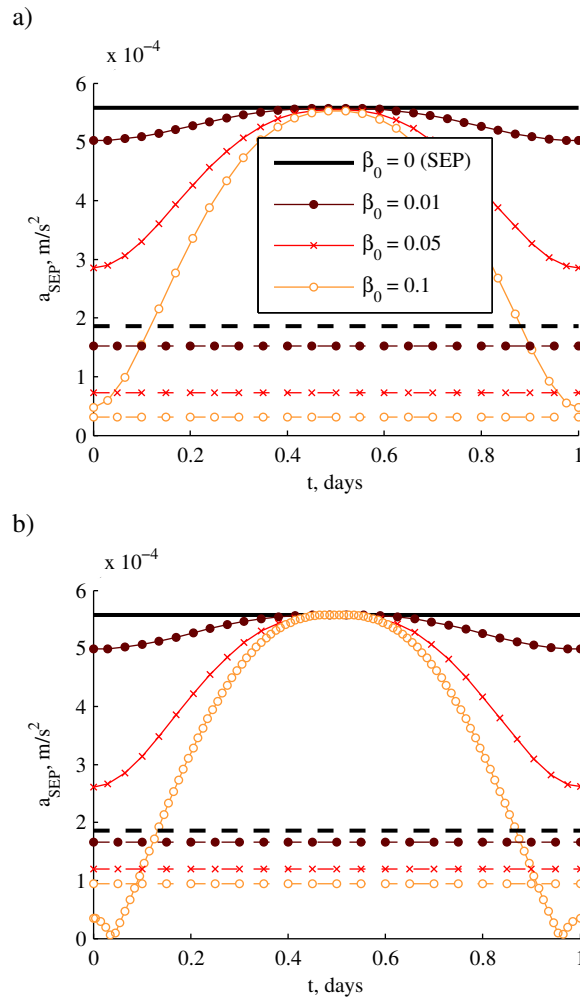
Fig. 3.14 Required SEP acceleration for a 35 km in-plane (solid lines) and out-of-plane (dashed lines) displaced GEO for different values of the sail lightness number β_0. a) Solstices. b) Equinoxes.

3.5   Mass budget analysis

The results in Fig. 3.6, Fig. 3.7 and Fig. 3.12 provide the performance of impulsive, SEP and hybrid sail control for an out-of-plane displaced GEO in terms of propellant consumption. However, the goal of the mission is to maximise the lifetime of a spacecraft carrying a given payload. It should therefore be investigated whether the mass fractions and specific impulses of Fig. 3.6, Fig. 3.7 and Fig. 3.12 allow for any payload mass to be left at the lifetimes shown in those figures. For this, the spacecraft mass budget is investigated. However, due to its poor performance, impulsive control is discarded as a viable option to maintain the out-of-plane displaced GEO and this section will therefore only consider the mass budget for a

hybrid sail and SEP propelled spacecraft. The corresponding mass budgets are based on what is proposed in Reference 133:

$$m_0 = m_{prop} + m_{tank} + m_{SEP} + m_P + m_{gimbal} + m_s + m_{pay} \tag{3.31}$$

The initial mass is broken down into seven elements. First, a propellant mass, m_{prop}, that follows from the initial and final spacecraft mass (see Eq. (2.15) and Eq. (3.29)), where the final mass is obtained after a certain lifetime L. Then, the mass of the tanks required to store the propellant, $m_{tank} = 0.1 m_{prop}$,[134] and the mass of the SEP thruster, m_{SEP}, which takes into account the control units and cabling related to the SEP subsystem. In Section 2.2.1 it was already indicated that the use of one thruster is assumed. This assumption will be assessed at the end of this section. The mass of the thruster is a function of the maximum power required by the SEP subsystem, $P_{SEP,max}$, which on its own is a function of the maximum thrust required during the mission, T_{max}:

$$m_{SEP} = k_{SEP} P_{SEP,max} \tag{3.32}$$

$$P_{SEP,max} = \frac{T_{max} I_{sp} g_0}{2 \eta_{SEP}} \tag{3.33}$$

with $k_{SEP} = 0.02$ kg/W[62] the specific performance of the SEP thruster and $\eta_{SEP} = 0.7$[135] its efficiency. Subsequently, in the case of SEP control a solar array with mass $m_P = k_{SA} P_{SEP,max}$ is assumed to provide electrical energy to the SEP system with $k_{SA} = 0.022$ kg/W the specific performance of the solar array.[62] In the case of hybrid sail control, it is assumed that part of the sail is covered with thin film solar cells for this purpose. The required area covered with solar cells can then be computed from the maximum power required by the SEP system:

$$A_{TF} = \frac{P_{SEP,max}}{W \eta_{TF}} \cos \gamma_{SEP,max} \tag{3.34}$$

The efficiency of the thin film is set to a conservative value of $\eta_{TF} = 0.05$ and $\gamma_{SEP,max}$ represents the angle between the Sun-sail line and the solar sail normal vector when $T = T_{max}$. From Eq. (3.34) the mass of the thin film $m_P = \sigma_{TF} A_{TF}$ can be computed with $\sigma_{TF} = 100$ g/m².[88] Note that the influence of the thin film solar cells on the performance of the sail is neglected. Then, the mass of a gimbal, $m_{gimbal} = 0.3 m_{SEP}$,[134] is taken into account to ensure that the solar sail and SEP thruster can steer independently of one another. Finally,

the mass of the sail can be computed through $m_s = \sigma_s A_s$ with σ_s the mass per unit area of the solar sail and the area of the sail, A_s, given through:

$$A_s = \frac{\beta_0 m_0}{\sigma^*} + A_{TF} \qquad (3.35)$$

For the sail loading σ_s a value of 5 g/m^2 is assumed as discussed in Section 2.2.2. Finally, and clearly, for an SEP-controlled spacecraft, both m_{gimbal} and m_s are set to zero.

For a given mission lifetime and for a particular specific impulse, the only unknowns for computing the payload mass, m_{pay}, are the initial mass and the maximum SEP thrust required during the mission, T_{max}, which are related since the initial mass is bounded by T_{max}. For SEP control, this maximum thrust occurs at $t = t_0$ causing $T_{max} = T_0$. With the required acceleration to maintain the out-of-plane displaced GEO given for a particular displacement distance, the maximum initial mass can be computed through $m_{0,max} = T_0 / a$. However, for hybrid sail control, the maximum thrust does not necessarily occur at $t = t_0$, but can also occur in autumn (when the seasonal transfer is taken into account, as is done in this mass budget analysis) as shown in Fig. 3.11b. The resulting maximum initial masses for both SEP and hybrid sail control are provided in Fig. 3.15 as a function of the maximum thrust magnitude and for each of the displacement distances used so far and for different sail lightness numbers.

The figure and accompanying table show that for SEP control and a maximum thrust magnitude of $T_{max} = 0.2$ N (see Section 3.4), maximum initial masses of 1075, 501 and 251 kg are possible for displacement distances of 35, 75 and 150 km, respectively. These initial masses increase by a factor 1.05 to 2.7 for hybrid sail control, depending on the sail lightness number and the displacement distance. These higher initial masses show another major advantage of hybrid sail control over SEP control in addition to the propellant mass savings shown in Fig. 3.7 and Fig. 3.12.

Using these initial masses and a specific impulse of 3200 s, the payload masses and lifetimes as depicted in Fig. 3.16 can be obtained.

Figure 3.16 shows that in almost all cases hybrid sail control outperforms SEP control. The only exception occurs for the largest displacement considered in combination with the largest value for the sail lightness number, $\beta_0 = 0.2$. Figure 3.16 furthermore shows that only hybrid sail control allows lifetimes equal to the lifetime of current geostationary spacecraft of 10 - 15 years, while still enabling a considerable payload to be taken onboard. For

71

example, for a 35 km out-of-plane displaced orbit, a near-term sail lightness number of 0.05 and an initial mass of 1729 kg, payload masses of 361 kg and 155 kg can be maintained in the displaced GEO for 10 and 15 years, respectively. Increasing the sail lightness number to a far-term value of 0.1, these payload masses are increased to 487 kg and 255 kg for 10 and 15 year missions, respectively.

A detailed mass breakdown for a set of mission cases is provided in Table 3.2. Comparing the breakdown for the same value for β_0 but for different mission lifetimes clearly shows the mass components that are dependent on the initial mass (or, equivalently, on the maximum thrust magnitude) and those that depend on the mission lifetime (e.g. the propellant mass, tank mass and payload mass). The table thus illustrates that for longer lifetimes, the payload mass decreases as part of the payload mass is translated into propellant mass (and accompanying tank mass). Some additional considerations with respect to the mass budget will be given below.

a)

b)

β_0	h_0, km		
	35	75	150
0 (SEP)	1075	501	251
0.01	1260	550	263
0.05	1729	697	316
0.1	2193	818	378
0.2	2912	1020	436
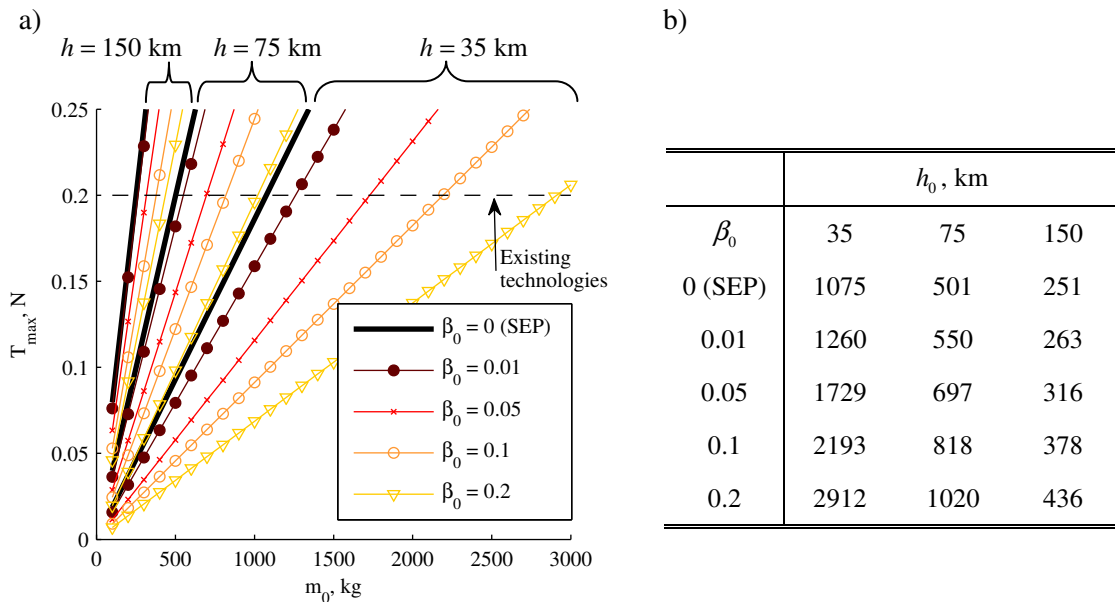
Fig. 3.15 a) Maximum thrust magnitude, T_{max}, as a function of the initial mass, m_0, for different values of the out-of-plane displacement distance, h, and the sail lightness number, β_0. b) Initial masses for a maximum thrust magnitude of 0.2 N.

a) $h = 35$ km   b) $h = 150$ km
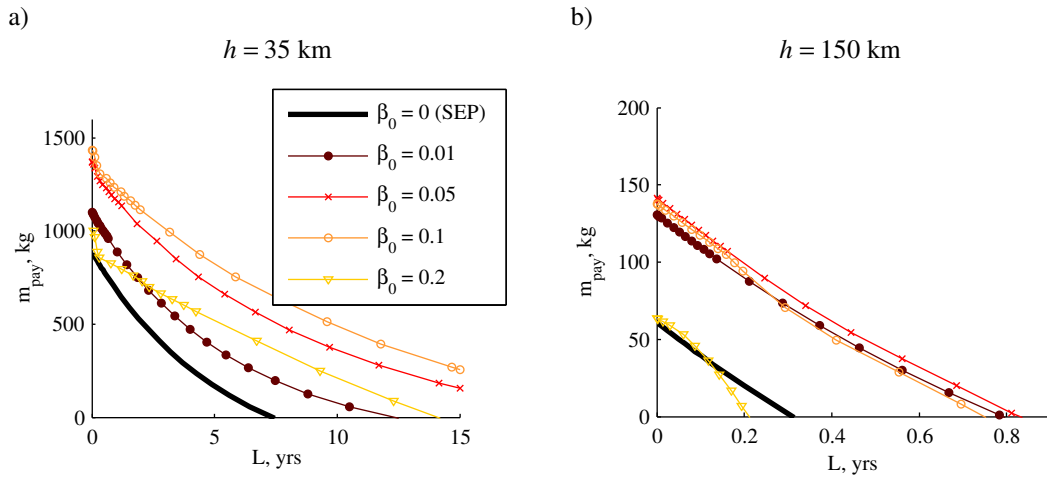
Fig. 3.16 Payload mass, m_{pay}, as a function of the mission lifetime, L, for a (a) 35 km and (b) 150 km out-of-plane displaced GEO, for different sail lightness numbers, β_0.

Table 3.2 Mass breakdown of a set of mission cases with different displacement distances, h, lifetimes, L, and solar sail lightness numbers, β_0. For the length of the solar sail, l_s, a square sail is assumed.

	$h = 35$ km			$h = 150$ km		
	$L = 5$ years		$L = 15$ years	$L = 0.2$ years		$L = 0.5$ years
	SEP	$\beta_0 = 0.05$	$\beta_0 = 0.05$	SEP	$\beta_0 = 0.05$	$\beta_0 = 0.05$
m_0, kg	1075	1729	1729	251	316	316
m_{prop}, kg	654.1	570.8	1064.1	37.7	38.8	86.8
m_{tank}, kg	65.4	57.1	106.4	3.8	3.9	8.7
m_{SEP}, kg	89.7	89.7	89.7	89.8	89.6	89.6
m_P, kg	99.7	3.9	3.9	99.7	5.7	5.7
m_{gimbal}, kg	0	26.9	26.9	0	26.9	26.9
m_s, kg	0	282.7	282.7	0	51.9	51.9
m_{pay}, kg	166.1	697.9	155.3	20.0	99.2	46.4
l_s, m	0	237.8	237.8	0	101.9	101.9
A_{TF}, m^2	0	39.2	39.2	0	56.9	56.9
T_{max}, N	0.2	0.2	0.2	0.2	0.2	0.2

First, note that the payload mass, as used so far in the mass budget analysis and as provided in Fig. 3.16 and Table 3.2, includes not only the actual payload of the mission, but also additional spacecraft subsystems that are not explicitly stated in the mass breakdown in Eq. (3.31). These include masses that account for, among others, the spacecraft structure, on-board data handling (OBDH), thermal and attitude dynamics and control system (ADCS).

According to Reference 62, these additional masses can be represented in the mass budget as a fraction of the dry mass: $m_{other} = f_{other} m_{dry} = f_{other} \left(m_0 - m_{prop} \right)$. Depending on the value chosen for f_{other}, the results in Fig. 3.17 can be obtained for the use of hybrid sail propulsion and for the near- and far-term sail lightness numbers of 0.05 and 0.1. The figure shows that for all f_{other} considered, a payload mass remains for a minimum lifetime of 10 years, while a 15 year mission is also feasible for smaller values of f_{other}. Considering the small geostationary communication satellite platform proposed in Reference 130, which has an initial mass similar to the platforms considered for the displaced GEO and considers a minimum payload mass of 200 kg, it becomes clear from Fig. 3.17 that a similar payload can be maintained in the displaced GEO for 10 years for $f_{other} \leq 0.2$.

a)
b)
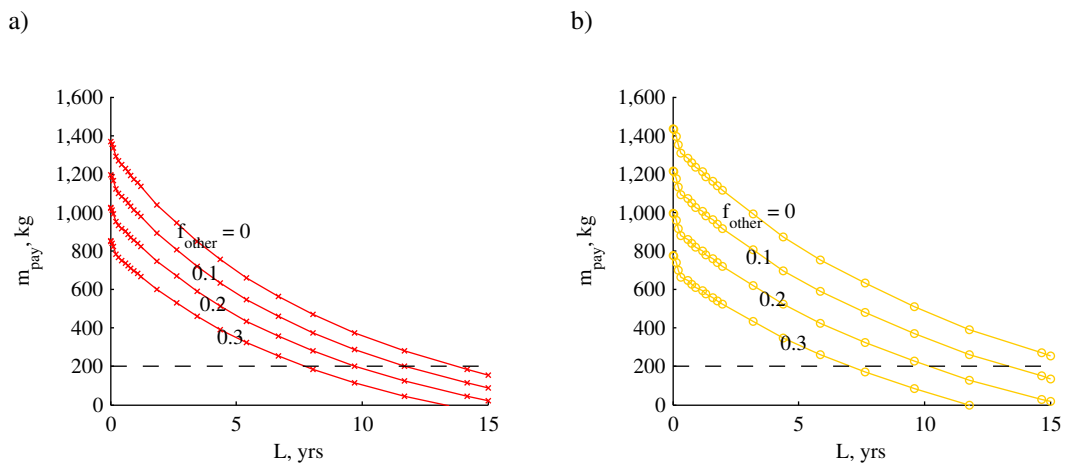
Fig. 3.17 Payload mass, m_{pay}, as a function of the mission lifetime, L, for a 35 km out-of-plane displaced GEO, taking into account the mass of other spacecraft subsystems as a fraction of the dry mass, f_{other}. a) Sail lightness number of 0.05. b) Sail lightness number of 0.1.

The results in Fig. 3.16 furthermore suggest that an optimal lightness number exists. For example, for the 35 km displaced GEO in Fig. 3.16a, the results for $\beta_0 = 0.1$ outperform the results for both smaller and larger values for β_0. Some details on this optimal lightness number are provided in Fig. 3.18. Figure 3.18a shows the increase in sail mass and the gain in initial, propellant, tank and power source mass that are achieved by increasing the value for β_0 for a 35 km out-of-plane displaced GEO. The difference between the two lines is thus the net increase in payload mass, which is provided in Fig. 3.18b. Both figures clearly show that for increasing β_0 beyond a certain value, the gain in initial, propellant, tank and power source mass no longer outweighs the required increased sail mass and increasing β_0 even further would only result in a net decrease of the payload mass. The figure furthermore

shows that the optimal value for β_0 depends on the mission lifetime, which is introduced through the dependency of m_{prop} and m_{tank} on both the mission lifetime and the sail lightness number. Note that m_{SEP} and m_{gimbal} are independent of the lightness number and mission lifetime and are therefore of no influence on the graphs in Fig. 3.18.
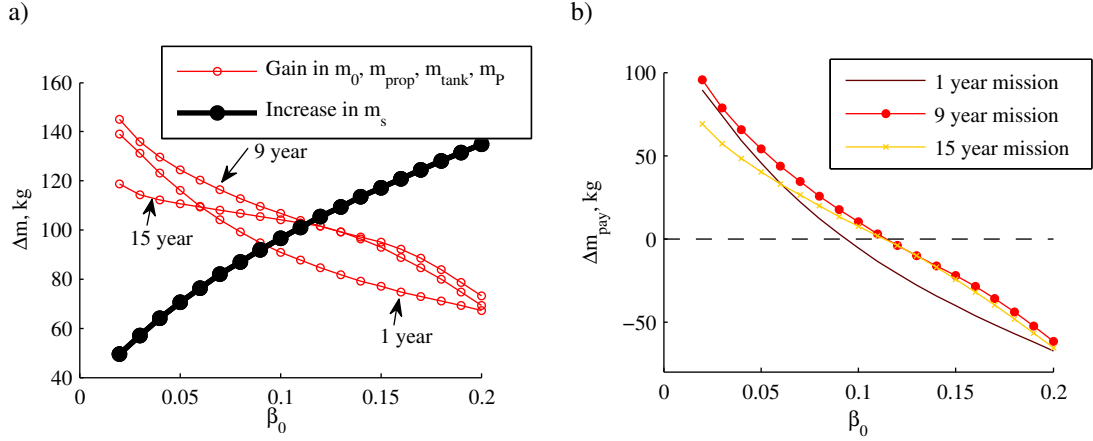
Fig. 3.18 Illustration of optimal solar sail lightness number for a 35 km out-of-plane displaced GEO. a) Increase in sail mass and gain in initial, propellant, tank and power source mass due to increase in sail lightness number, β_0. b) Increase in payload mass due to increase in sail lightness number, β_0.

Finally, it would be of interest to perform a sensitivity analysis on the results in Fig. 3.16. Here, this is achieved by including margins to the mass budget in Eq. (3.31). Two different margins are adopted, one for all subsystems that make use of well-proven technologies such as the SEP thruster and the propellant tanks, ε_{old}, and one for new technologies such as the solar sail and thin film solar cells. The new mass budget can then be written as:[136]

$$m_0 = \begin{cases} \varepsilon_{old}\left(m_{prop}+m_{tank}+m_{SEP}+m_P+m_{other}\right)+m_{pay} & \text{SEP} \\ \varepsilon_{old}\left(m_{prop}+m_{tank}+m_{SEP}+m_{gimbal}+m_{other}\right)+\varepsilon_{new}\left(m_P+m_s\right)+m_{pay} & \text{Hybrid} \end{cases}$$

(3.36)

which takes into account the previously discussed mass of the other subsystems. Using a range of values for both margins and using $f_{other}=0.2$, the results in Fig. 3.19 can be generated for a mission lifetime of 10 years. The results are presented as the difference, Δm_{pay}, with respect to the nominal case when $\varepsilon_{old}=\varepsilon_{new}=1$. Two grey, transparent surfaces are included in the figure for readability, where the surface at approximately -200 kg represents the boundary below which no payload can be carried on the mission for a lifetime of 10 years.
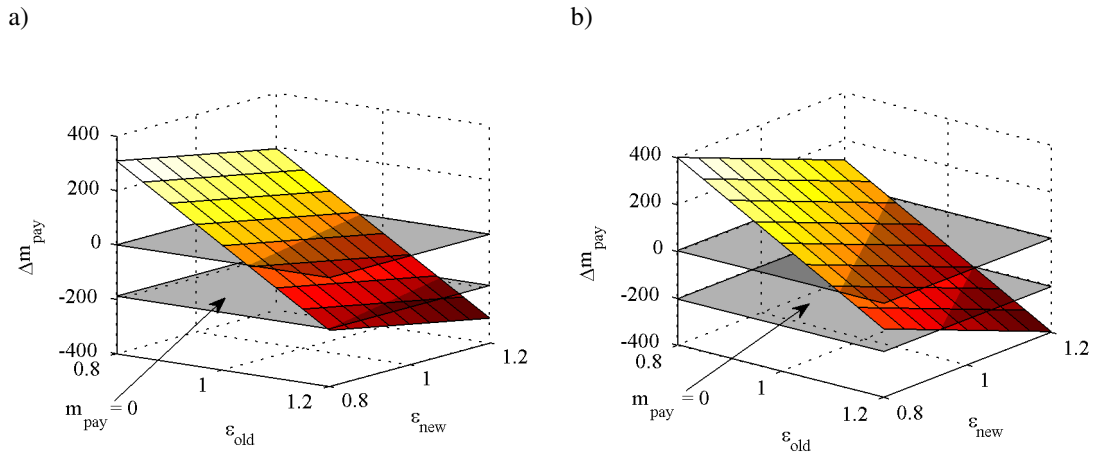
Fig. 3.19 Decrease in payload mass, Δm_{pay}, as a function of the margins on well-proven, ε_{old}, and new, ε_{new}, technologies with respect to the nominal case where $\varepsilon_{old} = \varepsilon_{new} = 1$ for a 10 year mission in a 35 km out-of-plane displaced GEO. a) Sail lightness number of 0.05. b) Sail lightness number of 0.1.

As noted previously, the analyses in this section assume the use of one SEP thruster. The main issue with this assumption is whether or not one thruster can deliver the required propellant throughput. Taking the NASA's Evolutionary Xenon Thruster (NEXT) as reference, see Table 2.1, an operational lifetime of 45,000 hours (i.e. over 5 years) should be possible with a propellant throughput of 800 kg.[137] Allowing a slightly larger specific impulse of 4000 s for the NEXT thruster than the 3200 s assumed so far, the results in Fig. 3.20 can be obtained for the propellant throughput. Where appropriate, the figures include the reference value of 800 kg and show that only for the 35 km displaced GEO the reference value is exceeded and a second SEP thruster could be required. Adding a second thruster would be possible, which would also provide a larger maximum thrust and would therefore enable a larger initial mass. Inspecting the separate mass components in Eq. (3.31) shows that all components scale linearly with the maximum thrust, including the payload mass.

Although the performance for a 35 km out-of-plane displaced orbit is promising, the performance of the higher displaced orbits is not, see Fig. 3.16b. The lifetime decreases drastically to approximately 0.5 year. Despite this short lifetime, the 150 km out-of-plane displaced GEO could still be of interest by using it to provide temporary displacements. Then, the displaced GEO is only maintained for a relatively short period of time to provide services when needed and is transferred into a Keplerian parking orbit when inoperative to save propellant mass. For such short durations, the 150 km displaced GEO can transform its rather short lifetime into multiple smaller mission segments extended over a much longer

lifetime. To show the feasibility of this concept, the next chapter will investigate the trajectory that is required to transfer the spacecraft from and to such a Keplerian parking orbit.
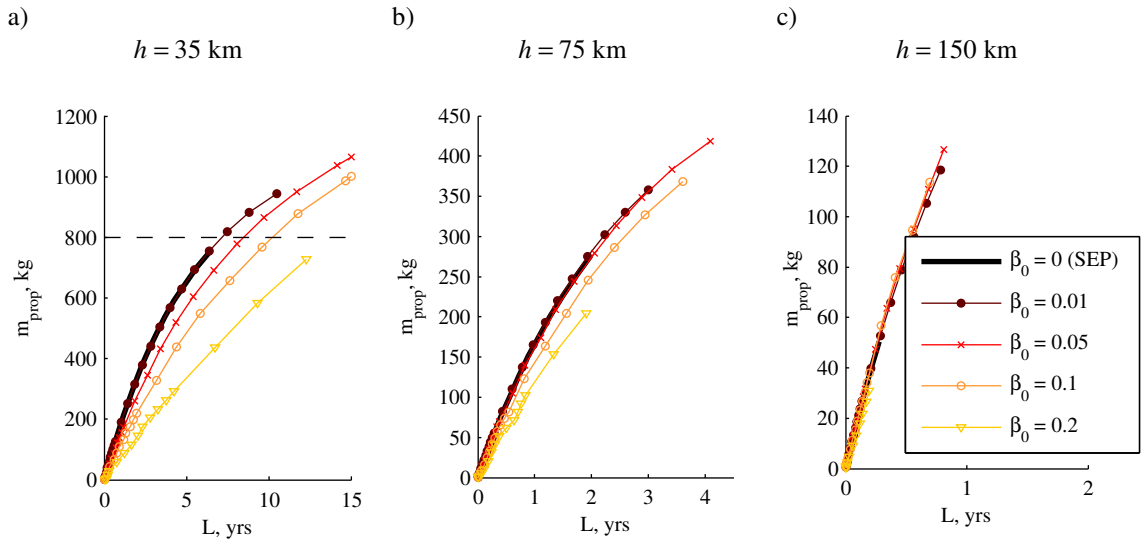
Fig. 3.20 Required propellant throughput (assuming a NEXT thruster specific impulse of 4000 s) for out-of-plane displaced GEOs maintained with hybrid sail control for different values of the solar sail lightness number, β_0, and displacement distances, h.

3.6 Orbital perturbations

A spacecraft in a (displaced) GEO experiences a set of perturbing effects. In this section, two particular perturbations are investigated, namely the J_2 and $J_{2,2}$ effects and the effect of non-ideal properties of the solar sail. These perturbations are used for illustration purposes and additional perturbing accelerations, such as third body perturbations from the Sun and the Moon, are therefore not considered.

3.6.1 J_2 and $J_{2,2}$ effects

Up to this point, the analyses for the displaced GEO have assumed a radially symmetrical mass distribution for the Earth. However, it is well-known that the Earth's actual gravity field is not radially symmetric, since the mass density distribution changes in north-south and east-west directions. Spacecraft in geostationary orbit are perturbed by this and require costly station-keeping manoeuvres.[127] A similar effect can be expected for the displaced GEO. This section will therefore investigate the influence of the Earth's non-uniform gravitational field on the lifetimes depicted in Fig. 3.7 and Fig. 3.12.

For this, the two most dominant perturbing accelerations will be considered, namely the so-called J_2 term (or Earth's oblateness) and the $J_{2,2}$ term. The first term considers deviations of the Earth's mass density distribution in north-south direction and causes a precession of the pole of the orbit plane. The second term is concerned with deviations in east-west direction. For most spacecraft orbiting the Earth the effect of the $J_{2,2}$ term will average out over periods longer than a day, but because a (displaced) GEO spacecraft is constantly located above the same point on Earth, it experiences a constant acceleration from the $J_{2,2}$ term and is therefore strongly perturbed. The effect is a librational motion around the nearest stable point either at 75°E or 105°W.[13]

Using a spherical reference frame with r the distance from the centre of the Earth, λ the geographical longitude and ϕ the geocentric latitude, the perturbing accelerations due to the J_2 term can be derived as:[126]

$$a_{J_2,r} = \frac{3}{2}\mu_\oplus J_2 \frac{R_\oplus^2}{r_{GEO}^4}\left(3\sin^2\phi - 1\right)$$
$$a_{J_2,\lambda} = 0 \tag{3.37}$$
$$a_{J_2,\phi} = -\frac{3}{2}\mu_\oplus J_2 \frac{R_\oplus^2}{r_{GEO}^4}\sin 2\phi$$

with $R_\oplus$ the radius of the Earth. Equation (3.37) shows that, while the J_2 perturbing acceleration for a GEO spacecraft is purely radial, for the displaced GEO a non-zero term in ϕ direction exists.

Similarly, for the $J_{2,2}$ term the accelerations are given by:[126]

$$a_{J_{2,2},r} = 9\mu_\oplus J_{2,2} \frac{R_\oplus^2}{r_{GEO}^4}\cos^2\phi\cos 2\left(\lambda - \lambda_{2,2}\right)$$
$$a_{J_{2,2},\lambda} = 6\mu_\oplus J_{2,2} \frac{R_\oplus^2}{r_{GEO}^4}\cos\phi\sin 2\left(\lambda - \lambda_{2,2}\right) \tag{3.38}$$
$$a_{J_{2,2},\phi} = 3\mu_\oplus J_{2,2} \frac{R_\oplus^2}{r_{GEO}^4}\sin 2\phi\cos 2\left(\lambda - \lambda_{2,2}\right)$$

with $\lambda_{2,2}$ a coefficient related to the $J_{2,2}$ term. The accelerations in Eq. (3.37) and (3.38) can be added and transformed to the reference frame defined in Fig. 3.8. To determine the effect of the J_2 and $J_{2,2}$ terms on the performance of SEP and hybrid sail propulsion for the

displaced GEO, the resulting accelerations in x_E, y_E and z_E direction, denoted by a_{J,x_E}, a_{J,y_E} and a_{J,z_E} respectively, should be added to Eq. (3.17). This results in:

$$a_{SEP,x_E} = a_{J,x_E} \qquad -\beta_0 \frac{m_0}{m} \frac{\mu_\odot}{r_s^2} (\cos\psi \sin\alpha_s \sin\delta_s + \sin\psi \cos\alpha_s)^2 \sin\alpha_s \cos\delta_s$$

$$a_{SEP,y_E} = a_{J,y_E} \qquad -\beta_0 \frac{m_0}{m} \frac{\mu_\odot}{r_s^2} (\cos\psi \sin\alpha_s \sin\delta_s + \sin\psi \cos\alpha_s)^2 \sin\alpha_s \sin\delta_s \qquad (3.39)$$

$$a_{SEP,z_E} = a_{J,z_E} + \frac{\mu_\oplus h}{r_{GEO}^3} - \beta_0 \frac{m_0}{m} \frac{\mu_\odot}{r_s^2} (\cos\psi \sin\alpha_s \sin\delta_s + \sin\psi \cos\alpha_s)^2 \cos\alpha_s$$

Equation (3.39) shows that the minimisation problem in Eq. (3.18) still holds: for a particular instant of time, the acceleration required from the SEP system can be minimised by finding the optimal solar sail pitch and yaw angles. However, because the additional terms a_{J,x_E} and a_{J,y_E} are not constant in direction along the displaced GEO in the $E(x_E, y_E, z_E)$ reference frame, the optimal sail yaw angle is also no longer constant. Therefore, applying the approach of Eq. (3.22) to solve for the optimal solar sail pitch and yaw angles would require a system of nonlinear equations to be solved rather than the single expression in Eq. (3.26). Therefore, the minimisation problem is once again solved using an SQP method,[132] similarly as was done for computing the performance of the in-plane displaced GEO in Section 3.4.2. As was explained, this function allows the definition of bounds for the sail pitch angle α_s, as shown in Fig. 3.9, and the inclusion of a constraint to ensure $(\hat{\mathbf{n}} \cdot \hat{\mathbf{r}}_s) \geq 0$. As for the non-perturbed case, the displaced GEO is discretised into nodes with a time interval of $\Delta t = 0.025$ days and at each node the minimisation problem is solved.

The results for a spacecraft positioned in a 35 km displaced GEO at a longitude of $\lambda = 0$ and with $I_{sp} = 3200$ s are provided in Fig. 3.21 and Fig. 3.22. In Fig. 3.21 the solar sail pitch and yaw angles are depicted to show their variation over one orbit due to the constantly changing a_{J,x_E} and a_{J,y_E} terms in Eq. (3.39).

The actual influence on the spacecraft lifetime is shown in Fig. 3.22, which provides the loss in lifetime in percentage of the nominal, i.e. the unperturbed lifetime. The figure shows that the J_2 and $J_{2,2}$ terms have a small effect on the lifetime, which becomes almost negligible for the smaller values of the solar sail lightness number. For example, for the unperturbed case and for $\beta_0 = 0.01$ the spacecraft reaches a lifetime of 15 years at a mass fraction of approximately 0.16. For the same mass fraction, but including the J_2 and $J_{2,2}$ perturbing effects, the lifetime percentage loss is 0.26 percent or 14 days. Note that the oscillating

behaviour for the case of hybrid sail propulsion is introduced by the influence of the seasonally changing Sun-sail line. Similar results can be obtained for the larger displacements of 75 and 150 km since the magnitude of the perturbing acceleration does not change significantly.

a)

b)
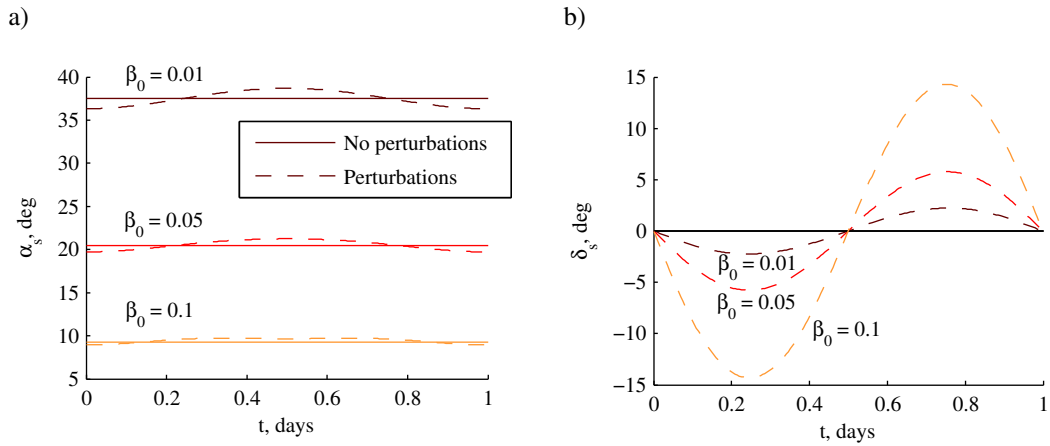
Fig. 3.21 Optimal solar sail pitch (a) and yaw (b) angles over one orbital period in winter when accounting for the perturbations due to the J_2 and $J_{2,2}$ terms of the Earth's gravity field for a spacecraft located at 0° longitude in a 35 km displaced GEO and for different values of the solar sail lightness number, β_0.
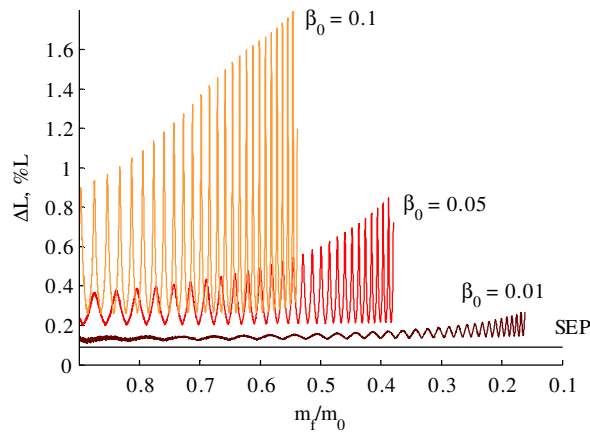
Fig. 3.22 Loss in mission lifetime as percentage of the nominal mission lifetime when accounting for the perturbations due to the J_2 and $J_{2,2}$ terms of the Earth's gravity field for a spacecraft located at 0° longitude in a 35 km displaced GEO and for different values of the solar sail lightness number, β_0.

3.6.2   Non-ideal solar sail

So far, the analysis of hybrid sail propulsion to maintain the displaced geostationary orbit has considered an ideal solar sail, i.e. a perfectly reflecting solar sail where the solar sail acceleration vector is aligned with the normal to the sail surface. However, in reality the optical properties of the sail are not ideal as explained in Section 2.2.2. This causes the magnitude of the solar radiation pressure force to decrease and to generate a tangential acceleration component in addition to the acceleration perpendicular to the solar sail. Clearly, this can have a significant effect on the sail's performance. This section will investigate this effect by adopting the parametric, degrading solar sail model of Section 2.2.2 using a similar approach to solving the minimisation problem as done in Section 3.6.1. Note that other degrading effects on the solar sail such as debris impact are not considered.

To analyse the effect of the non-ideal solar sail on the performance of hybrid sail propulsion for maintaining the displaced GEO, the solar sail acceleration in Eq. (3.17) is replaced by Eq. (2.36) with the optical coefficients dependent on time as given in Eq. (2.41). And, because only out-of-plane displaced GEOs are considered, $a_{x_E} = a_{y_E} = 0$ and $a_{z_E} = \mu_{\oplus} h / r_{GEO}^3$. This results in the following acceleration required from the SEP thruster:

$$a_{SEP,x_E} = \quad -\frac{1}{2}\beta_0 \frac{m_0}{m} \frac{\mu_{\odot}}{r_s^2} (\hat{\mathbf{r}}_s \cdot \hat{\mathbf{n}})\left(b_1 \cos\psi + \left(b_2\left(\hat{\mathbf{r}}_s \cdot \hat{\mathbf{n}}\right) + b_3\right)\sin\alpha_s \cos\delta_s\right)$$

$$a_{SEP,y_E} = \quad -\frac{1}{2}\beta_0 \frac{m_0}{m} \frac{\mu_{\odot}}{r_s^2} (\hat{\mathbf{r}}_s \cdot \hat{\mathbf{n}})\left(\quad\quad \left(b_2\left(\hat{\mathbf{r}}_s \cdot \hat{\mathbf{n}}\right) + b_3\right)\sin\alpha_s \sin\delta_s\right) \quad\quad (3.40)$$

$$a_{SEP,z_E} = \frac{\mu_{\oplus} h}{r_{GEO}^3} - \frac{1}{2}\beta_0 \frac{m_0}{m} \frac{\mu_{\odot}}{r_s^2} (\hat{\mathbf{r}}_s \cdot \hat{\mathbf{n}})\left(b_1 \sin\psi + \left(b_2\left(\hat{\mathbf{r}}_s \cdot \hat{\mathbf{n}}\right) + b_3\right)\cos\alpha_s \quad\quad\right)$$

with $(\hat{\mathbf{r}}_s \cdot \hat{\mathbf{n}}) = \cos\psi \sin\alpha_s + \sin\psi \cos\alpha_s$. In order to minimise this SEP acceleration, a similar approach as for the in-plane displaced GEO in Section 3.4.2 and the effect of the J_2 and $J_{2,2}$ terms in Section 3.6.1 is adopted: the displaced GEO is discretised into several nodes. At each node, the total radiation dose received is computed through a trapezoidal integration of Eq. (2.37), the optical coefficients are updates and the minimisation problem in Eq. (3.18) is solved using an SQP method.[132]

Results of this analysis are provided in Fig. 3.23. The figure shows that the lifetime that can be achieved for a particular mass fraction decreases when including the non-ideal sail properties (dashed lines). Clearly, this decrease becomes larger for increasing values of the sail lightness number. For $\beta_0 = 0.01$, the loss stays limited to a few days, up to approximately

12 percent of the lifetime for an ideal solar sail, see Fig. 3.23b. However, for $\beta_0 = 0.1$ the loss in lifetime for a particular mass fraction is significant and can be as much as 52 percent.

Note that the irregular behaviour of the plot in Fig. 3.23b is again due to the seasonally changing Sun-sail line. This can be further clarified from Fig. 3.23a, which shows that – depending on the time of year – the lifetime increases quickly or slowly for a decrease in the mass fraction. This pattern, which is especially clear for $\beta_0 = 0.1$, can be observed for both the ideal and non-ideal solar sail, but because both approaches consume propellant at a different rate, the pattern is out of phase, causing the irregular behaviour in Fig. 3.23b.

Finally, note that this section investigated the degradation of the solar sail. However, for both the pure SEP case and the hybrid sail cases, also the performance of the solar arrays or thin film cells can be effected by degradation. However, this effect will only be of influence for the mass budget considered in Section 3.5. It could be taken into account by slightly over-sizing the solar array (or thin film solar cell area) such that the required power output can even be generated at end of life. However, for the case of hybrid propulsion, the mass of the thin film cells is just a few kilograms, see Table 3.2. Over sizing the thin film cells will therefore have an almost negligible effect on the results provided in Fig. 3.16.

a)

b)
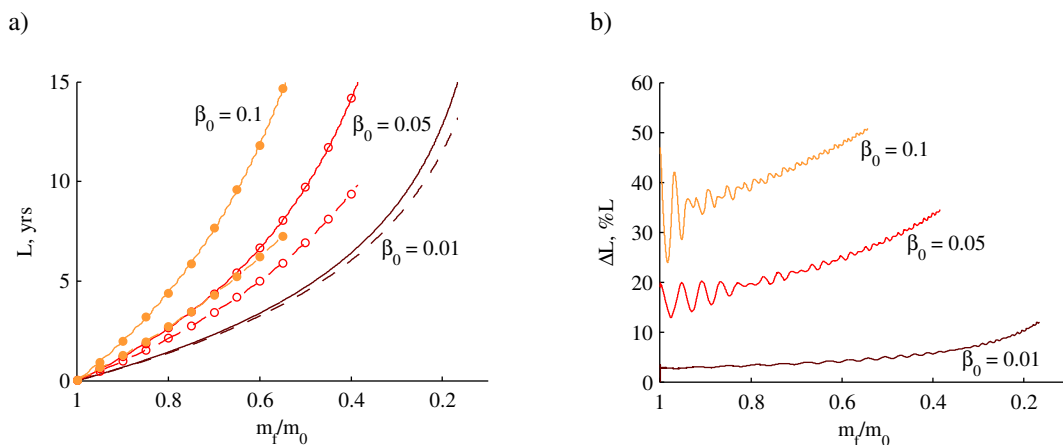
Fig. 3.23 Influence of non-ideal sail properties on the lifetime of a hybrid sail propulsion spacecraft in a 35 km displaced out-of-plane GEO for different values of the solar sail lightness number, β_0. a) Lifetime as a function of mass fraction for ideal (solid lines) and non-ideal (dashed lines). b) Percentage loss in lifetime.

3.7 Chapter summary

In this chapter the possibility of using displaced NKOs to provide a solution to future geostationary orbit congestion has been investigated.

It has been shown that, for equal displacements, a Type I NKO (i.e. an out-of-plane displaced geostationary orbit) outperforms geostationary orbits displaced *in* the equatorial plane in terms of acceleration required and with that in terms of propellant consumption, mission lifetime and/or payload mass capacity.

Chemical propulsion, to maintain the out-of-plane displaced GEO, was shown to perform very poorly due to a penalty on the ΔV for using pulsed rather than continuous control and a low specific impulse. Even the smallest displacements of 35 km, which is the minimum to rise above the geostationary station-keeping box, cannot be maintained for longer than a few months. Much better performance of a few years down to a few months in a 35 km and 150 km out-of-plane displaced orbit, respectively, can be observed for the use of SEP control. However, investigating the spacecraft mass budget showed that only for small displacements reasonable payload masses of a few hundred kilograms can be maintained for a few years. By adding a solar sail to the SEP system, thereby creating hybrid sail control, the demand on the SEP system can be lowered while enabling a mission that is impossible using only a solar sail due to the obliquity of the ecliptic and the inability of the sail to produce a thrust force in the direction of the Sun. Furthermore, making use of a seasonal transfer between orbits displaced above and below the equatorial plane increases the performance even further: for a 35 km out-of-plane displaced orbit, a near-term sail lightness number of 0.05 and a maximum SEP thrust magnitude of 0.2 N, lifetimes of 10 - 15 years (equal to current geostationary missions) can be achieved for payloads of 361 and 155 kg, respectively. For a far-term solar sail lightness number of 0.1 these payload masses can be increased to 255 - 487 kg. These payloads include not only the actual payload but also other subsystems such as OBDH, ADCS and structural mass. By estimating their mass as a fraction, i.e. 20 percent, of the spacecraft dry mass, a 200 kg pure payload mass can still be maintained for 10 years with both near-term and far-term sail lightness numbers. For smaller percentages, payloads can even be maintained in the displaced GEO for 15 years. Higher out-of-plane displaced orbits appeared to be especially useful for temporary displacements in which the spacecraft is only put into the displaced orbit for relatively short periods of time to provide coverage when needed. When not operational, the spacecraft can be transferred into a Keplerian parking orbit to save propellant mass.

Considering perturbations such as those generated by the J_2 and $J_{2,2}$ terms of the Earth's gravity field, it was shown that these have negligible effects for small sail lightness numbers. Contrary, perturbations due to non-ideal properties of the solar sail are significant, resulting

in a maximum loss in lifetime of up to 35 percent with respect to the ideal solar sail case for a near-term sail lightness number of 0.05.

Analysing the performance of the displaced GEO as defined and investigated in this chapter, it has been shown that, contrary to previous work proposed on the displaced GEO,[15-18] it is feasible to generate new geostationary slots where the spacecraft is truly stationary with respect to its ground station, by cancelling the residual in-plane acceleration by unconstrained propulsion techniques such as chemical propulsion or SEP. Furthermore, for all propulsion strategies considered, displacements well beyond the geostationary station-keeping box are enabled using near-term solar sails for the case of hybrid sail propulsion. It is therefore believed that the out-of-plane displaced GEO can provide an alternative to the geostationary orbit.

Chapter 4

Optimal transfers for displaced geostationary orbits

In the previous chapter, two types of transfers were considered to improve the performance of the displaced geostationary orbit. This chapter will investigate the optimisation of these transfers as well as the optimisation of the transfer from geostationary orbit to the displaced geostationary orbit, in order to investigate the accessibility of the displaced GEO. First, the optimal control problem for a general transfer to or from the displaced GEO is defined in Section 4.1. Then, in Sections 4.2 to 4.4 the general problem is applied to the transfer from GEO to displaced GEO, the transfer between north and south displaced GEOs and the transfer between the displaced GEO and a parking orbit, respectively. These sections assume the use of pure SEP to perform the transfers, which will be extended to the use of hybrid sail propulsion in Section 4.5. Note that for the hybrid sail case, it is assumed that hybrid propulsion is also used throughout the nominal mission, i.e. for maintaining the spacecraft in the displaced geostationary orbit. Finally, in Section 4.6 the results obtained with PSOPT are verified through a costate mapping approach and the chapter finishes with conclusions.

4.1   Optimisation of general displaced geostationary orbit transfer

Because the approach for the three types of transfers considered in this chapter is very similar, this section will provide the approach for a general case, which can subsequently be applied to the three particular cases. For all transfers, the objective is to minimise the amount of propellant consumed by the SEP thruster, which implies solving the accompanying optimal control problem, see Section 2.3.1.
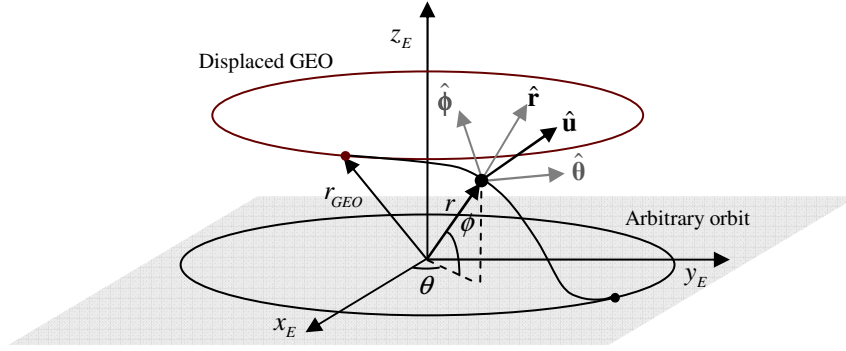
Fig. 4.1 Definition of spherical reference frame and control vector to describe a general displaced geostationary orbit transfer.

Figure 4.1 provides a definition of the general displaced geostationary orbit transfer and the reference frame employed. The figure shows that the transfer is described using the Earth centred reference frame defined in Section 3.4 and Fig. 3.8, only now using spherical coordinates $E(r, \theta, \phi)$. The in-plane angle θ is measured in the counter clockwise direction from the x_E-axis that points away from the Sun at all times and the out-of-plane angle ϕ is measured from the (x_E, y_E)-plane that is parallel to the equatorial plane. Note that this reference frame is especially of use when hybrid sail propulsion is considered, while another reference frame with less stringent constraints on the direction of the x_E-axis can be employed for the use of pure SEP.

As noted, for both an SEP-controlled spacecraft and a spacecraft employing hybrid sail propulsion, the objective is to minimise the propellant consumption, m_{prop}, at the final time, which results in the following objective function:

$$J = m_{prop,f} \tag{4.1}$$

The state vector at any point in the trajectory is given by:

$$\mathbf{x} = \begin{bmatrix} r & \theta & \phi & V_r & V_\theta & V_\phi & m_{prop} \end{bmatrix}^T \tag{4.2}$$

where V_r, V_θ and V_ϕ are the velocities in r, θ and ϕ direction, respectively. The control vector, $\mathbf{u}$, depends on the type of propulsion employed and is given through:

$$\mathbf{u} = \begin{cases} \mathbf{T} & \text{SEP} \\ \begin{bmatrix} \mathbf{T} & \hat{\mathbf{n}} \end{bmatrix}^T & \text{Hybrid} \end{cases} \tag{4.3}$$

86

with $\mathbf{T} = \begin{bmatrix} T_r & T_\theta & T_\phi \end{bmatrix}^T$ and $\hat{\mathbf{n}} = \begin{bmatrix} n_r & n_\theta & n_\phi \end{bmatrix}^T$. For SEP, the control vector consists of the Cartesian components of the SEP thrust magnitude. In the case of hybrid sail propulsion, the Cartesian components of the solar sail normal vector are added to that. Note that for both types of propulsion the Cartesian thrust components are used, rather than two angles and the vector magnitude, as these may give rise to ambiguities. When defining both angles in the interval $[0, 2\pi]$ there are at least two sets of angles that yield the same direction. Even by constraining one angle to the interval $[0, \pi]$, ambiguities can arise. For example, using two angles α and δ as defined in Fig. 3.8, where α is measured from the z-axis and δ from the $x-$axis in the (x, y)-plane, then, for the case when $\alpha = 0$, the value for δ is arbitrary. In contrast, using the Cartesian components, each set of control values corresponds to a unique thrust direction.[99] Additionally, using Cartesian components, smooth control profiles can be obtained, while the use of angles can lead to discontinuities. Again, taking as example the angles α and δ as defined in Fig. 3.8 and now considering that, over time, the thrust vector changes from the (y, z)-plane to the $(-y, z)$-plane, the change in α is smooth, but a discontinuity exists in the profile for δ. Again, using Cartesian coordinates as control variables, these discontinuities can be prevented.

Using a two-body model, the equations that describe the motion of the spacecraft in the transfer are:

$$
\dot{\mathbf{x}} = \begin{bmatrix}
V_r \\
V_\theta / (r \cos\phi) \\
V_\phi / r \\
V_\theta^2 / r + V_\phi^2 / r - \mu_\oplus / r^2 + \mathbf{a}_r \\
-V_r V_\theta / r + V_\theta V_\phi \tan\phi / r + \mathbf{a}_\theta \\
-V_r V_\phi / r - V_\theta^2 \tan\phi / r + \mathbf{a}_\phi \\
T / (I_{sp} g_0)
\end{bmatrix}
\tag{4.4}
$$

Again, depending on the type of propulsion system employed, the accelerations in the r, θ and ϕ directions are given by:

$$
\mathbf{a} = \begin{bmatrix} \mathbf{a}_r & \mathbf{a}_\theta & \mathbf{a}_\phi \end{bmatrix}^T = \begin{cases}
\dfrac{\mathbf{T}}{m} & \text{SEP} \\[2ex]
\dfrac{\mathbf{T}}{m} + \beta_0 \dfrac{m_0}{m} \dfrac{\mu_\odot}{r_s^2} (\hat{\mathbf{n}} \cdot \hat{\mathbf{r}}_s)^2 \hat{\mathbf{n}} & \text{Hybrid}
\end{cases}
\tag{4.5}
$$

with $m = m_0 - m_{prop}$ the instantaneous mass of the spacecraft. Note that an ideal solar sail model is assumed, as was done in Chapter 3.

The constraints involved in the general displaced geostationary transfer problem include at least one path constraint due to the use of the Cartesian components for the SEP control vector:

$$T = \sqrt{T_r^2 + T_\theta^2 + T_\phi^2} \leq T_{max} \tag{4.6}$$

with T_{max} the maximum allowable SEP thrust magnitude, which is set to 0.2 N as determined in Section 2.2.1. In addition, for the use of hybrid sail propulsion, the following path constraint needs to be taken into account to ensure that the magnitude of the sail normal vector equals unity and that the sail normal vector points away from the Sun at all times:

$$n = \sqrt{n_r^2 + n_\theta^2 + n_\phi^2} = 1 \tag{4.7}$$

$$\left(\hat{\mathbf{n}} \cdot \hat{\mathbf{r}}_s \right) \geq 0 \tag{4.8}$$

Furthermore, bounds on the states and controls can be defined that will apply to each of the three transfers in Sections 4.2 to 4.4:

$$
\begin{aligned}
\mathbf{x}_l &= [\quad R_\oplus + 100 \text{ km} \quad\quad 0 \quad -0.5\pi \quad -10 \text{ km/s} \quad -10 \text{ km/s} \quad -10 \text{ km/s} \quad 0 \ ]^T \\
\mathbf{x}_u &= [\, R_\oplus + 100{,}000 \text{ km} \quad 4\pi \quad 0.5\pi \quad\ 10 \text{ km/s} \quad\ 10 \text{ km/s} \quad\ 10 \text{ km/s} \quad m_0]^T \\
\mathbf{u}_l &= [-T_{max} \quad -T_{max} \quad -T_{max} \quad -1 \quad -1 \quad -1]^T \\
\mathbf{u}_u &= [\quad T_{max} \quad\ \ T_{max} \quad\ \ T_{max} \quad\ 1 \quad\ 1 \quad\ 1]^T
\end{aligned}
\tag{4.9}
$$

Equation (4.9) shows that wide bounds are set on the state variables in order not to restrict the search of the optimal control solver.

Besides the path constraints in Eqs. (4.6), (4.7) and (4.8) and the state and control bounds in Eq. (4.9), event constraints on the initial and final state vectors and bounds for the time variable need to be defined. However, these are problem specific and will therefore be defined for each of the transfers separately in Sections 4.2 to 4.4.

4.2 Transfer to displaced geostationary orbit

The first transfer that will be considered investigates the accessibility of the displaced geostationary orbit from Earth. For this, it is assumed that the spacecraft is first launched into the nominal geostationary orbit and is subsequently transferred from there to the displaced

geostationary orbit, see Fig. 4.2. Since this section only considers the use of SEP to perform the transfer, the control vector in Fig. 4.2 equals the SEP thrust vector. As noted before, an extension to hybrid sail propulsion is made in Section 4.5.

Although the transfer from Earth to the displaced GEO through the nominal geostationary orbit will not be the most optimal one (e.g. a small inclination change during the transfer to the geostationary orbit to set path towards the displaced orbit might be advantageous), it is assumed to serve as a good first estimate. Moreover, the reason for this approach is the fact that numerous spacecraft have already been launched into geostationary orbit and performance data for different launch vehicles can therefore easily be obtained. For example, the Ariane 5 launch vehicle can deliver up to 8000 kg into Geostationary Transfer Orbit (GTO)[138] of which the apogee approximately coincides with the geostationary orbit. The GTO is described by the following set of Keplerian elements $\begin{bmatrix} a_{GTO} & e_{GTO} & i_{GTO} & \omega_{GTO} \end{bmatrix} = \begin{bmatrix} 24474.5 \text{ km} & 0.7292 & 6° & 178° \end{bmatrix}$. With ω_{GTO} close to 180° it is assumed that apogee coincides with the ascending node and that the ΔV needed for the inclination change, ΔV_i, is given at that instant. Then, the ΔV needed to transfer from GTO to geostationary orbit is given by:

$$\Delta V = \Delta V_c + \Delta V_i = \left(V_{GEO} - V_{apo} \right) + 2V_{apo} \sin\left(\frac{\Delta i}{2} \right) \tag{4.10}$$

with ΔV_c the velocity change needed to circularise the GTO, $V_{GEO} = \sqrt{\mu_\oplus / r_{GEO}}$ the velocity in the geostationary orbit and $V_{apo} = V_{GEO}\sqrt{1 - e_{GTO}}$ the velocity at apogee of the GTO. The total ΔV can be computed to be 1.6 km/s. Using the rocket equation and a specific impulse of 446 s for the Ariane 5 cryogenic upper-stage,[138] the mass delivered in geostationary orbit can be shown to be 5496 kg. This mass well exceeds the maximum initial masses of 2912, 1020 and 436 kg in a 35, 75 and 150 km displaced geostationary orbit, respectively, see Fig. 3.15b. Therefore, over 2500 kg would be available to perform the transfer from GEO to displaced GEO. For the 150 km displaced orbits even a smaller class launch vehicle such as the Soyuz could possibly be used as it can deliver 450 kg directly into geostationary orbit (and possibly more when using an intermediate GTO).[139]

From Fig. 4.2 the following, case specific, constraints for the optimal control problem can be derived. First, the initial and final conditions are:

$$\begin{aligned}
\mathbf{x}_0 &= [r_{GEO} \quad \theta_0 \quad 0 \quad 0 \quad \sqrt{\mu_\oplus/(r_{GEO})} \quad 0 \quad 0]^T \\
\mathbf{x}_f &= [r_{GEO} \quad \theta_f \quad \phi_f \quad 0 \quad \sqrt{\mu_\oplus/r_{GEO}}\cos\phi_f \quad 0 \quad m_{prop,f}]^T
\end{aligned} \tag{4.11}$$
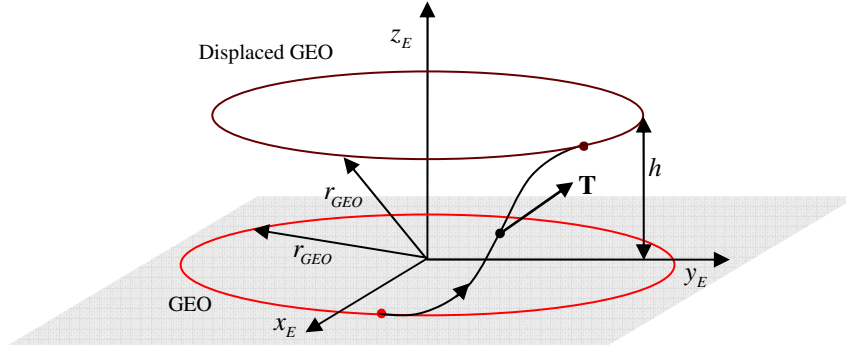
Fig. 4.2 Illustration of transfer from GEO to displaced GEO.

with $\phi_f = \sin^{-1}(h/r_{GEO})$ and the initial and final in-plane angles (θ_0 and θ_f) and the final propellant consumption free. Phasing between the geostationary orbit and the displaced geostationary orbit will have to ensure that the spacecraft is inserted into the displaced geostationary orbit at the correct longitude.

Note that the values for the initial mass, m_0, are taken equal to the maximum masses in Fig. 3.15b (i.e. for $\beta_0 = 0.2$) to obtain a conservative estimate of the quantity of propellant needed. Secondly, the bounds on the initial and final times are set as:

$$\begin{align} t_l &= 0 \\ t_u &= 10 \text{ days} \end{align} \tag{4.12}$$

Again, a rather wide bound on the independent variable is set in order not to limit the search of the optimal control solver.

4.2.1 Initial guess

As described in Section 2.3.4, PSOPT needs an initial guess to initialise the optimisation. To obtain this initial guess, a shape-based (or inverse) method is used where a particular shape for the transfer is assumed and the controls required to perform that transfer are sought for, similar to the approach used for the exponential sinusoids in Section 2.3.5. For this, the shape employed for the transfer from geostationary orbit to displaced GEO is considered in a rotating reference frame $R(x_R, y_R, z_R)$ that rotates with respect to an inertial frame $I(x_I, y_I, z_I)$ at constant angular velocity $\omega = \omega_{GEO}\hat{\mathbf{z}}_R$, see Fig. 4.3. In the rotating reference frame, spacecraft in the (displaced) geostationary orbit are stationary. The transfer between the orbits is assumed to lie in the (x_R, z_R)-plane only and is the shortest path possible

between the two orbits. Using a temporary variable, $s(t)$ (as illustrated in Fig. 4.3), a parabolic velocity profile, $\dot{s}(t)$ is assumed to ensure zero velocity at the start and end of the transfer:

$$\dot{s}(t) = a_1 t^2 + a_2 t + a_3 \tag{4.13}$$

The constants a_1, a_2 and a_3 can be partially derived from the following initial and final conditions:

$$
\begin{array}{ll}
1) \quad s_0 = s(t_0) = 0 & 2) \quad s_f = s(t_f) = \sqrt{h^2 + r_{GEO}^2 \left(1 - \cos\phi\right)^2} \\
3) \quad \dot{s}_0 = \dot{s}(t_0) = 0 & 4) \quad \dot{s}_f = \dot{s}(t_f) = 0
\end{array}
\tag{4.14}
$$
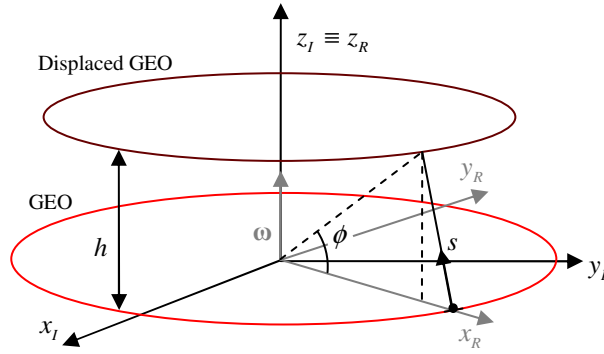
Fig. 4.3 Initial guess for GEO to displaced GEO transfer.

Equation (4.14)-3 with $t_0 = 0$ gives $a_3 = 0$ and from Eq. (4.14)-4 it follows that $a_2 = -a_1 t_f$.

The profile for the coordinate s can be derived by evaluating the following integral:

$$s(t) = \int_{t_0=0}^{t} \dot{s}(t)dt = a_1 t^2 \left(\frac{1}{3} t - \frac{1}{2} t_f\right) + a_4 \tag{4.15}$$

From Eq. (4.14)-1 it follows that $a_4 = 0$ and using Eq. (4.14)-2 gives $a_1 = -6 s_f / t_f^3$. Finally, using a differentiation of the velocity profile, the acceleration profile can be derived:

$$\ddot{s}(t) = \frac{d\dot{s}(t)}{dt} = a_1 (2t - t_f) \tag{4.16}$$

Transforming back to the $R(x_R, y_R, z_R)$ frame gives:

$$x_R(t) = r_{GEO} - s(t)\cos\left(\tfrac{1}{2}(\pi - \phi)\right) \quad ; \quad y_R(t) = 0 \quad ; \quad z_R(t) = s(t)\sin\left(\tfrac{1}{2}(\pi - \phi)\right)$$

$$\dot{x}_R(t) = -\dot{s}(t)\cos\left(\tfrac{1}{2}(\pi - \phi)\right) \qquad ; \quad \dot{y}_R(t) = 0 \quad ; \quad \dot{z}_R(t) = \dot{s}(t)\sin\left(\tfrac{1}{2}(\pi - \phi)\right) \qquad (4.17)$$

$$\ddot{x}_R(t) = -\ddot{s}(t)\cos\left(\tfrac{1}{2}(\pi - \phi)\right) \qquad ; \quad \ddot{y}_R(t) = 0 \quad ; \quad \ddot{z}_R(t) = \ddot{s}(t)\sin\left(\tfrac{1}{2}(\pi - \phi)\right)$$

The shape of the transfer and its velocity and acceleration profiles are now determined. The next step is to determine the direction and magnitude of the thrust force that will enable this transfer. For this, the equations of motion of Eq. (2.6) are used. Substituting $\mathbf{\omega} = \omega_{GEO}\hat{\mathbf{z}}_R$ and $\mathbf{a} = \mathbf{T}/m$ (with $\mathbf{T} = \begin{bmatrix} T_{x_R} & T_{y_R} & T_{z_R} \end{bmatrix}$) the components of the thrust acceleration in the rotating frame) yields:

$$\begin{pmatrix} T_{x_R} \\ T_{y_R} \\ T_{z_R} \end{pmatrix} = m \begin{pmatrix} \ddot{x}_R + \dfrac{\mu_\oplus}{r^3} x_R - 2\omega_{GEO}\dot{y}_R - \omega_{GEO}^2 x_R \\ \ddot{y}_R + \dfrac{\mu_\oplus}{r^3} y_R + 2\omega_{GEO}\dot{x}_R - \omega_{GEO}^2 y_R \\ \ddot{z}_R + \dfrac{\mu_\oplus}{r^3} z_R \end{pmatrix} \qquad (4.18)$$

with $r = \sqrt{x_R^2 + y_R^2 + z_R^2}$. Finally, substituting Eq. (4.17) and rewriting provides the required components of the SEP thrust vector. Note that these equations hold for both a transfer to a displaced geostationary orbit above the equatorial plane and below the equatorial plane by using the correct sign for the displacement distance h. In order to get an estimate for the mass profile, the transfer is discretised into several, equally spaced nodes and the mass at each node is approximated using Eq. (3.29). Furthermore, in correspondence with the analyses in Chapter 3, a specific impulse of 3200 s is used and finally, a transfer time of 1 day (i.e. $t_f = 1$ day) is assumed. The results for a 150 km displaced geostationary orbit are provided in Fig. 4.4. The figure shows that the thrust magnitude required exceeds the maximum thrust defined for the transfer. When using this initial guess to minimise the objective function in Eq. (4.1) with a limit on the thrust magnitude of 0.2 N, this may cause convergence problems in PSOPT. This can be circumvented by first performing an optimisation in which the square of the thrust is minimised (without a limit on the thrust magnitude), which places a penalty on large thrust values and usually has good convergence characteristics. The result from that optimisation can then serve as initial guess for the thrust-limited minimisation of the propellant mass as given in Eq. (4.1).
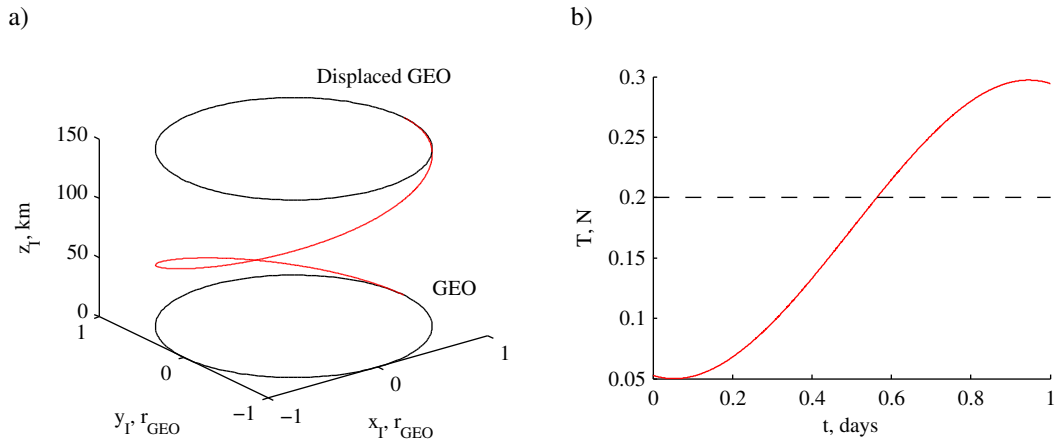
Fig. 4.4 Initial guess for the transfer from the geostationary orbit to a 150 km out-of-plane displaced geostationary orbit. a) Transfer. b) Thrust profile.

4.2.2 Results

Before using the results of the previous section as initial guess for PSOPT, the distribution of the nodes is changed into a Legendre-Gauss-Lobatto distribution, as is used by PSOPT. Subsequently, the results provided in Table 4.1 and Fig. 4.5 can be obtained. These results were obtained for an NLP tolerance of 10^{-6} and by setting the maximum number of iterations to 1000. Note that this number of iterations was never reached. Also note that, due to the symmetry of the problem, the results for orbits displaced above and below the equatorial plane are exactly the same if equal displacement distances are considered.

Table 4.1 Propellant mass, m_{prop}, required for a GEO to displaced GEO transfer for different values of the displacement distance, h, and the accompanying maximum initial mass, m_0.

h, km	m_0, kg	m_{prop}
±35	2912	260.5 g
±75	1020	186.8 g
±150	436	184.2 g

The required propellant mass in Table 4.1 shows that only a very small fraction of the 2500 kg available (see below Eq. (4.10)) is sufficient to perform the transfer from GEO to the displaced geostationary orbit. Furthermore, although one would expect that the transfer to smaller displacement distances requires less propellant than those to the higher displaced orbits, the larger initial mass causes the transfer to the 35 km displaced orbit to be more demanding in terms of propellant mass than those to the 75 and 150 km displaced orbits.
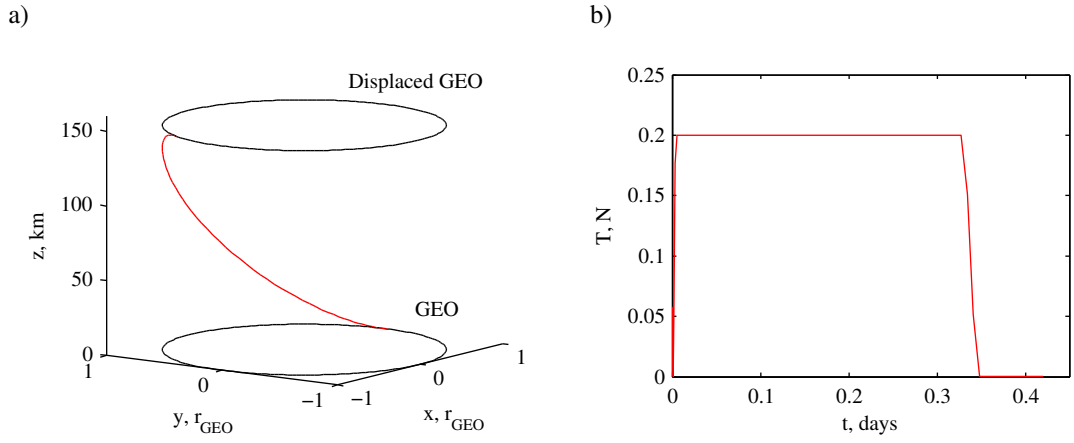
Fig. 4.5 Results for a GEO to displaced GEO transfer with h_f = 150 km. a) Transfer. b) Thrust profile.

4.3 Transfer between north and south displaced geostationary orbits

The obliquity of the ecliptic causes hybrid sail control for out-of-plane displaced GEOs to perform best when the spacecraft is displaced *above* the equatorial plane (north) in winter and *below* the equatorial plane (south) in summer. To take advantage of this, the spacecraft will have to be transferred from above the equatorial plane to below the equatorial plane and vice versa twice per year: once in spring (north to south) and once in autumn (south to north). This transfer is illustrated in Fig. 4.6.

In this case, the problem specific initial and final state vectors are given by:

$$\mathbf{x}_0 = [\, r_{GEO} \quad 0 \quad \phi_0 \quad 0 \quad \sqrt{\mu_\oplus / r_{GEO}} \cos\phi_0 \quad 0 \quad 0\,]^T$$
$$\mathbf{x}_f = [\, r_{GEO} \quad \theta_f \quad \phi_f \quad 0 \quad \sqrt{\mu_\oplus / r_{GEO}} \cos\phi_f \quad 0 \quad m_{prop,f}\,]^T \tag{4.19}$$

with the final propellant mass, $m_{prop,f}$, free. To ensure that the longitude of the spacecraft in the displaced GEO is unchanged after the transfer, the final in-plane angle θ_f is restricted to:

$$\theta_f = \omega_{GEO} t_f \tag{4.20}$$

94
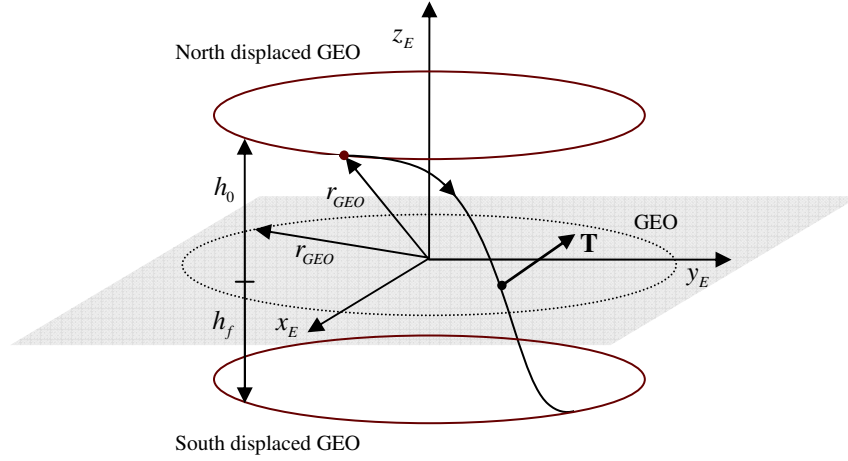
Fig. 4.6 Illustration of transfer between north and south displaced GEOs.

Furthermore, a maximum transfer time of one day is assumed to limit a potential disruption in the downlink to Earth during the transfer:

$$t_l = 0$$
$$t_u = 1 \text{ day}$$

(4.21)

Using a similar initial guess as for the GEO to displaced GEO transfer in Section 4.2.1, the results of the optimisation in PSOPT are given in the first row (for $\Delta d = 0$) of Table 4.2 with a selection of the corresponding thrust profiles in Fig. 4.7. Again, the table shows a relatively worse performance for smaller displacements which can be explained by the relatively larger initial mass. The first row in Table 4.2 furthermore shows that almost negligible amounts of propellant are needed to perform the seasonal transfer.

The reason for these small amounts of propellant can be understood when considering what happens when the propulsion system is switched off in the displaced GEO. Each point of the displaced GEO corresponds to a Keplerian orbit with semi-major axis, eccentricity and inclination equal to:[41]

$$a = \left[\frac{2}{r_{GEO}} - \frac{\rho^2}{r_{GEO}^3} \right]^{-1} ; \quad e = 1 - \frac{\rho^2}{r_{GEO}^2} ; \quad i = \tan^{-1}\left(\frac{h}{\rho} \right)$$

(4.22)

with ρ the radius of the displaced GEO projected onto the equatorial plane. With $\rho \approx r_{GEO}$, the semi-major axis approximately equals the radius of the (displaced) GEO, the eccentricity is approximately 0 and the inclination equals the out-of-plane angle of the displaced GEO, ϕ, see Fig. 4.1. The Keplerian orbit thus almost coincides with the displaced GEO on the

opposite side of the equatorial plane and only a small thrust is needed to overcome any remaining offset.

This description of the transfer also implies that the transfer closely passes by GEO and could therefore pose a collision risk to GEO spacecraft. In order to cope with this, the following path constraint is added to the optimal control problem:

$$\sqrt{r_{GEO}^2 - 2r \cdot r_{GEO} \cos\phi + r^2} \geq \Delta d \tag{4.23}$$

which ensures that the distance between the transfer and GEO is always larger than the value assigned to Δd.

Including this constraint provides the other results in Table 4.2, where the propellant mass is given for different values of Δd. The table shows that the constraint has a rather large impact on the propellant consumption, especially for smaller displacements. However, the increase in propellant mass still outweighs the savings that can be obtained from applying the transfer to increase the performance of the out-of-plane displaced GEO during the in-orbit phase.

Table 4.2 Required propellant mass in grams for optimised seasonal transfer including a constraint on the approach distance to GEO, Δd.

		h_0, km		
		±35	±75	±150
m_0, kg		2912	1020	436
	0	2.6 g	0.96 g	0.66 g
	5	243.0 g	52.6 g	20.1 g
Δd, km	10	Infeasible	123.3 g	42.1 g
	20	Infeasible	Infeasible	96.0 g
	35	Infeasible	Infeasible	227.4 g
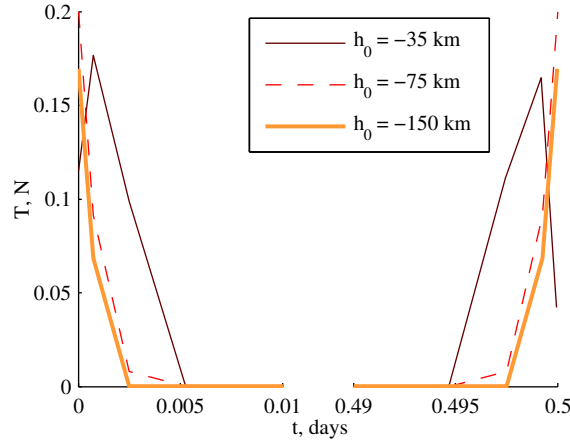
Fig. 4.7 Thrust profile for optimised seasonal transfer with $\Delta d = 0$.

4.4 Transfer between displaced geostationary orbit and parking orbit

For the case of temporary displacements, as discussed in Section 3.5, the spacecraft is transferred into an out-of-plane displaced GEO for a relatively short period of time to provide services and is transferred back into a Keplerian parking orbit when the services are no longer needed in order to save propellant mass. This parking orbit and the transfers that are involved in this concept are illustrated in Fig. 4.8. The figure shows that the parking orbit lies in the equatorial plane and inside GEO, where the distance between the parking orbit and GEO equals the absolute value of the displacement distance. In this way, the parking orbit is as close to the displaced GEO as possible without interfering with either GEO or the displaced GEO.

In case the transfer from the parking orbit to the displaced GEO is considered, the problem specific initial and final conditions are:

$$\mathbf{x}_0 = [r_{GEO} - |h| \quad 0 \quad 0 \quad 0 \quad \sqrt{\mu_\oplus/(r_{GEO} - |h|)} \quad 0 \quad 0]^T \tag{4.24}$$

$$\mathbf{x}_f = [r_{GEO} \quad \theta_f \quad \phi_f \quad 0 \quad \sqrt{\mu_\oplus/r_{GEO}} \cos\phi_f \quad 0 \quad m_{prop,f}]^T \tag{4.25}$$

with the final propellant mass, $m_{prop,f}$, and final in-plane angle, θ_f, free. Phasing between the parking orbit and the out-of-plane displaced GEO will have to ensure that the spacecraft is inserted into the displaced GEO at the correct longitude. Note that when the transfer from

the displaced orbit to the parking orbit is considered, the initial condition is given by Eq. (4.25) and the final condition by Eq. (4.24).

The problem specific bounds on the time allowed for the transfer are set to:

$$t_l = 0$$
$$t_u = 10 \text{ days}$$

(4.26)

Again, the same approach to generate the initial guess is adopted. Note however that this introduces a slight error, because the angular velocity of the parking orbit and (displaced) geostationary orbits are not equal. This means that the velocity of a spacecraft in the parking orbit in the rotating frame of reference of Fig. 4.3 is not zero. However, the difference in angular velocity with the (displaced) GEO is only 0.17 percent at most (i.e. for a 150 km displaced GEO) and proved not to cause any problems in the convergence of PSOPT.

The results of the optimisation are shown in Table 4.3 and Fig. 4.9, where again a minimum distance from GEO is taken into account. Although the required propellant mass is larger than for the seasonal transfer, it still requires only modest propellant budgets that are similar to the GEO to displaced GEO transfer in Section 4.2. Note that some of the cases considered are infeasible because the constraint on the minimum approach distance cannot be met: under the given dynamics and thruster capabilities, trajectories between 35 km north and south displaced orbits with a minimum approach distance of 20 and 35 km did not converge to a feasible solution.

However, in general, the use of such a transfer can be considered realistic. Finally, looking at the thrust profile in Fig. 4.9b, it becomes clear that the main change to the spacecraft orbit is a change in inclination, which is obtained by efficiently thrusting around the nodal crossing. This shape of transfer can be expected when once again considering that each point of the displaced GEO approximates a Keplerian orbit with radius equal to the radius of GEO but inclined at the out-of-plane angle ϕ. Then, considering the fact that the difference in radius between the parking orbit and GEO is small, the transfer can be approximated by a simple inclination change.
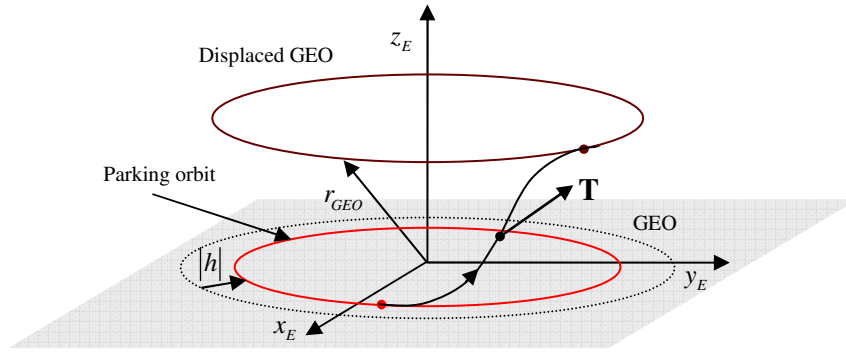
Fig. 4.8 Definition of parking orbit for temporary displacement and illustration of transfer between parking orbit and displaced GEO.

Table 4.3 Required propellant mass in grams for temporary displacement transfer including a constraint on the approach distance to GEO, Δd.

		Parking orbit to displaced GEO			Displaced GEO to parking orbit		
		h_f , km			h_0 , km		
		± 35	± 75	± 150	± 35	± 75	± 150
m_0 , kg		2912	1020	436	2912	1020	436
	0	277.8 g	204.0 g	173.7 g	292.0 g	208.9 g	176.2 g
	5	287.2 g	206.7 g	174.1 g	297.3 g	209.9 g	176.2 g
Δd , km	10	302.3 g	210.9 g	176.1 g	304.3 g	214.1 g	177.3 g
	20	Infeasible	221.4 g	179.5 g	Infeasible	224.6 g	181.1 g
	35	Infeasible	247.2 g	185.7 g	Infeasible	249.9 g	187.2 g

a)

b)
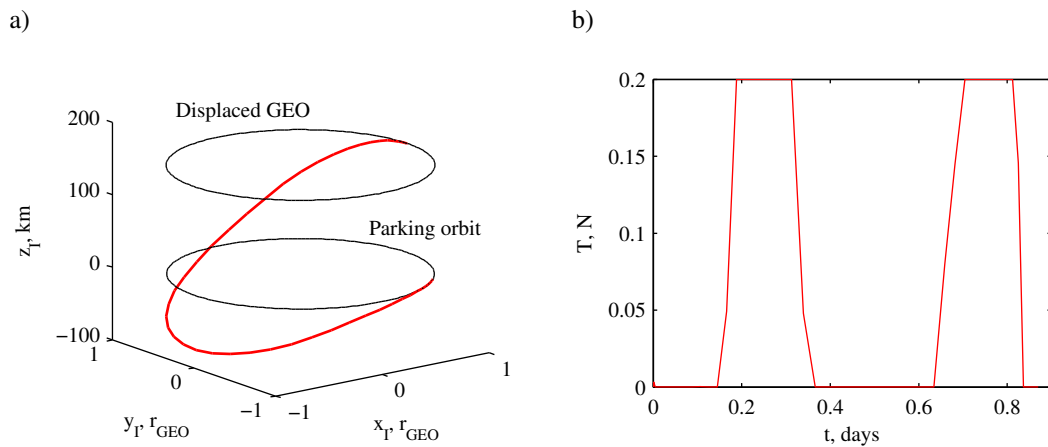
Fig. 4.9 Transfer from a 150 km out-of-plane displaced GEO to a parking orbit. a) Transfer. b) Thrust profile.

4.5   Hybrid sail propulsion

Although the propellant consumption for the transfer to the displaced GEO in Section 4.6.2 and the transfer to/from an equatorial parking orbit in the previous section was only modest, it is still interesting to investigate whether hybrid sail propulsion could improve these performances even further. Furthermore, note that the transfer between north and south displaced GEOs is not considered as it is already almost free when using pure SEP propulsion. The model for the two types of transfers using hybrid propulsion was already outlined in Section 4.1 and the results for the pure SEP transfers are used as initial guess.

It is important to note that the performance of hybrid sail propulsion depends on the time of year the transfer takes place. Here, the most favourable conditions are selected for the transfer from GEO to displaced GEO as the time of launch could be selected accordingly: winter for a transfer to a north displaced GEO and summer for a transfer to a south displaced GEO. Contrary, since the transfer from the parking orbit to the displaced GEO (and vice versa) can take place at any time during the year, an average performance is generated by assuming that this type of transfer takes place in spring/autumn.

Finally, the direction of the Sun-sail line is assumed constant during the transfer, which is a reasonable assumption because the transfers take approximately one day (or less) to complete.

The results for the hybrid transfers are provided in Fig. 4.10 for a range of solar sail lightness numbers. To limit the quantity of results presented, only the results for $h = \pm 35$ km and $h = \pm 150$ are provided and only for $\Delta d = 0$ (i.e. without including the constraint on the approach distance to geostationary orbit), but clearly similar improvements in terms of propellant mass consumption can be obtained for a displacement distance of 75 km and when the GEO approach constraint is included.

Figure 4.10 shows that by adding a solar sail to the SEP thruster and by increasing the solar sail lightness number, the SEP propellant consumption can indeed be decreased. Note again that it is assumed that hybrid propulsion is also used throughout the nominal mission, i.e. for maintaining the spacecraft in the displaced geostationary orbit. Otherwise, if the sail would only be used for the transfer, the savings in propellant as shown in Fig. 4.10 will not outweigh the additional mass of the sail. The savings indicated in Fig. 4.10 thus come in addition to the savings that can be established during the in-orbit phase by using hybrid propulsion, see Chapter 3. For particular cases, for example the transfer from GEO to the 35 km displaced GEO, large enough lightness numbers (i.e. $\beta_0 \geq 0.04$) can even result in a

propellant-free transfer, indicating that the transfer can be performed using only the solar sail. This clearly demonstrates the potential of hybrid sail propulsion as a way to gradually introduce solar sails for space applications, as was already discussed in Section 2.2.3.
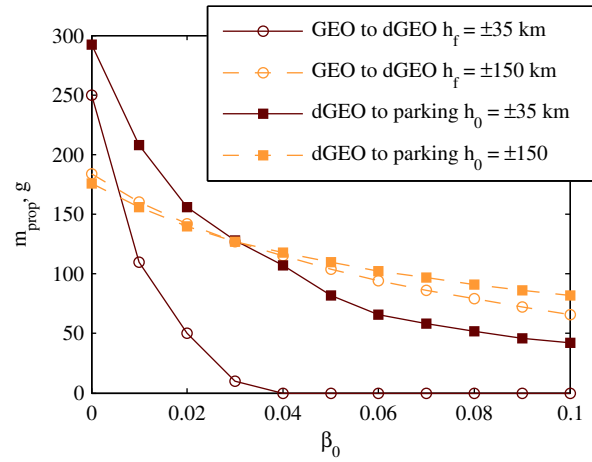
Fig. 4.10 SEP propellant consumption for hybrid transfers from GEO to displaced GEO and from displaced GEO to a parking orbit as a function of the sail lightness number, β_0, and for $\Delta d = 0$.

4.6   Results validation

In the previous sections, a range of optimal control problems have been solved using the direct pseudospectral method implemented in PSOPT. In order to check the validity of the solutions and the performance of PSOPT, this section aims at solving a subset of those problems through the indirect approach described in Section 2.3.2. In particular, the pure SEP transfers from GEO to displaced GEO, between north and south displaced geostationary orbits and from the displaced GEO to the parking orbit will be considered. For these transfers, the two-point boundary-value problem described in Section 2.3.2 needs to be defined, which differ from each other only in the boundary conditions. The resulting boundary-value problems are subsequently solved using a collocation method.[140]

4.6.1   Two-point boundary-value problem

Before starting the derivation of the boundary-value problem it is noted that a different definition of the SEP control variables will be used than what is given in Eq. (4.3). Rather than using the three Cartesian SEP thrust components, which were suitable for use in PSOPT, a control vector consisting of two angles and an equivalent of the thrust magnitude

is employed as this significantly simplifies the derivation of the optimal control law and also eliminates the path constraint on the total thrust magnitude in Eq. (4.6):

$$\mathbf{u} = \begin{bmatrix} \alpha_E & \delta_E & \tau \end{bmatrix}^T \tag{4.27}$$

where $-\pi \le \alpha_E \le \pi$ and $-\pi \le \delta_E \le \pi$ are the SEP thrust vector angles in the spherical reference frame (subscript 'E') used throughout the design of the displaced GEO transfers, see Fig. 4.1 and Fig. 4.11. Finally, the control parameter $0 \le \tau \le 1$ is used to indicate the fraction of the total available thrust, T_{max}, that is applied.
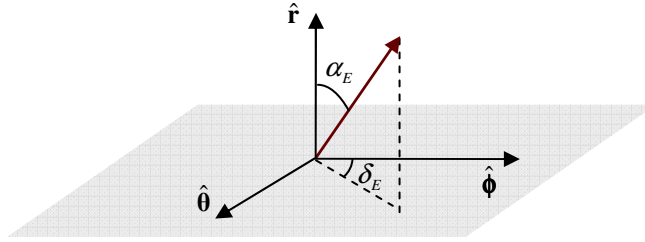
Fig. 4.11 Definition of SEP thrust angles.

The SEP accelerations in r, θ and ϕ direction then become:

$$\mathbf{a} = \begin{bmatrix} \mathbf{a}_r \\ \mathbf{a}_\theta \\ \mathbf{a}_\phi \end{bmatrix} = \frac{\tau T_{max}}{m} \begin{bmatrix} \cos \alpha_E \\ \sin \alpha_E \sin \delta_E \\ \sin \alpha_E \cos \delta_E \end{bmatrix} \tag{4.28}$$

By substituting these accelerations into the equations of motion in Eq. (4.4), the following Hamiltonian can be derived:

$$
\begin{aligned}
H = \boldsymbol{\lambda}^T \dot{\mathbf{x}} = {} & \lambda_r V_r + \lambda_\theta \frac{V_\theta}{r \cos \phi} + \lambda_\phi \frac{V_\phi}{r} + \lambda_{V_r} \left(\frac{V_\theta^2}{r} + \frac{V_\phi}{r} - \frac{\mu_\oplus}{r^2} + \frac{\tau T_{max}}{m} \cos \alpha_E \right) + \\
& \lambda_{V_\theta} \left(-\frac{V_r V_\theta}{r} + \frac{V_\theta V_\phi}{r} \tan \phi + \frac{\tau T_{max}}{m} \sin \alpha_E \sin \delta_E \right) + \\
& \lambda_{V_\phi} \left(-\frac{V_r V_\phi}{r} - \frac{V_\theta^2}{r} \tan \phi + \frac{\tau T_{max}}{m} \sin \alpha_E \cos \delta_E \right) + \lambda_{m_{prop}} \left(\frac{\tau T_{max}}{I_{sp} g_0} \right)
\end{aligned}
\tag{4.29}
$$

where λ_r, λ_θ, λ_ϕ, λ_{V_r}, λ_{V_θ}, λ_{V_ϕ} and $\lambda_{m_{prop}}$ are the costates associated with the state variables r, θ, ϕ, V_r, V_θ, V_ϕ and m_{prop}, respectively.

The adjoint equations can subsequently be derived as:

$$\dot{\lambda}_r = -\frac{\partial H}{\partial r} = \frac{1}{r^2}\left(\lambda_\theta \frac{V_\theta}{\cos\phi} + \lambda_\phi V_\phi + \lambda_{V_r}\left(V_\theta^2 + V_\phi - \frac{2\mu_\oplus}{r}\right) - \lambda_{V_\theta}\left(V_r V_\theta - V_\theta V_\phi \tan\phi\right)\right.$$
$$\left. - \lambda_{V_\phi}\left(V_r V_\phi + V_\theta^2 \tan\phi\right)\right)$$

$$\dot{\lambda}_\theta = -\frac{\partial H}{\partial\theta} = 0$$

$$\dot{\lambda}_\phi = -\frac{\partial H}{\partial\phi} = \frac{1}{r\cos^2\phi}\left(-\lambda_\theta V_\theta \sin\phi - \lambda_{V_\theta} V_\theta V_\phi + \lambda_{V_\phi} V_\theta^2\right)$$

$$\dot{\lambda}_{V_r} = -\frac{\partial H}{\partial V_r} = -\lambda_r + \lambda_{V_\theta}\frac{V_\theta}{r} + \lambda_{V_\phi}\frac{V_\phi}{r}$$

$$\dot{\lambda}_{V_\theta} = -\frac{\partial H}{\partial V_\theta} = -\lambda_\theta \frac{1}{r\cos\phi} - 2\lambda_{V_r}\frac{V_\theta}{r} + \lambda_{V_\theta}\left(\frac{V_r}{r} - \frac{V_\phi}{r}\tan\phi\right) + 2\lambda_{V_\phi}\frac{V_\theta}{r}\tan\phi$$

$$\dot{\lambda}_{V_\phi} = -\frac{\partial H}{\partial V_\phi} = -\lambda_\phi \frac{1}{r} - \lambda_{V_r}\frac{1}{r} - \lambda_{V_\theta}\frac{V_\theta}{r}\tan\phi + \lambda_{V_\phi}\frac{V_r}{r}$$

$$\dot{\lambda}_m = -\frac{\partial H}{\partial m_{prop}} = -\frac{\tau T_{max}}{m^2}\left(\lambda_{V_r}\cos\alpha_E + \lambda_{V_\theta}\sin\alpha_E \sin\delta_E + \lambda_{V_\phi}\sin\alpha_E \cos\delta_E\right)$$

(4.30)

Then, the optimal control law can be derived from the Hamiltonian in Eq. (4.29) by setting the partial derivatives with respect to the control variables equal to zero:

$$\frac{\partial H}{\partial\alpha_E} \to -\lambda_{V_r}\sin\alpha_E + \cos\alpha_E\left(\lambda_{V_\theta}\sin\delta_E + \lambda_{V_\phi}\cos\delta_E\right) = 0 \tag{4.31}$$

$$\frac{\partial H}{\partial\delta_E} \to \lambda_{V_\theta}\cos\delta_E - \lambda_{V_\phi}\sin\delta_E = 0 \tag{4.32}$$

$$\frac{\partial H}{\partial\tau} \to \frac{1}{m}\left(\lambda_{V_r}\cos\alpha_E + \lambda_{V_\theta}\sin\alpha_E \sin\delta_E + \lambda_{V_\phi}\sin\alpha_E \cos\delta_E\right) + \frac{\lambda_m}{I_{sp}g_0} \tag{4.33}$$

From Eq. (4.32) it can be derived that the optimal control law for the angle δ_E is given by:

$$\sin\delta_E = \frac{\lambda_{V_\theta}}{\sqrt{\lambda_{V_\theta}^2 + \lambda_{V_\phi}^2}}, \qquad \cos\delta_E = \frac{\lambda_{V_\phi}}{\sqrt{\lambda_{V_\theta}^2 + \lambda_{V_\phi}^2}} \tag{4.34}$$

By substituting these expressions into Eq. (4.31) the following optimal control law for the angle α_E can be derived:

$$\sin\alpha_E = \frac{\sqrt{\lambda_{V_\theta}^2 + \lambda_{V_\phi}^2}}{\sqrt{\lambda_{V_r}^2 + \lambda_{V_\theta}^2 + \lambda_{V_\phi}^2}}, \qquad \cos\alpha_E = \frac{\lambda_{V_r}}{\sqrt{\lambda_{V_r}^2 + \lambda_{V_\theta}^2 + \lambda_{V_\phi}^2}} \tag{4.35}$$

Finally, from Eq. (4.29) it becomes clear that the Hamiltonian depends linearly on the control parameter τ. Therefore, a bang-bang control is most optimal, where the switching times between thrust on and off can be determined from the condition in Eq. (4.33):

$$\frac{1}{m}\left(\lambda_{V_r}\cos\alpha_E + \lambda_{V_\theta}\sin\alpha_E\sin\delta_E + \lambda_{V_\phi}\sin\alpha_E\cos\delta_E\right) + \frac{\lambda_m}{I_{sp}g_0}\begin{cases}>0\rightarrow & \tau=1\\ \leq 0\rightarrow & \tau=0\end{cases} \qquad (4.36)$$

As stated in the introduction to this section, the boundary conditions on the states depend on the particular transfer considered, but they can be written in the following generalised form:

$$\boldsymbol{\phi}_0 = \begin{cases} r_0 - r_{GEO}\\ \theta_0\\ \phi_0 - \sin^{-1}\left(\dfrac{h_0}{r_{GEO}}\right)\\ V_{r,0}\\ V_{\theta,0} - \sqrt{\dfrac{\mu_\oplus}{r_{GEO}}}\cos\left(\sin^{-1}\left(\dfrac{h_0}{r_{GEO}}\right)\right)\\ V_{\phi,0}\\ m_{prop,0}\end{cases} = \mathbf{0}, \quad \boldsymbol{\phi}_f = \begin{cases} r_f - \left(r_{GEO}-\Delta r\right)\\ \phi_f - \sin^{-1}\left(\dfrac{h_f}{r_{GEO}}\right)\\ V_{r,f}\\ V_{\theta,f} - \sqrt{\dfrac{\mu_\oplus}{\left(r_{GEO}-\Delta r\right)}}\cos\left(\sin^{-1}\left(\dfrac{h_f}{r_{GEO}}\right)\right)\\ V_{\phi,f}\end{cases} = \mathbf{0} \quad (4.37)$$

Concerning the boundary conditions on the costates, the final conditions of the costate associated with the in-plane angle, λ_θ, and propellant mass, $\lambda_{m_{prop}}$, can be obtained from the transversality conditions in Eq. (2.52):

$$\lambda_\theta\left(t_f\right) = 0, \qquad \lambda_{m_{prop}}\left(t_f\right) = 1 \qquad (4.38)$$

Equation (4.4) (together with Eq. (4.28)) and Eqs. (4.30) to (4.38) describe the two-point boundary value problem for all the transfers associated with the displaced GEO. However, all transfers are time free problems, i.e. the terminal time, t_f, is not specified. The time of flight is therefore considered as a parameter in the boundary value problem for which an additional boundary condition needs to be specified. In particular, the condition that needs to be satisfied by the optimal choice of the final time is provided in Eq. (2.52) as one of the transversality conditions and is given by:[97]

$$H\left(t_f\right) = -\frac{\partial M}{\partial t_f} + \mathbf{v}^T\frac{\partial\boldsymbol{\phi}_f}{\partial t_f} = 0 \qquad (4.39)$$

The value of the Hamiltonian at the final time should thus equal zero.

The boundary-value problem is solved using the MATLAB® function *bvp4c*. Since the method implemented in *bvp4c* requires gradient information, the discontinuity introduced by Eq. (4.36) gives rise to singular Jacobian matrices. This discontinuity is therefore modelled using a smooth Heaviside function as follows:

$$\tau = \frac{1}{2}\left(\tanh\left(\frac{\frac{1}{m}\left(\lambda_{V_r}\cos\alpha_E + \lambda_{V_\theta}\sin\alpha_E\sin\delta_E + \lambda_{V_\phi}\sin\alpha_E\cos\delta_E\right) + \frac{\lambda_m}{I_{sp}g_0}}{a_H}\right) + 1\right) \quad (4.40)$$

The smaller the value for the parameter, a_H, the more Eq. (4.40) approximates the real discontinuity. In order to solve the boundary value problem for such small values for a_H, a continuation scheme is employed where a relatively large initial value for a_H is assumed. The results are subsequently used as an initial guess to solve the boundary value problem for a smaller value for a_H. This process is repeated until an acceptable approximation of the discontinuity is obtained. Note that the very first initial guess (for the largest value for a_H considered) is the solution from PSOPT, which provides an initial guess for the costate variables through the costate mapping theorem as explained in Section 2.3.3.

4.6.2 Transfer to displaced geostationary orbit

For the transfer from geostationary orbit to displaced GEO, the values for the initial and final out-of-plane displacements are $h_0 = 0$ km and $h_f = \pm 35$, 75 or 150 km and $\Delta r = 0$, respectively. Substituting these values into Eq. (4.37) gives the boundary conditions for this particular transfer. Subsequently implementing and solving the two-point boundary-value problem derived in the previous section provides the results in Fig. 4.12 for a displacement of 150 km. To generate these results a starting value for the parameter a_H of 10^{-4} is used, which is decreased with a step size of $\Delta a = 10^{-6}$ to a final value of $a_H = 3 \times 10^{-6}$. This final value is considered to be small enough to accurately model the discontinuity in the thrust profile. This can also be seen from Fig. 4.13, which shows the evolution of the modelling of the discontinuity at time $t = 0.335$ days. The figure shows that the continuation starts with a very smooth, inaccurate approximation of the discontinuity, but improves the approximation until an accurate representation of the discontinuity is obtained. Furthermore, Fig. 4.12c and Fig. 4.12d show the influence of the value for a_H on the objective function (i.e. the propellant consumption) and the time of flight. The figures show that, for the starting value of the parameter, the propellant mass and time of flight are larger than the PSOPT solution

and decrease for decreasing values of a_H. At the end of the continuation, both the objective function value and the flight time are slightly smaller than the PSOPT solution, but the differences are so small that they can be considered negligible.

A further comparison of the results from PSOPT and the indirect method in Fig. 4.12 proves that the two methods not only closely resemble each other in terms of objective function and time of flight, but also the thrust and state profiles match very closely. Although the figure only shows the results for the transfer to a 150 km displaced GEO, similar results can be obtained for the transfer to the other displacement distances. The results in Fig. 4.12 therefore prove the optimality of the solution provided by PSOPT.
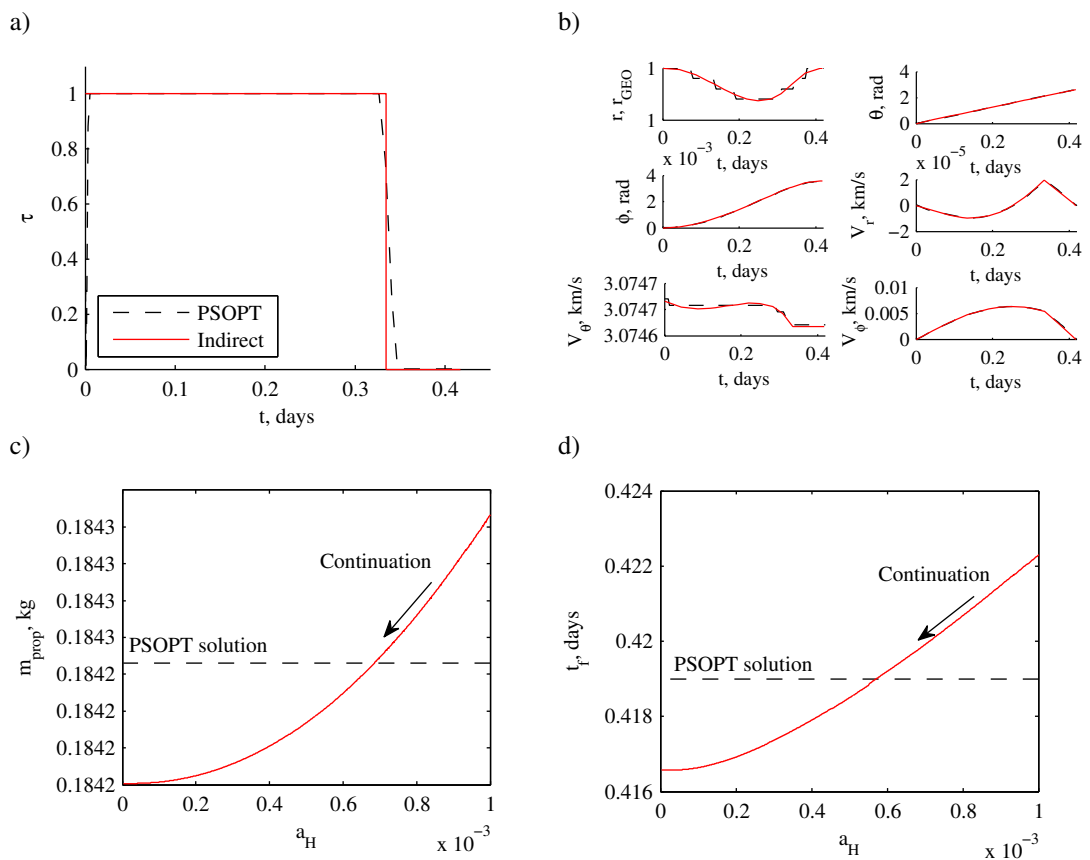
Fig. 4.12 Results of indirect approach for transfer from GEO to a displaced GEO with $h_f = 150$ km. a) Thrust profile. b) States profiles. c-d) Propellant consumption and time of flight as a function of the smooth Heaviside function parameter, a_H.
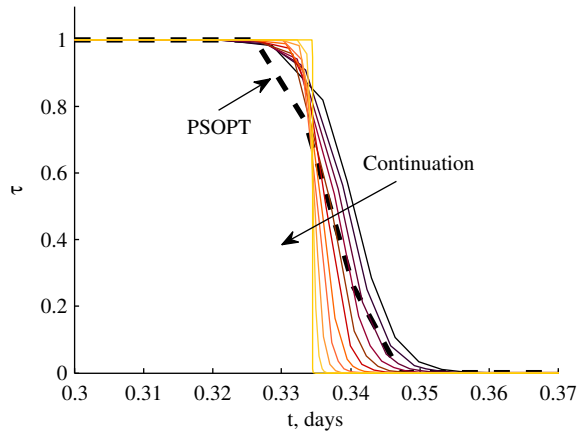
Fig. 4.13 Indirect approach for transfer from GEO to a displaced GEO with h_f = 150 km showing the evolution of the thrust discontinuity throughout the continuation.

4.6.3 Transfer between north and south displaced geostationary orbits

For the transfer between north and south displaced GEOs, the values for the initial and final out-of-plane displacements are $h_0 = -h_f = \pm 35$, 75 or 150 km and $\Delta r = 0$. By merely changing these parameters in the method developed in the previous section, the results in Fig. 4.14 can be obtained for a displacement distance of 150 km.

Figure 4.14a shows that the indirect method transforms the small thrust pulses at the start and end of the transfer into a proper bang-off-bang control. This also results in a slightly smaller propellant consumption than provided by PSOPT as shown in Fig. 4.12c. However, this difference is a negligible 0.2 g and the state profiles and time of flight very closely match the PSOPT result. It can therefore be concluded that also for the north to south transfers, the results of PSOPT are very close to optimal.
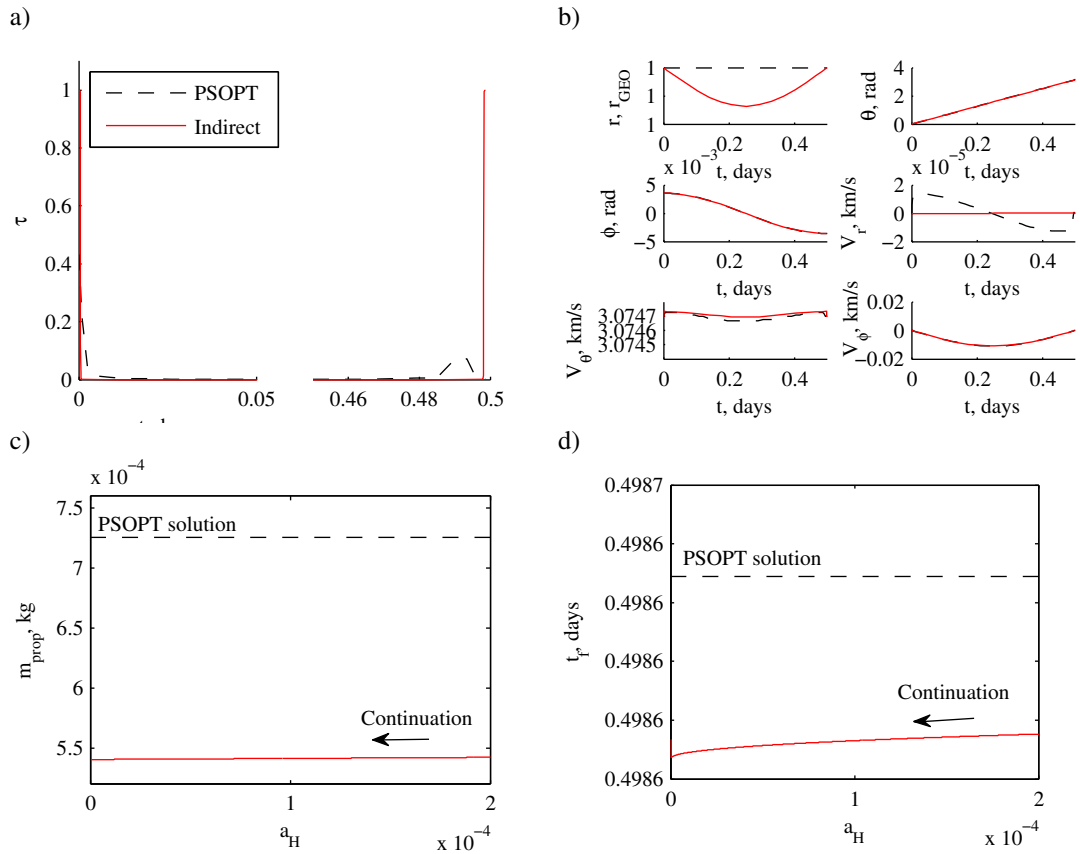
Fig. 4.14 Results of indirect approach for transfer between north and south displaced GEOs with $h_0 = - h_f = 150$ km. a) Thrust profile. b) States profiles. c-d) Propellant consumption and time of flight as a function of the smooth Heaviside function parameter, a_H.

4.6.4 Transfer between displaced geostationary orbit and parking orbit

The final test case that is considered to validate the results from PSOPT is the transfer from the displaced GEO to the equatorial parking orbit for which $h_0 = \pm 35$, 75 or 150 km, $h_f = 0$ km and $\Delta r = |h_0|$. The transfer in the opposite direction (i.e. from parking orbit to displaced GEO) is not considered as it is expected to provide very similar results.

Again, implementing the two-point boundary-value problem derived in Section 4.6.1 provides the results in Fig. 4.15 for a displacement of 150 km and for similar values for the smooth Heaviside function parameter as used in Section 4.6.2. Once more, a very clear match between the solution from PSOPT and the indirect method can be observed, where the indirect method improves the relatively smooth bang-off-bang profile returned by PSOPT. Only a slight difference in the time of flight can be observed, see Fig. 4.15d, which is improved by approximately 30 minutes by the indirect approach. However, the objective

function value found by the indirect method is again very similar to the one obtained by PSOPT and the validity of the result by PSOPT can therefore be confirmed.
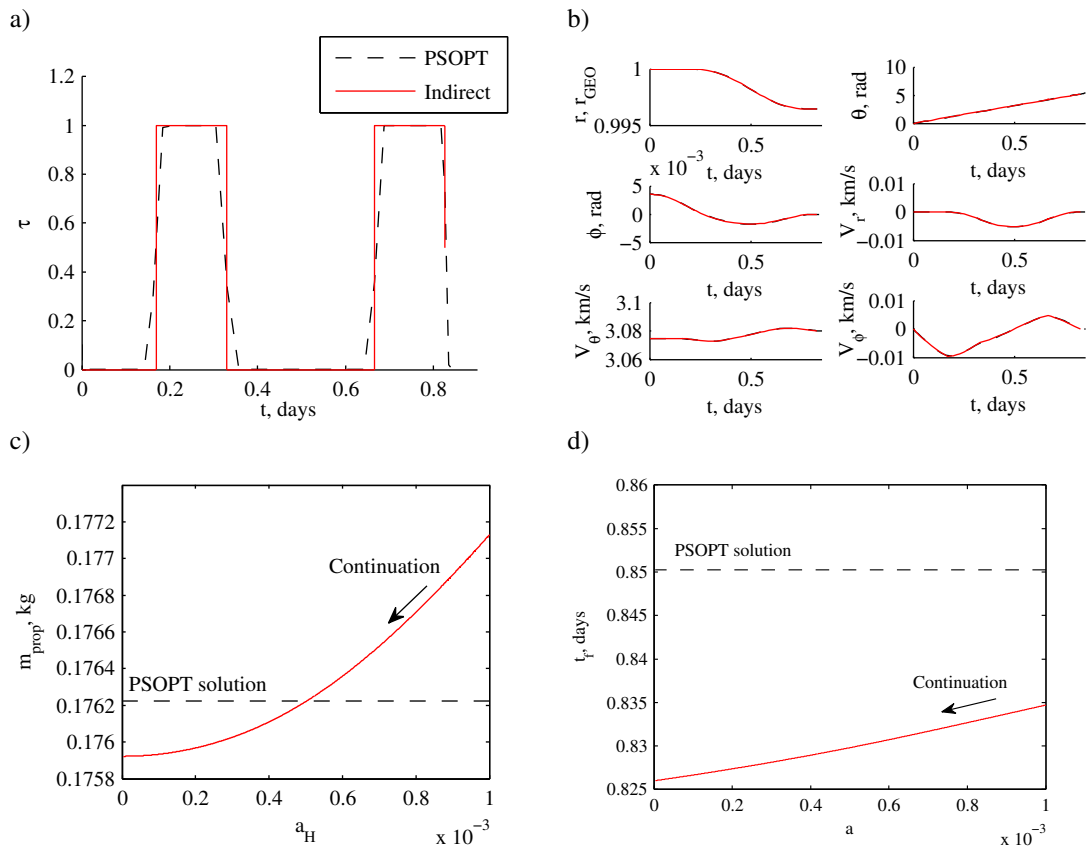
Fig. 4.15 Results of indirect approach for transfer from a displaced GEO with h_0 = 150 km to a parking orbit. a) Thrust profile. b) States profiles. c-d) Propellant consumption and time of flight as a function of the smooth Heaviside function parameter, a_H.

4.7   Chapter summary

This chapter has investigated the optimisation of transfers to the out-of-plane displaced geostationary orbits designed in Chapter 3 in order to evaluate their accessibility. Furthermore, the transfer between geostationary orbits displaced above and below the equatorial plane to take advantage of the seasonally changing Sun-line for hybrid sail propulsion has been investigated as well as the transfer between a displaced geostationary orbit and a Keplerian parking orbit to only provide temporary coverage from the displaced GEO when needed, and relieve the spacecraft when coverage is not required.

For the SEP transfer to the displaced GEO (starting from the nominal GEO), it was shown that only a modest propellant budget is required: between 184.2 and 260.5 gr, depending on the displacement distance considered. Since the initial mass of the spacecraft is far less than

the mass that Ariane 5 can launch into GEO, this propellant budget should be easily available and the displaced GEO can be considered accessible.

The SEP transfer between north and south displaced GEOs was shown to require even less propellant, between 0.66 and 2.6 gr, since there is a near-Keplerian connection between the two displaced GEOs. However, the spacecraft closely passes by the nominal geostationary orbit, which can be avoided through an additional path constraint. This increases the propellant consumption to a maximum of 227 gr for a displacement of 150 km and a minimum approach distance of 35 km. Despite this increase, the propellant savings that the transfer can establish during the mission are significant and easily outweigh the cost of the transfer.

Finally, the SEP transfer to enable temporary services was also shown to require only modest propellant budgets of a few hundred grams, even when a constraint on the approach distance is taken into account. This transfer can thus allow many transfers to and from the displaced GEO, thereby extending the mission lifetime of especially the higher displaced orbits.

Optimising the transfers for the use of hybrid sail propulsion showed significant reductions in propellant consumption. For example, for the transfer from GEO to a 35 km displaced GEO, the propellant consumption even dropped to zero for lightness numbers equal and larger than 0.04, indicating that the transfer can be performed using only the solar sail.

Finally, by optimising each of the transfers using an indirect method, which allows a more accurate modelling of the discontinuity in the bang-off-bang control profiles observed for all three types of transfers, and comparing the results, the optimality of the results was established.

Chapter 5

Optimal Earth to pole-sitter transfers-high-thrust launch

This chapter investigates the design of optimal transfers from Earth to a range of pole-sitter orbits in order to evaluate their accessibility and to allow for a determination of the pole-sitter mission performance in terms of payload capacity and/or mission lifetime. The chapter starts by introducing the concept of the pole-sitter orbit as well as defining a set of particular pole-sitter orbits that have been proposed in the literature. In Section 5.2, the design approach to obtain optimal transfers to these pole-sitter orbits is outlined. This approach divides the transfer into a high-thrust launch phase and a low-thrust transfer phase, which will be discussed in detail in Sections 5.2.1 and 5.2.2, respectively. Note that the high-thrust launch phase is replaced by a low-thrust launch phase in Chapter 6. The optimal control problem that needs to be solved in the low-thrust transfer phase is subsequently discussed in Section 5.3. Then, two methods to generate initial guesses for solving the optimal control problem will be provided in Section 5.4. Subsequently, in Sections 5.5 and 5.6 the results for the use of pure SEP and hybrid sail propulsion will be presented. These results will be validated in Section 5.7 and the chapter finishes with conclusions.

5.1   Pole-sitter orbit

The concept of the pole-sitter orbit was previously defined in Section 1.1.2 as an orbit that allows the spacecraft to be constantly above one of the Earth's poles, stationary with respect to the Earth. For this, it has to track the motion of the polar axis throughout the year by using low-thrust propulsion to counterbalance the gravitational attraction of the Earth and Sun. To

mathematically define the pole-sitter orbit, the motion of the polar axis is considered in the Earth-Sun CR3BP. The equations of motion for a spacecraft in the CR3BP were already provided in Section 2.1.1, but are repeated here for convenience:

$$\ddot{\mathbf{r}} + 2\boldsymbol{\omega} \times \dot{\mathbf{r}} + \nabla U = \mathbf{a} \tag{2.13}$$

For the Earth-Sun CR3BP, the mass ratio equals $\mu = 3.0404 \times 10^{-6}$, where the mass of the smaller body includes both the mass of the Earth and the Moon to approximate the influence of the Moon. Note that the CR3BP is used to demonstrate the feasibility of the pole-sitter concept and that more detailed analyses, taking into account the influence of the real ephemeris of the Earth, are conducted in Reference 141 through the use of a feedback control algorithm.

Due to the obliquity of the ecliptic and the rotation of the reference frame, the Earth's polar axis executes an apparent, clockwise motion, which can be described by a cone in the CR3BP reference frame as depicted in Fig. 5.1, where the nutation of the polar axis and the precession of the equinoxes are neglected. The cone half angle is equal to the obliquity of the ecliptic, $i_{obl} = 23.5°$.

As stated above, the pole-sitter spacecraft needs to track this apparent motion of the polar axis by applying a thrust-induced acceleration. The position, $\mathbf{r}$, and velocity, $\dot{\mathbf{r}}$, of the spacecraft at any time, t, during the year are therefore constrained to be:

$$\mathbf{r} = \begin{bmatrix} d_{PS} \sin i_{obl} \cos \theta + (1-\mu) \\ -d_{PS} \sin i_{obl} \sin \theta \\ d_{PS} \cos i_{obl} \end{bmatrix}, \quad \dot{\mathbf{r}} = \begin{bmatrix} -d_{PS} \sin i_{obl} \sin \theta \\ -d_{PS} \sin i_{obl} \cos \theta \\ 0 \end{bmatrix} \tag{5.1}$$

with d_{PS} the Earth-spacecraft distance and $\theta = \omega t$ the instantaneous angular position of the spacecraft along the pole-sitter orbit with $\theta = 0$ at the winter solstice and $\theta = \pi$ at the summer solstice, see Fig. 5.1.

Then, depending on the constraints imposed on the variation of the distance between the Earth and the spacecraft during the year, three types of pole-sitter orbits can be defined, which will be introduced and discussed in the next three subsections.
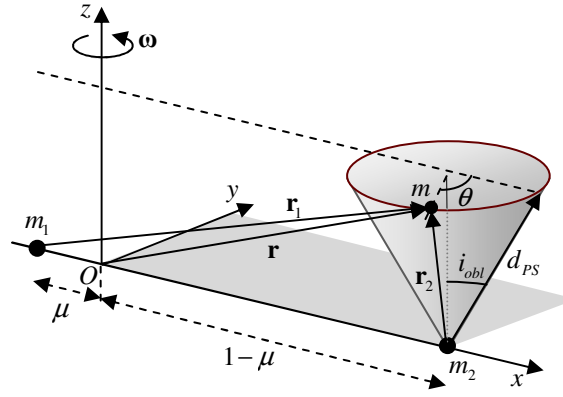
Fig. 5.1 Schematic of pole-sitter orbit in CR3BP reference frame.

5.1.1 Constant altitude pole-sitter orbit

Equation (5.1) and Fig. 5.1 describe a pole-sitter orbit that remains at a constant distance from the Earth, hence the zero velocity in z-direction. In that case, the pole-sitter orbit is referred to as a constant altitude pole-sitter orbit and the variable d_{PS} in Eq. (5.1) is constant. In the literature, a common value for this constant distance is $d_{PS} = 0.01$ AU,[32] which will therefore be used throughout the remainder of this chapter in case a constant altitude pole-sitter orbit is considered. The thrust-induced acceleration required to maintain this pole-sitter orbit is provided by the solid line in Fig. 5.3, which shows that the acceleration is nearly constant throughout the year: its value is minimum at the winter and summer solstices (0.220 mm/s^2) and maximum at the spring and autumn equinoxes (0.240 mm/s^2).

5.1.2 Tilted pole-sitter orbit

Although the assumption of a constant distance between the Earth and the pole-sitter spacecraft allows for a simple analysis of the pole-sitter orbit, this assumption is not required. Moreover, pole-sitter orbits with a varying Earth-spacecraft distance are more fuel optimal than those that remain at a constant distance. Therefore, so-called tilted pole-sitter orbits have been defined in the literature,[32] which follow the following sinusoidal law for the spacecraft-Earth distance:

$$d_{PS}(\theta) = d_{PS,\theta=0} + \left(d_{PS,\theta=\pi} - d_{PS,\theta=0}\right)\frac{1-\cos\theta}{2} \tag{5.2}$$

with $d_{PS,\theta=0}$ and $d_{PS,\theta=\pi}$ the distance from the Earth at the winter and summer solstice, respectively, see Fig. 5.2. When substituting Eq. (5.2) into Eq. (5.1), the position vector of

the spacecraft in the tilted orbit, $\mathbf{r}_{tilted}$, is still given by Eq. (5.1), but the velocity vector denotes:

$$\dot{\mathbf{r}}_{tilted} = \dot{\mathbf{r}} + \frac{1}{2}\left(d_{PS,\theta=\pi} - d_{PS,\theta=0}\right)\sin\theta \begin{bmatrix} \sin i_{obl}\cos\theta \\ -\sin i_{obl}\sin\theta \\ \cos i_{obl} \end{bmatrix} \tag{5.3}$$

In accordance with the work in Reference 32, the following values for the distance at the winter and summer solstices will be considered in this chapter: $d_{PS,\theta=0} = 0.01$ AU and $d_{PS,\theta=\pi} = 0.018$ AU. The thrust-induced acceleration that is needed to maintain this particular type of tilted pole-sitter orbit is added to Fig. 5.3. It shows that the acceleration profile varies much more throughout the year than for the constant altitude-pole-sitter orbit. A clear minimum of 0.146 mm/s^2 exists around the summer solstice when the spacecraft is farther from the Earth, while the maximum acceleration occurs at the winter solstice (0.243 mm/s^2) when the spacecraft is closest to the Earth.
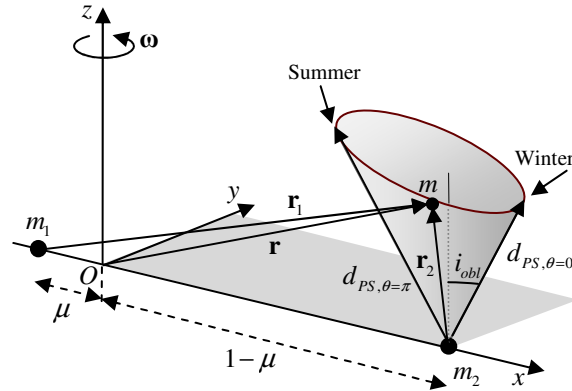
Fig. 5.2 Schematic of tilted pole-sitter orbit in CR3BP reference frame.
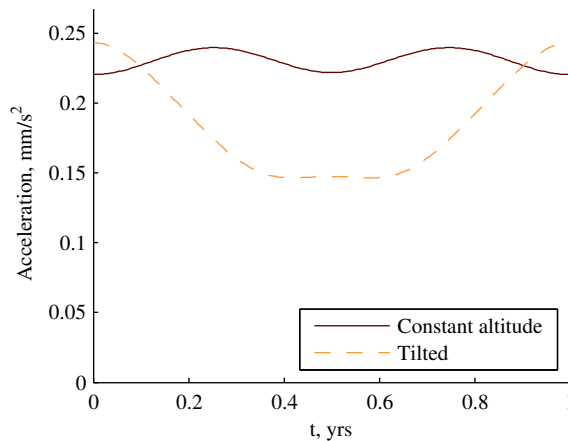
Fig. 5.3 Thrust-induced acceleration profiles to maintain constant and tilted pole-sitter orbits.

114

5.1.3 Optimal pole-sitter orbits

Rather than constraining the Earth-spacecraft distance to be fixed (either at a constant value or according to the sinusoidal law of Eq. (5.2)), it is also possible to leave this distance unconstrained in order to find optimal pole-sitter orbits. Here, optimal is defined as the pole-sitter orbit that minimises the propellant consumption of the spacecraft, while maintaining the pole-sitter condition defined in Eq. (5.1) at all times. To find these optimal orbits, the solution to a constrained optimal control problem needs to be found, which was obtained by Ceriotti and McInnes[32] using PSOPT. Details of this optimisation process are presented in Reference 32. Here, only the results for the pure SEP and hybrid sail cases are provided, see Fig. 5.4, where the hybrid sail case uses a sail lightness number of $\beta_0 = 0.035$. For that particular value of the lightness number it was shown that the spacecraft initial mass, for a given payload, is minimised over a range of mission lifetimes.[133]
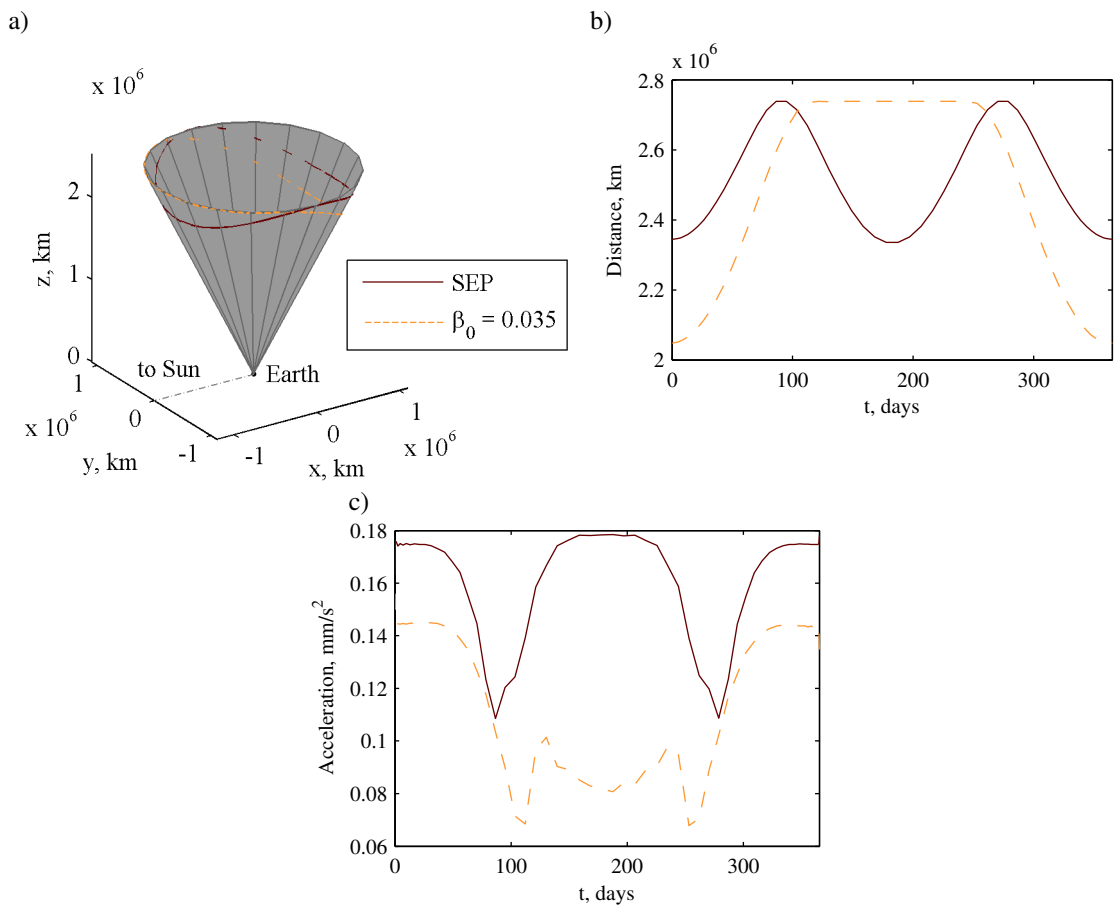
Fig. 5.4 Optimal SEP and hybrid sail pole-sitter orbits. a) Orbits in CR3BP. b) Distance from the Earth as a function of time. c) SEP acceleration as a function of time.[142]

Comparing the optimal SEP and hybrid sail pole-sitter orbits in Fig. 5.4a and Fig. 5.4b shows that the SEP orbit is symmetric around spring and autumn and is closest to the Earth at the

summer and winter solstices. Instead, in the hybrid case, the spacecraft is closest to the Earth in winter and farthest in summer, where a constraint on the maximum distance of 0.01831 AU (approximately 2.74 million km) is active. This constraint was set in order to prevent the trajectory from going too far away from the Earth, thereby excessively decreasing the spatial optical resolution or the data bandwidth of the platform: up to about 3 million km, a resolution of a few kilometres should be possible in the visible and infrared range of the spectrum,[30] enabling the applications noted in Section 1.1.2. Finally, in Fig. 5.4c the SEP acceleration is presented, which clearly shows that the hybrid case requires less acceleration from the SEP thruster throughout the year, due to the contribution of the solar sail.

The optimal pole-sitter orbits as presented in Fig. 5.4 are generated assuming an arbitrary initial mass as the actual initial mass will follow from the design of the Earth to pole-sitter transfers in this thesis. As long as the SEP thrust limit is not active along the optimal pole-sitter orbit, this assumption is valid. Then, the problem is fully scalable on the initial mass and the orbits presented in Fig. 5.4 hold for any initial mass and can be used as test cases for the design of optimal Earth to pole-sitter orbits.

5.1.4 Spacecraft architectures

Equation (2.13) considers a general thrust-induced acceleration, $\mathbf{a}$. However, depending on the type of propulsion employed, this acceleration can be made more explicit. Impulsive, chemical propulsion is considered not to be a viable type of propulsion for the pole-sitter mission and previous research has indicated that pure solar sail pole-sitter orbits do not exist.[32] Previous research[32, 143, 144] has therefore focussed on the use of either pure SEP or hybrid sail propulsion. In the latter case, the thrust-induced acceleration can be split into two components, $\mathbf{a}_{SEP}$ and $\mathbf{a}_s$, due to the SEP system and solar sail, respectively, as was done before during the investigations of hybrid propulsion for maintaining the displaced GEO in Eq. (3.12). The acceleration provided by both propulsion systems are given in Eq. (2.14) and Eq. (2.28), respectively, which shows that the optical sail model is employed in these studies. Clearly, due to the use of solar electric propulsion, the dynamics in Eq. (2.13) need to be augmented with the differential equation describing the mass flow in Eq. (2.15).

5.2   Transfer design approach

The challenge that immediately arises when designing a low-thrust transfer such as the Earth to pole-sitter transfer is the fact that, to reach the pole-sitter position from LEO, the spacecraft has to increase its orbit radius by a factor 200. For the use of low-thrust propulsion, the result will be a long duration spiral trajectory with hundreds or even thousands of orbital revolutions and transfer times in the order of months to years.[145] When using a direct method such as PSOPT for the trajectory optimisation, this poses a severe challenge as the optimal control problem becomes complex. To deal with this issue, the pole-sitter transfer is modelled by distinguishing between a launch phase and a transfer phase, see Fig. 5.5: the launch phase is modelled in a two-body approximation and is performed by the launch vehicle upper-stage that brings the spacecraft from a fixed inclination, low Earth parking orbit up to insertion into the transfer phase. The transfer phase is subsequently modelled in the Earth-Sun three-body problem and is performed using the on-board low-thrust propulsion system (i.e. either pure SEP or hybrid sail propulsion). The two phases are linked by requiring that the upper-stage launches the spacecraft into a two-body elliptic Keplerian orbit (marking the end of the launch phase) that coincides with the initial state vector of the transfer phase (marking the start of the transfer phase). The two-body elliptic Keplerian orbit will hereafter be referred to as the launch phase target orbit. In the following two subsections, both phases will be discussed in more detail.
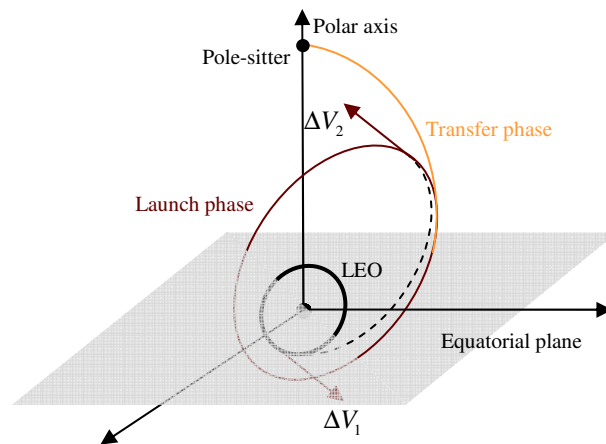
Fig. 5.5 Schematic of launch and transfer phases.

117

5.2.1 Launch phase

As stated in the introduction of this section, the launch phase is modelled in the two-body problem, rather than in the CR3BP used for the pole-sitter orbit in Section 5.1, because the spacecraft is relatively close to the Earth during that part of the transfer. Before providing the model used to describe this launch phase, it is noted that the objective is not to provide a detailed and optimal launch strategy, but a simple, though reliable, method to assess the relative efficiency of different transfer trajectories. This implies among others that only non-escape launches are considered, i.e. the eccentricity upon insertion into the transfer phase is constrained to be less than unity.

To perform the launch phase, the use of two different types of launchers will be considered, namely the Soyuz and Ariane 5 launch vehicles, both of the European Space Agency.

Soyuz launch vehicle

To model the launch phase for the Soyuz launch vehicle, Reference 139 is used, which provides the Soyuz performance through a set of reference missions, assuming a launch from Baikonur (45.6°N, 63.3°E). Due to ground-path safety rules and authorised drop-zone locations for expended stages, the first three stages can be launched into four launch azimuths, resulting in four initial parking orbit planes, see Table 5.1. Any remaining inclination changes can be provided by the Fregat upper-stage.

Table 5.1 Authorised launch azimuths and corresponding reference orbit inclinations for a Soyuz launch from Baikonur.[139]

Launch azimuth, deg	Reference orbit inclination, deg
60.7	51.8
34.8	64.9
25.9	70.4
-10.9	95.4

Reference 139 describes a typical non-escape Soyuz launch flight profile as follows: first, the three lower stages and the Fregat upper-stage are used to reach a low Earth parking orbit with an altitude of h_{park} = 200 km and one of four reference inclinations as provided in Table 5.2. Then, a first Fregat burn will put the payload on an intermediate transfer orbit with apogee altitude equal to the final orbit altitude and perigee altitude equal to 200 km. During this burn, the Fregat upper-stage can also provide a small change of inclination as needed. Finally, after coasting up to apogee of the intermediate transfer orbit, a second

Fregat burn raises the perigee and any remaining inclination change is carried out after which the spacecraft separates from the Fregat upper-stage. This description suggests that the Soyuz Fregat upper-stage approximates a two-body Hohmann transfer from a low Earth, 200 km circular parking orbit (hereafter simply referred to as 'parking orbit') to the final target orbit, where any inclination change is distributed over the first (apogee raise) Fregat burn, ΔV_1, and second (perigee raise) Fregat burn, ΔV_2, see also Fig. 5.5.

When applying this approach to launch a spacecraft into a general elliptical target orbit with inclination i_{target} and apogee and perigee altitudes h_{apo} and h_{peri}, the following Fregat burns are required:

$$\Delta V_1 = \sqrt{\frac{\mu_\oplus}{R_\oplus + h_{park}}} \sqrt{2 + e_t - 2\sqrt{1 + e_t} \cos\left(f_{\Delta i} \Delta i\right)} \tag{5.4}$$

$$\Delta V_2 = \sqrt{\frac{\mu_\oplus}{R_\oplus + h_{apo}}} \sqrt{2 - e_t - e_{target} - 2\sqrt{1 - e_t}\sqrt{1 - e_{target}} \cos\left(\left(1 - f_{\Delta i}\right)\Delta i\right)} \tag{5.5}$$

where $f_{\Delta i}$ is the fraction of the total inclination change $\Delta i = i_{target} - i_{park}$ provided during the first burn, with $0 \le f_{\Delta i} \le 1$. Note that these equations assume that the perigee and apogee of the target orbit coincide with the line of nodes. Furthermore, the eccentricity of the intermediate transfer orbit, e_t, is given by:

$$e_t = \frac{h_{apo} - h_{park}}{2R_\oplus + h_{apo} + h_{park}} \tag{5.6}$$

while the eccentricity of the target orbit, e_{target}, equals:

$$e_{target} = \frac{h_{apo} - h_{peri}}{2R_\oplus + h_{apo} + h_{peri}} \tag{5.7}$$

Finally, using the rocket equation, the mass that can be injected into the target orbit (i.e. the spacecraft mass plus adapter/dispenser mass of 100 kg)[139] can be determined from:

$$m_{target} = m_{park,\max} \exp\left[-\Delta V_{tot} / \left(I_{sp_F} g_0\right)\right] - m_F \tag{5.8}$$

with $\Delta V_{tot} = \Delta V_1 + \Delta V_2$, $I_{sp_F} = 330$ s the specific impulse of the Fregat upper-stage,[139] $m_F = 1000$ kg the mass of the Fregat upper-stage[139] and $m_{park,\max}$ the maximum mass in the parking orbit. This maximum parking orbit mass includes the mass of the Fregat upper-stage,

the adapter and the spacecraft and is obtained from extrapolating data in Reference 139 and is presented in Table 5.2.

Table 5.2 Soyuz launch vehicle performance in 200 km circular parking orbit.

Parking orbit inclination, deg	Maximum mass (Fregat + adapter + spacecraft) in parking orbit, kg
51.8	7185
64.9	6449
70.4	6294
95.4	6275

A validation of this approach is provided through the graphs in Fig. 5.6, which show the maximum mass (spacecraft + adapter) that can be launched into a circular (Fig. 5.6a) or elliptical (Fig. 5.6b-c) target orbit and the penalty on the launch performance when an inclination change needs to be performed (Fig. 5.6d). The lines indicate the performance as provided by Reference 139, while the round markers indicate the performance according to the model in Eqs. (5.4) to (5.8). Note that the best fit for Fig. 5.6d to the data in Reference 139 was found for $f_{\Delta i} = 0.15$. From the close resemblance between the two data sets in Fig. 5.6 it can be concluded that the launch model in Eqs. (5.4) to (5.8) is a good approximation of the Soyuz launch performance and can therefore be applied in the design and optimisation of the pole-sitter transfer.

As noted above, the launch model described in Eqs. (5.4) and (5.5) only holds for the case when the perigee and apogee of the final target orbit coincide with the line of nodes. It also holds when the final target orbit is circular or if the parking orbit and final target orbit are co-planar. However, for other cases, the model may provide a very good estimate of the launch vehicle's performance when only small inclination changes are required.

However, in case neither of these criteria hold, the model described in Eqs. (5.4) and (5.5) is inaccurate as it will significantly underestimate the ΔV required for the inclination change. In that case, a second model is adopted, which assumes that the orbital altitude of the parking orbit is first raised to the perigee and apogee of the final target orbit through a Hohmann transfer, after which an inclination change is executed to change the inclination of the intermediate orbit (which equals the inclination of the parking orbit) to the inclination of the final target orbit. This inclination change takes place at the ascending or descending node of the final target orbit, depending on where the orbital velocity is smallest. This approach requires three ΔV manoeuvres, given by:

$$\Delta V_1 = \sqrt{\frac{\mu_\oplus}{R_\oplus + h_{park}}} \sqrt{1 + \sqrt{1 + e_t}} \tag{5.9}$$

$$\Delta V_2 = \sqrt{\frac{\mu_\oplus}{R_\oplus + h_{apo}}} \sqrt{\sqrt{1 - e_t} - \sqrt{1 - e_{target}}} \tag{5.10}$$

$$\Delta V_3 = \left| \mathbf{V}_{A,int} - \mathbf{V}_{A,target} \right| \quad \vee \quad \Delta V_3 = \left| \mathbf{V}_{D,int} - \mathbf{V}_{D,target} \right| \tag{5.11}$$

with the subscript 'int' indicating the conditions in the intermediate orbit and the subscripts 'A' and 'D' representing the ascending and descending nodes, respectively.
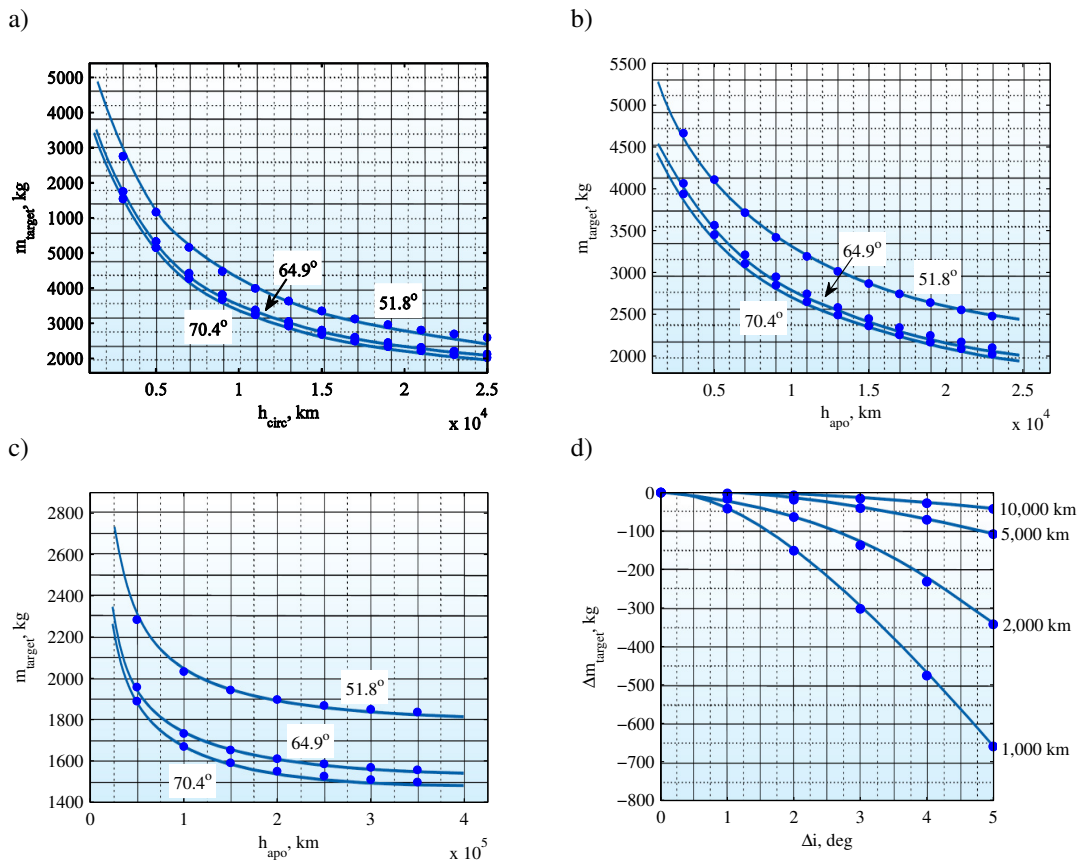
Fig. 5.6 Comparison of launch vehicle performance (spacecraft + adapter mass) from model (round markers) and from Reference 139 (solid lines) for (a) circular orbits and (b-c) elliptical orbits with a perigee altitude of 200 km for different inclinations of the initial parking orbit. (d) Penalty for an inclination change from a 51.8° circular orbit with different altitudes.

Ariane launch

For comparison purposes and also because less detailed information is available in the literature for the performance of the Ariane 5 launch vehicle, it is assumed that a similar launch strategy (either Eqs. (5.4)-(5.5) or Eqs. (5.9)-(5.11)) can be adopted for the cryogenic upper-stage (ESC-A) of Ariane 5. However, rather than assuming a 200 km altitude circular parking orbit, the parking orbit is assumed to be equal to the orbit of the International Space Station (400 km altitude and 51.6° inclination), for which it is given that Ariane 5 can deliver 19 tonnes.[138] Other details of the Ariane 5 upper-stage are provided in Table 5.3.

Table 5.3 Soyuz and Ariane 5 parking orbit and launch vehicle specifications.

Launcher	Parking orbit			Upper-stage		Adapter
	Altitude, km	Inclination, deg	Performance,[1] kg	Mass, kg	Specific impulse, s	Mass, kg
Soyuz	200	51.8 64.9 70.4 95.4	7185 6449 6294 6275	1000	330	100
Ariane 5	400	51.6	19000	4540	446	160

5.2.2 Transfer phase

As depicted in Fig. 5.5, the transfer phase starts from the launch phase target orbit up to insertion into the pole-sitter orbit. The initial condition of the transfer phase is therefore defined by the Keplerian elements of the launch phase target orbit, while the final condition satisfies Eqs. (5.1). While the launch phase is described using a two-body model, the transfer phase is modelled in the CR3BP using the equations of motion in Eq. (2.13) together with the differential equation for the mass in Eq. (2.15), where the thrust-induced acceleration depends on the type of propulsion system used, i.e. Eq. (2.14) for the use of pure SEP and Eq. (2.28) for the use of hybrid sail propulsion.

5.3   Optimal control problem

The overall objective is to find optimal trajectories from the low-Earth parking orbit (see Table 5.3) to the three types of pole-sitter orbits defined in Section 5.1. In this chapter, two different definitions of 'optimal' are considered:

---

[1] Including upper-stage and adapter mass.

- Case 1: Minimising the mass in the parking orbit, m_{park}, for a given mass injected into the pole-sitter orbit in order to minimise launch mass and therefore overall mission cost.
- Case 2: Maximise the spacecraft mass injected into the pole-sitter orbit, i.e. the mass at the end of the trajectory, m_f, by making full use of the launch vehicle performance into LEO (see Table 5.3) in order to maximise the payload mass and/or mission lifetime.

For both objectives the optimal control problem in the transfer phase needs to be solved, while linking the launch phase to the start of the transfer phase in the objective function (for optimisation case 1) or in an event constraint (for optimisation case 2). More specific details on the objective function and event constraints will be provided in Sections 5.3.1 and 5.3.2 for cases 1 and 2, respectively, as these are case-dependent. However, the other elements of the optimal control problem (as defined in Section 2.3.1) are similar for both cases and will therefore be discussed hereafter.

The state vector in the transfer phase is given by the Cartesian position and velocity vectors in the CR3BP reference frame of Fig. 2.3 and the mass of the spacecraft:

$$\mathbf{x} = \begin{bmatrix} x & y & z & \dot{x} & \dot{y} & \dot{z} & m \end{bmatrix}^T \tag{5.12}$$

while the controls, $\mathbf{u}$, are the Cartesian SEP thrust components and the solar sail normal components (in case of hybrid propulsion) in the CR3BP reference frame:

$$\mathbf{u} = \begin{cases} \begin{bmatrix} T_x & T_y & T_z \end{bmatrix}^T & \text{SEP} \\ \begin{bmatrix} T_x & T_y & T_z & n_x & n_y & n_z \end{bmatrix}^T & \text{Hybrid} \end{cases} \tag{5.13}$$

Again, as noted in Section 4.1, the Cartesian thrust components are used rather than two thrust angles and the thrust magnitude as these may give rise to ambiguities.[99] The dynamics of the spacecraft have been defined before by Eqs. (2.13), (2.14) (SEP acceleration), (2.28) (solar sail acceleration) and (2.15) (mass consumption).

Furthermore, bounds on the state and control variables can be defined as well as on the time of flight:

$$\begin{aligned} \mathbf{x}_l &= [(1-\mu)-0.01 \quad -0.01 \quad -0.02 \quad -0.1 \quad -0.1 \quad -0.1 \quad 0]^T \\ \mathbf{x}_u &= [(1-\mu)+0.01 \quad 0.01 \quad 0.02 \quad 0.1 \quad 0.1 \quad 0.1 \quad m_{park,\max}]^T \end{aligned} \tag{5.14}$$

$$\mathbf{u}_l = -\mathbf{u}_u = \begin{cases} [-T_{\max} \quad -T_{\max} \quad -T_{\max}]^T & \text{SEP} \\ [-T_{\max} \quad -T_{\max} \quad -T_{\max} \quad -1 \quad -1 \quad -1]^T & \text{Hybrid} \end{cases} \tag{5.15}$$

$$-3\pi \leq t_0 \leq \pi$$
$$-\pi \leq t_f \leq \pi$$

<div align="right">(5.16)</div>

Equation (5.16) shows that the final time is free (i.e. injection into the pole-sitter orbit at any time during the year is allowed, which spans from $-\pi$ to π), but that the maximum transfer time cannot exceed 2 years. Furthermore, note that the determination of the maximum thrust magnitude in the transfer, $T_{\max}$, in Eq. (5.15) also depends on the optimisation case, as will be discussed in Sections 5.3.1 and 5.3.2.

Finally, the following path constraints have to be considered, similar to the path constraints defined in Eqs. (4.6) to (4.8) for the displaced GEO transfers, again depending on the type of propulsion system employed:

$$\mathbf{c}\left(\mathbf{x}(t),\mathbf{u}(t),t\right) = \begin{cases} \sqrt{T_x\left(t\right)^2 + T_y\left(t\right)^2 + T_z\left(t\right)^2} \leq T_{\max} & \text{SEP/Hybrid} \\ \sqrt{n_x\left(t\right)^2 + n_y\left(t\right)^2 + n_z\left(t\right)^2} = 1 \\ \hat{\mathbf{r}}_1\left(t\right)\cdot\hat{\mathbf{n}}(t) \geq 0 \end{cases} \quad \text{Hybrid}$$

<div align="right">(5.17)</div>

5.3.1   Linking launch and transfer phases - Case 1

For the first type of objective function, where the mass in the parking orbit is minimised for a given mass injected into the pole-sitter orbit to minimise overall mission cost, the objective function is:

$$J = m_{park}$$

<div align="right">(5.18)</div>

In order to compute this objective function, the start of the transfer phase is linked to the launch phase by converting the initial state vector of the transfer phase from the CR3BP reference frame in Fig. 2.3 to the inertial, Earth fixed, equatorial reference frame $EQ\left(x_{EQ}, y_{EQ}, z_{EQ}\right)$ shown in Fig. 5.7 and subsequently transforming it to Keplerian elements. This transformation thus links the three-body transfer phase with the two-body launch phase and the actual true anomaly in the Keplerian orbit corresponding to the initial state vector in the three body problem is not of importance. Subsequently, using Eqs. (5.4) to (5.8), the mass required to be launched into the parking orbit, m_{park}, can be computed and used as performance indicator.

However, in doing so, it must be kept in mind that the launch model in Eqs. (5.4) to (5.8) cannot consider escape launches. Therefore, in case the start of the transfer phase

corresponds to an eccentricity larger than unity, a transformation is applied to reduce this eccentricity below 1 in order to be able to compute an objective function value. Another transformation is subsequently applied to penalise this objective function value such that the transfer is discarded in the optimisation process. The two transformations that are employed are illustrated in Fig. 5.8. For the transformation of the eccentricity the following step function is used:

$$e_{trans} = H_1 (e_{max} - e) + e \tag{5.19}$$

with e the original eccentricity, e_{trans} the transformed eccentricity and H_1 a smooth Heaviside function defined as:

$$H_1 = \frac{1}{2} \left(1 + \tanh \left(\frac{e - e_{max}}{a_H} \right) \right) \tag{5.20}$$

with $e_{max} = 0.995$ and $a_H = 0.001$. Note that the *smooth* Heaviside function is used rather than a discontinuous step function in order to prevent non-differentiable points in the objective function when solving the optimal control problem.

Then, to penalise the objective function value, Eq. (5.18) is modified into:

$$J = f_{penalty} m_{park} \tag{5.21}$$

with

$$f_{penalty} = \left(f_{penalty,max} - 1 \right) H_1 + 1 \tag{5.22}$$

and $f_{penalty,max} = 100$.

Note that a transformation is adopted rather than a simple constraint because, while the final solution of PSOPT will satisfy this constraint, intermediate calculations may not and problems will therefore occur when computing the objective function.

The event constraints for this type of objective function can be defined as follows:

$$\boldsymbol{\phi}_0 \left(\mathbf{x}(t_0), \mathbf{u}(t_0), \mathbf{p}, t_0 \right) = \begin{cases} e_{max} - e_0 \geq 0 \\ a_0 (1 - e_0) - r_{peri,min} \geq 0 \\ a_{0,max} - a_0 \geq 0 \end{cases} \tag{5.23}$$

$$\boldsymbol{\phi}_f \left(\mathbf{x}(t_f), \mathbf{u}(t_f), \mathbf{p}, t_f \right) = \begin{cases} \mathbf{x}_{PS}(t_f) - \mathbf{x}_f = \mathbf{0} \\ m_{mission,0} - m_f = 0 \end{cases} \tag{5.24}$$

with a_0 and e_0 the semi-major axis and eccentricity of the Keplerian orbit corresponding to the initial state vector of the low-thrust transfer phase, i.e. the launch phase target orbit.
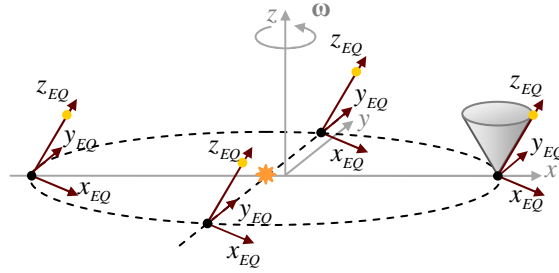
Fig. 5.7 Pole-sitter in CR3BP reference frame (gray) and in inertial, Earth fixed, equatorial reference frame (coloured).
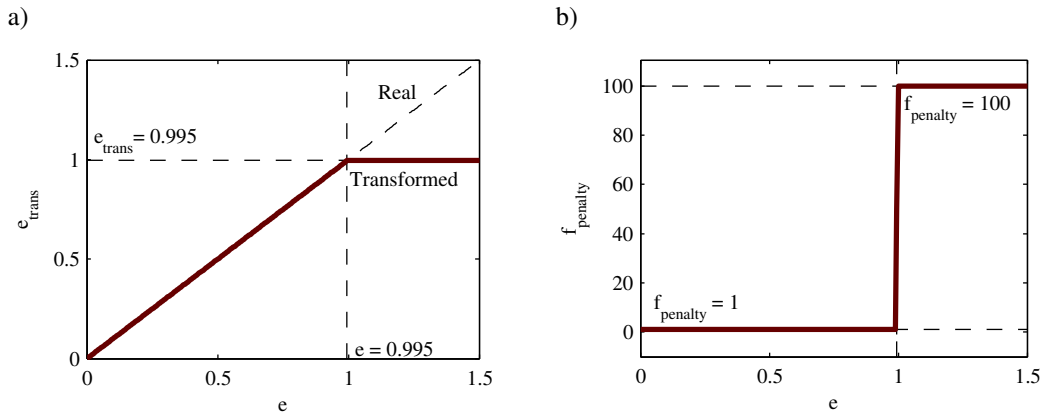
Fig. 5.8 Transformed eccentricity (a) and corresponding penalty on objective function (b) to enable use of launch model for escape orbits.

Although the penalty on the objective function should already guide the final optimal solution to an eccentricity smaller than 1, the first event in Eq. (5.23) is included to ensure this by setting $e_{max} = 0.995$. The second event in Eq. (5.23) is included to prevent numerical problems with automatic differentiation in PSOPT. The numerical difficulties arise when the perigee of the launch phase target orbit coincides with the parking orbit. Then, the second Fregat burn, ΔV_2 in Eq. (5.5), becomes zero, its derivative infinite and the optimal control solver exits with an error. The second constraint in Eq. (5.23) thus ensures that the perigee of the launch phase target orbit and the parking orbit do not coincide by setting a minimum perigee radius, $r_{peri,min}$, that is 50 km above the parking orbit.

The final constraint in Eq. (5.23) has to be included due to the two-body approximation used for the launch phase model. The larger the launch phase target orbit, the farther the spacecraft is from the Earth in the launch phase, the less accurate the two-body launch phase

model is. Therefore, a constraint is included to ensure that the semi-major axis of the launch phase target orbit does not exceed a particular maximum value, $a_{0,max}$, which is set to $a_{0,max} = 500,000$ km.

The event constraint on the final state vector in Eq. (5.24) makes sure that the state vector of the spacecraft at the final time, t_f, corresponds to the pole-sitter position, $\mathbf{x}_{PS}$, at that time (see for example Eq. (5.1) for the constant altitude pole-sitter orbit). Finally, since this case considered the minimisation of the mass in the parking orbit for a given mass injected into the pole-sitter orbit, $m_{mission,0}$, the final constraint in Eq. (5.24) ensures that the mass at the end of the low-thrust transfer indeed equals $m_{mission,0}$, which is set to a value of 1000 kg.[32]

With the mass at the end of the transfer known, the maximum thrust magnitude, T_{max}, can also be determined. For this, a conservative approach is adopted by assuming that the spacecraft is inserted at the location in the pole-sitter orbit where the maximum acceleration is required. Then, the spacecraft is sure to be able to provide the required thrust levels throughout the pole-sitter mission. The values of this maximum acceleration as well as the maximum thrust magnitude to be used for optimisation case 1 are provided in Table 5.4.

Table 5.4 Maximum acceleration for each type of pole-sitter orbit and maximum thrust magnitude in low-thrust transfer phase for optimisation case 1.

Pole-sitter type	Maximum acceleration, mm/s^2	Maximum thrust magnitude, N
Constant	0.240	0.240
Tilted	0.243	0.243
SEP optimal	0.175	0.175
Hybrid optimal	0.145	0.145

5.3.2 Linking launch and transfer phases – Case 2

For the second type of objective, i.e. maximising the mass injected into the pole-sitter orbit in order to maximise the payload mass and/or mission lifetime, the objective function is:

$$J = -\frac{1}{f_{penalty}} m_f \tag{5.25}$$

with m_f the mass at the end of the low-thrust transfer phase. Equation (5.25) shows that again a penalty on the objective function is introduced when the eccentricity at the start of

the transfer phase is larger than 1. Although this eccentricity is not required to compute m_f, it is required to compute one of the event constraints, which are defined as:

$$\boldsymbol{\phi}_0 \left(\mathbf{x}(t_0), \mathbf{u}(t_0), \mathbf{p}, t_0 \right) = \begin{cases} e_{\max} - e_0 \geq 0 \\ a_0 (1 - e_0) - r_{peri,\min} \geq 0 \\ a_{0,\max} - a_0 \geq 0 \\ m_{park,\max} - m_{park} \geq 0 \end{cases} \qquad (5.26)$$

$$\boldsymbol{\phi}_f \left(\mathbf{x}(t_f), \mathbf{u}(t_f), \mathbf{p}, t_f \right) = \mathbf{x}_{PS}(t_f) - \mathbf{x}_f = \mathbf{0} \qquad (5.27)$$

Because the mass injected into the pole-sitter is optimised, the second event constraint in Eq. (5.24) cancels, while a constraint is added to those in Eq. (5.23). This new constraint concerns the mass required in the parking orbit, m_{park}, to insert the (to be optimised) mass into the pole-sitter orbit, which cannot exceed the launcher performance, $m_{park,\max}$, see Table 5.3. This mass is computed in exactly the same way as computing the objective function for optimisation case 1 in Section 5.3.1, i.e. including a transformation of the eccentricity in case an escape trajectory is considered and the subsequent penalty on the objective function in case the eccentricity is indeed larger than 1.

Note that, comparing the objective functions and event constraints for both optimisation case 1 in Section 5.3.1 and optimisation case 2 in this section, shows that the objective function of case 1 is transformed into an event constraint for case 2, while the objective function of case 2 is an event constraint in case 1.

Finally, since the mass upon injection is not known a priori, the maximum thrust magnitude cannot be determined in the way as was done for case 1. Instead, an iterative approach is applied by assuming an initial value for the maximum thrust magnitude, computing the maximised injected mass and updating the thrust magnitude accordingly. This new thrust magnitude is obtained by multiplying the maximum acceleration in the pole-sitter orbit by the injected mass. A new optimisation is run with the updated maximum thrust magnitude and this is repeated until the maximum thrust magnitude converges.

5.4 Initial guess

The optimal control problem defined in the previous section will be solved using PSOPT for which an initial guess of the transfer to the pole-sitter orbit is required in order to initiate the

optimisation. In this section, two types of initial guesses will be considered in order to test a newly developed shape-based approach (see Section 5.4.1) and to show the ability of PSOPT to converge to the same solution for different initial guesses. The second type of initial guess, that exploits manifold-like trajectories that wind onto the pole-sitter orbit, will be discussed in Section 5.4.2.

Note that this section only considers the search for initial guesses for pure SEP transfers as the initial guess for the hybrid transfers will be the optimised SEP transfers.

5.4.1 Expo-elliptic shape-based approach

The simplicity of the exponential sinusoidal (exposin) shape, see Section 2.3.5, allows a quick implementation and has therefore been considered for generating the initial guess for the transfer to the pole-sitter orbits. For this, the pole-sitter orbits are approximated by a highly elliptic orbit where the perigee radius, $r_{PS,peri}$, coincides with the parking orbits defined in Table 5.3 and the apogee radius, $r_{PS,apo}$, coincides with the pole-sitter at the winter solstice (i.e. the point closest to the Earth for the tilted and optimal pole-sitter orbits). This is illustrated in Fig. 5.9 for one particular example (the optimal SEP pole-sitter orbit of Fig. 5.4). The semi-major axis and eccentricity of these approximated pole-sitter orbits are then given through:

$$a_{PS} = \frac{r_{PS,peri} + r_{PS,apo}}{2}, \qquad e_{PS} = \frac{r_{PS,apo} - r_{PS,peri}}{r_{PS,apo} + r_{PS,peri}} \tag{5.28}$$

with the subscript 'PS' indicating the conditions in the approximated pole-sitter orbit. Furthermore, the parking orbit is assumed to lie in the same plane as the approximated pole-sitter orbit, as the exposin shape can only consider two dimensional transfers.

From initial investigations it appeared that the ΔV-impulses to be given in order to insert the spacecraft into the exposin transfer orbit and into the approximated pole-sitter orbit were significant and did not allow PSOPT to converge to an optimal solution. This thesis therefore proposes an improvement of the exponential sinusoids by replacing the sinusoid in the shape function by the Jacobi elliptic function $\text{sn}(t,k)$. This introduces the modulus, k, of the elliptic function as an additional free parameter, while for setting $k = 0$ the function degenerates to $\sin(t)$ and the exponential of the elliptic function reduces to the exposin shape. In other words this new shape, coined here as the expo-elliptic shape, generalises the exponential sinusoids.
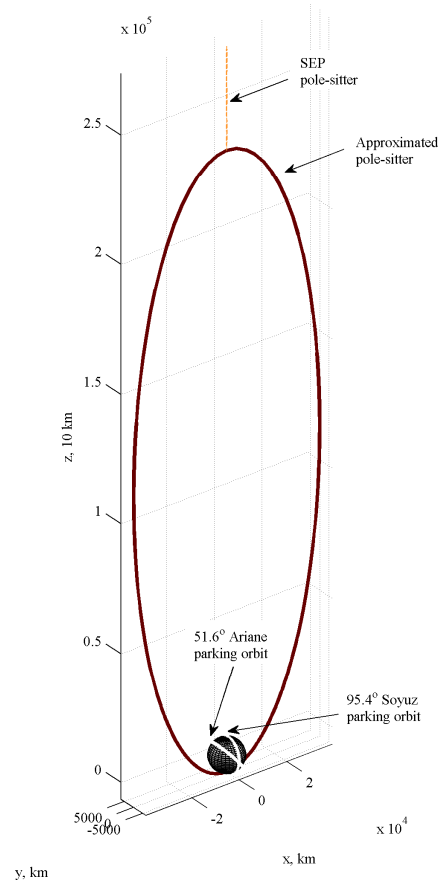
Fig. 5.9 Approximated SEP pole-sitter orbit.

Replacing the sinusoid in Eq. (2.82) by the Jacobi elliptic function gives:

$$r = k_0 \exp\left[k_1 \operatorname{sn}\left(k_2 \theta + \phi, k \right) \right] \tag{5.29}$$

The Jacobi elliptic functions $\operatorname{sn}(t,k)$, $\operatorname{cn}(t,k)$ and $\operatorname{dn}(t,k)$ are defined as the solutions of the following system of differential equations:[146, 147]

$$\begin{aligned}
\dot{x} &= yz \\
\dot{y} &= -zx \\
\dot{z} &= -k^2 xy
\end{aligned} \tag{5.30}$$

with initial conditions $\operatorname{sn}(0,k) = x(0) = 0$, $\operatorname{cn}(0,k) = y(0) = 1$ and $\operatorname{dn}(0,k) = z(0) = 1$. The parameter k is the modulus of the Jacobi elliptic functions and satisfies $0 < k < 1$. When k approaches 0 from the right, $\operatorname{sn}(t,k) \to \sin(t)$, while when k approaches 1 from the left,

130

$\operatorname{sn}(t,k) \to \tanh(t)$.[146] Therefore, as indicated previously, the expo-elliptic shape contains the exponential sinusoidal shape as for $k \to 0$, Eq. (5.29) tends to Eq. (2.82).

To illustrate the effect of the modulus on the trajectory shape, Fig. 5.10 shows the trajectories that can be obtained by varying the value for k while keeping the other shape parameters fixed. The figure shows that a whole new family of shapes originates from the single exposin shape
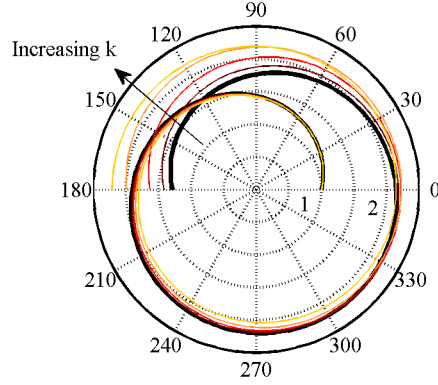
Fig. 5.10 Influence of elliptic modulus k, set between 0.1 and 0.9, on expo-elliptic shape with k_0 $= k_1 = 1$, $k_2 = 0.3$ and $\phi = 0$. The thick black line is the corresponding exposin shape, i.e. $k = 0$.

As for the exponential sinusoids, also for the expo-elliptic shape the angular rate and normalised thrust histories can be derived analytically under the assumption of tangential thrust:

$$\dot{\theta}^2 = \left(\frac{\mu_C}{r^3}\right)\frac{1}{\tan^2 \gamma + k_1 k_2^2 \operatorname{sn}(\operatorname{dn}^2 + k^2 \operatorname{cn}^2) + 1} \tag{5.31}$$

$$a = \frac{\tan\gamma}{2\cos\gamma}\left(\frac{1}{\tan^2 \gamma + k_1 k_2^2 \operatorname{sn}(\operatorname{dn}^2 + k^2 \operatorname{cn}^2) + 1} - \frac{k_2^2\left((1-2k_1\operatorname{sn})(\operatorname{dn}^2 + k^2 \operatorname{cn}^2) - 4k^2 \operatorname{sn}^2\right)}{\left(\tan^2 \gamma + k_1 k_2^2 \operatorname{sn}(\operatorname{dn}^2 + k^2 \operatorname{cn}^2) + 1\right)^2}\right) \tag{5.32}$$

$$\tan\gamma = k_1 k_2 \operatorname{cn} \cdot \operatorname{dn} \tag{5.33}$$

With sn, cn and dn the abbreviations for $\operatorname{sn}(k_2\theta + \phi, k)$, $\operatorname{cn}(k_2\theta + \phi, k)$ and $\operatorname{dn}(k_2\theta + \phi, k)$, respectively.

The condition to ensure the feasibility of the expo-elliptic shape around apoapsis and periapsis (as provided in Eq. (2.87) for the exposin shape) can be written as

$\left|k_1 k_2^2 \, \mathrm{dn}\left(K,k\right)^2\right| < 1$. Here, K is used to indicate the periodicity of the Jacobi elliptic functions, where $\mathrm{sn}\left(t,k\right)$ and $\mathrm{cn}\left(t,k\right)$ are $4K$ periodic in t and $\mathrm{dn}\left(t,k\right)$ is $2K$ periodic in t, and can be computed using:

$$K = \int_0^{\pi/2} \frac{du}{\sqrt{1-k^2 \sin^2 u}} \tag{5.34}$$

The issue is, however, that in some specific cases the minimum of the denominator in Eq. (5.31) does not occur at periapsis or apoapsis. An example of that is given in Fig. 5.11.
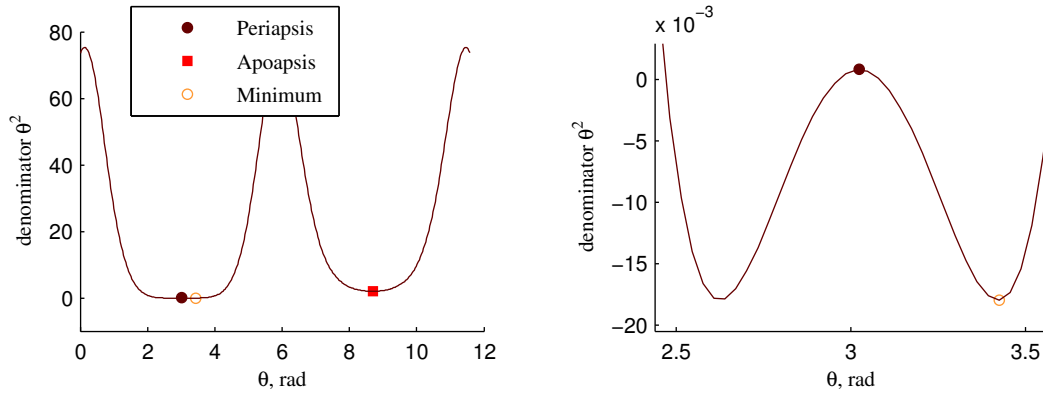
Fig. 5.11 Profile of the denominator in Eq. (5.31) for $k_1 = 10$, $k_2 = 0.86$, $\phi = 1.5\pi$ and $k = 0.93$ and showing the values at periapsis, apoapsis and the absolute minimum.

The figure shows that, although the denominator in Eq. (5.31) is positive at periapsis, the absolute minimum is negative and thus $\dot{\theta}^2 < 0$. To find this absolute minimum the derivative of the denominator of Eq. (5.31) with respect to θ is set equal to zero and the second order derivative is required to be positive. Evaluating the first order derivative and substituting the identities $\mathrm{sn}^2 + \mathrm{cn}^2 = 1$ and $k^2 \mathrm{sn}^2 + \mathrm{dn}^2 = 1$ results in:

$$\left[k_1 k_2^3 \left(4k_1 k^2 \, \mathrm{sn}^3 - 6k^2 \, \mathrm{sn}^2 - 2k_1\left(1+k^2\right)\mathrm{sn}+1+k^2\right)\right]\mathrm{cn}\,\mathrm{dn} = 0 \tag{5.35}$$

The case $\mathrm{cn}\,\mathrm{dn} = 0$ corresponds to a minimum or maximum at periapsis and apoapsis, while the third order polynomial in between brackets provides any other minima or maxima occurring in the denominator of Eq. (5.31). This third order polynomial can be solved numerically for sn, ignoring the complex roots and the roots with absolute value larger than unity since $-1 \le \mathrm{sn} \le 1$. The minimum of the polynomial can subsequently be found from the second order derivative which yields the condition:

132

$$2k_1k_2{}^4\left(6k_1k^2\,\mathrm{sn}^2-6k^2\,\mathrm{sn}-k_1\left(1+k^2\right)\right)\left(\left(1-\mathrm{sn}^2\right)\left(1-k^2\,\mathrm{sn}^2\right)\right)+$$
$$k_1k_2^3\left(4k_1k^2\,\mathrm{sn}^3-6k^2\,\mathrm{sn}^2-2k_1\left(1+k^2\right)\mathrm{sn}+\left(1+k^2\right)\right)\left(2k^2\,\mathrm{sn}^2-\left(1+k^2\right)\right)\mathrm{sn}>0 \tag{5.36}$$

Finally, if this minimum is positive, the feasibility condition is satisfied.

A validation of the performance of the expo-elliptic shape for a range of orbital transfers and rendezvous transfers is provided in Appendix A. Hereafter it is applied to provide the initial guess for the Earth to pole-sitter transfer.

The initial guess for the transfer to the pole-sitter can be obtained by considering a transfer from an orbit with initial radius $r_0\left(\theta_0\right)=r_{park}$ to an orbit with final radius $r_f\left(\theta_f\right)=a_{PS}\left(1-e_{PS}^2\right)/\left(1+e_{PS}\cos\theta_f\right)$ over a, to be optimised, transfer angle ψ_t, where $\theta_f=\theta_0+\psi_t+2\pi N$ with N the number of full revolutions allowed. Assuming k_2, ϕ and k are fixed, the other two shape parameters can be determined from the initial and final radii constraints through Eq. (5.29). First:

$$k_1=\log\left(\frac{r_f}{r_0}\right)\Bigg/\left(\mathrm{sn}\left(k_2\theta_f+\phi,k\right)-\mathrm{sn}\left(k_2\theta_0+\phi,k\right)\right) \tag{5.37}$$

and subsequently

$$k_0=\frac{r_0}{\exp\left[k_1\,\mathrm{sn}\left(k_2\theta_0+\phi,k\right)\right]} \tag{5.38}$$

Then, the angular rate, acceleration and flight path angle profiles can be determined from Eqs. (5.31) to (5.33).

The objective now is to find suitable initial guesses that will provide a feasible and optimal solution by PSOPT. For this, the following objective function is adopted:

$$J=\max\left[0,\Delta V_0-\Delta V_{upper\text{-}stage,\,\max}\right]+\Delta V_f+\max\left(a\right) \tag{5.39}$$

First, it must be noted that, like the exponential sinusoids, the expo-elliptic shape cannot satisfy the boundary constraints on the velocity. Therefore, the impulses to be given at the start, ΔV_0, and end, ΔV_f, of the transfer in order to match the initial and final orbital velocities have to be taken into account. These are calculated as follows:

$$\Delta V_0 = \sqrt{\left(V_{r,park} - V_{r,0}\right)^2 + \left(V_{\theta,park} - V_{\theta,0}\right)^2}$$

$$\Delta V_f = \sqrt{\left(V_{r,PS} - V_{r,f}\right)^2 + \left(V_{\theta,PS} - V_{\theta,f}\right)^2} \tag{5.40}$$

with V_r and V_θ the radial and transverse velocities.

As Eq. (5.39) shows, the impulses are not just summed. Instead, the performance of the Soyuz and Ariane upper-stages is taken into account by only considering the portion of the ΔV given at the parking orbit that exceeds the maximum performance of the launcher, $\Delta V_{upper\text{-}stage,\,max}$:

$$\Delta V_{upper\text{-}stage,\,max} = I_{sp} g_0 \ln\left(\frac{m_{park,max}}{m_{upper\text{-}stage} + m_{adapter} + m_{pay}}\right) \tag{5.41}$$

The specific impulse, the maximum performance in the parking orbit, $m_{park,max}$, the mass of the upper-stage, $m_{upper\text{-}stage}$, and the mass of the adapter, $m_{adapter}$, can all be found in Table 5.3. For now, the payload mass to be delivered to the approximated pole-sitter orbit, m_{pay}, is assumed to equal the 1000 kg mass of optimisation case 1 in Section 5.3.1. Substituting the values of all variables into Eq. (5.41) results into the following performance for the Soyuz and Ariane 5 launch vehicles, respectively: $\Delta V_{upper\text{-}stage}\big|_{Soyuz} = 3.542$ km/s and $\Delta V_{upper\text{-}stage}\big|_{Ariane} = 5.266$ km/s.

The final term in Eq. (5.39) considers the maximum acceleration encountered during the transfer. In order to find this maximum acceleration, the polar angle along the transfer is discretised into $50(N+1)$ equally spaced nodes after which the maximum value is determined numerically. Tests showed that 50 nodes per full revolution are sufficient to capture this maximum value.

The decision vector for the optimisation of the objective function in Eq. (5.39) is five dimensional, $\mathbf{x} = \begin{bmatrix} k_2 & \phi & k & \psi_t & \theta_0 \end{bmatrix}^T$ and a genetic algorithm[148] with suggested default settings is employed to try to locate the global optimum. Bounds on the decision vector are set as follows:

$$\begin{bmatrix} 0.01 & 0 & 0 & 0 & 0 \end{bmatrix}^T \leq \mathbf{x} \leq \begin{bmatrix} 1 & 2\pi & 1 & 2\pi & 2\pi \end{bmatrix}^T \tag{5.42}$$

Finally, the feasibility condition as defined in Eqs. (5.35) and (5.36) is satisfied by introducing a penalty on the objective function when violated through a simple *if* statement.

Note that such a penalty could cause the genetic algorithm to perform an indefinite search, but tests showed that enough feasible solutions are created to prevent this.

The results for the constant altitude pole-sitter orbits and the optimal SEP and hybrid pole-sitter orbits are provided in Fig. 5.12 and Fig. 5.13. For comparison purposes, both figures also include the results for the use of the exponential sinusoids which are generated by setting $k = 0$ in all of the above. Note that the results for the constant altitude pole-sitter orbits can also be used for the transfer to the tilted pole-sitter orbit since the minimum distance of the tilted pole-sitter orbit is equal to the distance of the constant altitude pole-sitter orbit.

a)   b)
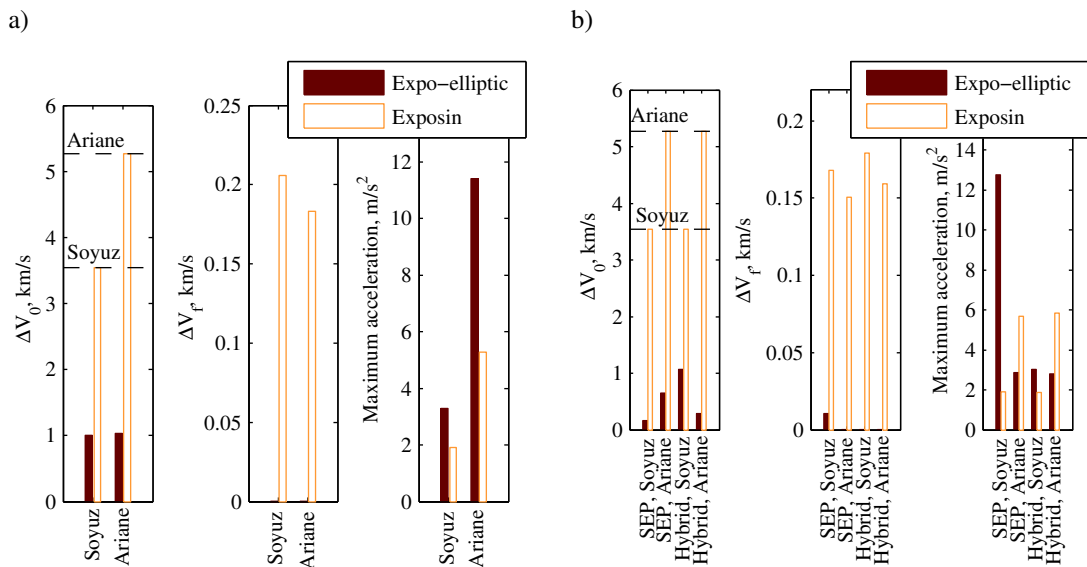
Fig. 5.12 Performance of the expo-elliptic and exposin shapes ($N = 0$) for the transfer from parking orbit to approximated constant altitude pole-sitter orbit (a) and optimal SEP and hybrid pole-sitter orbits (b) for both Soyuz and Ariane 5 launch phases. From left to right: ΔV required at parking orbit (including maximum ΔV provided by Soyuz and Ariane 5 upper-stages (black dashed line)), ΔV required at approximated pole-sitter orbit and maximum acceleration occurring during the transfer.

Figure 5.12 clearly illustrates the capability of the expo-elliptic shape to much better satisfy the boundary constraints in terms of velocity than the exponential sinusoids as both the values for the initial and final ΔVs are significantly smaller. This already becomes clear from looking at (a subset of) the trajectories in Fig. 5.13. The figure shows that the expo-elliptic trajectory nicely winds onto the approximated pole-sitter orbit, while the exposin trajectory intersects the pole-sitter orbit at an angle, causing a large mismatch in the final velocity. However, in some cases, this better performance comes at the cost of a larger required maximum acceleration during the trajectory (see the right bar plot in Fig. 5.12a and

Fig. 5.12b). When optimising the objective functions in Eqs. (5.18) and (5.25) with a limit on the thrust magnitude as given in the order of tenths of a Newton (e.g. see Section 5.3.1) this may cause convergence problems. This can be circumvented in a similar way as was explained for the displaced geostationary transfers in Section 4.2.1, by first performing an optimisation in which the square of the thrust is minimised (without a limit on the thrust magnitude) which can serve as initial guess for the thrust-limited minimisation of the mass (either in parking orbit, i.e. optimisation case 1, or in pole-sitter orbit, optimisation case 2). Finally, since the expo-elliptic shape can only generate two-dimensional trajectories, the trajectories provided in Fig. 5.12 and Fig. 5.13 for a Soyuz launch can serve as initial guess for a transfer starting from a parking orbit with each of the four parking orbit inclinations.

a)

b)

c)

d)
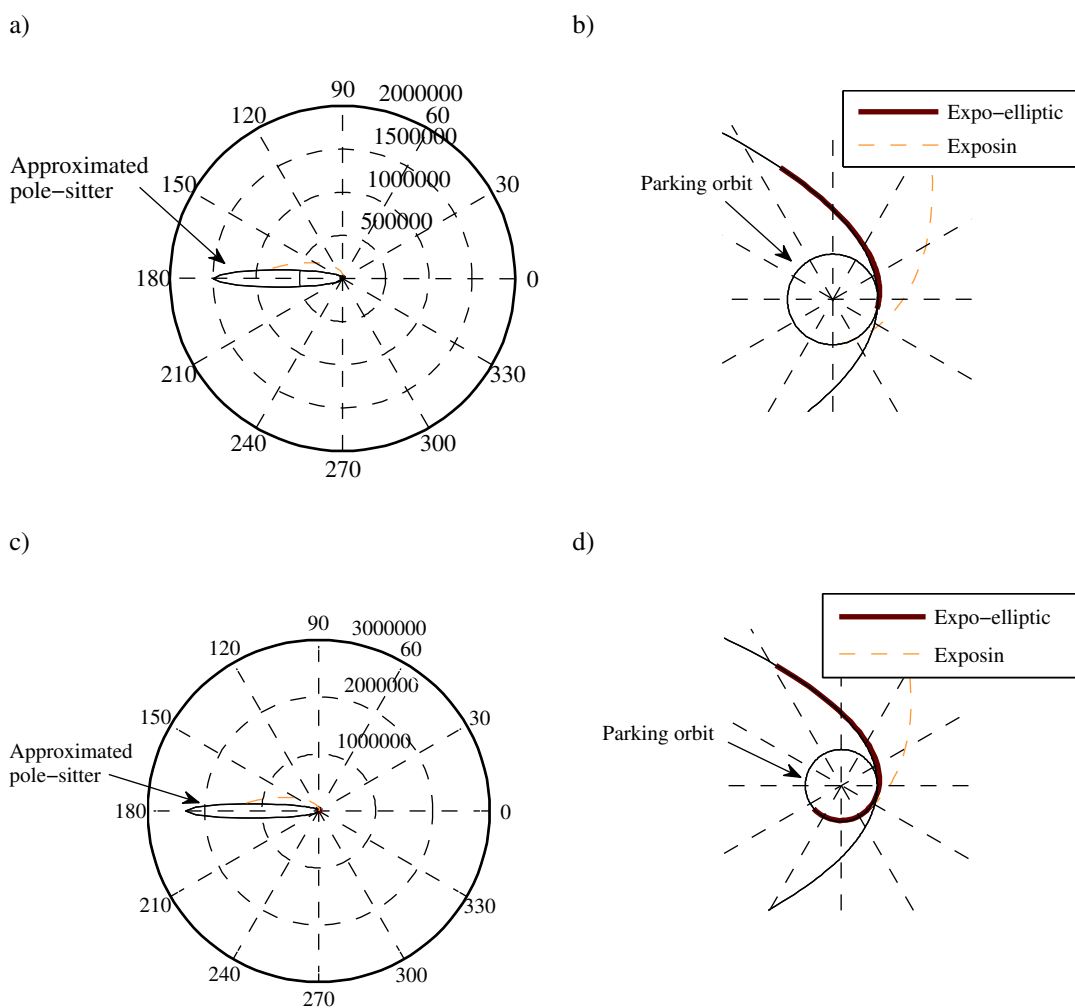
Fig. 5.13 Optimal expo-elliptic and exposin trajectories for the constant altitude pole-sitter orbit and a Soyuz launch (a-b) and the optimal SEP pole-sitter orbit and an Ariane 5 launch (c-d).

5.4.2 Manifold-like trajectories

A second method of generating the initial guess for the transfer to the pole-sitter makes use of a ballistic transfer phase. For this, manifold-like trajectories that automatically wind onto the pole-sitter orbit are created through a backwards integration of the equations of motion in Eq. (2.13) with $\mathbf{a} = \mathbf{0}$ starting from different locations along the pole-sitter orbit. Note that no manoeuvre needs to be applied to enter the pole-sitter orbit at the end of this ballistic transfer phase.

When allowing a maximum integration time of half a year, truncating the transfer at the point of closest approach to the Earth and discarding those transfers that attain an altitude of less than 200 km, the results in Fig. 5.14 are obtained for the constant, tilted and optimal pole-sitter orbits.

The performance of the different ballistic transfer phases can be assessed by linking the launch phase, as described in Section 5.2.1, to the start of each ballistic transfer. For this, the initial state vector of the transfer phase is transformed from the CR3BP reference frame to the inertial, Earth fixed, equatorial reference frame, see Fig. 5.7, and is subsequently transformed to Keplerian elements. From initial investigations it could be concluded that the apogee and perigee of this corresponding Keplerian orbit do not coincide with the line of nodes, nor is the inclination change required to patch the start of the manifold to the parking orbit small. Therefore, the launch model in Eqs. (5.9) to (5.11) is used.

Furthermore, depending on the case considered (i.e. minimising the mass in the parking orbit (case 1) or maximising the mass inserted into the pole-sitter orbit (case 2)), either the mass at the end of the transfer phase (and therefore at the end of the launch phase) is known (1000 kg for case 1) or the mass in the parking orbit is known ($m_{park,\max}$ for case 2).

To optimise this objective function, rather than truncating the manifold at the point of closest approach to the Earth, a simple grid search can find the optimal location along the manifold to link the launch phase (i.e. the optimal time spent in the transfer phase, t_t) and the optimal initial condition of the integration, i.e. the point where the transfer phase winds onto the pole-sitter orbit, θ. The decision vector thus equals $\mathbf{y} = \begin{bmatrix} t_t & \theta \end{bmatrix}^T$. For the grid search, bounds of $25 \le t_t \le 75$ days for the constant and tilted pole-sitter orbits and $50 \le t_t \le 100$ days for the optimal pole-sitter orbits are chosen. Furthermore, $0 \le \theta \le 2\pi$ and step sizes of $\Delta t_t = 0.05$ days and $\Delta\theta = 0.01\pi$ are selected. These step sizes are considered small enough to capture the optimal solution. Note that, in case the altitude in the transfer phase becomes less

than 200 km or if the eccentricity of the initial state vector is larger than 1, a penalty is introduced on the objective function through a simple *if* statement.
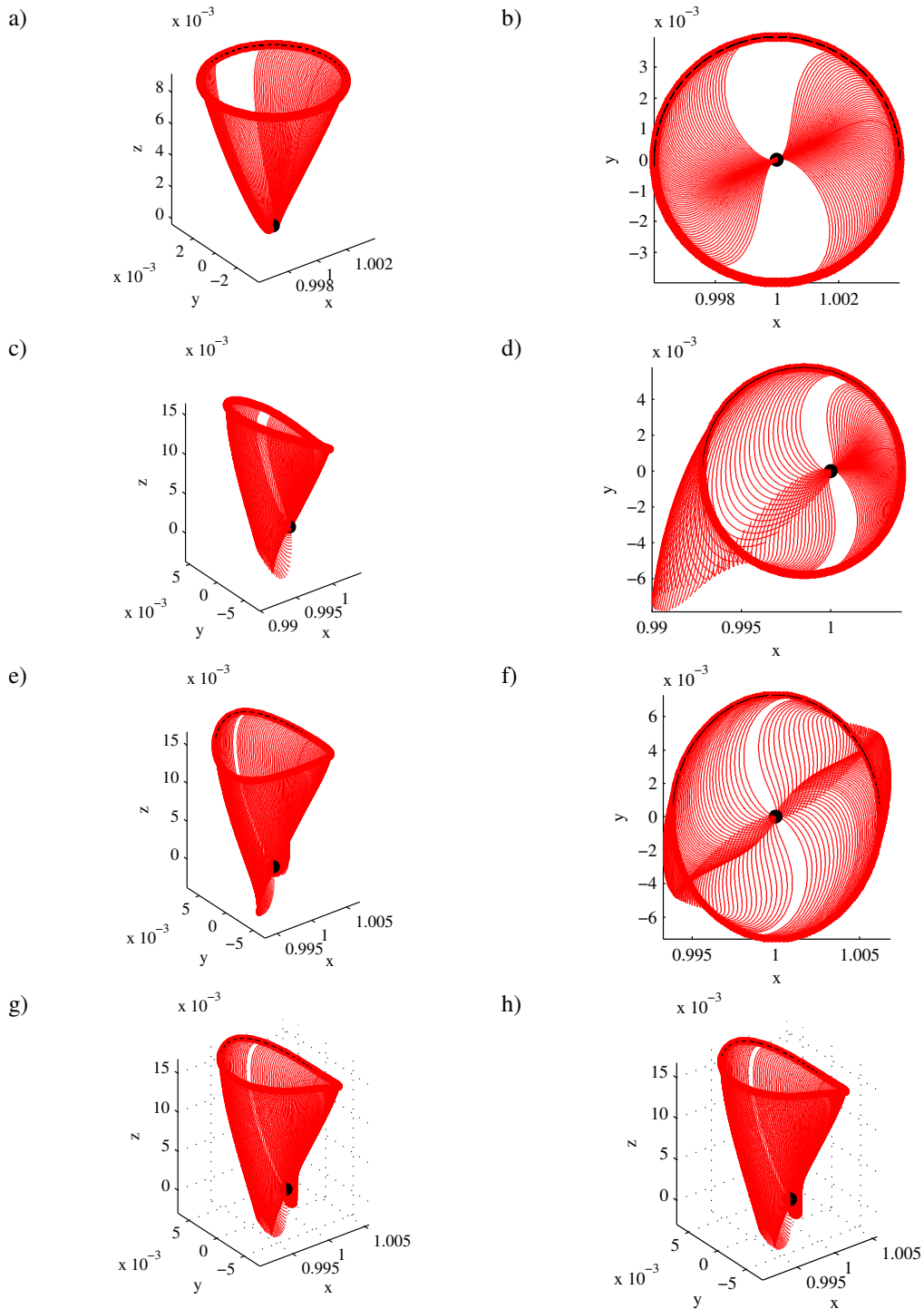
Fig. 5.14 Ballistic transfer phases in CR3BP frame to the constant altitude (a-b), tilted (c-d), optimal SEP (e-f) and optimal hybrid (g-h) pole-sitter orbits. Manifolds that attain an altitude of less than 200 km are omitted.

Also note that, because the transfer phase is ballistic and independent of the mass of the spacecraft, the same manifold will be optimal for both optimisation cases considered. However, the end result (i.e. the mass required in the parking orbit or the mass injected into the pole-sitter orbit) will be different.

The optimal solutions found in the grid search are provided in Fig. 5.15 and Table 5.5. Note that, to more easily interpret the graphs, Fig. 5.15 (and all subsequent figures) presents the results in a reference frame similar to the reference frame employed for the CR3BP, but centred in the Earth and in dimensional form. The results shows that for case 1 and a Soyuz launch, the larger the parking orbit inclination, the smaller the objective value, i.e. m_{park}. This is due to the fact that the inclination of the initial state vector of the ballistic transfer phase is close to 90°. The launcher's upper-stage thus has to provide the required change between the parking orbit inclination and the inclination of the start of the transfer, which increases for decreasing inclination of the parking orbit and thus penalises the performance. For case 1, the largest parking orbit inclination is thus favourable. Furthermore, considering the maximum mass that the launch vehicles can deliver into the parking orbit, see Table 5.2, it becomes clear that delivering a 1000 kg spacecraft to the pole-sitter orbit is feasible for all parking orbit inclinations of the SEP and hybrid optimal pole-sitter orbits. However, for the constant altitude and tilted pole-sitter orbits, only an Ariane launch or the use of the 95.4 deg parking orbit for a Soyuz launch allow for this. Finally, in general, the two types of optimal pole-sitter orbits perform much better in terms of mass required in the parking orbit compared to the constant altitude and tilted pole-sitter orbits, which shows a first benefit of the optimal pole-sitter orbits.

While the largest parking orbit inclination for a Soyuz launch is most favourable for all pole-sitter orbit types for a case 1 optimisation, this is not true for a case 2 optimisation. Instead, for the optimal SEP and hybrid pole-sitter orbits, the smallest parking orbit inclination is most favourable. This is due to the fact that, the smaller the parking orbit inclination, the better the performance of the Soyuz launch vehicle in the parking orbit (a difference of over 900 kg exists between the performance in the 51.8° and 95.4° parking orbits, see Table 5.2). This higher mass in the parking orbit eventually translates into a larger mass at injection than when considering a parking orbit with an inclination closer to the inclination of the pole-sitter orbit. Therefore, for case 2, the smallest parking orbit inclination can be more favourable.

Table 5.5 Optimal ballistic transfers for constant altitude, tilted and optimal pole-sitter orbits for Soyuz and Ariane 5 launches, indicating the transfer phase time, t_t, the point of pole-sitter injection, θ, and the objective function values for optimisation cases 1 and 2.

	Parking orbit inclination, deg	t_t, days	θ, deg	Constant altitude pole-sitter Case 1 m_{park}, kg	Case 2 m_f, kg	t_t, days	θ, deg	Tilted pole-sitter Case 1 m_{park}, kg	Case 2 m_f, kg
Soyuz	51.8	36.0	9.0	8066	771	58.6	271.8	7326	960
	64.9	36.0	9.0	7175	787	58.6	271.8	6719	916
	70.4	36.1	9.0	6824	837	58.6	271.8	6475	941
	95.4	35.9	180.0	6097	1061	58.7	271.8	5974	1106
Ariane	51.6	36.0	9.0	14826	2605	58.6	271.8	13834	3129

	Parking orbit inclination, deg	t_t, days	θ, deg	SEP optimal pole-sitter Case 1 m_{park}, kg	Case 2 m_f, kg	t_t, days	θ, deg	Hybrid optimal pole-sitter Case 1 m_{park}, kg	Case 2 m_f, kg
Soyuz	51.8	65.2	91.8	6102	1373	69.3	273.6	6200	1333
	64.9	65.2	91.8	5953	1175	69.5	273.6	6022	1149
	70.4	65.3	91.8	5890	1144	69.6	273.6	5947	1123
	95.4	65.4	91.8	5782	1179	69.8	273.6	5814	1166
Ariane	51.6	65.2	91.8	12126	4231	69.3	273.6	12266	4129

Finally, comparing the performance of the Soyuz and Ariane 5 launchers, it becomes clear that launching with a Soyuz is favourable when minimising the mass in the parking orbit. The poor performance of Ariane 5 for this case is mainly due to its heavier upper-stage. Contrary, when maximising the mass in the pole-sitter orbit, launching with Ariane 5 is clearly favourable, which is due to the fact that the maximum launch vehicle performance into the parking orbit is 2.5-3 times larger than for a Soyuz launch and the specific impulse of the Ariane 5 upper-stage is much higher than the specific impulse of the Soyuz Fregat upper-stage, see Table 5.3.

It must be noted, however, that none of the ballistic transfers satisfy the constraint on the maximum allowable semi-major axis of the launch phase target ellipse in Eqs. (5.23) and (5.26). Introducing that constraint provided no feasible solutions.
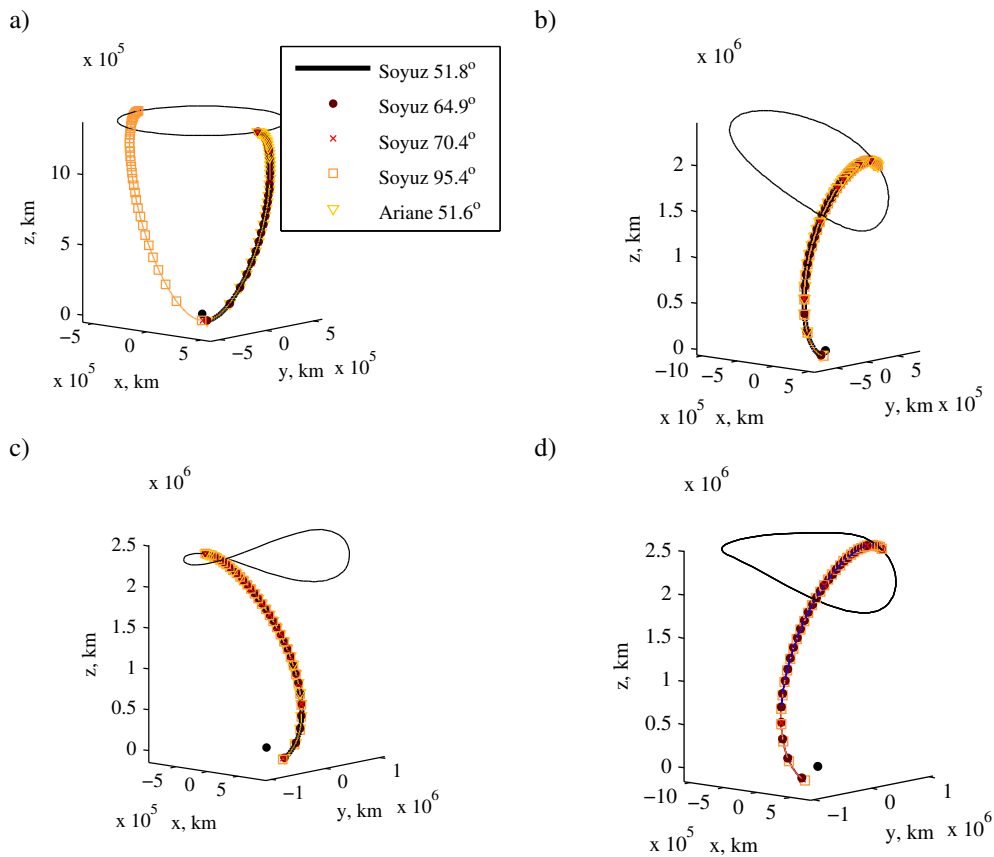
Fig. 5.15 Optimal ballistic transfer phases for constant altitude (a), tilted (b), optimal SEP (c) and optimal hybrid (d) pole-sitter orbits for a Soyuz and Ariane 5 launch and different parking orbit inclinations.

5.5 Results - SEP

Using the results of Sections 5.4.1 and 5.4.2 as an initial guess, the final optimal transfers to the different types of pole-sitter orbits can be obtained. This section will provide these results for the use of pure SEP, while Section 5.6 will do so for the use of hybrid sail propulsion. First, the results for the constant altitude pole-sitter orbits will be provided, followed by those for the tilted pole-sitter orbits and finally the results for the optimal SEP pole-sitter orbit will be given.

All results are generated using an NLP tolerance of at least 10^{-5}, a maximum number of iterations of 5000 (which is never reached) and a mesh refinement is used to eventually obtain solutions with 40 nodes.

Furthermore, note that, although new units were introduced in the CR3BP (see Section 2.1.1), the mass and thrust magnitudes are used in their dimensional form. The

reason for this is the fact that the dimensionless mass and thrust magnitudes are in the order of 10^{-18}, which causes problems when solving the optimal control problem in PSOPT with machine precision and the NLP tolerance.

Finally, note that initial investigations showed that, contrary to the ballistic manifold-like trajectories, the required inclination change between the parking orbit and the initial state vector of the low-thrust transfer phase is very small. Therefore, the launch model presented in Eqs. (5.4) to (5.5) is used as it allows a quicker, two-burn only launch phase and complies with the launch sequence description provided by Reference 139.

5.5.1   Constant altitude pole-sitter

Case 1: Minimising mass in parking orbit
The first optimisations carried out are those for the constant altitude pole-sitter orbits, using pure SEP with a maximum thrust magnitude as provided in Table 5.4 (i.e. 0.240 N) and minimising the mass in the parking orbit. These optimisations are performed using both types of initial guesses defined in Section 5.4 to show their applicability and performance as initial guess.

The full set of results in terms of objective function value is provided in Table 5.6. The table immediately shows the resemblance in terms of the mass required in the parking orbit for both types of initial guesses. This proves their applicability for the problem under consideration and a validation of the optimality of the results produced by PSOPT as it converges to the same optimal solution for the use of different initial guesses.

The table furthermore confirms the conclusion that was already drawn from the results for the ballistic transfers in Table 5.5, namely that (for a Soyuz launch) the best performance is obtained for a parking orbit with the largest inclination of 95.4°. Any subsequent investigations and optimisations for case 1 will therefore only consider that particular inclination.

Table 5.6 Constant altitude pole-sitter orbit using SEP, optimisation case 1: minimised mass in parking orbit and inclination at start of low-thrust transfer phase (i.e. inclination of launch phase target orbit) for both the expo-elliptic and manifold-like initial guesses.

	Parking orbit inclination, deg	Expo-elliptic initial guess		Manifold initial guess	
		m_{park}, kg	i_0, deg	m_{park}, kg	i_0, deg
Soyuz	51.8	5691	51.9	5691	51.9
	64.9	5675	65.1	5675	65.2
	70.4	5666	70.7	5666	70.7
	95.4	5648	95.3	5647	95.3
Ariane	51.6	11719	52.1	11719	51.5

For example, Fig. 5.16 only shows detailed results for the 95.4° Soyuz launch and an Ariane 5 launch. From the thrust profiles and the transfers in the Earth inertial reference frame, see Fig. 5.16b and c, respectively, the resemblance between the results generated with the different types of initial guesses once again becomes clear. However, inspecting the results in the CR3BP reference frame in Fig. 5.16a, shows a clear difference which suggests that the time during the year when injection takes place has little or no influence on the mass required in the parking orbit. This observation will be explored further in Section 5.5.2.

The final results for the optimisation case 1, constant altitude pole-sitter orbits can be summarised as follows: minimised masses in the parking orbit of 5648 and 11719 kg are required for a Soyuz and Ariane 5 launch, respectively. These masses provide an improvement over the ballistic transfers to the constant altitude pole-sitter orbits as presented in Table 5.5 of 449 and 3107 kg, respectively. These mass savings can be attributed to the fact that, rather than the upper-stage having to perform the inclination change between the parking orbit and the pole-sitter orbit, the SEP thruster can much more efficiently perform this inclination change. This explanation can be underlined by the value of the inclination at the start of the transfer phase, i_0, see Table 5.6, which very closely matches the inclination of the parking orbit.
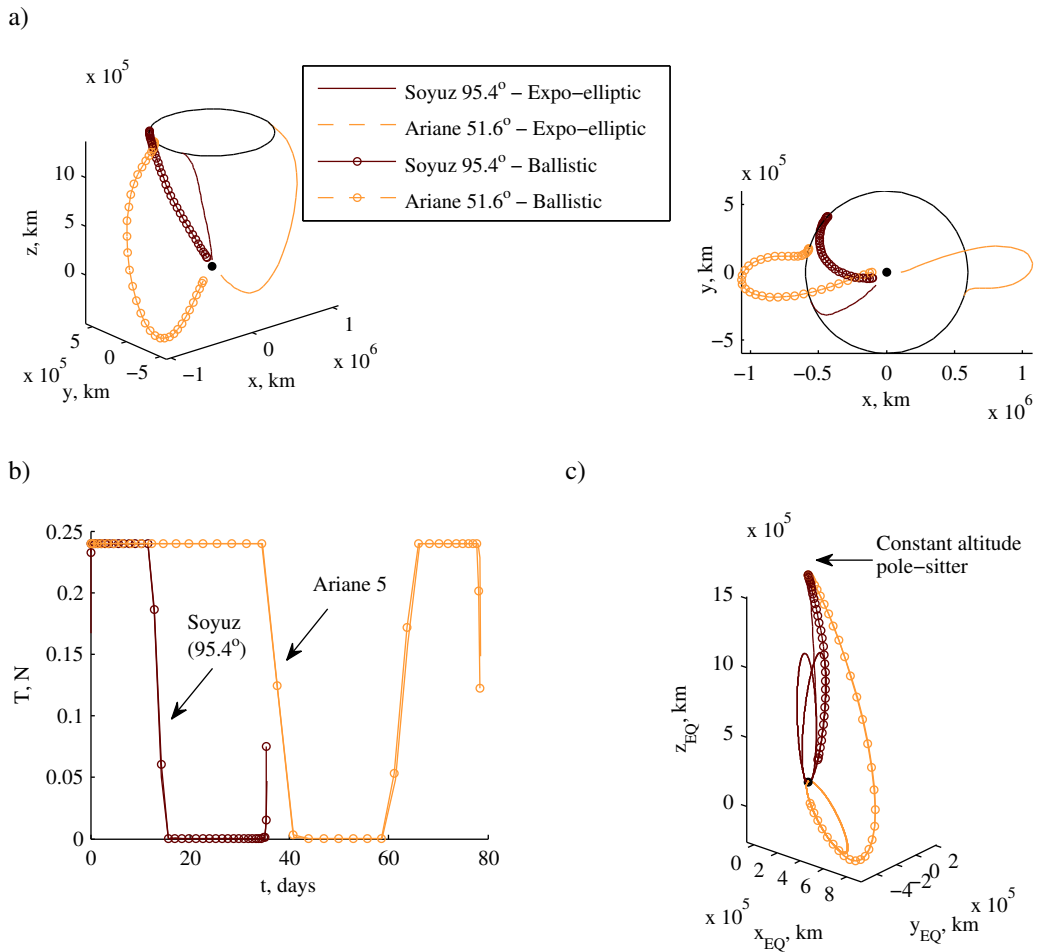
Fig. 5.16 Constant altitude pole-sitter orbit using SEP, optimisation case 1: optimal transfer phases using both the expo-elliptic and manifold-like initial guesses. a) Transfers in CR3BP frame. b) Thrust profiles. c) Transfers in Earth inertial reference frame including the launch phase target orbit.

Case 2: Maximising mass in pole-sitter orbit

By using the results for the minimisation of the mass in the parking orbit as initial guess, the results for the second type of objective, i.e. maximising the mass injected into the pole-sitter, can be generated. While the results for the ballistic transfer to the constant altitude pole-sitter orbit showed that for a Soyuz launch a parking orbit with inclination closest to 90 deg is most favourable, the SEP results showed a similar trend as for the ballistic transfers to the optimal pole-sitter orbits. Those transfer showed that the smallest parking orbit inclination is most favourable due to the better Soyuz launch vehicle performance into LEO. To limit the results presented, this section therefore only presents the results for an inclination of 51.8° in Table 5.7.

Table 5.7 Constant altitude pole-sitter orbit using SEP, optimisation case 2: maximised injection mass at pole-sitter orbit, m_f, and iterative scheme to determine the maximum thrust magnitude, T_{max}.

	Parking orbit inclination, deg	SEP					
		Iteration 1		Iteration 2		Iteration 3	
		$T_{\max}$, N	m_f , kg	$T_{\max}$, N	m_f , kg	$T_{\max}$, N	m_f , kg
Soyuz	51.8	0.240	1522	0.365	1543	0.370	1543
Ariane	51.6	0.240	4265	1.024	4453	1.069	4455

Furthermore, as explained previously, the maximum thrust magnitude during the low-thrust transfer phase is determined through an iterative approach, where an initial value for the thrust magnitude of 0.240 N (as used for case 1) is assumed. The injected mass that results from that optimisation is then used to update the maximum thrust magnitude by multiplying it with the maximum acceleration in the pole-sitter orbit. This acceleration was previously provided in Table 5.4 and equals 0.240 mm/s^2 for the constant altitude pole-sitter orbit. The evolution of the maximum thrust magnitude and the optimised injected mass are also provided in Table 5.7, which clearly shows that both variables converged after three iterations.

Comparing the results for a Soyuz launch and an Ariane 5 launch in Table 5.7 and Fig. 5.17 shows a very clear scalability of the transfer, which is a result of the fact that the maximum SEP thrust magnitude is allowed to scale proportionally with the increase in the injected mass that the Ariane 5 launch can establish, i.e. the maximum acceleration is kept constant. To show this even more clearly, Fig. 5.17 includes the acceleration profiles rather than the thrust profiles (which differ in absolute magnitude) as well as the profile of the ratio of the current mass and the mass at injection. These graphs are nearly equal for the Soyuz and Ariane 5 launch cases. Any differences can be attributed to the slightly different parking orbits from which the transfer is initiated.

The final results for optimisation case 2 of the constant altitude pole-sitter orbit can be summarised as follows: a maximum injected mass of 1543 and 4455 kg can be established for a Soyuz and Ariane 5 launch, respectively, with maximum thrust magnitudes of 0.370 and 1.069 N. As for the results for optimisation case 1, these optimal SEP transfers

significantly outperform the ballistic transfers to the constant altitude pole-sitter orbits as they can establish gains in the injected mass of 772 and 1850 kg, respectively.
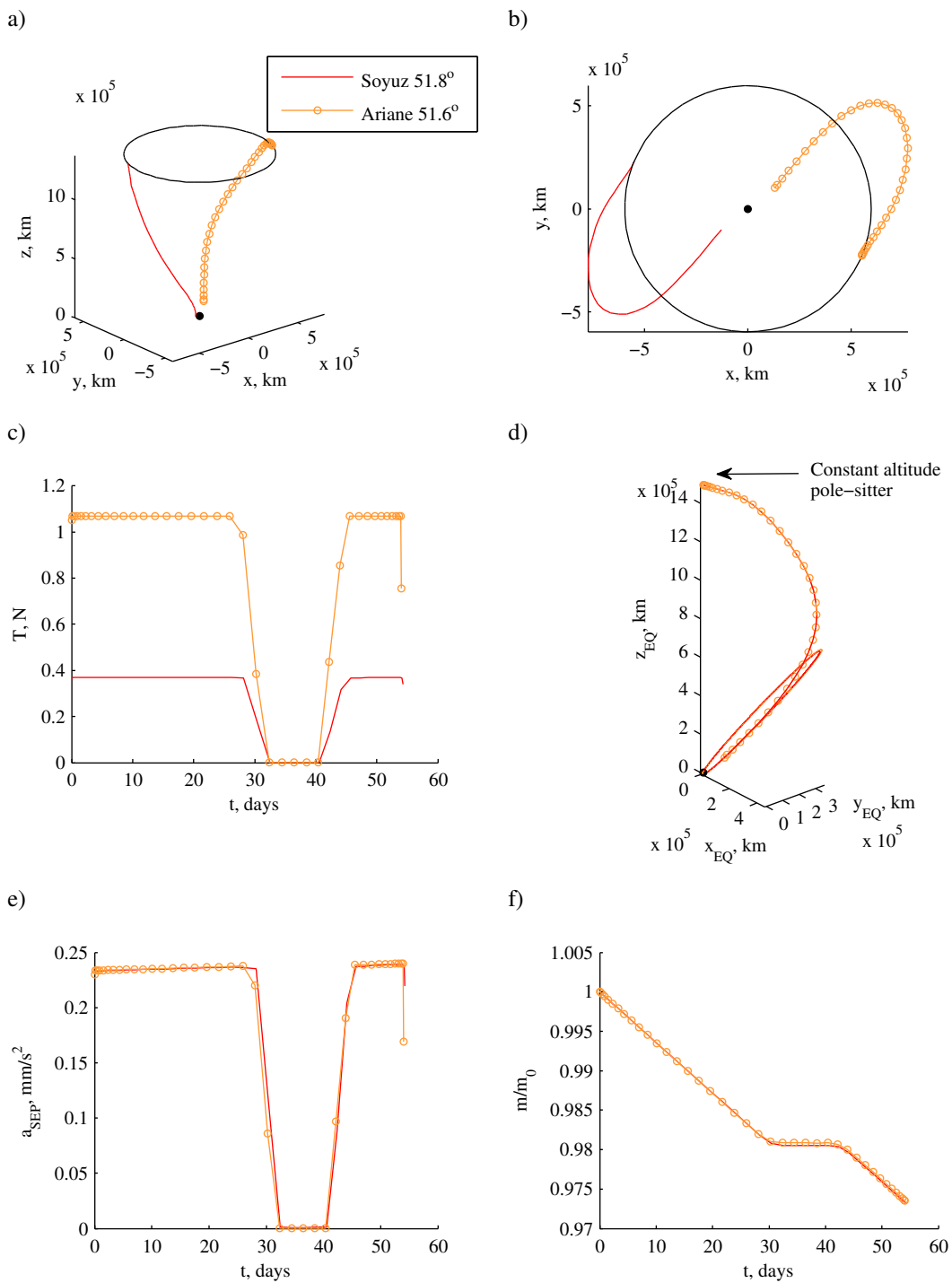
Fig. 5.17 Constant altitude pole-sitter orbit using SEP, optimisation case 2: a-b) Transfers in CR3BP frame. c) Thrust profiles. d) Transfers in Earth inertial reference frame including the launch phase target orbit. e) Acceleration profile. f) Ratio of current mass and mass at injection.

5.5.2   Tilted pole-sitter orbit

The approach used for generating the optimal transfer to the constant altitude pole-sitter orbit in the previous subsection can also be applied to the transfer to the tilted pole-sitter orbit: for optimisation case 1 both initial guesses are considered (and were shown to perform equally well), a maximum thrust of 0.243 N (see Table 5.4) is employed and only a parking orbit inclination of 95.4° for a Soyuz launch is considered. For optimisation case 2, a similar iterative approach to obtain the correct maximum thrust magnitude is adopted, as shown in Table 5.7, and a parking orbit inclination of 51.8° is used for a Soyuz launch.

The results are presented in Fig. 5.18, Fig. 5.19 and Table 5.8. Of interest is the fact that, for all cases, the spacecraft is injected very close to the winter solstice where the Earth-spacecraft distance is minimum. Since the distance at the winter solstice is equal to the Earth-spacecraft distance for the constant altitude pole-sitter orbit, the results are also nearly equal to the results for the transfer to the constant altitude pole-sitter. This confirms the observation made from the results in Fig. 5.16 for the constant altitude pole-sitter orbit that the time of year at which the spacecraft is injected into the pole-sitter orbit is of little importance. More important is the distance from Earth to the pole-sitter at injection, which leads to a flexible launch window for the constant altitude pole-sitter orbit as the spacecraft can be injected into the pole-sitter orbit at any time during the year without a penalty on the mass required in the parking orbit or the mass injected into the pole-sitter orbit.

Finally, Fig. 5.19 once again shows the clear scalability of the problem between the Soyuz and Ariane 5 launches for optimisation case 2.

The results for the tilted pole-sitter orbits can be summarised as follows: masses of 5647 kg (Soyuz) and 11720 kg (Ariane 5) are required in the parking orbit to inject a 1000 kg spacecraft into the pole-sitter orbit, which is an improvement of 327 and 2114 kg with respect to the ballistic transfer. Furthermore, maximum masses of 1543 and 4454 kg can be injected into the pole-sitter orbit for a Soyuz and Ariane launch, respectively, which also improves the ballistic transfers by 583 and 1325 kg, respectively.

a)

b)

c)

d)
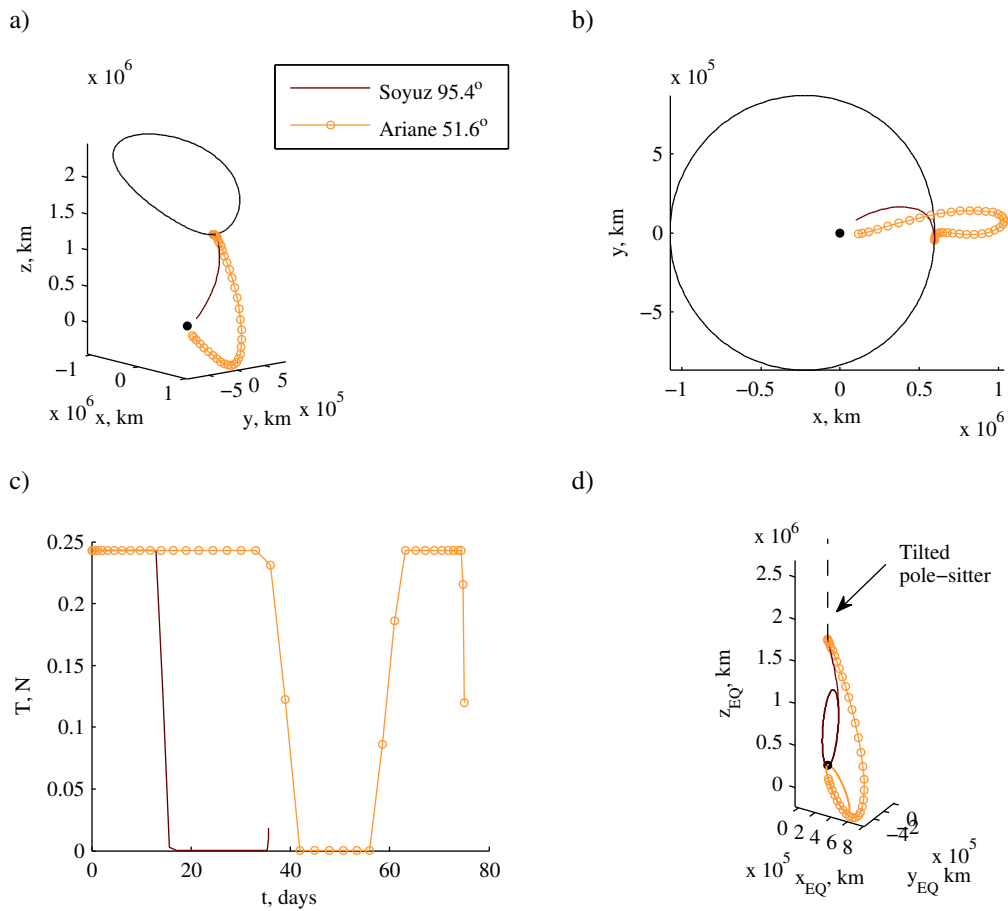
Fig. 5.18 Tilted pole-sitter orbit using SEP, optimisation case 1: a-b) Transfers in CR3BP frame. c) Thrust profiles. d) Transfers in Earth inertial reference frame including the launch phase target orbit.

Table 5.8 Tilted pole-sitter orbit using SEP, optimisation cases 1 and 2: minimised mass in parking orbit, m_{park}, maximised injection mass at pole-sitter orbit, m_f, and iterative scheme to determine the maximum thrust magnitude, T_{max}.

	Parking orbit inclination, deg	Case 1	Case 2					
		m_{park}, kg	Iteration 1		Iteration 2		Iteration 3	
			T_{max}, N	m_f, kg	T_{max}, N	m_f, kg	T_{max}, N	m_f, kg
Soyuz	51.8		0.243	1534	0.373	1543	0.375	1543
	95.4	5647						
Ariane	51.6	11720	0.243	4283	1.041	4452	1.082	4454

148
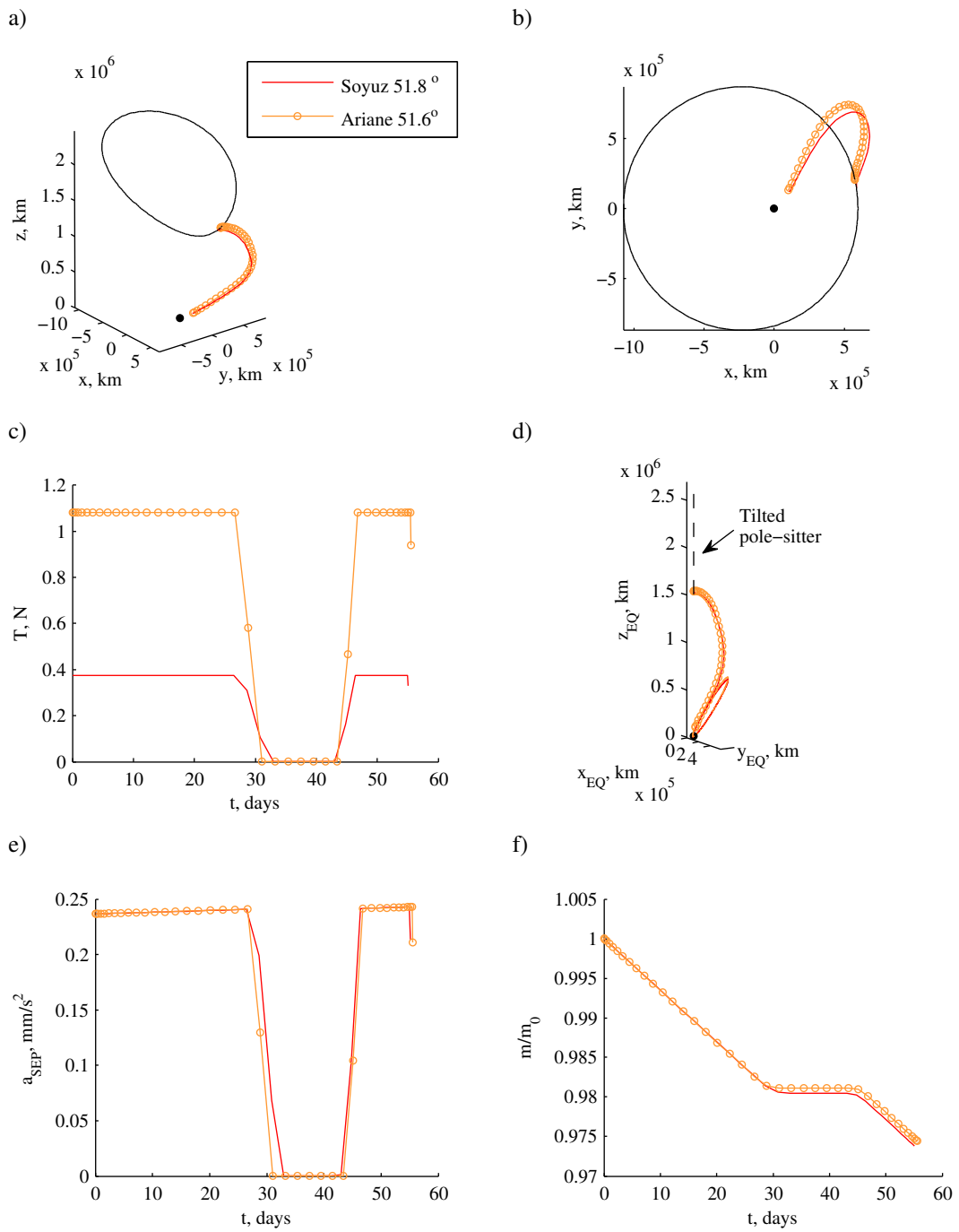
Fig. 5.19 Tilted pole-sitter orbit using SEP, optimisation case 2: a-b) Transfers in CR3BP frame. c) Thrust profiles. d) Transfers in Earth inertial reference frame including the launch phase target orbit. e) Acceleration profile. f) Ratio of current mass and mass at injection.

5.5.3 Optimal SEP pole-sitter orbit

All approaches developed and all conclusions drawn in the previous two sections are used in this section to obtain the final transfers to the optimal SEP pole-sitter orbit. The only

difference in the approach for solving the optimal control problem is the fact that the optimal pole-sitter orbit cannot be described through an analytical law. It is therefore described numerically using a discretisation of the orbit and using interpolation to obtain the pole-sitter conditions at the final time of the transfer. This implies that the option of automatic differentiation cannot be used within PSOPT and numerical derivatives are used instead (see also Section 2.3.4).

The results are presented in Fig. 5.20 and Table 5.9. For conciseness only the results for optimisation case 2 are provided in the figure, which again shows the clear scalability of the transfer between the Soyuz and Ariane 5 launch cases. Although the results seem to resemble the results for the constant altitude and tilted pole-sitter orbits in terms of minimised mass required in the parking orbit and maximised injected mass, there is one very clear advantage of the SEP optimal pole-sitter orbit: the thrust magnitude required to maintain this mass in the pole-sitter orbit is much lower, which will automatically translate into a lower propellant mass and thus into a larger payload mass or a longer mission lifetime as will be demonstrated at the end of Section 5.6. In addition, with thrust magnitudes of order 1 N for the constant altitude and tilted pole-sitter orbits and a thrust magnitude of 0.775 N for the optimal SEP pole-sitter orbit, clustering of multiple SEP thrusters will be required. The difference in required thrust magnitude may then lead to the use of one thruster less for the optimal SEP pole-sitter orbit.

Finally, note that the optimal SEP transfers presented in Table 5.9 outperform the ballistic transfers for all cases.

Table 5.9 Optimal SEP pole-sitter orbit, optimisation cases 1 and 2: minimised mass in parking orbit, m_{park}, maximised injection mass at pole-sitter orbit, m_f, and maximum thrust magnitude, T_{max}.

| | Parking orbit inclination, deg | Case 1 | Case 2 | |
		m_{park} , kg	m_f , kg	T_{max} , N
Soyuz	51.8		1537	0.269
Soyuz	95.4	5682		
Ariane	51.6	11716	4439	0.775
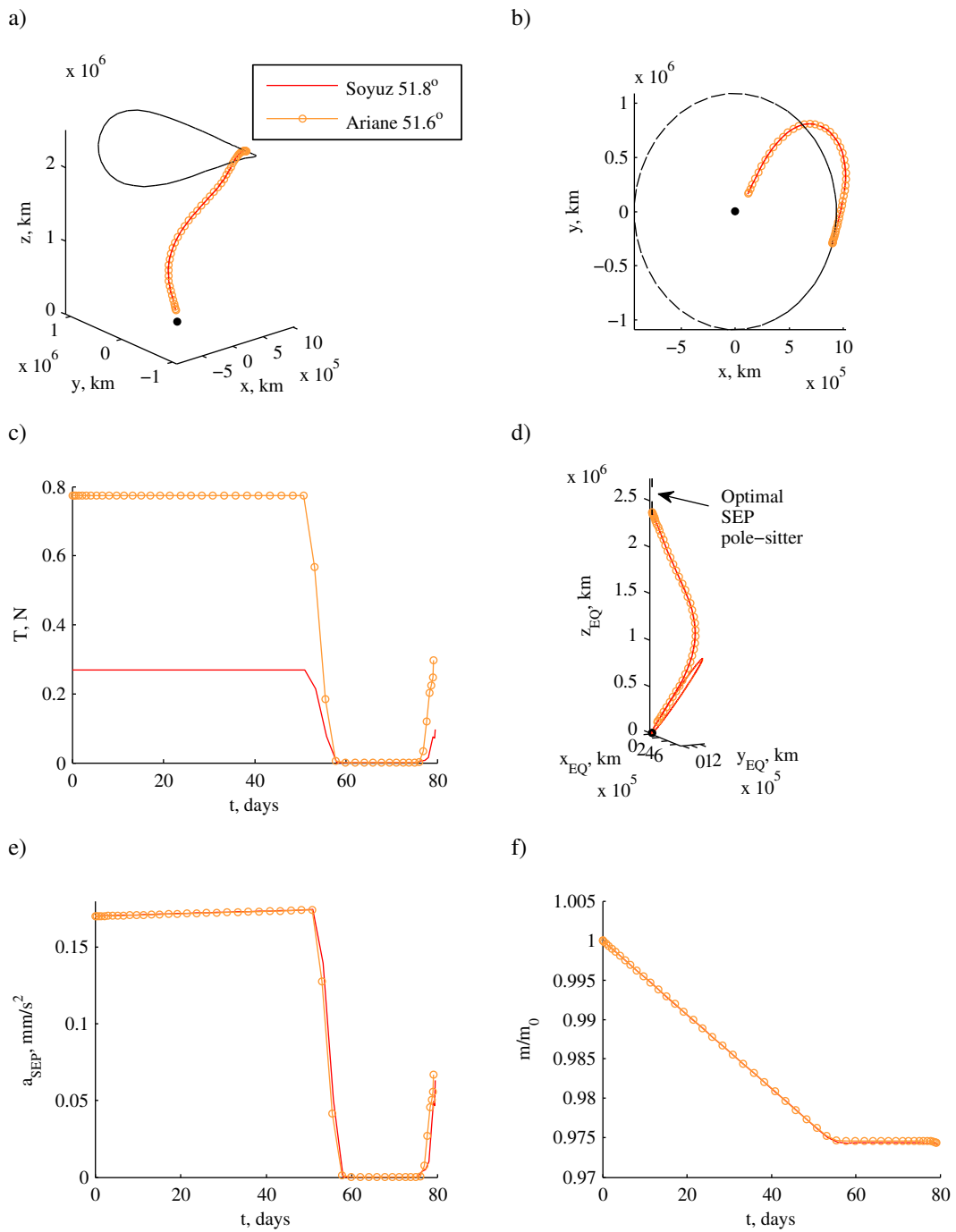
**Fig. 5.20 Optimal SEP pole-sitter orbit, optimisation case 2. a-b) Transfers in CR3BP frame. c)
Thrust profiles. d) Transfers in Earth inertial reference frame including the launch phase
target orbit. e) Acceleration profiles. f) Ratio of current mass and mass at injection.**

5.6   Results – hybrid sail propulsion

With the optimal Earth to pole-sitter transfers for the use of pure SEP known, these transfers can be used as initial guesses to generate optimal transfers using hybrid sail propulsion. Particular cases will be selected in order to limit the quantity of results presented, while still clearly demonstrating the potential of hybrid sail propulsion. First, since it was shown that the constant and tilted pole-sitter orbits perform equally well, only hybrid sail transfers to the constant altitude pole-sitter orbit will be considered, as similar results can be expected for the tilted pole-sitter orbits. Especially, because, as will be demonstrated below, the hybrid sail transfers inject the spacecraft at the winter solstice, where the Earth-spacecraft distances are the same for the two types of pole-sitter orbits. Furthermore, only the best performing launch configuration will be used for each of the optimisation cases, i.e. a Soyuz launch into a 95.4° parking orbit for optimisation case 1 and an Ariane 5 launch for optimisation case 2. Finally, the optimal hybrid sail transfer to the optimal hybrid pole-sitter orbit will also be provided.

5.6.1   Constant altitude pole-sitter orbit

The results for the use of hybrid sail propulsion for the transfer to the constant altitude pole-sitter orbit can be found in Table 5.10 and detailed results for the hybrid transfer using a Soyuz launch are presented in Fig. 5.21.

When minimising the mass in the parking orbit, it is clear that this mass decreases for increasing values of the sail lightness numbers. Gains of 6 to 100 kg can be established, depending on the value of the lightness number. Moreover, inspecting the transfers in Fig. 5.21, shows that the transfer changes from a transfer on the Sunward side of the pole-sitter orbit to a transfer on the Earthward side when larger values of β_0 are considered. For those values of the lightness number, the contribution of the sail to the required acceleration becomes significant and the optimal control solver finds that the sail can much better contribute to the direction of this required acceleration when it is directed away from the Sun.

For maximising the mass injected into the pole-sitter, again the increased performance of hybrid sail propulsion is clear as the injected mass increases for increasing values of the lightness number. Gains of 26 to 208 kg can be established, depending on the value for β_0.
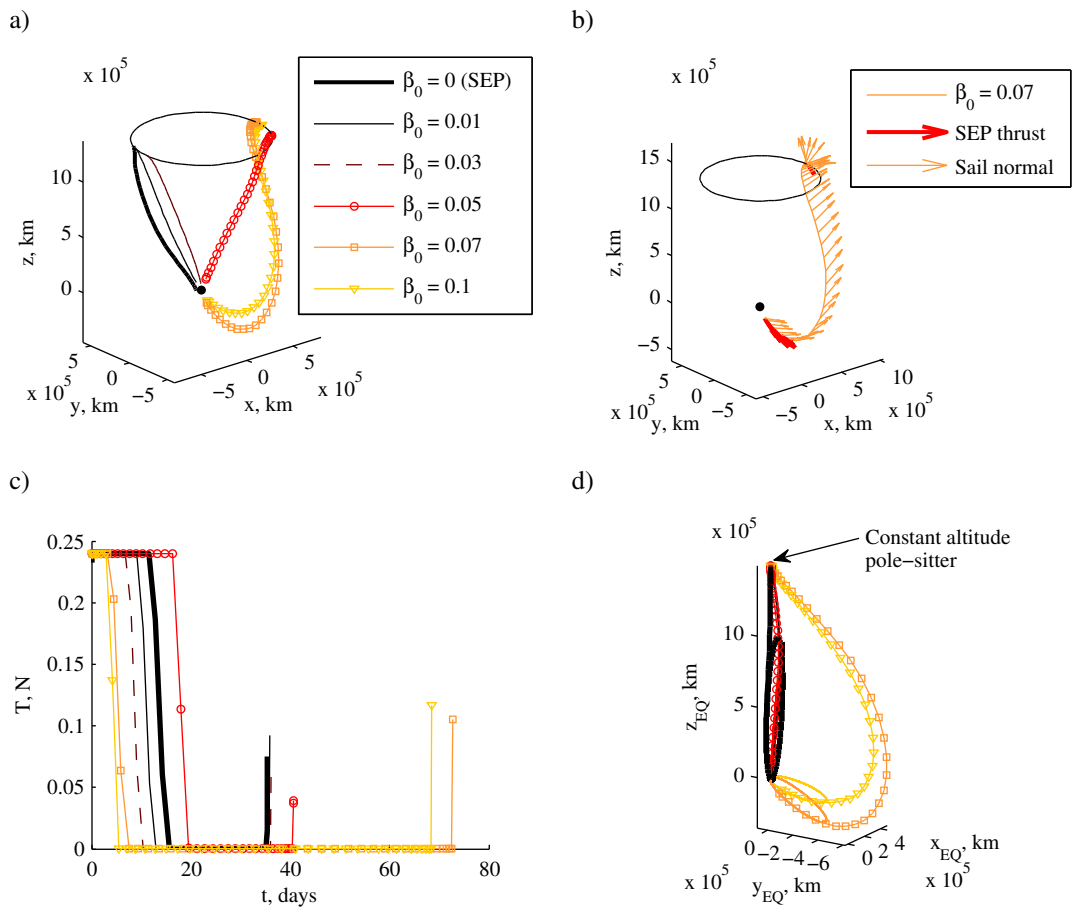
**Fig. 5.21 Constant altitude pole-sitter orbit, optimisation case 1 using a Soyuz launch from 95.4°
parking orbit and for different values of the sail lightness number, β_0. a) Transfers in CR3BP
frame. b) Transfer in CR3BP frame with SEP and solar sail acceleration vectors for β_0 =
0.07. c) Thrust profiles. d) Transfers in Earth inertial reference frame including the launch
phase target orbit.**

Table 5.10 Constant altitude pole-sitter using hybrid sail propulsion, optimisation cases 1 and 2: minimised mass in parking orbit, m_{park}, and maximised injection mass at pole-sitter orbit, m_f, for a range of solar sail lightness numbers, β_0.

	Parking orbit inclination, deg	Optimisation case	Objective function	β_0					
				0 (SEP)	0.01	0.03	0.05	0.07	0.1
Soyuz	95.4	1	m_{park}	5648	5642	5636	5626	5571	5548
Ariane	51.6	2	$-m_f$	4455	4481	4571	4611	4634	4663

5.6.2   Optimal hybrid pole-sitter orbit

While for the constant altitude pole-sitter orbit a range of sail lightness numbers were considered, for the transfer to the optimal hybrid pole-sitter orbit only the lightness number that is used in the orbit itself will be investigated, i.e. $\beta_0 = 0.035$. The results for both optimisation cases are provided in Table 5.11, which also includes the results for the optimal SEP pole-sitter orbit (using pure SEP in the transfer) for comparison purposes. More detailed results for optimisation case 2 are presented in Fig. 5.22, which again clearly demonstrates the scalability between the Soyuz and Ariane 5 launches.

The table shows that, once again, hybrid propulsion establishes a decrease in the mass required in the parking orbit for optimisation case 1 and an increase in the mass injected into the pole-sitter orbit for optimisation case 2. In both cases the gain is approximately 60 kg. Moreover, comparing the thrust magnitudes required for optimisation case 2, another clear advantage of hybrid sail propulsion emerges: while the mass injected into the pole-sitter orbit is greater than for the pure SEP case, the maximum thrust magnitude required to maintain the spacecraft in orbit is lower. This directly follows from the fact that part of the required acceleration is provided by the solar sail and the demand on the SEP thruster is therefore less.
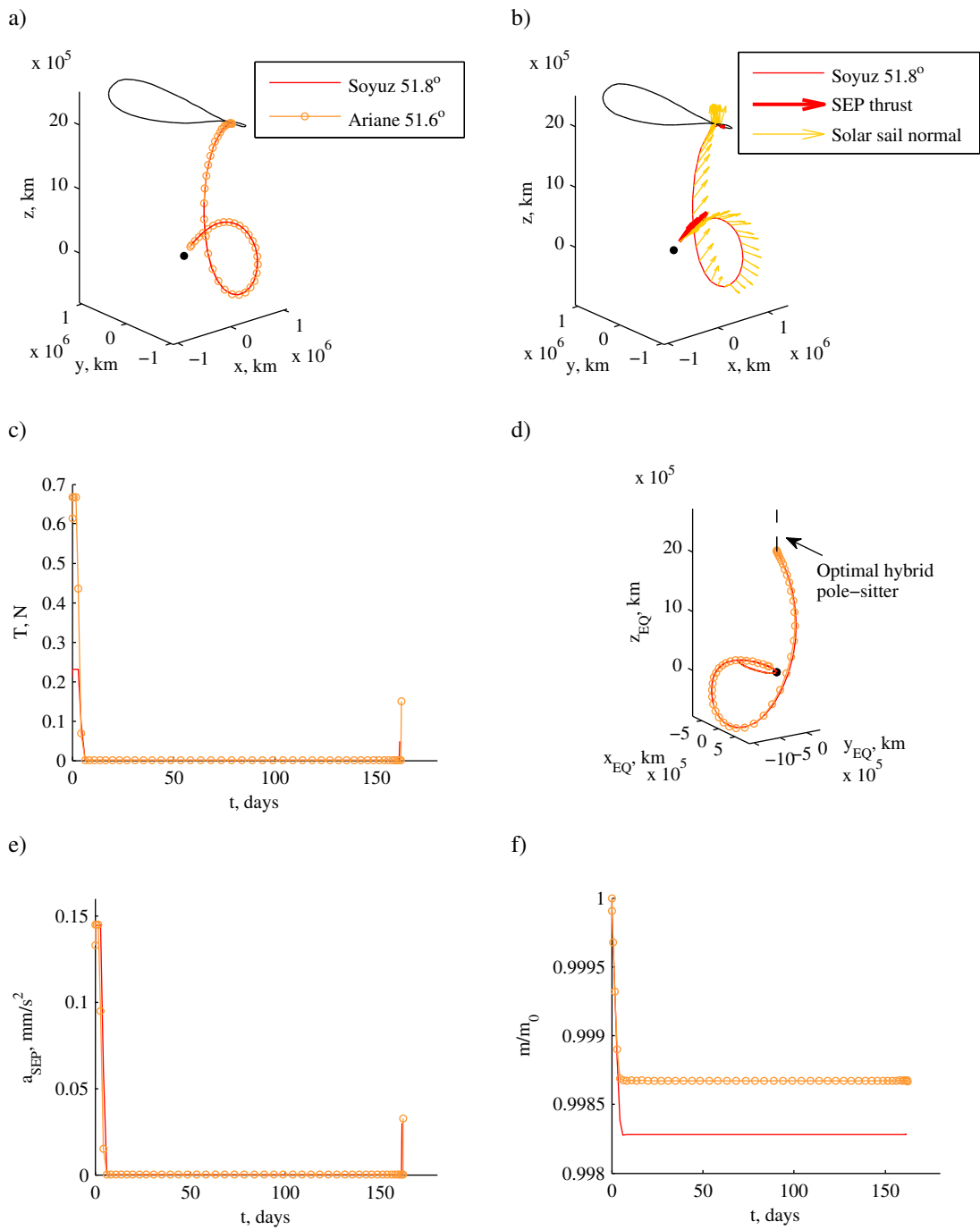
Fig. 5.22 Optimal hybrid pole-sitter orbit, optimisation case 2. a) Transfers in CR3BP frame. b) Soyuz 51.8° transfer in CR3BP frame including SEP and solar sail acceleration vectors. c) Thrust profiles. d) Transfers in Earth inertial reference frame including the launch phase target orbit. e) Acceleration profiles. f) Ratios of current mass and mass at injection.

Table 5.11 Comparison of optimal transfers to optimal SEP ($\beta_0 = 0$) and hybrid ($\beta_0 = 0.035$) pole-sitter orbits. a) Optimisation case 1, minimised mass in parking orbit in kg. b) Optimisation case 2, maximised injected mass, m_f, in kg and maximum thrust magnitude, T_{max}, in N.

a) Case 1

	Parking orbit inclination, deg	SEP optimal pole-sitter	Hybrid optimal pole-sitter,
Soyuz	95.4	5682	5621
Ariane	51.6	11716	11633

b) Case 2

	Parking orbit inclination, deg	SEP optimal pole-sitter		Hybrid optimal pole-sitter	
		m_f	T_{max}	m_f	T_{max}
Soyuz	51.8	1537	0.269	1595	0.231
Ariane	51.6	4439	0.775	4599	0.667

The transfers developed throughout this chapter serve the purpose of allowing an estimate of the pole-sitter mission performance in terms of payload capacity and/or mission lifetime. Clearly, to maximise these performance indices, the results of the second optimisation case will serve as starting point. To show once more the potential of an Ariane 5 launch over a Soyuz launch and, moreover, to show the potential of hybrid propulsion, Fig. 5.23 shows the payload mass that can be carried onboard the spacecraft for a particular lifetime using these maximised injected masses. Reference 142 provides details on the approach to obtain these results. The mass budget used in these calculations is very similar to the one presented for the displaced GEO in Chapter 3 in Eq. (3.36). Only slight differences exist as the mass budget considered here uses a slightly more conservative estimate for the specific performance of the solar arrays and a slightly smaller sail size since the sail area does not include the area of the thin film solar cells. Furthermore, radiators are included to dissipate excess power generated by the thin film solar cells since the attitude of the thin films relative to the Sun is constrained by the optimal attitude of the sail. Therefore, while for the SEP case the solar panels can be tilted away from the Sun when power is not needed, this cannot be achieved with the thin film solar cells. Finally, a relatively conservative estimate is used for the fraction of the spacecraft dry mass reserved for other subsystems, $f_{other} = 0.3$, and margins are included (as was done in Fig. 3.19) with $\varepsilon_{old} = 1.05$ for well-proven technologies and $\varepsilon_{new} = 1.2$ for new technologies. The payload mass in Fig. 5.23 thus represents the real payload mass reserved for the scientific and/or telecommunication payload of the mission.

The figure clearly illustrates the increase in payload mass for a particular lifetime that an Ariane 5 launch can provide as well as the increase in both payload mass and mission lifetime that hybrid sail propulsion can establish. Particularly, the lifetime is extended by 2.0 and 2.4 years for a 100 kg payload mass[142] and for a Soyuz and Ariane 5 launch, respectively.
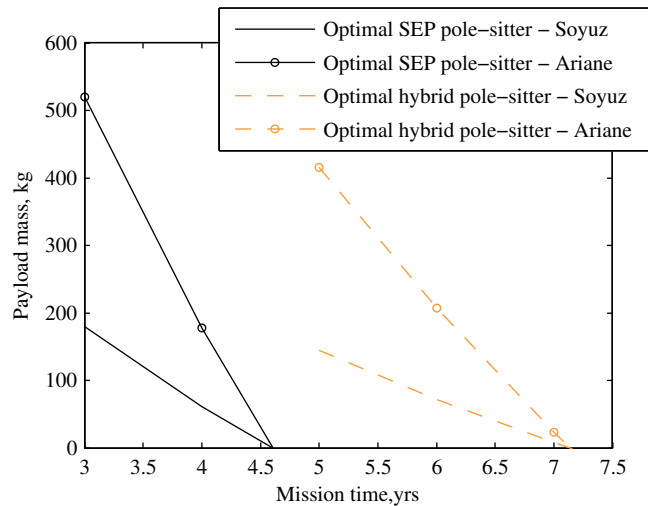
Fig. 5.23 Payload mass as a function of the mission lifetime for the optimised pole-sitter injection masses and for both the SEP and hybrid optimal pole-sitter orbits and for a Soyuz and Ariane 5 launch.[142]

5.7   Results validation

The optimality of the results for the transfers associated with the displaced geostationary orbit was verified through an indirect approach by analytically deriving the optimality conditions and solving the associated Hamiltonian boundary-value problem, see Section 4.6. Although a similar approach could be adopted to verify the optimality of the Earth to pole-sitter transfers developed in this chapter, a different method is preferred here in order to also test the performance of PSOPT against another direct pseudospectral method. A subset of the transfers considered in this chapter will therefore be optimised using the pseudospectral optimal control solver GPOPS.[112] The main difference with PSOPT is the fact that, while PSOPT implements a Legendre (or Chebyshev) pseudospectral method, GPOPS is an implementation of the Gauss pseudospectral method.[107, 149, 150] The collocation points are therefore the Legendre-Gauss points, as explained in Section 2.3.3. Another difference between the two optimal control solvers is the fact that PSOPT is coded in C++, while GPOPS is implemented in MATLAB®. Otherwise, the two software packages are very

similar: GPOPS can solve the NLP problem using the same NLP solver employed by PSOPT (i.e. IPOPT or SNOPT), it has the ability to solve multiple-phase optimal control problems, it uses automatic differentiation to obtain any problem related derivatives, and so on.

In this section, GPOPS (with suggested default settings) will be used to optimise the pure SEP transfers. Furthermore, for illustration purposes, only the transfer to the constant altitude pole-sitter orbit and for minimising the mass in the parking orbit, i.e. optimisation case 1, will be considered. The same problem as described throughout Sections 5.2 to 5.4 is implemented in GPOPS, except that only the expo-elliptic trajectories are considered as initial guess since PSOPT already demonstrated the equal performance of the two types of initial guesses, as discussed in Section 5.4.

Table 5.12 Comparison of PSOPT and GPOPS performances for the transfer to the constant altitude pole-sitter orbits and minimising the mass in the parking orbit (i.e. optimisation case 1).

| | Parking orbit inclination, deg | Minimised mass in parking orbit, kg | |
		PSOPT	GPOPS
Soyuz	51.8	5691	5691
	64.9	5675	5675
	70.4	5666	5666
	95.4	5648	5647
Ariane	51.6	11719	11724

The results are presented in Table 5.12 and in Fig. 5.24, which show a very clear resemblance between the results obtained with PSOPT and GPOPS. The only significant difference can be observed in the point of injection into the pole-sitter orbit for a Soyuz launch phase from a 95.4° parking orbit and for an Ariane launch. However, it was already previously concluded that this injection point is of negligible influence on the minimised mass in the parking orbit. The results in Table 5.12 and Fig. 5.24a confirm this, because for a 95.4° Soyuz launch, the mass required in the parking orbit is nearly the same for both solvers, while the injection point differs greatly. The point of injection is also different when considering an Ariane launch, but from Table 5.12 and Fig. 5.24f it becomes clear that GPOPS converged prematurely to a slightly underperforming solution. However, the difference in mass required in the parking orbit with the optimal solution found by PSOPT is

very small (only 5 kg). The optimality of the results generated by PSOPT can therefore be confirmed.
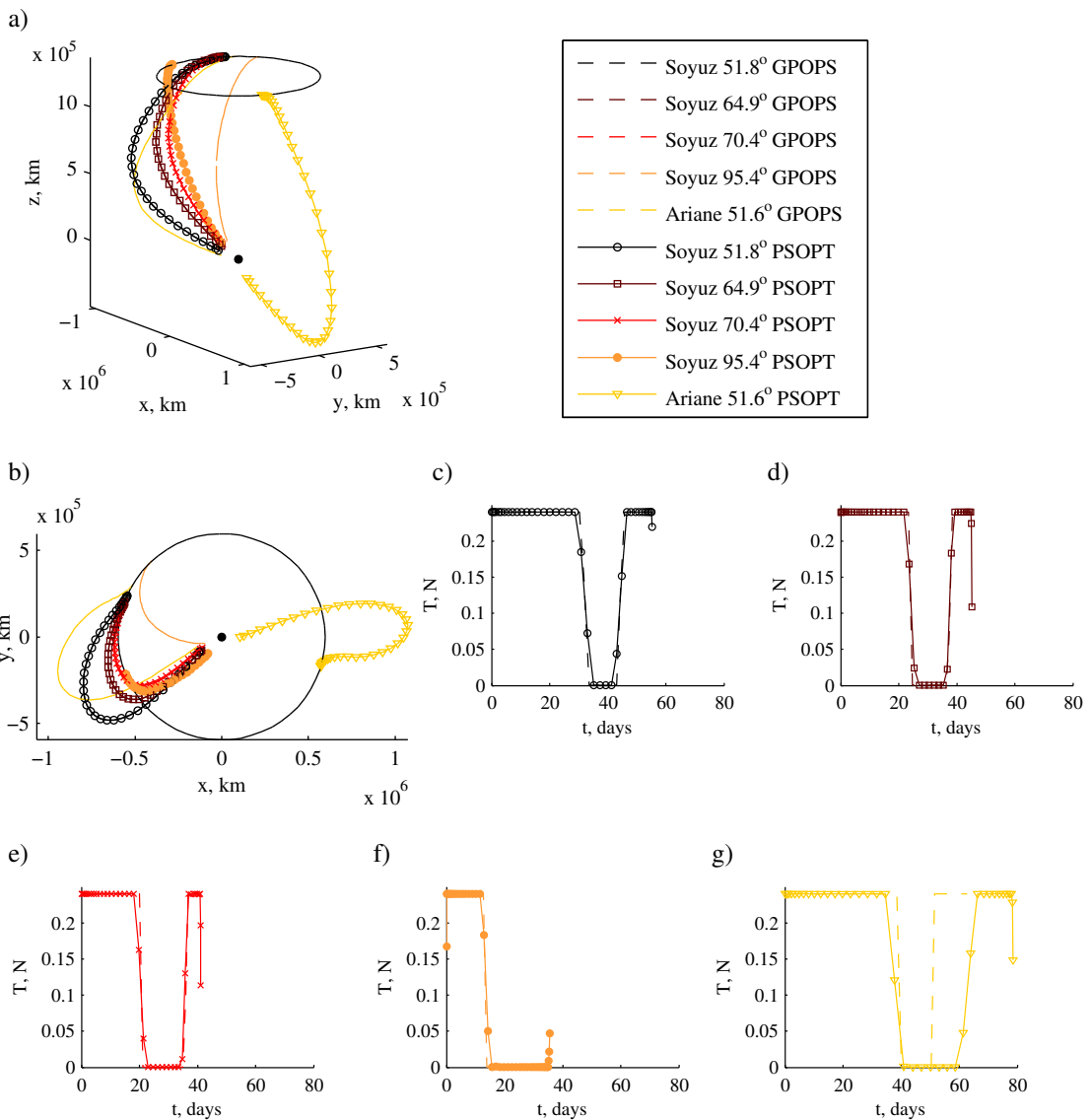
Fig. 5.24 Comparison of optimal transfers to constant altitude pole-sitter orbits generated with GPOPS (dashed lines) and PSOPT (marked lines). a-b) Transfer phases in CR3BP frame. c-g) Thrust profiles for a Soyuz launch from a 51.8° (c), 64.9° (d), 70.4° (e) and 95.4° (f) parking orbit and for an Ariane launch (g).

5.8   Chapter summary

In this chapter, optimal transfers from LEO to a range of true pole-sitter orbits have been investigated in order to evaluate their accessibility. The pole-sitter orbits considered include a 0.01 AU constant altitude pole-sitter orbit, a tilted pole-sitter orbit with minimum and maximum Earth-spacecraft distances of 0.01 AU and 0.018 AU, respectively, and fuel-

optimal pole-sitter orbits using pure SEP and hybrid propulsion (with a sail lightness number of $\beta_0 = 0.035$). Both Soyuz and Ariane 5 launches have been considered (from a range of inclined parking orbits), for which an accurate launch model has been developed that was successfully verified against a set of reference missions provided in the Soyuz launch manual. Furthermore, either the mass required in LEO has been minimised for a 1000 kg spacecraft to be inserted into the pole-sitter orbit to minimise launch and mission costs, or the spacecraft mass upon injection into the pole-sitter orbit has been maximised to allow for a maximum mission lifetime and/or payload mass capacity.

To generate an initial guess for the transfer, a new shape-based approach has been developed that makes use of expo-elliptic sinusoids and can be regarded as a generalisation of the exponential sinusoids. Its performance has been successfully verified against an initial guess based on ballistic manifold-like trajectories that wind onto the pole-sitter orbit. Furthermore, it has been demonstrated that the expo-elliptic shape outperforms the conventional exponential sinusoidal shape on a range of test cases (including the pole-sitter transfer) on the satisfaction of the boundary conditions and the amount of thrust required throughout the transfer.

From the ballistic manifold-like trajectories it can be concluded that, for minimising the mass in LEO, the largest Soyuz parking inclination of 95.4°, which is closest to the inclination of the pole-sitter orbit, is most optimal. Contrary, for maximising the mass injected into the pole-sitter orbit, the smallest Soyuz parking orbit inclination of 51.8° can be more optimal, because the performance of Soyuz from Earth into this parking orbit is much greater than into higher inclined parking orbits. This can eventually translate into a higher mass injected into the pole-sitter orbit. Furthermore, it can be concluded that for minimising the mass required in LEO to inject a 1000 kg spacecraft into the pole-sitter orbit, not all ballistic transfers are feasible as the mass required in LEO for the constant and titled pole-sitter orbits exceeds the Soyuz launch vehicle performance into the lower inclination parking orbits.

Because the minimum Earth-spacecraft distance is equal for the constant altitude and tilted pole-sitter orbits (at winter solstice), the low-thrust transfers to both types of pole-sitter orbits perform equally well as the spacecraft is always injected at the point closest to the Earth. The altitude of the pole-sitter orbit thus has a greater influence on the performance of the transfer than the time of year at which the spacecraft is injected into the pole-sitter orbit. This leads to a flexible launch window for the transfer to the constant altitude pole-sitter orbit. Due to the larger Earth-spacecraft distance for the optimal SEP pole-sitter orbit, the

results are slightly worse than for the constant and tilted orbits: a minimised mass in the parking orbit of 5682 kg (Soyuz launch) and a maximised mass in the SEP pole-sitter orbit of 4439 kg (Ariane launch) with a corresponding maximum thrust magnitude of 0.775 N.

Finally, introducing hybrid propulsion to the transfer to the constant altitude and optimal hybrid pole-sitter orbits showed the potential of hybrid propulsion as it significantly decreases the mass required in the parking orbit or alternatively increases the mass injected into the pole-sitter orbit. Depending on the sail lightness number, a gain of 100 kg in the parking orbit can be achieved and an additional 208 kg can be injected into the constant altitude pole-sitter orbit. As final proof of the potential of hybrid propulsion, the maximised injected masses into the optimal hybrid pole-sitter orbit have been used to determine the pole-sitter mission performance in terms of payload capacity and mission lifetime. This analysis showed that, for a true payload of 100 kg, the lifetime with respect to the optimal SEP pole-sitter orbit can be increased by 2.0 and 2.4 years for a Soyuz and Ariane 5 launch, respectively.

Finally, a subset of the cases considered throughout the chapter have been optimised with an alternative pseudospectral optimal control solver, GPOPS, to establish the validity of the results.

Chapter 6

Optimal Earth to pole-sitter transfers-low-thrust launch

In order to obtain a full low-thrust trajectory from low Earth orbit to the pole-sitter orbit, this chapter investigates the possibility of replacing the upper-stage launch phase with a low-thrust launch phase, as discussed previously, using the SEP thruster. The approach to design this low-thrust launch phase will be outlined in Section 6.1. Since the result will be a multi-revolution, long duration spiral, the objective will be to minimise the time spent in the spiral. For that, a locally optimal steering law will be derived in Section 6.1.1 and the use of orbital averaging to reduce the computational effort for integrating such a spiral will be explained in Section 6.1.2. The resulting optimal control problem will then be discussed in Section 6.2. Although in the previous chapter a large number of pole-sitter orbits have been investigated (i.e. constant altitude, tilted and optimal pole-sitter orbits), this chapter will only consider a subset of transfers to the constant altitude and optimal SEP pole-sitter orbits for which the results are presented in Sections 6.3.1 and 6.3.2, respectively. An analysis of the time spent in eclipse during the spiral will subsequently be provided in Section 6.3.3. Finally, in Section 6.4, an assessment of the accuracy of the orbital averaging technique will be made and the chapter finishes with conclusions.

6.1   Low-thrust spiral design approach

To obtain a full low-thrust trajectory from the parking orbit to the pole-sitter orbit, the upper-stage launch phase as designed in Section 5.2.1 is replaced by a low-thrust spiral, see Fig. 6.1. To model the low-thrust spiral, it is assumed that the optimal transfer phases as

obtained throughout Chapter 5 remain unchanged. The problem then becomes to find the thrust profile in each revolution of the spiral such that the spiral starts from the parking orbit and that the end of the spiral coincides with the start of the optimised transfer phase. Furthermore, with the spiral expected to take many months, up to more than a year, the objective is to minimise the time spent in the spiral.
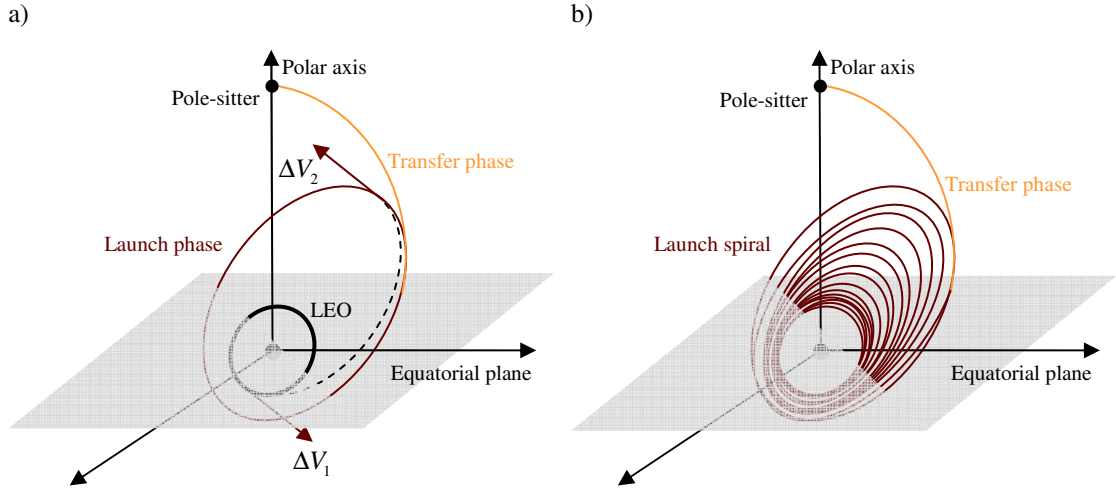
Fig. 6.1 Comparison of high-thrust launch phase (a) and low-thrust launch phase (b).

6.1.1 Locally optimal steering laws

To minimise the time spent in the spiral, locally optimal steering laws are derived to maximise the time rates of change of the orbital elements. The orbital elements have previously been defined in Fig. 2.2, where the reference direction is chosen to be the x_{EQ}-axis of the inertial, Earth fixed equatorial reference frame of Fig. 5.7. The optimal steering laws are similar to what has been suggested by Gao[151] and are illustrated in Fig. 6.2:

- To change the semi-major axis, a tangential steering law is applied around perigee over an angle $2p_s\pi$.
- To change the eccentricity, a so-called inertial steering law is used where the spacecraft thrusts perpendicular to the line of apsides around apogee over an angle $2p_e\pi$.
- To change the inclination, an out-of-plane steering law is applied around the nodal crossings over an angle $p_i\pi$ with opposite thrusting direction along the ascending and descending nodes.

Note that the third steering law is a simplification of the approach suggested in Reference 151, resulting in a slightly underperforming steering law. However, this simplification is assumed to be valid because the required inclination changes are only minimal (a maximum of 0.5°, see for example Table 5.6).

These locally optimal steering laws are applied in each revolution of the spiral. The controls in each revolution are therefore the thrust magnitudes of the in-plane, $f_{in} \geq 0$, and out-of-plane, $f_{out} \geq 0$, thrust accelerations and the parameters $-1 \leq p_s \leq 1$, $-1 \leq p_e \leq 1$ and $-1 \leq p_i \leq 1$ that represent the fraction of the orbit around perigee, apogee and the nodal line where one of three controls is applied. The sign of these three parameters indicate an increase (positive) or decrease (negative) in the corresponding orbital element.
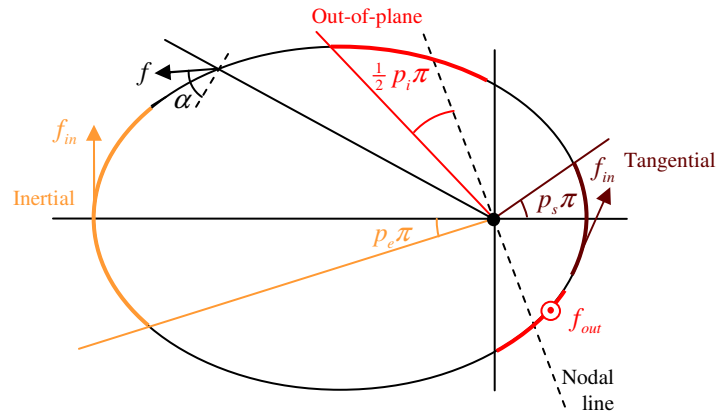
Fig. 6.2 Illustration of the launch spiral steering laws.

6.1.2 Orbital averaging

To investigate the influence of different control profiles on the launch spiral through an integration of the full set of equations of motion would require a huge computational effort. Therefore, the orbital averaging technique is used, which approximates the equations of motion by calculating the change in the orbital elements during a single revolution and dividing this change by the orbital period.

For the launch spiral, this change in the orbital elements can be computed when starting from Gauss' variational equations as a function of the eccentric anomaly, E :[38]

$$\frac{da}{dE} = \frac{2a^3}{\mu_C}\left(f_r e \sin E + f_t \sqrt{1-e^2}\right)$$

$$\frac{de}{dE} = \frac{a^2}{\mu_C}\left[f_r\left(1-e^2\right)\sin E + f_t\left(2\cos E - e - e\cos^2 E\right)\sqrt{1-e^2}\right]$$

$$\frac{di}{dE} = \frac{a^2}{\mu_C}f_n\left(\frac{\cos\omega\cos E - e\cos\omega}{\sqrt{1-e^2}} - \sin\omega\sin E\right)\left(1-e\cos E\right) \tag{6.1}$$

$$\frac{d\Omega}{dE} = \frac{a^2}{\mu_C}f_n\left(\frac{\sin\omega\cos E - e\sin\omega}{\sqrt{1-e^2}} + \cos\omega\sin E\right)\frac{\left(1-e\cos E\right)}{\sin i}$$

$$\frac{d\omega}{dE} = -\cos i\frac{d\Omega}{dE} - \frac{a^2}{e\mu_C}\left[f_r\left(\cos E - e\right)\sqrt{1-e^2} - f_t\left(2-e^2 - e\cos E\right)\sin E\right]$$

with μ_C the gravitational parameter of the central body. The variational equations are usually given in a form in which they are differentiated with respect to time, but a change of independent variable is made by dividing those equations by:

$$\frac{dE}{dt} = \frac{na}{r} + \frac{1}{nae}\left[f_r\left(\cos\theta - e\right) - f_t\left(1+\frac{r}{a}\right)\sin\theta\right] \approx \frac{na}{r} \tag{6.2}$$

with n the mean motion. The approximation on the right hand side of Eq. (6.2) is obtained by assuming that the thrust acceleration is small compared to the gravitational acceleration. The same assumption thus applies to Eq. (6.1).

The radial and transverse acceleration components, f_r and f_t, respectively, can be defined through the pitch angle, α, see Fig. 6.2, as follows:

$$f_r = f_{in}\sin\alpha, \qquad f_t = f_{in}\cos\alpha \tag{6.3}$$

The pitch angle can be made more explicit when considering the separate steering laws. For the tangential steering law, the pitch angle has to equal the flight path angle such that the in-plane acceleration is parallel to the velocity vector:[8]

$$\sin\alpha = \frac{e\sin E}{\sqrt{1-e^2\cos^2 E}}, \qquad \cos\alpha = \sqrt{\frac{1-e^2}{1-e^2\cos^2 E}} \tag{6.4}$$

Note that these expression can also be derived by determining the pitch angle for which the change in semi-major axis is maximised, i.e. by substituting Eq. (6.3) into Eq. (6.1) and evaluating $\partial\left(da/dE\right)/\partial\alpha = 0$ and $\partial^2\left(da/dE\right)/\partial\alpha^2 \leq 0$.[151]

For the inertial steering law, the pitch angle should equal the true anomaly:

$$\sin \alpha = \frac{\sin E \sqrt{1-e^2}}{1-e\cos E}, \qquad \cos \alpha = \frac{\cos E - e}{1-e\cos E} \qquad (6.5)$$

while for the out-of-plane steering law, the radial and transverse accelerations are simply set equal to zero. Contrary, the acceleration component in normal direction, f_n, is set equal to zero for the tangential and inertial steering laws and is set unequal to zero for the out-of-plane steering law. Summarised, the three acceleration components can be described by:

$$f_r = \begin{cases} f_{in} \dfrac{e\sin E}{\sqrt{1-e^2\cos^2 E}} \\ f_{in} \dfrac{\sin E\sqrt{1-e^2}}{1-e\cos E} \\ 0 \end{cases} \qquad f_t = \begin{cases} f_{in}\sqrt{\dfrac{1-e^2}{1-e^2\cos^2 E}} \\ f_{in} \dfrac{\cos E - e}{1-e\cos E} \\ 0 \end{cases} \qquad f_n = \begin{cases} 0 & \text{Tangential} \\ 0 & \text{Inertial} \\ f_{out} & \text{Out-of-plane} \end{cases} \qquad (6.6)$$

Substituting Eq. (6.6) into Eq. (6.1) and integrating over the eccentric anomalies where the separate steering laws are applied, provides the change in orbital elements after one revolution. Subsequently dividing by 2π (instead of the orbital period since the eccentric anomaly is used rather than time) gives the sought for approximation of the equations of motion:

$$\frac{d\mathbf{x}_{oe}}{dt} = \frac{1}{2\pi} \int_{E_0}^{E_f} \frac{d\mathbf{x}_{oe}}{dE} dE \qquad (6.7)$$

with $\mathbf{x}_{oe}$ the vector of orbital elements, $\mathbf{x}_{oe} = \begin{bmatrix} a & e & i & \Omega & \omega \end{bmatrix}^T$. The integral represents the change in an orbital element during one revolution, assuming all other orbital elements are constant except for the eccentric anomaly.[145]

The full derivation has been performed by Gao,[151] and therefore only the result (adapted for the definitions used in this chapter) is provided here:

166

$$\frac{d\overline{a}}{dE} = \frac{1}{2\pi}\left(\frac{2a^3}{\mu_C}f_{in}\,\text{sign}\left(p_s\right)\int_{E_{s,0}}^{E_{s,f}}\sqrt{1-e^2\cos^2 E}\,dE + \frac{2a^3}{\mu_C}f_{in}\,\text{sign}\left(p_e\right)\sqrt{1-e^2}\left[\sin E\right]_{E_{e,0}}^{E_{e,f}}\right)$$

$$\frac{d\overline{e}}{dE} = \frac{1}{2\pi}\left(\frac{2a^2}{e\mu_C}\left(1-e^2\right)f_{in}\,\text{sign}\left(p_s\right)\left(\int_{E_{s,0}}^{E_{s,f}}\sqrt{1-e^2\cos^2 E}\,dE - \int_{E_{s,0}}^{E_{s,f}}\frac{1}{\sqrt{1-e^2\cos^2 E}}dE\right.\right.$$

$$\left.+\left[\ln\left(\sin E + \frac{1}{e}\sqrt{1-e^2\cos^2 E}\right)\right]_{E_{s,0}}^{E_{s,f}}\right)$$

$$\left.+\frac{a^2}{\mu_C}f_{in}\,\text{sign}\left(p_e\right)\sqrt{1-e^2}\left[\tfrac{3}{2}E - 2e\sin E + \tfrac{1}{4}\sin 2E\right]_{E_{e,0}}^{E_{e,f}}\right)$$

$$\frac{d\overline{i}}{dE} = \frac{1}{2\pi}\frac{a^2}{\mu_C}f_{out}\,\text{sign}\left(p_i\right)\sum_{i=1}^{2}\left[\frac{\left(1+e^2\right)\cos\omega\sin E - \tfrac{3}{2}eE\cos\omega - \tfrac{1}{4}e\cos\omega\sin 2E}{\sqrt{1-e^2}}\right.$$

$$\left.+\sin\omega\cos E - \tfrac{1}{4}e\sin\omega\cos 2E\right]_{E_{n_i,0}}^{E_{n_i,f}}$$

$$\frac{d\overline{\Omega}}{dE} = \frac{1}{2\pi}\frac{a^2}{\mu_C\sin i}f_{out}\,\text{sign}\left(p_i\right)\sum_{i=1}^{2}\left[\frac{\left(1+e^2\right)\sin\omega\sin E - \tfrac{3}{2}eE\sin\omega - \tfrac{1}{4}e\sin\omega\sin 2E}{\sqrt{1-e^2}}\right.$$

$$\left.-\cos\omega\cos E + \tfrac{1}{4}e\cos\omega\cos 2E\right]_{E_{n_i,0}}^{E_{n_i,f}}$$

$$\frac{d\overline{\omega}}{dE} = \frac{1}{2\pi}\left(\frac{-2a^2}{e^2\mu_C}\sqrt{1-e^2}f_{in}\,\text{sign}\left(p_s\right)\left[\sqrt{1-e^2\cos^2 E} + \sin^{-1}\left(e\cos E\right)\right]_{E_{s,0}}^{E_{s,f}}\right. \tag{6.8}$$

$$\left.+\frac{-a^2}{e\mu_C}f_{in}\,\text{sign}\left(p_e\right)\left[\tfrac{1}{4}\cos 2E - e\cos E\right]_{E_{e,0}}^{E_{e,f}}\right) - \cos i\frac{d\overline{\Omega}}{dE}$$

where the overbar indicates the averaged orbital elements. Equation (6.8) still includes a few terms for which no analytical expression could be found. Gao[151] approximates those terms as follows:

$$\int_{E_{s,0}}^{E_{s,f}}\sqrt{1-e^2\cos^2 E}\,dE \approx \int_{E_{s,0}}^{E_{s,f}}\left(\sqrt{1-e^2} + \left(1-\sqrt{1-e^2}\right)\sin^2 E\right)dE =$$

$$\left[\sqrt{1-e^2}E + \left(1-\sqrt{1-e^2}\right)\left(\tfrac{1}{2}E - \tfrac{1}{4}\sin 2E\right)\right]_{E_{s,0}}^{E_{s,f}} \tag{6.9}$$

$$\int_{E_{s,0}}^{E_{s,f}}\sqrt{1-e^2\cos^2 E}\,dE - \int_{E_{s,0}}^{E_{s,f}}\frac{1}{\sqrt{1-e^2\cos^2 E}}dE \approx \int_{E_{s,0}}^{E_{s,f}}\frac{-e^2\cos^2 E}{\sqrt{1-e^2 q}}dE =$$

$$\frac{-e^2}{\sqrt{1-e^2 q}}\left[\tfrac{1}{2}E + \tfrac{1}{4}\sin 2E\right]_{E_{s,0}}^{E_{s,f}} \tag{6.10}$$

where Eq. (6.10) appeared to be accurate for $q = 0.8$.[151, 152] Furthermore, the summation in Eq. (6.8) is included to account for the out-of-plane thrust arcs around both nodal crossings

and the subscripts '0' and 'f' indicate the initial and final value of the eccentricities E_s, E_e and E_{n_i} during which the tangential, inertial and out-of-plane steering laws occur, respectively.

Similar to the change in orbital elements, the change in mass can be computed by starting from Eq. (2.15):

$$\frac{d\bar{m}}{dE} = -\frac{1}{2\pi} \int_{t_0}^{t_f} \frac{T}{I_{sp}g_0} dt = -\frac{1}{2\pi} \int_{E_0}^{E_f} \frac{1}{n}(1 - e\cos E)\frac{T}{I_{sp}g_0} dE = -\frac{1}{2\pi}\frac{1}{n}\frac{T}{I_{sp}g_0}\left[E - e\sin E\right]_{E_0}^{E_f} \quad (6.11)$$

which can be written into the following form when considering the three separate steering laws:

$$\frac{d\bar{m}}{dE} = -\frac{1}{2\pi}\frac{1}{n}\frac{mf_{in}}{I_{sp}g_0}\left(E_{s,f} - e\sin E_{s,f} - \left(E_{s,0} - e\sin E_{s,0}\right) + E_{e,f} - e\sin E_{e,f} - \left(E_{e,0} - e\sin E_{e,0}\right)\right)$$

$$\quad (6.12)$$

$$-\frac{1}{2\pi}\frac{1}{n}\frac{mf_{out}}{I_{sp}g_0}\sum_{i=1}^{2}\left(E_{n_i,f} - e\sin E_{n_i,f} - \left(E_{n_i,0} - e\sin E_{n_i,0}\right)\right)$$

Equation (6.12) leads to a slightly conservative estimate of the propellant consumption as the in-plane and out-of-plane thrust components are not combined into one single thrust component.

Finally, note that the dynamics in Eq. (6.8) neglect any perturbation on the low-thrust spiral. However, it can be expected that the J_2 effect of the Earth's non-uniform gravitational field and shadowing have a significant influence on the spiral at low altitudes.[145, 152 153] Also, it can be expected that, starting from LEO, the spacecraft spends many revolutions at low altitudes and therefore inside the radiation belts. For future research, it could therefore be interesting to investigate the possibility to use the launcher's upper-stage to first raise the orbital altitude above the radiation belts and subsequently initiate the spiral. For higher altitudes in the spiral, third body perturbations from the Sun can be expected to have an influence on the dynamics of the low-thrust spiral. This could be taken into account by considering the Sun's gravity perturbation to be constant over one orbit since its period is significantly greater than the period of the spacecraft's orbit.[154] Alternatively, a double averaging technique could be employed where the second averaging takes place over the period of the Sun.[155, 156]

6.2 Optimal control problem

The objective is to find minimum-time spirals from the parking orbit up to injection into the optimised low-thrust transfer phases that were generated in the previous chapter. The objective function of the optimal control problem then becomes:

$$J = t_f \tag{6.13}$$

with t_f the final time of the transfer (and setting the initial time equal to zero, $t_0 = 0$). In order to find the optimal control profile in the spiral such that the boundary conditions are satisfied (i.e. the start of the spiral coincides with the parking orbit and the end of the spiral coincides with the start of the transfer phase) and the time of flight is minimised, the approach defined in the previous subsections is implemented in PSOPT. The state variables, $\mathbf{x}$, are the averaged orbital elements in the inertial, Earth fixed equatorial reference frame of Fig. 5.7 and the averaged spacecraft mass:

$$\mathbf{x} = \begin{bmatrix} \bar{a} & \bar{e} & \bar{i} & \bar{\Omega} & \bar{\omega} & \bar{m} \end{bmatrix}^T \tag{6.14}$$

The initial state vector is given by the parking orbit as defined in Table 5.3, while the final state vector should coincide with the initial state vector of the optimised low-thrust transfer phases of Section 5.5.1 (constant altitude pole-sitter orbit) and Section 5.5.3 (optimal SEP pole-sitter orbit), which are indicated by the subscript '$t,0$':

$$\mathbf{x}_0 = \begin{bmatrix} R_\oplus + h_{park} & 0.01 & i_{park} & \Omega_{park} & \omega_{park} & m_{park} \end{bmatrix}^T \tag{6.15}$$

$$\mathbf{x}_f = \begin{bmatrix} a_{t,0} & e_{t,0} & i_{t,0} & \Omega_{t,0} & \omega_{t,0} & m_{t,0} \end{bmatrix}^T \tag{6.16}$$

The ascending node, argument of perigee and mass in the parking orbit are free. Note that the eccentricity of the parking orbit is increased from zero to 0.01 in order for the fifth equation in Eq. (6.8) to hold, as it approaches a singularity for $e = 0$.[157] A future change to modified equinoctial elements could circumvent this problem.[145, 158, 159] However, the use of classical orbital elements is preferred here because they have a clear, intuitive physical meaning.

The controls are the parameters indicating the size of the thrust arc for each steering law and the in-plane and out-of-plane thrust magnitudes:

$$\mathbf{u} = \begin{bmatrix} p_s & p_e & p_i & T_{in} & T_{out} \end{bmatrix}^T \tag{6.17}$$

Note that the orbital averaging technique of Section 6.1.2 already reduces the size of the optimal control problem significantly by limiting it to a set of 5 control parameters in each revolution of the spiral. However, with hundreds of revolutions to be expected in the spiral, the optimisation problem would still be very large: the number of static parameters is as much as 5 times the number revolutions. However, by using a direct pseudospectral method, PSOPT reduces the problem further into a problem where the number of variables is only 5 times the number of collocation points and interpolation is used to obtain the control profile in the other revolutions.

The equations of motion used in PSOPT are given by Eqs. (6.8) and (6.12), which means that the independent variable of the optimal control problem is the eccentric anomaly rather than what is commonly used, i.e. time. This is done, because PSOPT uses a Lagrange-Gauss-Lobatto distribution to discretise the interval of the independent variable, which results in a larger concentration of nodes at the start and end of that interval. With the orbital period in the last few revolutions expected to be very long, choosing time as the independent variable could give rise to multiple nodes per revolution. Theoretically this means that the control profile can change over these last few nodes, leading to different steering laws, and consequently different equations of motion, within the same revolution. When using the eccentric anomaly as time variable, this problem does not occur since each revolution of the spiral takes an equal portion of the independent variable interval and with hundreds of spiral revolutions, the chance of multiple nodes in the last few spiral revolutions becomes negligible.

Finally, the following path constraints are included:

$$\left|p_s\right| + \left|p_e\right| \leq 1 \tag{6.18}$$

$$\sqrt{T_{in}^2 + T_{out}^2} \leq T_{\max} \tag{6.19}$$

where the first path constraint ensures that the thrust arcs for tangential and inertial steering do not overlap, while the second path constraint ensures that the total thrust magnitude does not exceed the maximum thrust magnitudes determined in Chapter 5 for the different types of pole-sitter orbits.

While new approaches were developed to obtain accurate initial guesses for the transfers associated with the displaced geostationary orbits in Chapter 4 and for the Earth to pole-sitter transfers in Chapter 5, it appeared that a simple trial and error method is sufficient to generate suitable initial guesses for the launch spiral. Moreover, considering the fact that the

inclination of the parking orbit is very close to the inclination at the start of the transfer, two dimensional initial guesses appeared to suffice.

6.3 Results

The results for the Earth to pole-sitter transfers employing a low-thrust launch phase will only be provided for a subset of the transfers considered in the previous chapter. In particular, the spiral will be computed for the transfer to the constant altitude pole-sitter orbits for optimisation case 1 (i.e., minimisation of the mass in the parking orbit for a 1000 kg spacecraft to be injected into the pole-sitter orbit) and for the transfer to the optimal SEP pole-sitter orbits for optimisation case 2 (i.e. maximising the mass injected into the pole-sitter orbit). The results are generated with PSOPT using an NLP tolerance of 10^{-4}, a maximum number of iterations of 5000 (which is never reached) and a mesh refinement that eventually generates solutions with 50 nodes and will be provided in Sections 6.3.1 and 6.3.2, respectively. Subsequently, in Section 6.3.3, an eclipse analysis will be performed for each of the optimal low-thrust spirals.

6.3.1 Constant altitude pole-sitter orbit

By implementing the optimal control problem described in Section 6.2 in PSOPT, the results as presented in Table 6.1 can be obtained. More detailed results are shown in Fig. 6.3 for the transfer employing a Soyuz launch from a 95.4° parking orbit and for an Ariane 5 launch. The results show a dramatic decrease in the mass required in the parking orbit when the low-thrust spiral, rather than the Fregat launch, is employed: on average 3276 kg (i.e. 58 percent) for a Soyuz launch and 5705 kg (i.e. 49 percent) for an Ariane 5 launch. This could allow for a significant reduction in mission cost through the use of a dual launch or even a smaller launcher. However, this comes at an equally large increase in the time of flight. Considering a Hohmann transfer time for the high-thrust launch results in launch phase times of approximately 40 days, which increases to an average of 520 days for the low-thrust spiral, which is 13 times that of the high-thrust launch phase. The reason for this is the fact that nearly 2000 revolutions are made, most of them in low Earth orbit, until enough altitude is gained to make the required substantial changes to the orbital elements.

A way to reduce the transfer time in the spiral could be by clustering multiple SEP thrusters to obtain a larger maximum thrust. For example, by adding one SEP thruster (thereby

doubling the maximum thrust magnitude) the transfer time in the spiral can be halved without a penalty on the mass required in the parking orbit.

Table 6.1 Time optimal low-thrust spirals for transfer to constant altitude pole-sitter orbits: mass in parking orbit, m_{park}, propellant consumption in spiral, $m_{prop,sp}$, and minimised time spent in spiral, t_{sp}.

| | Parking orbit inclination, deg | High-thrust launch phase | Low-thrust launch phase | | | |
		m_{park}, kg	m_{park}, incl. upper-stage and adapter, kg	m_{park}, excl. upper-stage and adapter, kg	$m_{prop,sp}$, kg	t_{sp}, days
Soyuz	51.8	5691	2408	1308	279.2	514.5
	64.9	5675	2397	1297	276.0	523.1
	70.4	5666	2393	1293	276.3	526.0
	95.4	5648	2379	1279	269.9	557.3
Ariane	51.6	11719	6014	1314	278.3	479.4
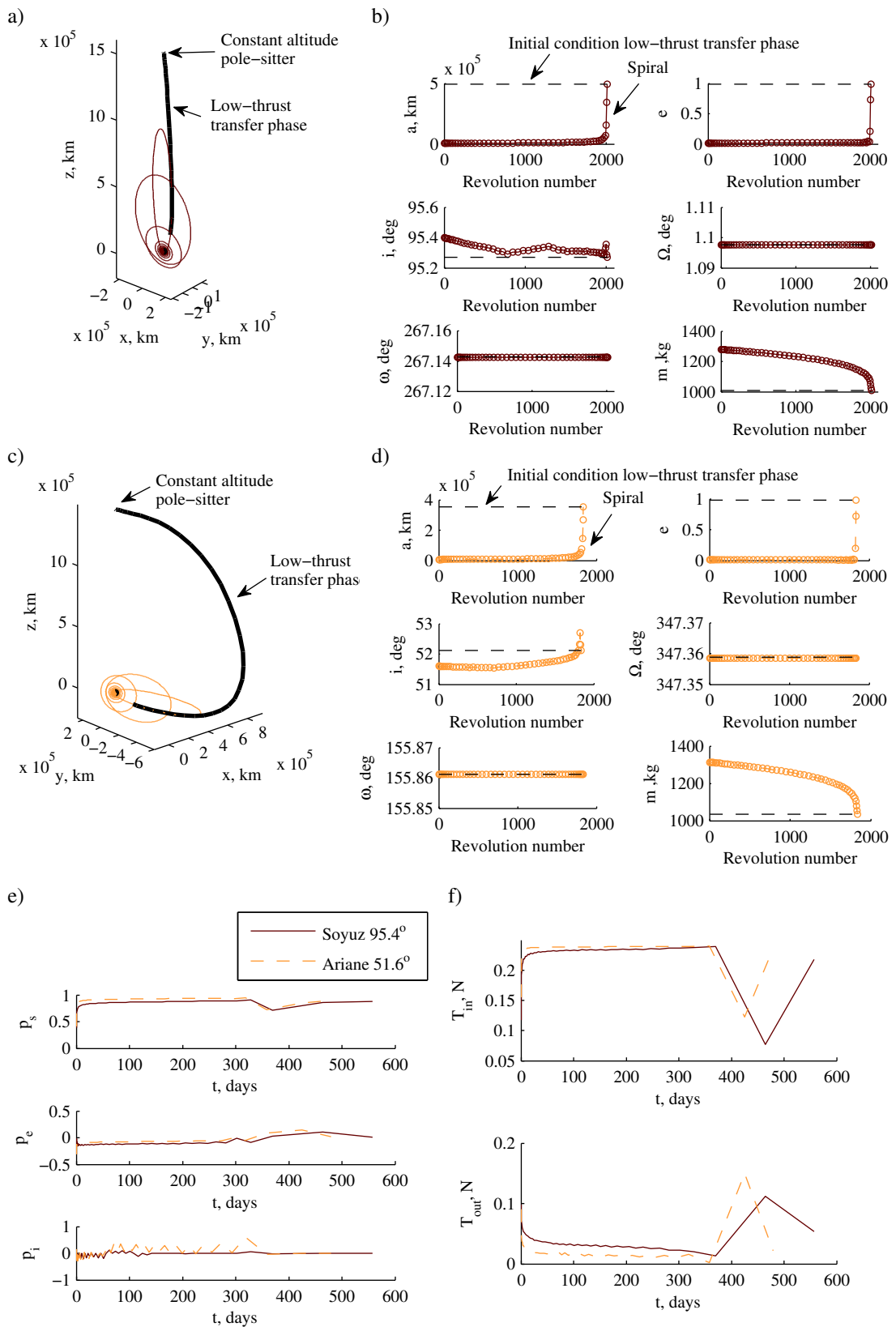
Fig. 6.3 Optimised launch spiral and transfer phase (a, c) and state (b, d) and control (e, f) profiles for a transfer to the constant altitude pole-sitter and for a Soyuz launch (95.4° parking orbit) and Ariane 5 launch.

6.3.2 Optimal SEP pole-sitter orbit

Rather than minimising the mass in the parking orbit, Chapter 5 also investigated the option of maximising the mass injected into the pole-sitter orbit. In order to determine this maximised mass using a minimum-time spiral, it is assumed that the mass in the parking orbit equals the maximum launcher performance provided in Table 5.3. However, since the upper-stage and adapter do not need to be carried along in the spiral, the masses of those elements are subtracted. The resulting mass in the parking orbit is therefore 6085 and 14300 kg for a Soyuz (51.8° parking orbit) and Ariane 5 launch, respectively.

Although this approach will change the mass injected into the optimal low-thrust transfer phases designed in Section 5.5.3, Chapter 5 has illustrated that the transfer is fully scalable with the mass if the maximum thrust magnitude changes accordingly, indicating that the optimal transfer phase will not change for a different mass at the start of the transfer. Through scaling, the mass injected into the pole-sitter orbit can be computed by multiplying the mass injected into the low-thrust transfer phase by a factor 0.974 that can be derived from Fig. 5.20f. Clearly, with a larger mass injected into the pole-sitter orbit, the maximum thrust required throughout the mission lifetime will also change. Therefore, the same iterative approach as used throughout Chapter 5 to converge to the correct maximum thrust magnitude is adopted in this section to determine the available thrust in the low-thrust spiral.

The results are presented in Table 6.2 and Fig. 6.4. The table again demonstrates the gains that the low-thrust launch phase can establish over the high-thrust launch phase. The mass injected into the pole-sitter orbit can be increased by a factor 2.95 and 2.41 for a Soyuz and Ariane 5 launch, respectively. However, again, this improved performance comes at the cost of a long time of flight, namely approximately 800 days in the low-thrust spiral. Furthermore, rather high maximum thrust magnitudes, especially for an Ariane 5 launch, would be required.

Finally, Fig. 6.4 again shows the scalability of the transfer with the mass (i.e. as long as the maximum thrust magnitude is allowed to scale accordingly, i.e. the maximum acceleration is kept constant), as the low-thrust spirals for both the Soyuz and Ariane 5 launches are very similar. Any differences can, amongst others, be attributed to the fact that the parking orbit is slightly different for the two cases. Since the parking orbit altitude of the Ariane 5 launcher is higher than for the Soyuz launcher, this could also explain the shorter spiral time for the Ariane 5 case. Further differences between the two sets of results are introduced by the fact that the end conditions (i.e. the initial state vector of the low-thrust transfer phase) are slightly different.

Table 6.2 Time optimal low-thrust spirals for transfer to optimal SEP altitude pole-sitter orbits: mass injected into pole-sitter orbit, m_f, mass in parking orbit, m_{park}, propellant consumption in spiral, $m_{prop,sp}$, minimised time spent in spiral, t_{sp}, and maximum thrust magnitude, T_{max}.

| | Parking orbit inclination, deg | High-thrust launch phase | | Low-thrust launch phase | | | |
		m_f, kg	m_{park}, kg	$m_{prop,sp}$, kg	m_f, kg	t_{sp}, days	T_{max}, N
Soyuz	51.8	1537	6085	1427	4537	811.5	0.794
Ariane	51.6	4439	14300	3310	10704	791.4	1.873
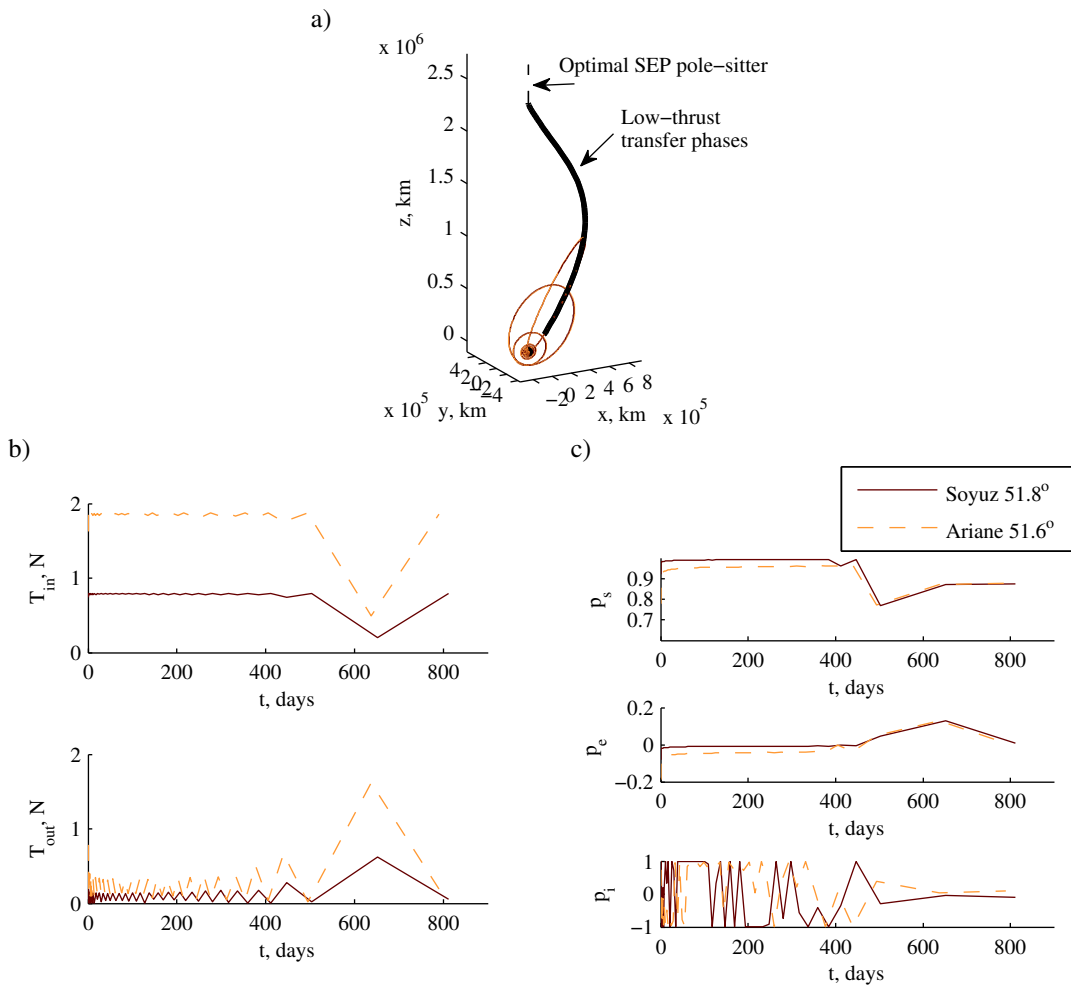
Fig. 6.4 Optimised launch spiral and transfer phase (a) and control profiles (b, c) for a transfer to the optimal SEP pole-sitter for a Soyuz launch (51.8° parking orbit) and Ariane 5 launch.

6.3.3 Eclipse analysis

The dynamics of the spacecraft in the low-thrust spiral, see Eq. (6.8), did not include the restrictions that eclipses impose on the use of the SEP thruster. However, it can be expected that during eclipses, limited or no thrust is available, which will have an influence on the low-thrust spiral, and an investigation of the time spent in eclipse is therefore required. This section provides a preliminary analysis of this time spent in eclipse.

For this, the spiral is transformed from the inertial, Earth fixed equatorial reference frame depicted in Fig. 5.7 to the Earth fixed ecliptic reference frame $EC(x_{EC}, y_{EC}, z_{EC})$ shown in Fig. 6.5. This reference frame is centred at the Earth with the (x_{EC}, y_{EC})-plane in the ecliptic plane and the x_{EC}-axis pointing away from the Sun at all times. Note that this reference frame is very similar to the frame defined to analyse the displaced geostationary orbit in Chapter 3, see Fig. 3.8, but is rotated to have the (x_{EC}, y_{EC})-plane in the ecliptic plane. The result is that the shadow of the Earth is always directed along the x_{EC}-axis. When the Sun's rays are furthermore assumed to be parallel to the x_{EC}-axis, the spacecraft is in eclipse when the following conditions are satisfied:

$$x_{EC} > 0, \quad \sqrt{y_{EC}^2 + z_{EC}^2} < R_{\oplus} \tag{6.20}$$
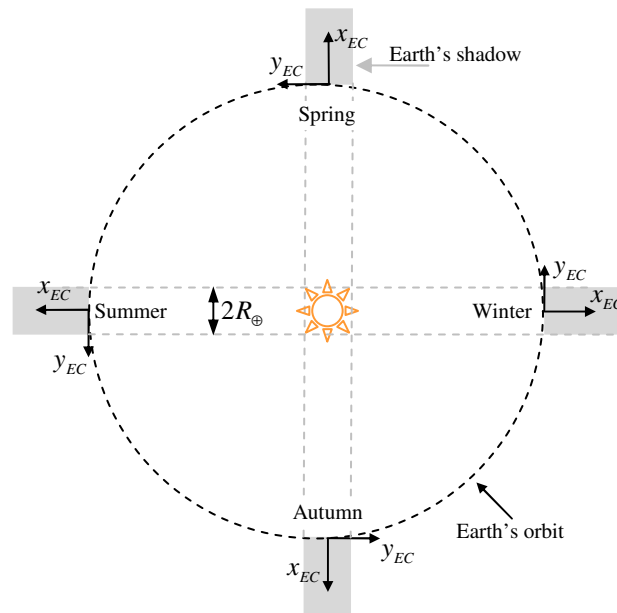
Fig. 6.5 Schematic of reference frame to evaluate the eclipse time in the low-thrust spiral.

176

By monitoring the time of entering and exiting the Earth's shadow and summing these occurrences, the total time spent in eclipse can be determined. The result in terms of the time spent in eclipse as a percentage of the total time elapsed during the spiral is shown in Fig. 6.6. A detailed illustration of the time in eclipse is provided in Fig. 6.7 for the transfer from a 51.8° parking orbit (i.e. for a Soyuz launch), which shows the spiral in the newly defined reference frame of Fig. 6.5, where black arcs indicate the time that the spacecraft is in eclipse.

Figure 6.6 clearly shows that, as expected, most of the eclipses occur at the start of the transfer when the spacecraft is at low altitudes. The time spent in eclipse in that part of the spiral is significant and can be as much as 40 percent of the time. However, it highly depends on the time of year and value of the right ascension of the ascending node at the start of the spiral. For example, the initial revolutions of the spiral starting from the 95.4° parking orbit are almost perpendicular to the direction of the sunlight, while those for the spiral starting from the other parking orbits are parallel to the direction of the sunlight. In the latter case, the spiral spends much of its time 'behind' the Earth.

Towards the end of the spiral, the spacecraft spends much less time in eclipse and the percentage of time spent in eclipse therefore decreases, to an average of 5.0 percent. This corresponds to a total eclipse time of 25 days. Due to the dependency of the time in eclipse on the time of year and ascending node at the start of the spiral, including these variables in the objective function could possibly decrease the eclipse time. However, this will come at the cost of an increase in the time of flight and/or propellant consumption.
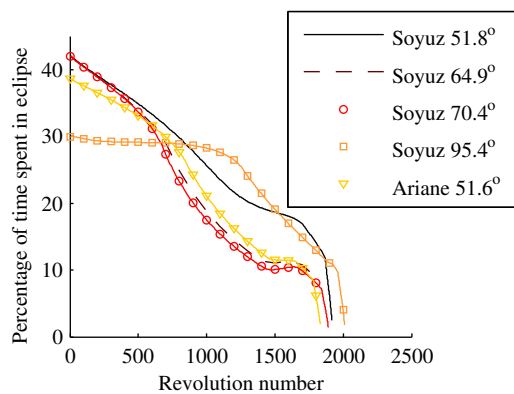
Fig. 6.6 Percentage of the time spent in eclipse during the low-thrust spiral to the constant altitude pole-sitter orbit.

a)

b)

c)
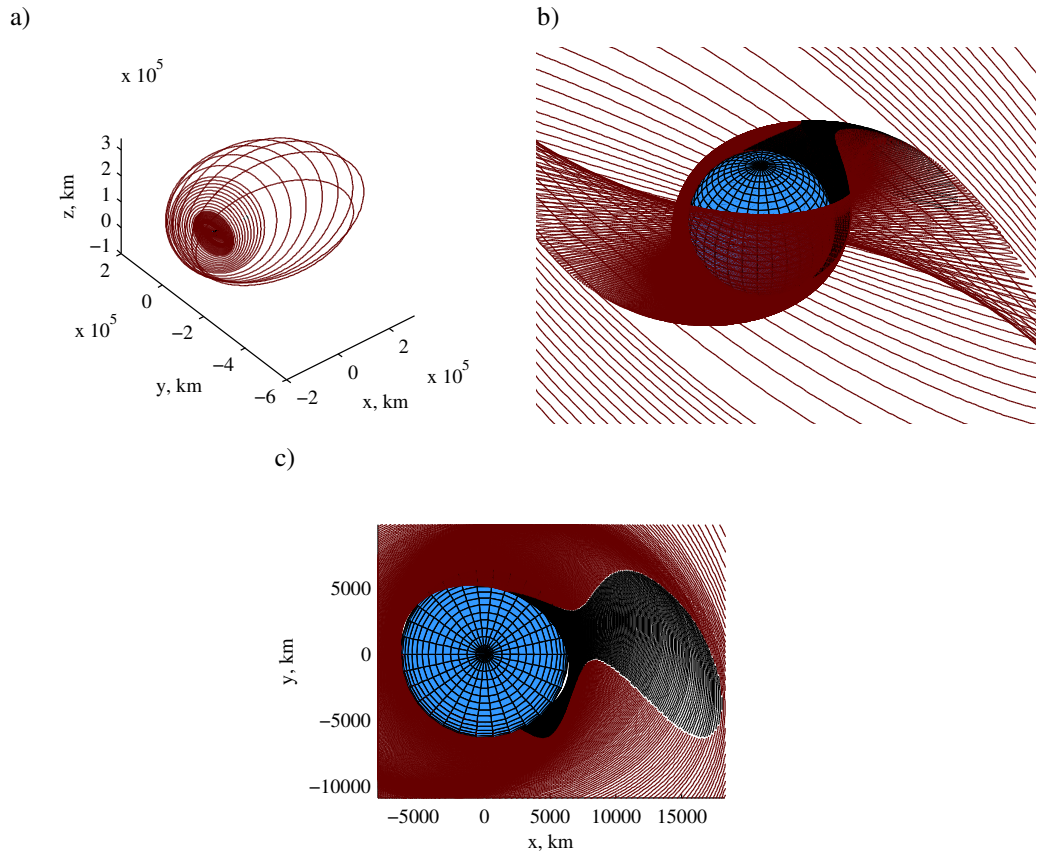
Fig. 6.7 Eclipses (in black) during the low-thrust spiral from a 51.8° parking orbit to the constant altitude pole-sitter orbit in the reference frame of Fig. 6.5.

6.4   Orbital averaging accuracy analysis

The results in Sections 6.3.1 and 6.3.2 have been obtained through the use of orbital averaging. For that, assumptions have been made such as the fact that the thrust acceleration is small compared to the gravitational acceleration. While this assumption will hold for revolutions of the low-thrust spiral close to the Earth, the assumption will break down at distances far from the Earth. Since the spiral reaches altitudes of several 100,000 kilometres, it is worth investigating the accuracy of the orbital averaging method for the low-thrust spiral and to determine whether the solutions presented in Fig. 6.3 and Fig. 6.4 truly enable an injection of the spacecraft into the low-thrust transfer phase (i.e. whether the final state vector of the low-thrust spiral coincides with the initial state vector of the low-thrust transfer phase). To this end, the results in Fig. 6.3 and Fig. 6.4 are reintegrated using the full set of

equations of motion and an interpolation of the optimal control profiles in Fig. 6.3e-f and Fig. 6.4b.

The results of this reintegration are provided by the dashed red lines in Fig. 6.8 for the low-thrust spiral for the transfer to the constant altitude pole-sitter orbit and for a Soyuz launch with a parking orbit inclination of 95.4° (see Fig. 6.3). For clarity, only the last few revolutions are shown. It appears that the reintegration is very accurate up to these last few revolutions, where both the semi-major axis and eccentricity become very large, the assumptions made for the orbital averaging technique no longer hold and the reintegrated solution diverges from the solution of PSOPT. In order for the reintegrated solution to match the solution of PSOPT (and therefore, satisfy the initial conditions at the start of the low-thrust transfer phase), the last few revolutions have been reoptimised.

a)   b)
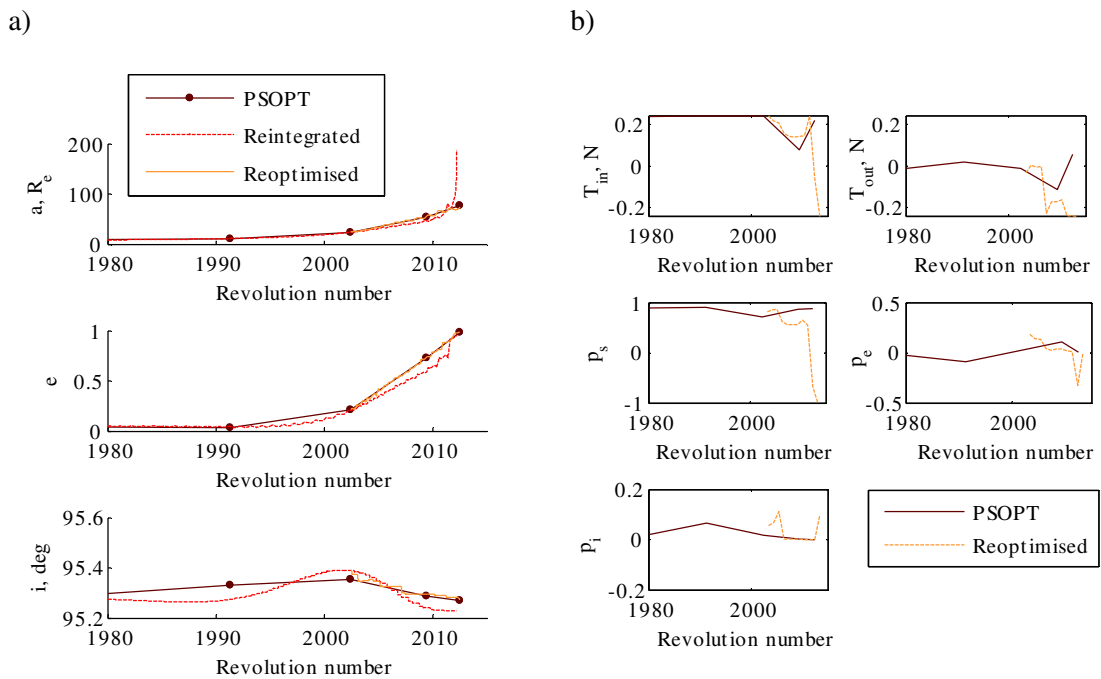
Fig. 6.8 Reoptimized integrated solution to match the result from PSOPT for the transfer to the constant altitude pole-sitter orbit and for a parking orbit inclination of 95.4°. a) State profiles. b) Control profiles.

This optimisation aims at matching the result from PSOPT using the sequential quadratic programming (SQP) method[132] that was previously used in Chapter 3. Using the result from PSOPT as initial guess, the control variables (i.e. the in and out-of-plane thrust magnitudes and the size of the arcs over which one of the three steering laws is applied) are reoptimised. For this, the optimisation loops over the last few revolutions and aims to find in each revolution the control variables to minimise a weighted sum of the error of the Keplerian

elements with respect to the nominal Keplerian elements (i.e. the optimised result from PSOPT).

The results of the reoptimisation are added to the results in Fig. 6.8 and show that, within the control bounds (e.g. a maximum thrust magnitude of 0.240 N), the result of PSOPT can be reproduced and the end of the spiral coincides with the initial state vector of the transfer phase. This indicates that, using the full set of equations of motion, rather than the orbital averaging method, the boundary conditions as imposed on the low-thrust launch spiral can be met.

6.5   Chapter summary

In this chapter, the high-thrust, upper-stage launch phase considered in the previous chapter has been replaced by a minimum time low-thrust spiral in order to obtain a full low-thrust transfer from parking orbit to insertion into the pole-sitter orbit. This spiral has been considered for the transfers to the constant altitude and optimal SEP pole-sitter orbits. The results showed significant gains with respect to the high-thrust launch case. When considering the mass required in the parking orbit to inject a 1000 kg spacecraft into the pole-sitter orbit, the low-thrust spiral reduces this required mass by 58 (Soyuz) or 49 (Ariane 5) percent compared to the high-thrust launch case. When considering the maximum mass that can be injected into the pole-sitter orbit, the low-thrust launch phase can deliver 2.95 or 2.41 times the mass that can be delivered using a high-thrust launch phase. However, these increased performances come at the cost of a significant increase in the required time of flight (at least a factor 13). Furthermore, the spacecraft spends quite a considerable amount of time in eclipse, on average, 5.0 percent of the spiral time, which corresponds to approximately 25 days. Since during this time only limited, or possibly no thrust is available, future analyses will have to incorporate these effects.

Finally, since the orbital averaging technique is valid under the assumption that the thrust acceleration is small compared to the gravitational acceleration, the accuracy of the orbital averaging technique breaks down at large distances from the Earth and a satisfaction of the final boundary conditions cannot be ensured. Therefore, the control variables in the last few revolutions of the spiral have been successfully reoptimised through an SQP method, using the full spacecraft dynamics, and proved the feasibility of the low-thrust spiral.

Chapter 7

Optimal transfers between north and
south pole-sitter orbits

This chapter will investigate a type of transfer associated with the pole-sitter orbit that can be employed to overcome limitations in the observations of the Earth's polar regions during the Arctic and Antarctic winters. During that time, the polar regions are not illuminated due to the tilt of the polar axis with respect to the ecliptic plane, which could potentially limit the mission scientific return. Therefore, by transferring the spacecraft to a pole-sitter orbit above the opposite pole before the start of the polar winter, the spacecraft hovers only above the pole that is lit. The chapter starts by defining this north-to-south transfer in Section 7.1. Then, in Sections 7.2 and 7.3 the optimal control problem that needs to be solved in the transfer is derived and the initial guess to solve the optimal control problem is provided. Note that this chapter will only consider the constant altitude and optimal pole-sitter orbits. To show the design approach and demonstrate the concept, initial results will be presented for the north-to-south transfer between constant pole-sitter orbits in Section 7.4. First, minimum SEP propellant transfers will be sought and will be presented for both the use of SEP and hybrid propulsion. Then, additional transfers, that trade-off propellant consumption and useful observation time per pole, will be investigated. The same approach will be extended to north-to-south transfers between the optimal SEP and hybrid pole-sitter orbits in Section 7.5. In Section 7.6, a validation of the results will be given and the chapter finishes with conclusions.

7.1 North-to-south pole-sitter transfer definition

In order to underline the need for a transfer between north and south pole-sitter orbits, Fig. 7.1a shows the elevation of the Sun at the north pole and the Arctic circle (i.e. at a latitude of $\phi = 66.5°$). The top plot clearly shows that, for the north pole, the Sun does not rise above the horizon from the autumn equinox (September) to the spring solstice (March), during which time it is permanently dark at the north pole. Clearly, a similar plot but mirrored in the horizontal axis can be generated for the south pole. Furthermore, the bottom plot in Fig. 7.1a illustrates the fact that the Arctic circle marks the edge of the region where the Sun does not rise above the horizon for at least one day per year.

The light and dark conditions of the north and south poles can also be illustrated in the pole-sitter orbit in the CR3BP, see Fig. 7.1b. For that, the (north) pole-sitter orbit shown in Fig. 5.1 is mirrored in the ecliptic plane to create a south pole-sitter orbit. Then, viewed in the synodic frame, the poles are illuminated when the spacecraft is in the Sunward part of either the north or south pole-sitter orbit, while darkness dominates when the polar axis is leaning away from the Sun.

When performing observations in the visible part of the electromagnetic spectrum, these dark conditions can impose severe constraints, leading to a loss in the mission scientific return. A solution to this issue would be if the spacecraft follows the north pole-sitter orbit from March to September and then transfers to the south pole-sitter orbit to observe the south pole from September to March.

a)
b)
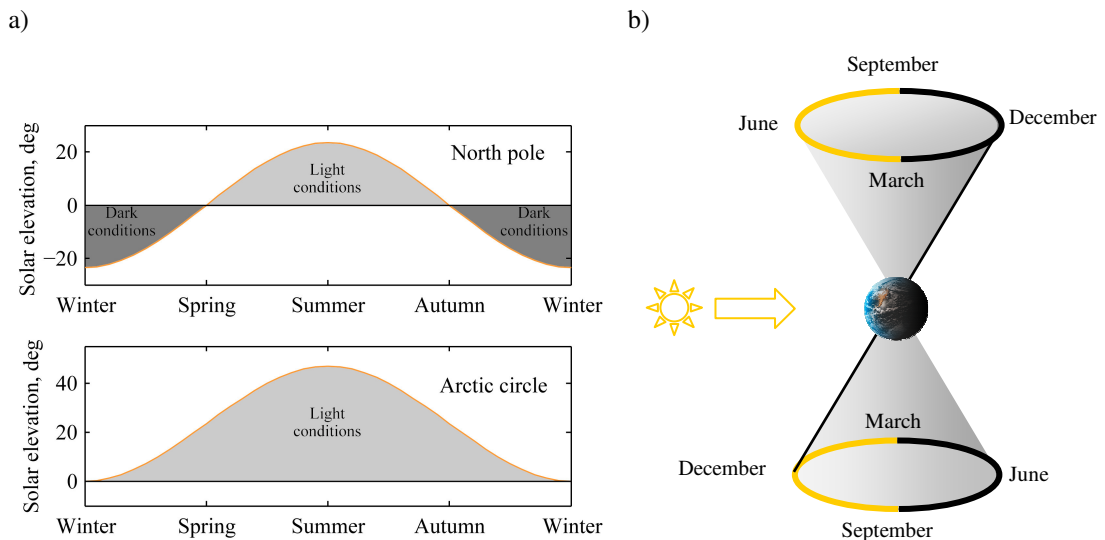
Fig. 7.1 a) Solar elevation angle at the north pole and Arctic circle. b) Schematic of dark (black line) and light (yellow line) conditions on the north and south poles during the year.

Depending on the time allowed to perform this transfer, two types of transfers can be defined: a short duration transfer and a long duration transfer. The short duration transfer considers flight times of less than half a year and leaves the north pole-sitter orbit between the summer solstice ($t = \pi$) and autumn equinox ($t = \frac{3}{2}\pi$) and enters the south pole-sitter between the autumn equinox ($t = \frac{3}{2}\pi$) and winter solstice ($t = 2\pi$), see Fig. 7.2. Since the transfer cannot be performed instantly, the observation time per pole will always be less than half a year, where the observation time is the time the spacecraft spends in either the north or south pole-sitter orbit. This results in the fact that the poles cannot be viewed throughout the full period when lighting conditions occur. Therefore, a long-duration transfer is defined. Then, the spacecraft leaves the north pole-sitter between autumn and winter and, with a transfer time of half a year to one year, the spacecraft enters the south pole-sitter between summer and autumn. Then, the observation time per pole is also half a year to one year, which automatically implies that part of the observations are performed when the polar regions are in darkness.

Note that due to the symmetry of the problem, the transfers designed to transfer from a north pole-sitter to a south pole-sitter can also be employed for the trajectory from south-to-north, assuming that the lower mass at the start of the south-to-north transfer does not influence the trajectory to great extent.
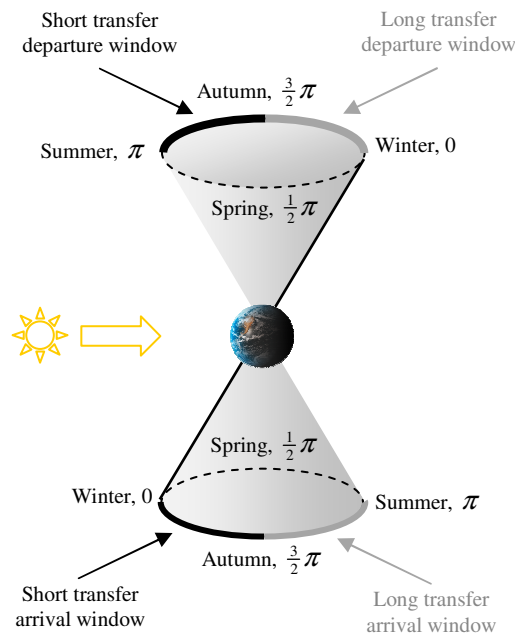
Fig. 7.2 Illustration of the departure and arrival conditions in the north and south pole-sitter orbits for short and long duration transfers.

7.2 Optimal control problem

In order to design and optimise the short and long duration transfers defined in the previous section, the optimal control problem in the respective transfer needs to be solved. Initially, the objective will be to find minimum SEP propellant transfers, leading to the following objective function:

$$J = -m_f \tag{7.1}$$

with m_f the mass at the end of the transfer. Since the transfer will be modelled in the circular restricted three-body problem, similarly to the Earth to pole-sitter transfer in Chapter 5, the state vector is given by the Cartesian position and velocity vectors in the CR3BP frame, see Fig. 2.3, and the mass of the spacecraft:

$$\mathbf{x} = \begin{bmatrix} x & y & z & \dot{x} & \dot{y} & \dot{z} & m \end{bmatrix}^T \tag{7.2}$$

while the controls, $\mathbf{u}$, are dependent on the type of propulsion employed:

$$\mathbf{u} = \begin{cases} \begin{bmatrix} T_x & T_y & T_z \end{bmatrix}^T & \text{SEP} \\ \begin{bmatrix} T_x & T_y & T_z & n_x & n_y & n_z \end{bmatrix}^T & \text{Hybrid} \end{cases} \tag{7.3}$$

with $\mathbf{T} = \begin{bmatrix} T_x & T_y & T_z \end{bmatrix}^T$ and $\mathbf{n} = \begin{bmatrix} n_x & n_y & n_z \end{bmatrix}^T$ the Cartesian SEP thrust and solar sail normal components in the CR3BP reference frame. The use of the Cartesian components requires the inclusion of the following path constraints:

$$\mathbf{c}\big(\mathbf{x}(t), \mathbf{u}(t), t\big) = \begin{cases} \sqrt{T_x(t)^2 + T_y(t)^2 + T_z(t)^2} \leq T_{max} & \text{SEP/Hybrid} \\ \sqrt{n_x(t)^2 + n_y(t)^2 + n_z(t)^2} = 1 \\ \hat{\mathbf{r}}_1(t) \cdot \hat{\mathbf{n}}(t) \geq 0 \end{cases} \quad \text{Hybrid} \tag{7.4}$$

which also describe the path constraint to ensure that the solar sail acceleration is always pointing away from the Sun.

The dynamics of the spacecraft in the north-to-south transfer are described by the same set of equations of motion used for the low-thrust transfer phase of the Earth to pole-sitter transfer in Chapter 5: Eqs. (2.13), (2.14) (for the use of SEP), (2.28) (for the use of hybrid sail propulsion) and (2.15) (to compute the mass consumption). As for the design of hybrid optimal Earth to pole-sitter transfers, an optical solar sail model is adopted.

184

Bounds on the state and control variables can be defined, as well as on the time of flight:

$$
\begin{aligned}
\mathbf{x}_l &= \left[(1-\mu)-0.02 \quad -0.02 \quad -0.02 \quad -0.1 \quad -0.1 \quad -0.1 \quad 0\right]^T \\
\mathbf{x}_u &= \left[(1-\mu)+0.02 \quad 0.02 \quad 0.02 \quad 0.1 \quad 0.1 \quad 0.1 \quad m_{mission,0}\right]^T
\end{aligned}
\tag{7.5}
$$

$$
\mathbf{u}_l = -\mathbf{u}_u = \begin{cases}
\left[-T_{\max} \quad -T_{\max} \quad -T_{\max}\right]^T & \text{SEP} \\
\left[-T_{\max} \quad -T_{\max} \quad -T_{\max} \quad -1 \quad -1 \quad -1\right]^T & \text{Hybrid}
\end{cases}
\tag{7.6}
$$

$$
\left.\begin{aligned}
\pi \le t_0 \le \tfrac{3}{2}\pi \\
\tfrac{3}{2}\pi \le t_f \le 2\pi
\end{aligned}\right\} \quad \text{Short transfer}
$$

$$
\left.\begin{aligned}
\tfrac{3}{2}\pi \le t_0 \le 2\pi \\
3\pi \le t_f \le \tfrac{7}{2}\pi
\end{aligned}\right\} \quad \text{Long transfer}
\tag{7.7}
$$

The variable $m_{mission,0}$ represents the spacecraft mass upon injection into the pole-sitter orbit and the value for the maximum thrust magnitude, $T_{\max}$, in Eq. (7.6) is taken equal to the values established for the different types of pole-sitter orbits in Chapter 5. Equation (7.7) furthermore shows different types of bounds on the initial, t_0, and final time, t_f, in order to force the optimal solution into a short or long duration transfer as defined in Section 7.1.

Finally, the following event constraints can be defined as:

$$
\boldsymbol{\phi}_0\left(\mathbf{x}(t_0),\mathbf{u}(t_0),\mathbf{p},t_0\right) = \mathbf{x}_{PS,N}(t_0) - \mathbf{x}_0 = \mathbf{0}
\tag{7.8}
$$

$$
\boldsymbol{\phi}_f\left(\mathbf{x}(t_f),\mathbf{u}(t_f),\mathbf{p},t_f\right) = \begin{cases}
x_{PS,S}(t_f) - x_f = 0 \\
y_{PS,S}(t_f) - y_f = 0 \\
z_{PS,S}(t_f) - z_f = 0 \\
\dot{x}_{PS,S}(t_f) - \dot{x}_f = 0 \\
\dot{y}_{PS,S}(t_f) - \dot{y}_f = 0 \\
\dot{z}_{PS,S}(t_f) - \dot{z}_f = 0
\end{cases}
\tag{7.9}
$$

with the subscripts '0' and 'f' indicating the conditions at the initial and final time of the transfer, the subscript 'PS' indicating the conditions in the pole-sitter orbit and finally the subscripts 'N' and 'S' referring to the north and south pole-sitter orbits, respectively. Equation (7.8) shows that the full initial state vector should match the full state vector in the north pole-sitter orbit at the initial time, t_0. This also includes the mass of the spacecraft. For this, the mass profile in the pole-sitter orbit is computed starting from the injected spacecraft mass and the injection position as obtained in Chapter 5 for each of the types of pole-sitter

orbits. By subsequently assuming that the north-to-south transfer takes place in the first year of the pole-sitter mission, the mass at the start of the transfer can be computed through interpolation, using the location where the transfer is initiated. Equation (7.9) finally shows that the final position and velocity vectors of the transfer should match the conditions in the south pole-sitter orbit at the final time of the transfer, t_f .

7.3   Initial guess

Due to the good performance of the inverse method developed to generate the initial guesses for the transfer between north and south displaced geostationary orbits (as well as for the other displaced GEO transfers) in Section 4.2.1, a similar approach will be applied to obtain an initial guess for the north-to-south pole-sitter transfer. This implies that a particular shape for the trajectory (that satisfies the boundary constraints) is assumed, after which the thrust profile required to follow that shape is obtained from the equations of motion.

Note that the initial guesses developed in this section assume the use of only the SEP thruster, since the initial guesses for the hybrid transfers will be the optimised SEP trajectories.

The initial guess approach will be demonstrated for a transfer between constant altitude pole-sitter orbits, but can clearly be extended to provide an initial guess for north-to-south transfers between the optimal pole-sitter orbits. The approach starts from the boundary conditions of the trajectory by assuming that the initial and final state vectors are fixed and coincide with the north and south pole-sitter orbits in the following way: $x_0 = x_f$, $y_0 = -y_f$ and $z_0 = -z_f$ and therefore $\dot{x}_0 = -\dot{x}_f$, $\dot{y}_0 = \dot{y}_f$ and $\dot{z}_0 = -\dot{z}_f$, see Fig. 7.3. The actual values for the initial and final position depend on the value chosen for the angle ξ , whose definition is also provided in Fig. 7.3. Subsequently, a parabolic velocity profile is assumed between the initial and final state vectors as follows:

$$\dot{\mathbf{r}}(t) = \mathbf{a}_1 t^2 + \mathbf{a}_2 t + \mathbf{a}_3 \tag{7.10}$$

with $\mathbf{r} = \begin{bmatrix} x & y & z \end{bmatrix}^T$ the position vector, the overhead dot indicating the derivative with respect to time and $\mathbf{a}_1$, $\mathbf{a}_2$ and $\mathbf{a}_3$ vectors of constants.

186

Initial condition

ξ

$\parallel z$

$\parallel y$

x

ξ
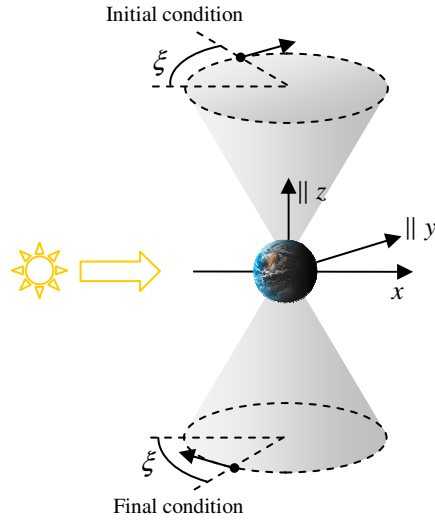
Final condition

Fig. 7.3 Definition of boundary conditions for the initial guess for the north-to-south pole-sitter transfer.

From the initial and final velocity conditions it can be shown that $\mathbf{a}_3 = \dot{\mathbf{r}}_0$ and $\mathbf{a}_2 = (1/t_f)(\dot{\mathbf{r}}_f - \dot{\mathbf{r}}_0) - \mathbf{a}_1 t_f$ (with the subscripts '0' and 'f' again indicating the conditions at the initial and final times). By integrating Eq. (7.10), the following shape for the position vector can be found:

$$\mathbf{r}(t) = \mathbf{a}_1\left(\frac{1}{3}t^3 - \frac{1}{2}t_f t^2\right) + \frac{1}{2t_f}\left(\dot{\mathbf{r}}_f - \dot{\mathbf{r}}_0\right)t^2 + \dot{\mathbf{r}}_0 t + \mathbf{a}_4 \qquad (7.11)$$

Again, from the initial and final position conditions it can be shown that $\mathbf{a}_4 = \mathbf{r}_0$ and $\mathbf{a}_1 = -(6/t_f^3)(\mathbf{r}_f - \mathbf{r}_0 - \frac{1}{2}(\dot{\mathbf{r}}_0 + \dot{\mathbf{r}}_f)t_f)$. Finally, differentiating Eq. (7.10) gives the profile of the acceleration vector, resulting in the following final position, velocity and acceleration profiles:

$$\mathbf{r}(t) = -6\frac{\mathbf{r}_f - \mathbf{r}_0 - \frac{1}{2}\left(\dot{\mathbf{r}}_0 + \dot{\mathbf{r}}_f\right)t_f}{t_f^3}\left(\frac{1}{3}t^3 - \frac{1}{2}t_f t^2\right) + \frac{1}{2t_f}\left(\dot{\mathbf{r}}_f - \dot{\mathbf{r}}_0\right)t^2 + \dot{\mathbf{r}}_0 t + \mathbf{r}_0$$

$$\dot{\mathbf{r}}(t) = -6\frac{\mathbf{r}_f - \mathbf{r}_0 - \frac{1}{2}\left(\dot{\mathbf{r}}_0 + \dot{\mathbf{r}}_f\right)t_f}{t_f^3}\left(t^2 - t_f t\right) + \frac{1}{t_f}\left(\dot{\mathbf{r}}_f - \dot{\mathbf{r}}_0\right)t + \dot{\mathbf{r}}_0 \qquad (7.12)$$

$$\ddot{\mathbf{r}}(t) = -6\frac{\mathbf{r}_f - \mathbf{r}_0 - \frac{1}{2}\left(\dot{\mathbf{r}}_0 + \dot{\mathbf{r}}_f\right)t_f}{t_f^3}\left(2t - t_f\right) + \frac{1}{t_f}\left(\dot{\mathbf{r}}_f - \dot{\mathbf{r}}_0\right)$$

The required thrust profile to execute this shape-based transfer can now easily be extracted from the equations of motion by substituting Eq. (7.12) into the equations of motion (i.e. Eqs. (2.13)and (2.14)) and rewriting for the thrust vector, $\mathbf{T}$:

$$
\begin{pmatrix} T_x \\ T_y \\ T_z \end{pmatrix} = m \begin{pmatrix} \ddot{x} + \left(\dfrac{1-\mu}{r_1^3}(x+\mu) + \dfrac{\mu}{r_2^3}\left(x-(1-\mu)\right) \right) - 2\dot{y} - x \\[3mm] \ddot{y} + \left(\dfrac{1-\mu}{r_1^3} + \dfrac{\mu}{r_2^3} \right) y + 2\dot{x} - y \\[3mm] \ddot{z} + \left(\dfrac{1-\mu}{r_1^3} + \dfrac{\mu}{r_2^3} \right) z \end{pmatrix} \tag{7.13}
$$

In order to obtain an approximation for the mass profile during the transfer, the initial guess defined in Eqs. (7.12) and (7.13) is discretised into a set of nodes that are equally distributed along the transfer. The mass profile at the ith node is then approximated through the recurrence relation provided in Eq. (3.29).

a)

b)

c)
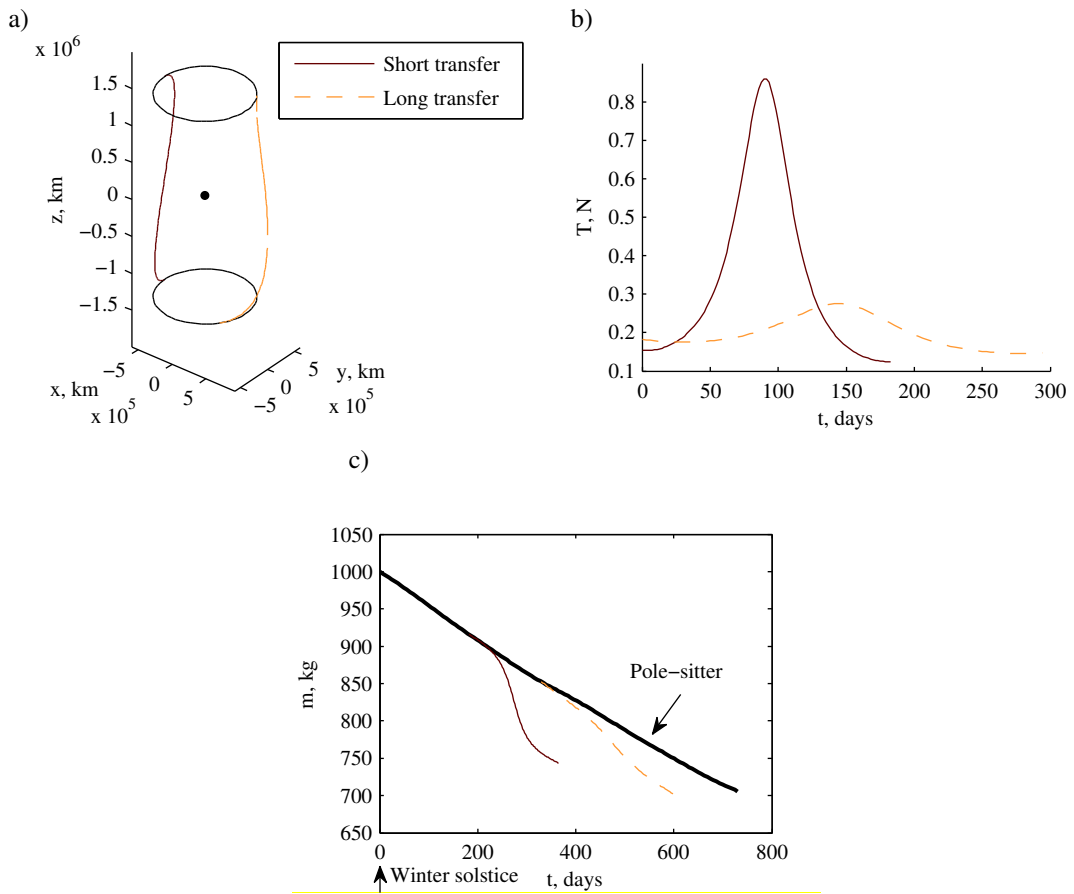
Fig. 7.4 Initial guess for short and long transfer between constant altitude pole-sitter orbit orbits. a) Transfers in CR3BP frame. b) Thrust profiles in transfer. c) Mass profiles as function of mission time, including mass profile in pole-sitter orbit.

The result for the north-to-south transfer between the 0.01 AU constant altitude pole-sitter orbits is presented in Fig. 7.4 for $\xi = 0°$ and $\xi = 145°$ for the short and long duration transfers, respectively. These values for the angle ξ were shown to provide the best thrust

profiles in terms of maximum thrust magnitude required. The transfer times then equal half a year and 294 days, respectively. Furthermore, optimisation case 1 is considered (see Section 5.3.1), which implies that the mass at injection is 1000 kg and for illustration purposes it is assumed that the spacecraft is injected into the pole-sitter orbit at the winter solstice. The figure shows that the mass at the start of the transfer decreased to a value of 915.8 kg and 875.1 kg for the short and long duration transfer, respectively, due to the consumption of propellant in the north pole-sitter orbit. The figure also shows that the required thrust magnitude is rather high for the short duration transfer, while the long duration transfer shows more acceptable thrust levels. However, as was previously noted in Section 5.4, this can be taken into account in the optimisation process by first performing an optimisation in which the square of the thrust is minimised (without a limit on the thrust magnitude) which can serve as initial guess for the thrust-limited minimisation of propellant mass.

7.4   Constant altitude pole-sitter orbit

Using the initial guess developed in the previous section, the fuel-optimal transfers between north and south constant altitude pole-sitter orbits can be generated. As stated before, the results in this section are used to demonstrate the concept and design approach of the north-to-south pole-sitter transfers. Therefore, only the results for the test case described in the previous section will be provided, i.e. for optimisation case 1, which implies that the mass upon injection into the north pole-sitter orbit is 1000 kg and the maximum thrust magnitude is $T_{\max} = 0.240$ N. Furthermore, since it was demonstrated that the point of injection is of no influence to the performance in LEO for the constant altitude pole-sitter orbit, and in order to consider a general case, it is assumed that the spacecraft is injected into the constant altitude pole-sitter orbit at the winter solstice, i.e. $m = 1000$ kg at $t = t_0 = 0$.

The optimal control problem is solved using PSOPT using a mesh refinement to eventually obtain solutions consisting of 75 nodes, a maximum number of iterations of 5000 (which is never reached) and a convergence tolerance of 10^{-6}.

7.4.1   Results - SEP

For the use of pure SEP, the results are provided in Fig. 7.5. Both the results for the short and long transfers are presented, which require a propellant consumption of 21.9 and 30.1 kg, respectively. The declination plots in Fig. 7.5.c and Fig. 7.5d show that the pole-sitter

spacecraft correctly follows the declination of the Sun and they also clearly show the difference between the short and long duration transfers: while the short duration transfer observes both the north and south poles for a short period every year (21.9 days per pole), the long-duration transfer allows to observe both poles every three years but for a much longer duration (239.2 days per pole). However, as was already previously noted, part of these observations are taken during a negative solar declination, i.e. when the poles are not illuminated. This, in combination with the fact that the short duration transfer outperforms the long transfer in terms of propellant consumption (despite the higher initial mass at the start of the transfer), favours the short duration transfer for the north-to-south pole-sitter transfers. Its only disadvantage is the relatively short observation period per pole. However, as will be shown in the next section, this can be improved significantly at the cost of a slight increase in the propellant consumption.

7.4.2   Improved observations times

When designing the SEP minimum propellant transfers, the observation time of the polar regions is not taken into account. If the purpose of the transfer is to visit both the north and south poles with one spacecraft only, that is justifiable. However, if the purpose of the transfer is to enable observations of the poles in light conditions only, it can be concluded that the observation time for the short transfer in Fig. 7.5 is very limited. Therefore, in order to increase the time spent above each of the poles, the objective function in Eq. (7.1) can be expanded to allow for a trade-off between propellant consumption and time spent in each of the pole-sitter orbits (or equivalently transfer time). To establish this, a weighted sum approach is adopted such that the new objective function becomes:

$$J = \frac{m_f - m_0}{m_0} + w \frac{t_f - t_0}{2\pi} \qquad (7.14)$$

The first term on the right hand side of Eq. (7.14) represents the minimisation of the propellant consumption, while the second term represents the minimisation of the transfer time (and thus maximisation of the observation time per pole), which is traded-off to the propellant mass through the weight factor w.
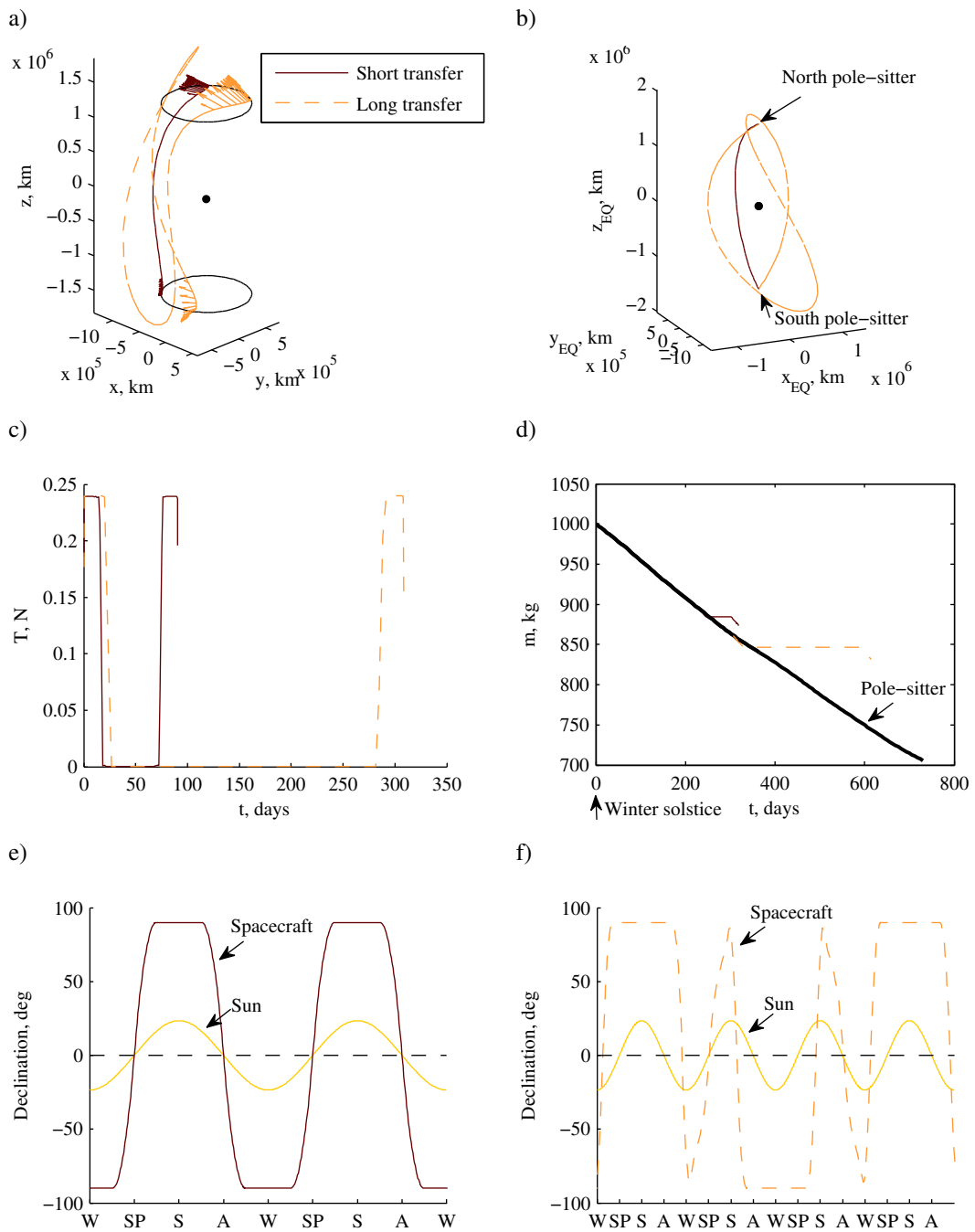
Fig. 7.5 Minimum propellant transfers between constant altitude pole-sitter orbits. a) Transfers in CR3BP frame including SEP thrust vectors. b) Transfers in Earth inertial reference frame. c) Thrust profiles in transfer. d) Mass profiles as function of mission time. e-f) Declination plots for short (e) and long (f) transfers.
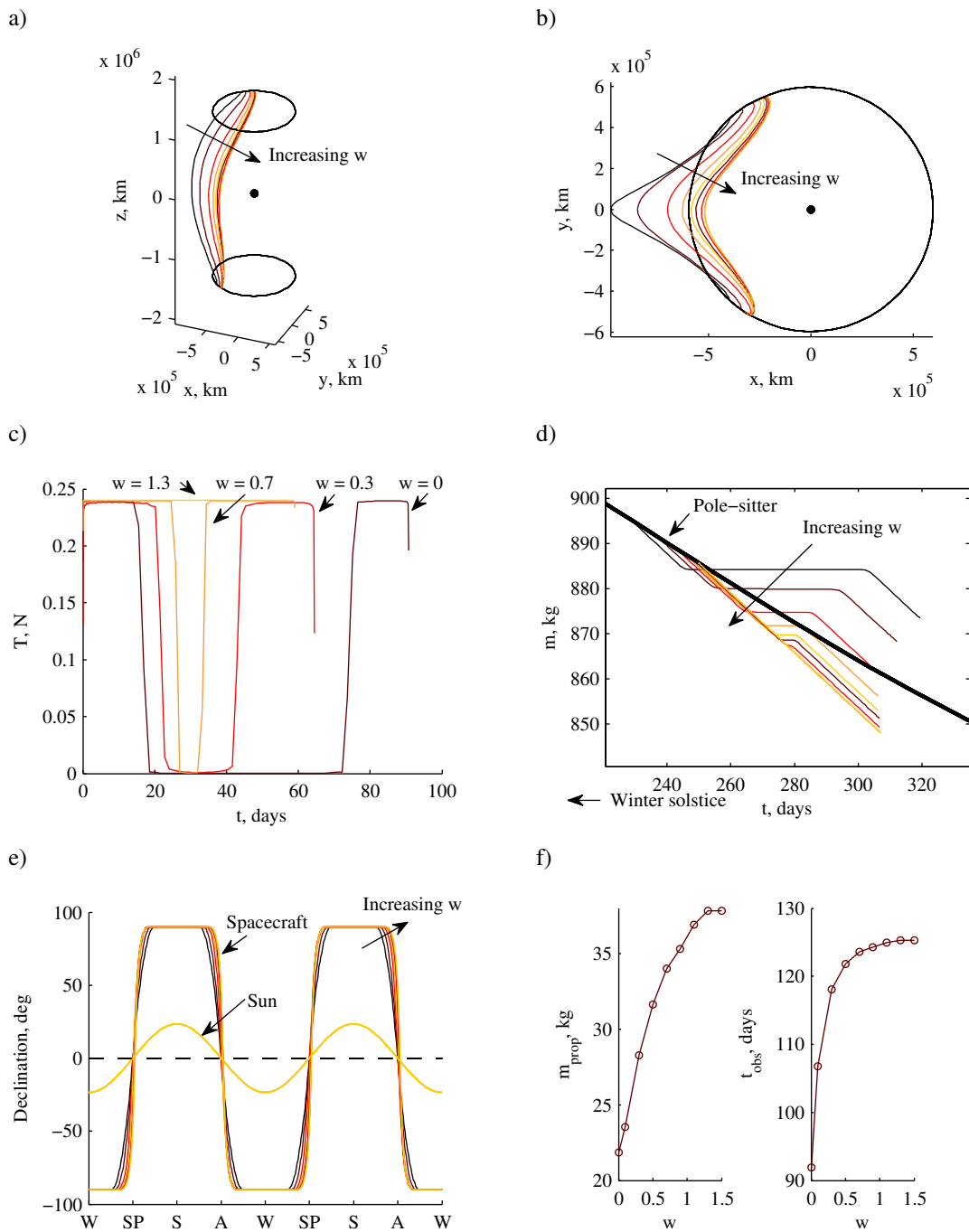
Fig. 7.6 Short transfers between constant altitude pole-sitter orbits optimised for different values of the objective weight factor, w = [0 0.1 0.3 0.5 0.7 0.9 1.1 1.3 1.5]. a-b) Transfers in CR3BP frame. c) Thrust profiles in transfer. d) Mass profiles as function of mission time. e) Declination profiles. f) Propellant consumption and observation time per pole per year as function of the objective function weight.

The results for the short transfer of Fig. 7.5 are provided in Fig. 7.6 for the following values of the weight factor: w = 0, 0.1, 0.3, 0.5, 0.7, 0.9, 1.1, 1.3 and 1.5. The plots show that, as

expected, increasing the weight factor, w, increases the observation time per pole at the cost of additional propellant. For example, for a propellant mass increase of 16.0 kg the observation time is increased from 91.9 to 125.3 days (i.e. for $w = 1.5$). The figure furthermore shows that an upper bound exists for the propellant mass and observation time. This bound is reached when the spacecraft thrusts continuously at maximum thrust magnitude along the transfer, see Fig. 7.6c. In that case, the time of flight cannot be reduced any further despite increasing the weight factor in the objective function.

In order to put the demand on the SEP thruster for performing these transfers in perspective, Fig. 7.6d also provides the mass profile of the spacecraft if it would stay in the pole-sitter orbit, instead of transferring to the pole-sitter on the other side of the ecliptic. From the figure it becomes clear that, for small values of the weight factor, it is more expensive to stay in the pole-sitter than to perform the transfer, i.e. for $w \leq 0.3$. This implies that the transfer could enable an increase in the payload mass or a possible extension of the pole-sitter mission lifetime, although at the cost of a decrease in the total observation time. However, it can be envisaged that during the transfer additional science is performed by the spacecraft payload. Although the view of the polar regions deteriorates with respect to the pole-sitter position, during the first and last stages of the transfer, when the spacecraft moves relatively slowly with respect to the Earth, high-latitude observations can still be performed.

7.4.3   Results - hybrid sail propulsion

In order to investigate the potential of adding a solar sail to the SEP thruster to improve the performance of the transfers presented in the previous section, this section provides the results for the use of hybrid sail propulsion. The results are created for a range of solar sail lightness numbers, ranging from $\beta_0 = 0.01$ to $\beta_0 = 0.1$ with a step size of 0.01. The results for $\beta_0 = 0.01$ are generated using the minimum propellant, pure SEP transfers of Section 7.4.1, while a continuation scheme is used to generate the optimal results for subsequent values of β_0.

The results are shown in Fig. 7.7, Fig. 7.8 and Fig. 7.9, where Fig. 7.7 provides detailed results for $\beta_0 = 0.02$, while Fig. 7.8 and Fig. 7.9 only provide the main outcomes for other values of the sail lightness number.

Inspecting the results shows an interesting, but to be expected, change in the shape of the trajectory when adding a solar sail to the SEP thruster, see Fig. 7.9: for $\beta_0 > 0.01$, the trajectory switches from a Sunward trajectory for the pure SEP case to an Earthward

trajectory for the hybrid sail case. This occurs because, for an Earthward trajectory, the required acceleration is more aligned with the direction of the Sun-vector, which is ideal for increasing the contribution of the solar sail. Apparently, for $\beta_0 = 0.01$ the solar sail cannot contribute enough to enable this quicker, Earthward trajectory.

Considering the operational difficulty noted in Section 2.2.3 concerning the relative angle between the SEP thrust force and the solar sail (which cannot be such that it lies in the plane of the solar sail, i.e. different from 90°), Fig. 7.9d illustrates that for the majority of the thrust profiles this introduces no problems. However, especially at the start and end of the thrust pulses, the relative angle is close to 90°, which needs to be monitored closely.
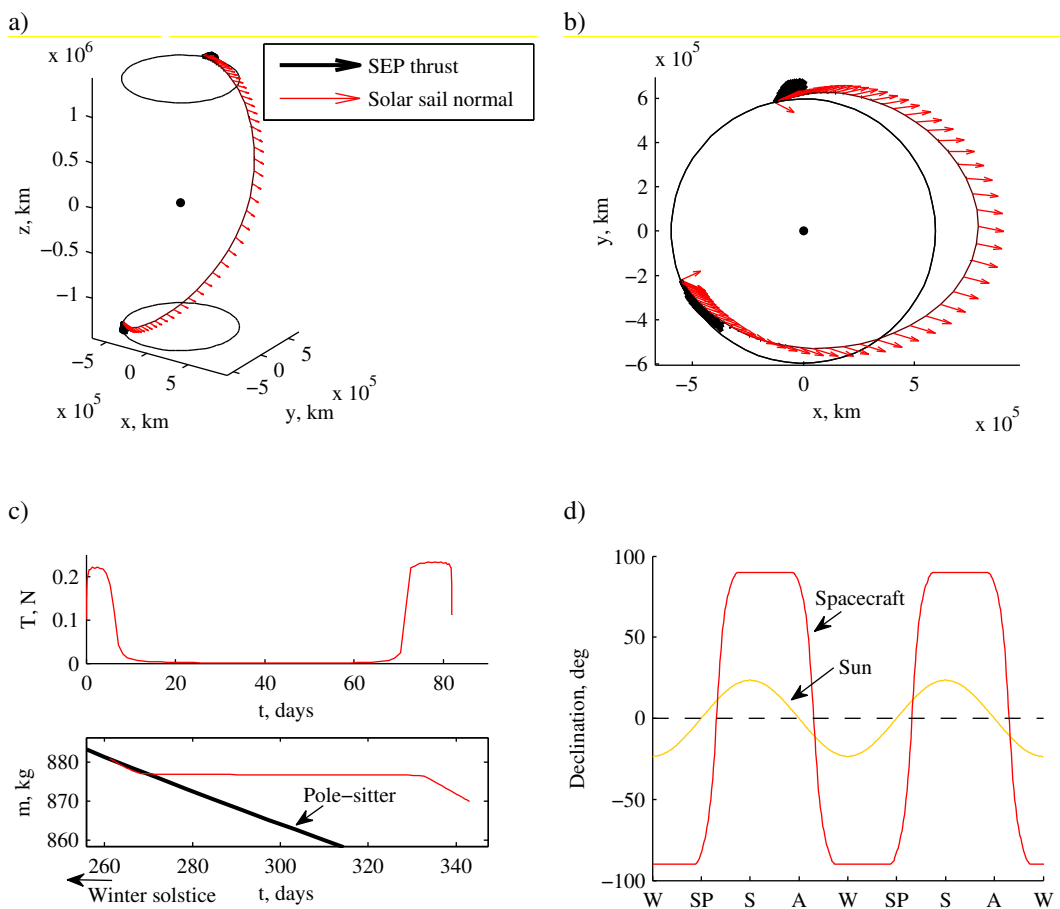
Fig. 7.7 Hybrid propulsion, minimum propellant, short transfer between constant altitude pole-sitter orbits for $\beta_0 = 0.02$. a-b) Transfer in CR3BP frame. c) Thrust profile as a function of transfer time and mass profile as function of mission time. d) Declination plot.

Figure 7.8 shows the improvements that hybrid sail propulsion can establish over the pure SEP case for the transfer between constant altitude pole-sitter orbits. It shows that, in general, by increasing the sail lightness number, hybrid sail propulsion allows for significant propellant mass savings, while also increasing the observation time per pole. However, note that the optimisation only minimises the propellant consumption. The increased observation time is therefore an advantageous side-effect and therefore does not obey a smooth increasing profile for increasing values of the sail lightness number. For example, for $\beta_0 = 0.01$, the reduction in the propellant consumption comes at the cost of a decrease in the time of flight because, as noted, it cannot enable the faster, Sunward trajectory. Note that further improvements in the observation time can be established by considering the objective function in Eq. (7.14).

Finally, if the lightness number is increased far enough, the required SEP propellant mass becomes zero, indicating that the transfer can be performed using only the solar sail. The figure therefore clearly shows the potential of hybrid sail propulsion as transition phase between pure SEP and pure solar sail missions: it enables a reduction of the propellant mass with respect to the pure SEP case, while enabling a mission that would require sail technology that is currently not available.
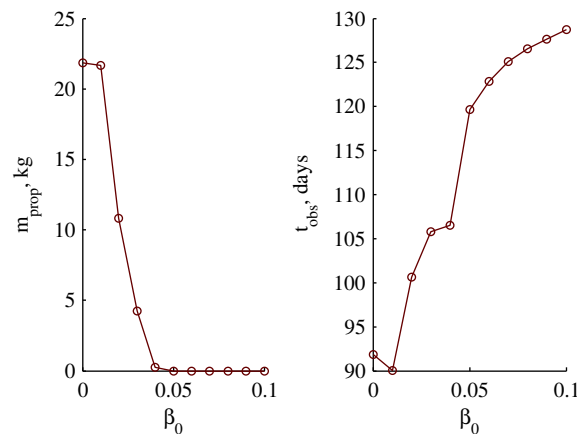
Fig. 7.8 Propellant consumption and observation time per pole per year as a function of the sail lightness number, β_0, for hybrid transfers between constant altitude pole-sitter orbits.
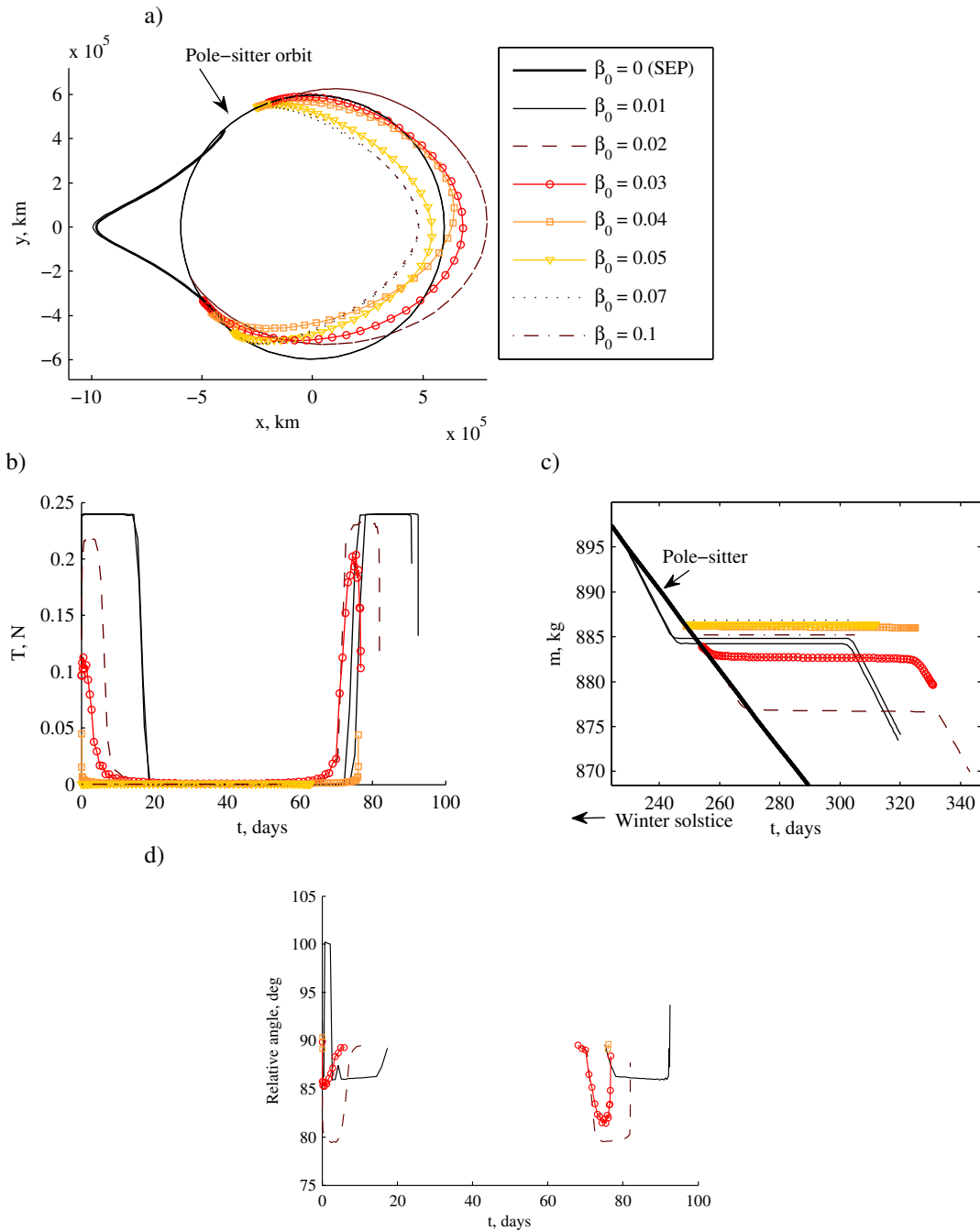
Fig. 7.9 Hybrid propulsion, minimum SEP propellant transfers between constant altitude pole-sitter orbits for different values of the sail lightness number, β_0. a) Transfers in CR3BP frame. b) Thrust profiles in transfers. c) Mass profiles as function of mission time. d) Relative angle between the SEP thrust vector and solar sail normal vector.

7.5   Optimal pole-sitter orbits

Building upon the findings for the north-to-south transfers between constant altitude pole-sitter orbits in the previous section, this section investigates these transfers for the SEP and

hybrid optimal pole-sitter orbits that were defined in Section 5.5.3. Therefore, for the hybrid case, only one value for the lightness number will be considered, namely $\beta_0 = 0.035$. In particular, the cases where the spacecraft mass injected into the pole-sitter orbits is maximised will be investigated, i.e. the results for optimisation case 2 in Sections 5.5.3 and 5.6.2. This implies that for a Soyuz launch, the mass upon injection into the pole-sitter orbits is 1537 and 1595 kg for the SEP and hybrid pole-sitter orbits, respectively, while for an Ariane launch these values increase to 4439 and 4599 kg. The corresponding values for the maximum thrust magnitudes are 0.269/0.231 N (Soyuz launch) and 0.775/0.667 N (Ariane launch). Finally, the injection locations as found in Sections 5.5.3 and 5.6.2 will be used to find the mass at the start of the north-to-south transfer.

The results for the SEP pole-sitter orbit are shown in Fig. 7.10 and Fig. 7.11, where the following values for the weight factor in the objective function of Eq. (7.14) are used: $w = 0$, 0.25, 0.5, 1.0 and 1.5. The case for $w = 0$ thus represents the fuel-optimal case.

The first observation from Fig. 7.10 is the clear resemblance between the Soyuz and Ariane 5 cases that was also observed for the Earth to pole-sitter transfer in Chapter 5, indicating the scalability of the transfer with the mass. Any remaining differences between the Soyuz and Ariane 5 solutions (e.g. in the acceleration profile for $w = 0$ in Fig. 7.10c) can be attributed to a premature convergence of PSOPT.

Second, as for the transfer between constant altitude pole-sitter orbits, increasing the weight factor of the objective function shows an increase in the observation time up to observation times of 94 days in Fig. 7.11a. The associated cost in terms of additional propellant consumption can be compared to the cost of staying in the pole-sitter orbit in Fig. 7.10d. For $w \le 0.5$, it is more costly to stay in the pole-sitter orbit than it is to transfer to the south pole-sitter orbit. This can again lead to a significant extension of the mission lifetime as is shown in Fig. 7.11b. That figure shows that, for $w = 0$, the gain in propellant is 279.6 kg after 5 years. Increasing the weight factor leads to smaller gains and for $w = 1.5$ even a small loss of 45.3 kg can be observed after 5 years.

Because very similar results can be obtained for the hybrid case, detailed plots are omitted here. However, summarised results are provided in Fig. 7.11a, which shows that, for large values of the weight factor, the hybrid case can obtain similar observation times as for the pure SEP case, but for a much lower propellant consumption. For example, for the fuel-optimal case, mass savings of 18.5 and 52.3 kg can be established for a Soyuz and Ariane 5 launch, respectively, which corresponds to an 81 percent reduction in propellant consumption.
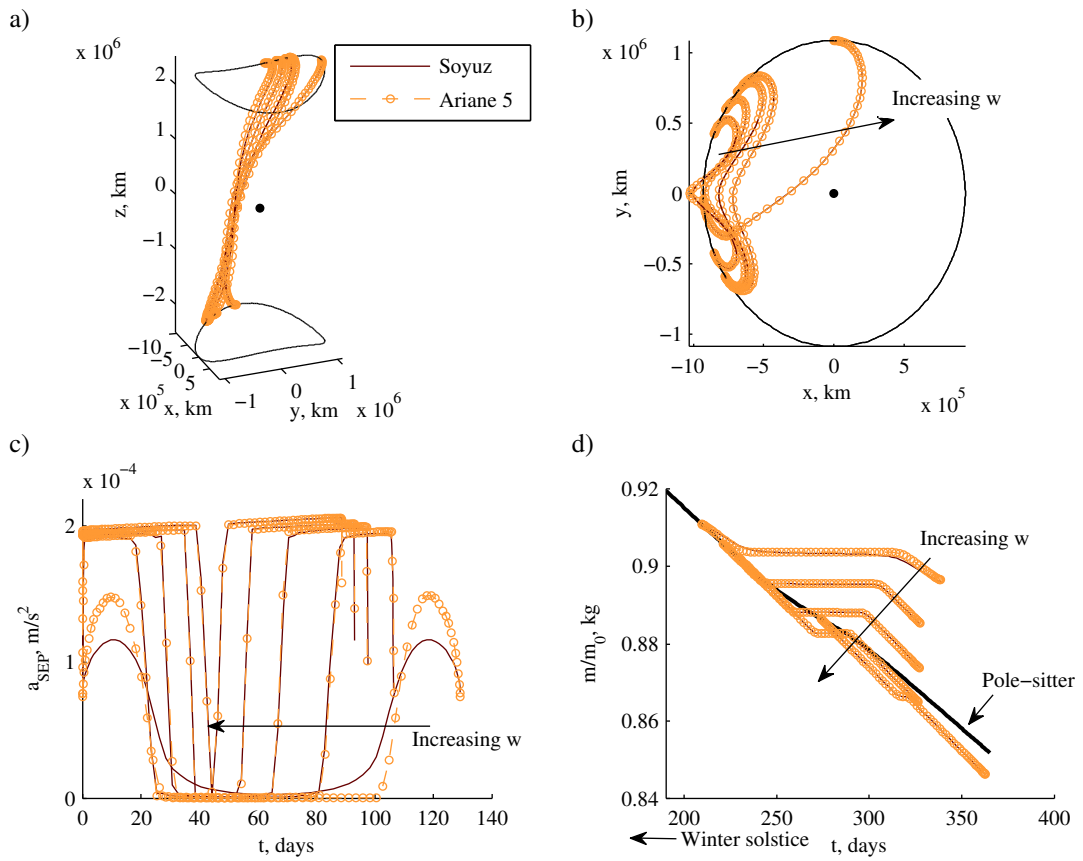
Fig. 7.10 Optimised north-to-south transfers between the optimal SEP pole-sitter orbits for different values of the objective weight factor, $w = [0\ 0.25\ 0.5\ 1.0\ 1.5]$. a-b) Transfers in CR3BP reference frame. c) Acceleration profiles. d) Ratios of current mass and mass at injection as a function of mission time.
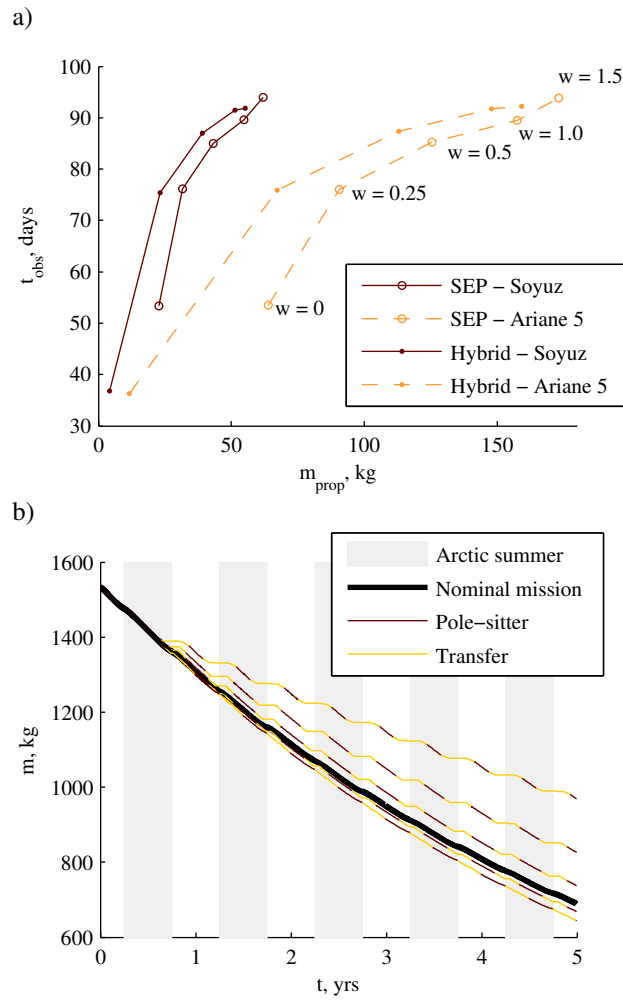
Fig. 7.11 a) Observation time per pole per year as a function of the propellant consumption for the optimal SEP and hybrid pole-sitter orbits. b) Mass profiles throughout the pole-sitter mission for the optimal SEP pole-sitter orbit and a Soyuz launch including the north-to-south pole-sitter transfer. Shaded areas highlight the half of the year when the north pole is lit.

7.6 Results validation

Similar to the validation of the results for the Earth to pole-sitter transfers using a high-thrust launch phase in Chapter 5, the results for the transfer between north and south pole-sitter orbits will be validated by optimising a subset of the cases considered in Sections 7.4 and 7.5 with GPOPS. In particular, the fuel-optimal (i.e. $w = 0$), SEP transfers between constant altitude pole-sitter orbits will be considered. Both the short and long duration transfers will be investigated by implementing the optimal control problem defined in Section 7.2 in

199

GPOPS and using the initial guess defined in Section 7.3. The suggested default settings in GPOPS are adopted and a mesh refinement to obtain solutions with 75 nodes is used.
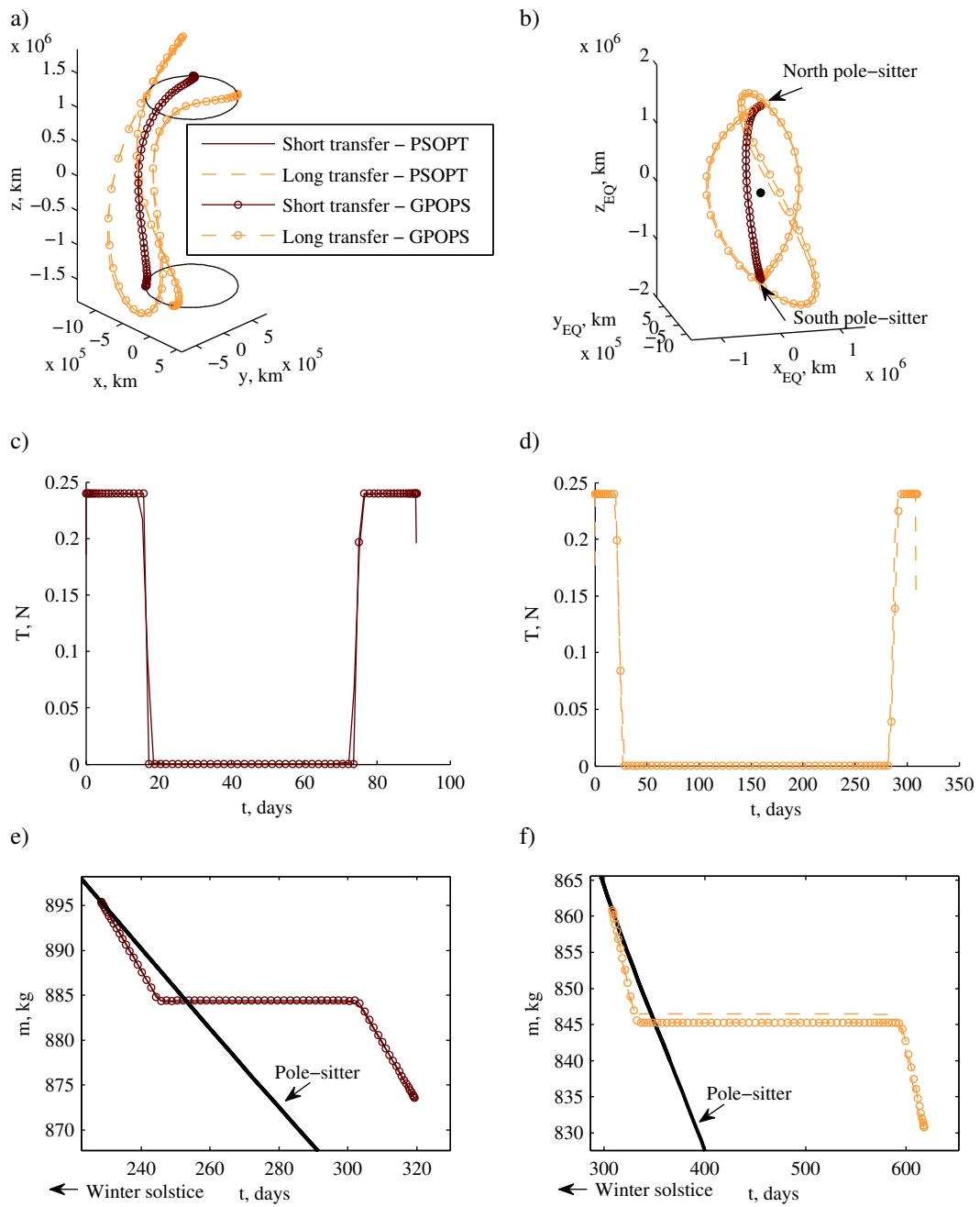
Fig. 7.12 Comparison of optimal transfers between north and south constant altitude pole-sitter orbits generated with GPOPS (dashed lines) and PSOPT (marked lines). a) Transfers in CR3BP reference frame. b) Transfers in Earth inertial reference frame. c-d) SEP thrust profiles. e-f) Mass profiles as function of mission time.

The results, which are provided in Fig. 7.12, show again a very close resemblance between the optimal trajectories generated by PSOPT and GPOPS, not only in terms of objection function value and trajectory profile, but also in terms of thrust and mass profile. This confirms the optimality of the results generated by PSOPT.

7.7   Chapter summary

In this chapter, transfers between pole-sitter orbits above the north pole and south pole have been investigated, to overcome limitations in observations introduced by the tilt of the polar axis, which causes the polar regions to be alternately situated in darkness. The transfers considered in this thesis therefore allow for observations of the polar regions in light conditions only and can in addition allow for the observation of both the north and south poles with one single spacecraft during one single mission.

Two types of transfers exist: a short duration transfer where the spacecraft visits both the north and south poles every year and during light conditions only and a long duration transfer where the spacecraft visits the north and south poles every three years, but with much longer observation times (though part of the observations are performed during dark conditions). The short duration transfer outperforms the long duration transfer in terms of propellant consumption. Furthermore, since the long duration transfer partially remains above the polar regions when they are not illuminated, this type of transfer can be considered of less importance than the short duration transfer. However, since the latter has relatively short observation times per pole, it was shown that through a trade-off between propellant consumption and transfer time, the observation time can be increased significantly, while still requiring less propellant than when the spacecraft would maintain its pole-sitter position. This can enable an extension of the pole-sitter mission or alternatively an increase in the payload mass. For example, for the fuel-optimal SEP pole-sitter orbit, the gain with respect to remaining in the pole-sitter orbit is 279.6 kg after 5 years, which can significantly increase the mission lifetime and/or payload mass.

By adding a solar sail to the SEP thruster it was shown that hybrid sail propulsion allows for significant propellant mass savings with respect to the pure SEP case, while increasing the observation time. These propellant mass savings increase for increasing values of the sail lightness number and for large enough lightness numbers, the transfer between constant altitude pole-sitter orbits can even be performed using only the solar sail. As such, hybrid sail propulsion can be seen as a useful technique for the transition between pure SEP and

pure solar sail missions and to pull the technology development of solar sail technology. For the transfer between optimal SEP and hybrid pole-sitter orbits, observations times of up to 94 days per pole can be achieved at the cost of propellant consumptions of approximately 61.9 kg (Soyuz launch) and 173.1 kg (Ariane 5 launch) for the optimal SEP pole-sitter orbit and 55.3 kg (Soyuz launch) and 159.3 kg (Ariane 5 launch) for the optimal hybrid pole-sitter orbit. This shows propellant savings of 6.6 and 13.8 kg by employing hybrid sail propulsion for a Soyuz and Ariane 5 launch, respectively. For shorter observations times, these mass savings can be increased up to 81 percent of the propellant required for the pure SEP transfer.

Finally, the optimality of the transfers generated by PSOPT have been verified by optimising a subset of the transfers with GPOPS.

Conclusions

In this chapter, the thesis research objectives will be revisited and the conclusions that can be drawn with respect to the research objectives will be presented. Finally, a discussion on possible future research will be given.

Summary and conclusions

Displaced geostationary orbits and transfers

The first research objective of this thesis comprised an investigation of the use of displaced non-Keplerian orbits to generate new geostationary slots as a solution to the congestion of geostationary orbit (GEO). This solution would have to provide true geostationary conditions, outside the geostationary station-keeping box. Such a solution was found by displacing the geostationary orbit out of the equatorial plane through the use of low-thrust propulsion. Alternatively, orbits displaced in the equatorial plane are possible, but these require a higher acceleration than the out-of-plane displaced orbits.

In compliance with the second research objective, the out-of-plane displaced GEOs have been investigated and optimised for the use of different types of propulsion system. For comparison purposes and to highlight the expected better performance of hybrid sail propulsion, three propulsion techniques have been considered, namely pulsed (i.e. chemical), pure solar electric propulsion (SEP) and hybrid sail propulsion. Note that a pure solar sailing displaced GEO mission is not feasible due to the obliquity of the ecliptic that causes the direction of the required acceleration to be outside the achievable range of the solar sail. For each type of propulsion method, a full mission design has been obtained by deriving the maximum lifetime that can be achieved for particular final-to-initial mass fractions and specific impulses. For this, the fuel-optimal SEP and solar sail steering laws have been

derived for the use of hybrid sail propulsion. The results come in the form of a set of mission analysis plots that can be used for future reference as they are generated for a range of displacement distances, solar sail lightness numbers and specific impulses.

The results show the poor performance of pulsed rather than continuous control. This type of propulsion can therefore be discarded as viable option for maintaining the displaced GEO as it can only maintain the displaced GEO for a few months at best.

Rather than considering the lifetime as a function of the mass fraction, a mass budget analysis allowed deriving the performance of pure SEP and hybrid sail propulsion in terms of mission lifetime as a function of payload mass. Then, it becomes clear that, using pure SEP, only the minimum displacement to rise above the geostationary station keeping box, i.e. 35 km, can be maintained for a few years with a payload mass of a few hundred kilograms.

By adding a solar sail to the SEP system, the demand on the SEP system can be lowered significantly, which can be improved even further by alternating the displacement between above (autumn-spring) and below (spring-autumn) the equatorial plane to take advantage of the seasonally changing Sun-sail line. This transfer between north and south displaced geostationary orbits has been optimised for the SEP propellant consumption, which showed that the transfer comes nearly for free, because the north and south displaced GEOs are almost connected by a Keplerian orbit. Since this Keplerian orbit passes close to geostationary orbit, thereby posing collision risk to GEO spacecraft, slightly larger (but still very modest) propellant budgets are required depending on the allowed approach distance to GEO.

Employing this north-to-south transfer, hybrid sail propulsion significantly outperforms the pure SEP case both in terms of payload mass capacity and mission lifetime. It provides lifetimes of 10 to 15 years (equivalent to current geostationary missions) for a 35 km displaced orbit and for payload masses of 155 to 361 kg for the use of a near-term solar sail with a sail lightness number of 0.05. This requires an initial spacecraft mass of 1729 kg. Using pure SEP such payload masses can be maintained for only 3.1 to 5.1 years. For a slightly larger, future value of the sail lightness number of 0.1, payload masses of 255 to 487 kg can be maintained for 10 to 15 years (similar masses with pure SEP only allow mission lifetimes of 2.2 to 4.1 years). These payloads include not only the actual payload but also other subsystems such as OBDH, ADCS and structural mass. By estimating their mass as a fraction, i.e. 20 percent, of the spacecraft dry mass, a 200 kg pure payload mass can still be maintained for 10 years with both near-term and far-term sail lightness numbers. For

smaller percentages, payloads can even be maintained in the displaced GEO for 15 years. Although in all analyses the use of one SEP thruster is assumed (with a maximum thrust magnitude of 0.2 N), clustering multiple SEP thrusters allows a linear increase in these payload masses.

Despite the use of hybrid sail propulsion, higher out-of-plane displaced orbits perform considerably less well than the 35 km displaced GEO. However, applications can be envisaged where the spacecraft is only maintained in the displaced orbit for relatively short periods of time to provide coverage when needed. When not operational, the spacecraft is transferred into a Keplerian parking orbit to save propellant. Optimising this transfer showed that only a modest propellant budget of approximately 0.2 kg is required, again depending on the allowed approach distance to GEO as well as the displacement distance. Using hybrid sail propulsion, this mass budget can be reduced significantly by 72 percent for a 35 km displaced GEO and a sail lightness number of 0.05.

Perturbing accelerations due to the J_2 and $J_{2,2}$ terms of the Earth's gravitational field have a small effect on the previously mentioned lifetimes, which reduces to negligible values for small solar sail lightness numbers. Contrary, non-ideal properties of the solar sail can potentially have a great influence on the lifetime, reducing it by 12 to 52 percent for increasing values of the sail lightness number.

Finally, in response to the third research objective, an additional transfer related to the displaced GEO has been investigated to assess the additional cost that comes with launching a spacecraft into the displaced GEO rather than into GEO. For this, a transfer between GEO and displaced GEO has been optimised for the SEP propellant consumption. This transfer again requires mass budgets of approximately 0.2 kg, which is only a very small fraction of the (at least) 2500 kg that was considered to be available for the transfer after an Ariane 5 launch into GEO. This available mass comes from the lower initial spacecraft mass for the displaced GEO mission than for a GEO mission. Furthermore, using hybrid sail propulsion, the transfer can be performed using only the solar sail (i.e. at zero propellant consumption) for a 35 km displaced GEO and a sail lightness number of 0.04.

All transfers have been successfully optimised using both a direct and indirect optimisation method for validation and verification purposes and to demonstrate the applicability and performance of the direct pseudospectral optimal control solver for the transfers investigated in this thesis.

Summarised, the following main conclusions can be drawn:

- New geostationary slots with true geostationary conditions and outside the geostationary station keeping box are possible through the use of a displaced NKO, where displacing the orbit *out* of the equatorial plane outperforms the case of displacing the orbit *in* the equatorial plane.
- The out-of-plane displaced GEO is accessible from GEO using a low-thrust transfer which requires only a modest SEP propellant consumption, but can also be performed for free using near-term solar sail technology.
- Maintaining the displaced GEO using only a solar sail is not possible.
- Maintaining the displaced GEO using pulsed (i.e. chemical) propulsion is not a viable option as it provides too short mission lifetimes.
- Maintaining the displaced GEO using SEP allows lifetimes of a few years (e.g. 5 years for a 166 kg payload (spacecraft excluding propulsion subsystem)) for the minimum required displacement.
- Maintaining the displaced GEO using hybrid propulsion allows lifetimes of 10 to 15 years for the minimum required displacement (155 to 487 kg payload (spacecraft excluding propulsion subsystem), depending on the sail technology used). Actual payload masses (i.e. communications payload) of 200 kg can be maintained for at least 10 years.
- A transfer between north and south displaced GEO orbits can significantly improve the performance of the mission for the use of hybrid propulsion and requires a negligible to small propellant budget.
- To limit propellant consumption (especially for displacements larger than the minimum required) it is possible to transfer the spacecraft to a Keplerian orbit when coverage is not required at the cost of only a modest propellant consumption.
- The J_2 and $J_{2,2}$ terms of the Earth's gravitational field have a small to negligible effect on the displaced GEO mission performance, while non-ideal properties of the solar sail can have a significant influence.

The mission analysis and systems design for the displaced GEO has thus shown the potential of displaced non-Keplerian orbits and hybrid sail propulsion to generate new and true geostationary slots outside the geostationary station keeping box for both near-term and far-term solar sail technology.

Pole-sitter orbits

The first research objective associated with the pole-sitter orbit required the investigation of optimal transfers from LEO to true pole-sitter orbits in order to determine whether the pole-

sitter orbit is accessible from Earth and, if so, what the performance in terms of mass required in LEO or mass upon injection would be.

For this, a trajectory model has been developed that divides the transfer into a launch phase and a transfer phase. The launch phase start from LEO and ends in a two-body, highly elliptic orbit that coincides with the start of the transfer phase. Both high-thrust and low-thrust propulsion has been investigated for this launch phase: for the high-thrust launch phase a Soyuz or Ariane 5 upper-stage is used for which a Hohmann transfer-like model has been developed, which was verified against a range of reference launch missions in the launcher's manual. For the low-thrust launch phase, the SEP thruster is used to spiral out from LEO, resulting in a low-thrust spiral. This spiral is modelled by considering locally optimal steering laws to minimise the spiral time by optimally changing the orbital elements. Furthermore, orbital averaging is used to significantly speed up the integration of the equations of motion in the spiral.

The transfer phase, which stretches from the end of the launch phase up to the pole-sitter orbit, has been modelled in the Sun-Earth circular restricted three body problem and both ballistic, pure SEP and hybrid sail propulsion have been considered to perform the transfer phase. This complies with the research objective that states that different propulsion strategies, with particular focus on hybrid sail propulsion, had to be investigated and compared.

The full transfer has been optimised for two objective functions. The first one minimises the mass required in LEO for a 1000 kg spacecraft to be inserted into the pole-sitter orbit. This will allow a minimisation of launch and thus mission costs. Considering different LEO inclinations for a Soyuz launch phase, the smallest mass is obtained for the inclination closest to 90° (i.e. the inclination of the pole-sitter orbit). The second objective function maximises the spacecraft mass upon injection into the pole-sitter orbit to allow for a maximum mission lifetime and/or payload mass capacity. Contrary to the first type of objective function, for maximising the mass injected into the pole-sitter orbit, the smallest LEO inclination that can be reached by the Soyuz launch vehicle (i.e. 51.8°) is most optimal for the majority of the cases, because the launch vehicle performance into the lower inclined LEOs is much greater.

In order to solve the optimal control problem, two types of initial guesses have been developed: one based on a novel shape-based approach using expo-elliptic sinusoids and one based on ballistic manifold-like trajectories that wind onto the pole-sitter orbit. The optimal control solver converges to the same solution for both initial guesses, which demonstrates

the applicability of the newly developed shape-based approach for the problem under consideration. Furthermore, the expo-elliptic shape outperforms the conventional exponential sinusoidal shape on a range of test cases (including the pole-sitter transfer) on the satisfaction of the boundary conditions and the amount of thrust required throughout the transfer.

Results have been created for a range of pole-sitter orbits, including constant altitude, tilted and fuel-optimal pole-sitter orbits. The minimum altitude of the tilted pole-sitter orbit was taken equal to the altitude of the constant altitude pole-sitter orbit. Since injection into the tilted orbit always takes place at that minimum altitude, both pole-sitter orbits perform equally well and the launch window to the constant altitude pole-sitter orbit can be considered flexible as the time of year at which injection takes place is less important than the altitude at which injection takes place. The fuel-optimal orbits, for which the altitude is greater, therefore perform slightly worse, but have the advantage of a smaller required SEP maximum thrust magnitude.

For the fuel-optimal pole-sitter orbits, minimum masses in LEO of 5682 kg (SEP) and 5621 kg (hybrid) are required for a Soyuz launch. An Ariane 5 launch requires much larger masses. Furthermore, maximised masses of 1537/4439 kg (Soyuz/Ariane 5) and 1595/4599 kg can be injected into the fuel-optimal orbits for the pure SEP and hybrid sail propulsion cases, respectively. These injected masses can be scaled linearly with an increase in the allowed thrust magnitude. The advantage of hybrid sail propulsion is thus clear as it provides gains in mass required in LEO and mass injected into the pole-sitter orbits. Its potential becomes even clearer when using the above maximised injected masses in a mission performance analysis: for a payload of 100 kg, the pole-sitter mission lifetime can be extended by 2.0 years (Soyuz) and 2.4 years (Ariane 5) with respect to a pure SEP mission.

Finally, assuming the transfer phase fixed, the upper-stage launch phase can be replaced by a time-optimum low-thrust SEP spiral. This allows for a dramatic decrease in the mass required in the parking orbit or an increase in the mass injected into the pole-sitter orbit, but at the cost of an increased time of flight. For example, the maximised mass that can be delivered to the SEP fuel-optimal pole-sitter orbit increases to 4537/10704 kg (Soyuz/Ariane 5) at the cost of a 40 times larger time of flight. Another disadvantage is the time spent in eclipse during the spiral, which can become considerable and should be accounted for.

Regarding the final research objective, an additional transfer associated with the pole-sitter orbit has been investigated that allows a seasonal transfer of the spacecraft between pole-

sitter orbits above the north and south poles to only observe the pole that is illuminated, rather than following one pole-sitter orbit all year round. Both a short transfer, that leaves the north pole-sitter orbit before the Arctic winter and enters the south pole-sitter orbit just after the start of the Antarctic summer, and a long transfer, that starts just after the Arctic winter and ends just before Antarctic summer, exist. However, the long transfer is more demanding from a propellant consumption point of view and observes the polar regions also partially during the polar winters. It is therefore considered a less favourable option.

Deriving the optimal control problem for both the use of pure SEP and hybrid sail propulsion (in compliance with the research objective) minimum-fuel transfers can be obtained, but these allow only short observations times, i.e. the transfer is initiated far before the start of the Arctic winter and ends well into the Antarctic summer. When using hybrid propulsion, the observation time increases for increasing values of the lightness number, while the propellant consumption decreases. For large enough values of the lightness number (on the boundary of what would be possible in the near-term), the transfer can even be performed using only the solar sail. As such, hybrid sail propulsion can be seen as a useful tool for the transition between pure SEP and pure solar sail missions and to pull the technology development of sail technology.

To increase the observation time further, additional optimisations that trade-off propellant consumption and observation time have been performed. That way, observation times of up to 94 days can be achieved for the fuel-optimal pole-sitter orbits for propellant masses ranging between 55.3 and 173.1 kg, depending on the propulsion method employed and the launch configuration (i.e. the mass injected into the pole-sitter orbit). For shorter observations times, hybrid propulsion enables mass savings with respect to the pure SEP case of up to 81 percent. Furthermore, for shorter observation times, the transfer requires less propellant than the pole-sitter orbit itself. For example, for the optimal SEP pole-sitter orbit, the gain with respect to remaining in the pole-sitter orbit is 279.6 kg after 5 years, which can significantly increase the mission lifetime and/or payload mass.

All transfers associated with the pole-sitter concept have successfully been optimised using two different direct pseudospectral methods for verification purposes.

Summarised, the following main conclusions can be drawn:

- A range of pole-sitter orbits (constant altitude, tilted, fuel-optimal) are accessible from Earth using ballistic, SEP and hybrid sail transfers.
- To obtain an initial guess for the low-thrust transfers, a new shape-based approach based on Jacobi elliptic functions has been developed successfully and outperforms the conventional

exponential sinusoidal shape on a range of test cases in terms of satisfaction of the boundary conditions and the amount of thrust required throughout the transfer.

- When using the launcher's upper-stage to escape from a LEO parking orbit and minimising the mass required in LEO to inject a predetermined mass into the pole-sitter orbit, the largest Soyuz parking orbit inclination (that is closest to 90 deg) performs best. When maximising the mass injected into the pole-sitter orbit by exploiting the full launcher capacity into LEO, the smallest Soyuz parking orbit inclination is most optimal.

- For the constant altitude pole-sitter orbit the launch window is flexible, while for non-constant altitude pole-sitter orbits the distance at injection is of importance and the launch window is no longer flexible.

- Hybrid sail propulsion enables gains in mass required in LEO or mass injected into the pole-sitter orbit with respect to the pure SEP option. The increased mass injected into the pole-sitter orbit, together with the smaller propellant consumption in the hybrid pole-sitter orbit, allows an extension of the pole-sitter mission by 2-2.4 years.

- When using a low-thrust spiral to escape from LEO, the mass required in LEO can be reduced and the mass injected into the pole-sitter can be increased significantly with respect to the upper-stage approach at the cost of an equally significant increase in the time of flight.

- A seasonal transfer of the spacecraft between pole-sitter orbits above the north and south poles is possible to only observe the pole that is illuminated or to visit both poles with one single spacecraft within one mission.

- Considering the minimum-fuel transfers, hybrid sail propulsion allows both a reduction in the propellant consumption and faster transfers (i.e. longer observation times per pole) compared to the pure SEP case. For advanced sail technology the transfer can even be performed using only the sail.

- Trading off propellant consumption and observation time per pole is also possible. For the slower transfers (i.e. shorter observation times per pole), the transfer requires less propellant than the pole-sitter orbit itself, allowing an extension of the mission lifetime and/or increase in the payload capacity.

With the design of the LEO-to-pole-sitter and north-to-south transfers, the accessibility of a broad range of pole-sitter orbits has been demonstrated, while highlighting the potential of hybrid sail propulsion. Combined with the north-to-south transfer, that enables to overcome observation limitations introduced by the polar winter, a full analysis of the pole-sitter concept has been enabled.

Future research

In addition to the research presented in this thesis, analyses can be thought off that could complement or improve the results presented. These considerations are given below.

Displaced geostationary orbits

The dynamics used to generate displaced geostationary orbits and to evaluate their performance considered a two-body model. Afterwards, the effects of the non-uniformity of the Earth's gravitational field and non-ideal properties of the solar sail on this performance have been investigated. However, other perturbations also act on a spacecraft in (displaced) geostationary orbit, including third body perturbations of the Sun and Moon and periods of no thrust due to eclipses during the equinoxes. Higher-fidelity results could therefore be obtained by including these perturbations in the spacecraft dynamics.

Except for these perturbations, the mission analysis of the displaced geostationary orbit is essentially complete. However, the concept could benefit from a more detailed systems engineering analysis to establish a realistic mission scenario, including communication, thermal and power analyses.

Also, contingency scenarios could be investigated in case the SEP thruster or solar sail fails. In the latter case, smaller out-of-plane displacements could still be maintained with the use of only the SEP thruster, without deteriorating the mission lifetime too much. Alternatively, a scenario as described for the higher out-of-plane displaced GEOs can be implemented where the spacecraft is transferred between a parking orbit and the displaced GEO to provide coverage only when needed. This can lead to considerable savings of propellant, enabling relatively long mission lifetime. Otherwise, if the SEP thruster fails, the pure solar sail orbits defined by Baig and McInnes[18] could be investigated. Although they do not allow for full geostationary conditions and rather small displacements, they could serve as backup option.

Pole-sitter transfers – high-thrust launch phase

The transfer to the pole-sitter orbits has been designed by dividing the trajectory into a high-thrust launch phase and a low-thrust transfer phase. For the launch phase, a strategy was adopted that could be verified against a set of reference missions provided by the Soyuz launch vehicle manual.[139] Furthermore, it allowed a simple, though reliable, method to compare the performance of different transfer trajectories. However, the limitation is that

only non-escape launches are considered. Future research could investigate the possibility of a launch to escape, either through the use of an intermediate parking orbit or a direct ascent profile. It is expected that the transfer can benefit from such an escape launch strategy since the results indicated that launches to very high eccentricities are preferred.

Additional improvements can potentially be obtained for the use of an Ariane 5 launch. For the Ariane 5 launch vehicle, a similar launch profile was assumed as for a Soyuz launch due to the lack of detailed information in the literature and also for comparison purposes. However, by using more accurate launch models, specifically developed for Ariane 5, improvements could possibly be achieved.

Finally, for the design of the low-thrust transfer phase, a new shape-based approach has been developed to generate initial guesses for the optimal control solver. While its potential has been shown for transfers to pole-sitter orbits (in Chapter 4) as well as for time-fixed and time-free circle-to-circle and circle-to-ellipse transfers (in Appendix A), the additional computational effort that comes with this good performance is significant. This is due to the need for a nested root-finding algorithm compared to a single root-finding algorithm for the exponential sinusoidal shape against which the expo-elliptic shape is compared. In order to further develop this shape-based approach and to compare it with other, state of the art, shapes, investigations to reduce this computation effort are required.

Pole-sitter transfers – low-thrust launch phase

In order to compute the evolution of the low-thrust spiral that replaces the previously described high-thrust launch phase, the dynamics in the spiral are described using Keplerian elements. Although they have a clear, intuitive physical meaning, it is known that Keplerian elements can cause singularities for zero eccentricity and zero inclination orbits. This also has an effect on the orbital averaging technique employed that reduces the computation effort when integrating the equations of motion in the spiral. The implication is that the circular parking orbit, from where the transfer is initiated, needs to be approximated with a slightly elliptic orbit. Although this approximation will not have a significant influence on the results presented in Chapter 6, an improved approach could be obtained by considering the use of (modified) equinoctial elements, which have specifically been developed to overcome these singularities. They have been used before for the orbital averaging technique to compute multi-revolution spirals[145, 153] and a similar technique could be employed for the low-thrust launch phase spiral in future research.

The accuracy of the results obtained for the low-thrust spiral could furthermore benefit from including effects such as Earth shadowing, Earth oblateness and third body perturbations into the spacecraft dynamics. The estimation of the time in eclipse has shown that, especially at low-altitudes, the spacecraft spends a large amount of time in eclipse during which limited or no thrust will be available. This can have a considerable effect on the evolution of the spiral. Furthermore, at low altitudes, the spacecraft travels through the Van Allen radiation belts, which can have significant impact on spacecraft subsystems. Future research may therefore investigate the possibility to use the upper-stage to first raise the orbit altitude above the radiation belts and subsequently initiate the spiral. At these higher altitudes, third body perturbations (e.g. from the Sun) will become important, which could be taken into account by considering the Sun's gravitational perturbation to be constant over one orbit since its period is significantly greater than the period of the spacecraft's orbit.[154] Alternatively, a double averaging technique could be employed where the second averaging takes place over the period of the Sun.[155, 156]

Finally, concerning the low-thrust spiral, future research may investigate the use of hybrid sail propulsion in the spiral in addition to the pure SEP case considered in this thesis. This will most certainly lower the propellant consumption in the spiral, leading to further gains in mass required in LEO or mass injected into the pole-sitter orbit. However, when doing so, operational limitations such as the solar sail turning rate and the relative orientation of the SEP exhaust and the solar sail need to be taken into account. Especially, at low altitudes when rapid changes in the solar sail orientation over one revolution can be expected, these limitations might impose severe constraints on the use of the solar sail in the spiral.

Hybrid sail propulsion

This thesis has shown the potential of pure solar electric propulsion and of hybrid sail propulsion for enabling the concept of displaced geostationary orbits and transfers to and between pole-sitter orbits. For both concepts, models for the acceleration generated by the SEP thruster and solar sail have been employed that might benefit from future research.

For the SEP thruster, the effect of solar array degradation might be investigated as this may reduce the available power (and consequently thrust magnitude) over the mission lifetime. This could be taken into account by slightly over sizing the solar arrays (in case of pure SEP) or the thin film solar cells (in case of hybrid sail propulsion) to ensure enough power is available at end of life. This effect has to be taken into account in, for example, the mass budget analysis for the displaced geostationary orbit in Chapter 3. While the effect of a

slightly larger area of thin film solar cells will be minimal (the current mass of the thin films is only a few kilograms), a larger effect might result from over sizing the solar arrays.

Concerning the SEP thruster, future research can also focus on modelling a penalty on the specific impulse for throttling between zero-thrust and maximum thrust, since for the analyses in this thesis, throttling is performed under the assumption of a fixed specific impulse.

Finally, considering the solar sail, medium to high fidelity models have been used throughout this thesis. However, with the successful IKAROS and NanoSail-D2 solar sail missions, in-flight data may allow for a future refinement of these models. Also additional effects, such as solar sail degradation due to space debris impact, may be considered in future research to enhance the solar sail model even further.

Non-Keplerian orbits using hybrid sail propulsion

The discussion above has focussed on recommendations with respect to details in the dynamical and system models used throughout this thesis. However, more high level recommendations can also be made based on the results in this thesis that have clearly demonstrated the potential of non-Keplerian orbits to enhance space applications on Earth and the use of hybrid sail propulsion to enable these non-Keplerian orbits and improve their performances. Therefore, building on this excellent performance, a whole range of other applications can be thought of that could benefit in a similar way from non-Keplerian orbits and/or hybrid sail propulsion.

A first example is space weather monitoring, which is of importance because geomagnetic storms can cause satellite failure, overload power grids on Earth and present hazardous conditions to astronauts. The warning time for a solar storm with current infrastructure (i.e. the ACE satellite at the L_1-point) is relatively short, approximately one hour.[160] Furthermore, in the early 2020s ACE will need to be replaced. Currently, studies such as the Geostorm mission are being conducted, where a spacecraft is positioned at a sub-L_1-point using a solar sail, doubling the warning time with respect to a spacecraft at the L_1-point.[41] Potentially further increased warning times can be obtained with hybrid sail propulsion or, alternatively, hybrid sail propulsion could enable similar warning times but for lower performance solar sails. Finally, through the SEP thruster, hybrid sail propulsion could also provide a back-up option in case the solar sail should fail to deploy.

Other missions that could benefit from the use of NKOs and/or hybrid sail propulsion include a subsolar point mission, where hybrid sail propulsion can be used to enter regions that are inaccessible for the solar sail in the circular restricted three body problem.[56] Then, a spacecraft can be positioned between the Earth and Sun (i.e. an extreme case of an apogee above the Sunlit side of the Earth), much closer than the L_1-point. Similarly, a sub-dawn or sub-dusk mission could be investigated to perform dedicated Earth observation research.

Bibliography

[1].   Tsiolkovsky, K. E. *Исследование мировых пространств реактивными приборами ("The Exploration of Cosmic Space by Means of Reaction Devices")*, 1903.

[2].   Goddard, R. H. "A Method of Reaching Extreme Altitudes," *Smithsonian Miscellaneous Collections*. Vol. 71, No. 2, 1919.

[3].   Perring, W. G. A. "A Critical Review of German Long-Range Rocket Development," *Journal of the American Rocket Society*. Vol. 00, No. 65, 1946, pp. 1-17.

[4].   Furniss, T. *A History of Space Exploration and Its Future*: Mercury Books London, 2005.

[5].   Edelson, B. I. "Communication Satellites: The Experimental Years," *Acta Astronautica* Vol. 11, No. 7-8, 1984, pp. 407-413. Doi: 10.1016/0094-5765(84)90081-X

[6].   Noordung, H. *Das Problem der Befahrung des Weltraums - der Raketen-Motor*. Berlin: Richard Carl Smidt & Co., 1929.

[7].   Bentley, R. M., and Owens, A. T. "SYNCOM Satellite Program," *Journal of Spacecraft and Rockets* Vol. 1, No. 4, 1964, pp. 395-399. Doi: 10.2514/3.27667

[8].   Wertz, J. R. *Mission Geometry; Orbit and Constellation Design and Management*. El Segundo, USA/London, UK: Space Technology Library, Microcosm Press/Kluwer Academic Publishers, 2001.

[9].   Jehn, R., Rossi, A., Flohrer, T., and Navarro-Reyes, D. "Reorbiting of Satellites in High Altitudes," *5th European Conference on Space Debris*. Vol. ESA SP-672, Darmstadt, Germany, 2009.

[10].   Inter-Agency Space Debris Coordination Committee. "IADC Space Debris Mitigation Guidelines IADC-02-01 Revision 1." 2007.

[11].   UN COPUOS. "Long-term Sustainability of Outer Space Activities, Preliminary Reflections," *47th session of the United Nations Committee on the Peaceful Uses of Outer Space (UN COPUOS) Scientific and Technical Subcommittee*. Vienna, Austria, 2010.

[12].   ITU. "Constitution of ITU: Chapter VII - Special Provision for Radio - Article 44-PP - 98."

[13]. Flury, W. "Space Debris Issues in the Geostationary Ring " *Collection of Technical Papers 2 (A00-25001 06-32), AIAA International Communications Satellite Systems Conference and Exhibit*. AIAA-2000-1120, Oakland, California, 2000.

[14]. Smith, D. A., Martin, C., Kassebom, M., Petersen, H., Shaw, A., Skidmore, B., Smith, D., Stokes, H., and Willig, A. "A Mission to Preserve the Geostationary Region," *Advances in Space Research* Vol. 34, 2004, pp. 1214-1218. Doi: doi:10.1016/j.asr.2003.02.042

[15]. Forward, R. L. "Light-levitated Geostationary Cylindrical Orbits Using Perforated Light Sails," *Journal of the Astronautical Sciences*. Vol. 32, 1984, pp. 221-226.

[16]. Fisher, H. J., and Haerting, A. "Why Light-levitated Geostationary Cylindrical Orbits Are Not Feasible," *Journal of the Astronautical Sciences*. Vol. 40, 1992, pp. 329-333.

[17]. Van de Kolk, C. "Stability of Levitated Cylindrical Orbits by Using Solar Sails (AAS 99-335)," *AAS/AIAA Astrodynamics Specialist Conference*. Fridwood, Alaska, 1999.

[18]. Baig, S., and McInnes, C. R. "Light-Levitated Geostationary Cylindrical Orbits Are Feasible," *Journal of Guidance, Control, and Dynamics* Vol. 33, No. 3, 2010, pp. 782-793. Doi: 10.2514/1.46681

[19]. Launius, R. D., and Jenkins, D. R., eds. *To Reach the High Frontier - A History of U.S. Launch Vehicles*: The University Press of Kentucky, 2002.

[20]. Schutz, B. E., Zwally, H. J., Shuman, C. A., Hancock, D., and DiMarzio, J. P. "Overview of the ICESat Mission," *Geophysical Research Letters* Vol. 32, No. L21S01, 2005. Doi: 10.1029/2005GL024009

[21]. Wingham, D. J., Francis, C. R., Baker, S., Bouzinac, C., Brockley, D., Cullen, R., de Chateau-Thierry, P., Laxon, S. W., Mallow, U., Macvrocordatos, C., Phalippou, L., Ratier, G., Rey, L., Rostan, F., Viau, P., and Wallis, D. W. "CryoSat: A Mission to Determine the Fluctuations in Earth's Land and Marine Ice Fields," *Advances in Space Research* Vol. 37, 2006, pp. 841-871. Doi: 10.1016/j.asr.2005.07.027

[22]. European Space Agency. "ESA Portal - Arctic Ice Nears Record Low." Retrieved from http://www.esa.int/esaCP/SEMPQF0UDSG_index_0.html, 15 May 2012.

[23]. Lazzara, M. A., Coletti, A., and Diedrich, B. L. "The Possibilities of Polar Meteorology, Environmental Remote Sensing, Communications and Space Weather Applications from Artificial Lagrange Orbit," *Advances in Space Research* Vol. 48, No. 11, 2011, pp. 1880-1889. Doi: 10.1016/j.asr.2011.04.026

[24]. Gautier, D. L., Bird, K. J., Charpentier, R. R., Grantz, A., Houseknecht, D. W., Klett, T. R., Moore, T. E., Pitman, J. K., Schenk, C. J., Schuenemeyer, J. H., Sørensen, K., Tennyson, M. E., Valin, Z. C., and C.J., W. "Assessment of Undiscovered Oil and Gas in the Arctic," *Science* Vol. 324, No. 5931, 2009, pp. 1175-1179. Doi: 10.1126/science.1169467

[25]. Johannessen, O. M., Alexandrov, V. Y., Frolov, I. Y., Sandven, S., Pettersson, L. H., VBobylev, L. P., Kloster, K., Smirnov, V. G., Mironov, Y. U., and Babich, N. G. *Remote Sensing of Sea Ice in the Northern Sea Route - Studies and Applications*. Chichester, UK: Praxis Publishing Ltd, 2007.

[26]. Anderson, P., and Macdonald, M. "Extension of the Molniya Orbit Using Low-Thrust Propulsion," *21st AAS/AIAA Space Flight Mechanics Meeting, AAS 11-236*. New Orleans, USA, 2011.

[27]. Anderson, P., and Macdonald, M. "Extension of highly elliptical Earth orbits using continuous low-thrust propulsion " *Journal of Guidance, Control, and Dynamics*, 2012, In Press.

[28]. Forward, R. L. "Statite: A Spacecraft That Does Not Orbit," *Journal of Spacecraft and Rockets* Vol. 28, No. 5, 1991, pp. 606-611. Doi: 10.2514/3.26287

[29]. Waters, T. J., and McInnes, C. R. "Periodic Orbits Above the Ecliptic in the Solar-Sail Restricted Three-Body Problem," *Journal of Guidance, Control, and Dynamics* Vol. 30, No. 3, 2007, pp. 687-693. Doi: 10.2514/1.26232

[30]. Ceriotti, M., McInnes, C. R., and Diedrich, B. L. "The Pole-sitter Mission Concept: An Overview of Recent Developments and Possible Future Applications," *62nd International Astronautical Congress*. Cape Town, South Africa, 2011.

[31]. Ceriotti, M., Diedrich, B., and McInnes, C. "Novel Mission Concepts for Polar Coverage: An Overview of Recent Developments and Possible Future Applications," *Acta Astronautica* Vol. 80, 2012, pp. 89-104. Doi: 10.1016/j.actaastro.2012.04.043

[32]. Ceriotti, M., and McInnes, C. R. "Generation of Optimal Trajectories for Earth Hybrid Pole Sitters," *Journal of Guidance, Control, and Dynamics* Vol. 34, No. 3, 2011, pp. 847-859. Doi: 10.2514/1.50935

[33]. Driver, J. "Analysis of an Arctic Polesitter," *Journal of Spacecraft and Rockets* Vol. 17, No. 3, 1980, pp. 263-269. Doi: 10.2514/3.57736

[34]. Ceriotti, M., and McInnes, C. R. "Hybrid Solar Sail and SEP Propulsion for Novel Earth Observation Missions," *61st International Astronautical Congress*. Prague, Czech Republic, 2010.

[35]. Golan, O. M., and Breakwell, J. V. "Low Thrust Power-Limited Transfer For a Pole Squatter," *AIAA/AAS Astrodynamics Conference*. Minneapolis, Minnesota, 1988.

[36]. Hughes, G. W. "A Realistic, Parametric Compilation of Optimised Heliocentric Solar Sail Trajectories." PhD thesis, Department of Aerospace Engineering, University of Glasgow, 2005.

[37]. Kepler, J., (Translated by William H. Donahue),. *New Astronomy*. Cambridge, UK: Cambridge University Press, 1992.

[38]. Battin, R. H. *An Introduction to the Mathematics and Methods of Astrodynamics, Revised Edition*. Reston, USA: American Institute of Aeronautics and Astronautics, Inc., 1999.

[39]. Newton, I. "Philosophiæ Naturalis Principia Mathematica." 1687.

[40]. Euler, L. *Theoria Motuum Planetarum et Cometarum*. Berlin: Ambrosius Haude, 1744.

[41]. McInnes, C. R. *Solar Sailing: Technology, Dynamics and Mission Applications*. Berlin: Springer-Praxis Books in Astronautical Engineering, Springer-Verlag, 1999.

[42]. McInnes, C. R. "Dynamics, Stability, and Control of Displaced Non-Keplerian Orbits," *Journal of Guidance, Control, and Dynamics* Vol. 21, No. 5, 1998, pp. 799-805. Doi: 10.2514/2.4309

[43]. McKay, R. J., Macdonald, M., Biggs, J., and McInnes, C. "Survey of Highly Non-Keplerian Orbits with Low-Thrust Propulsion," *Journal of Guidance, Control, and Dynamics* Vol. 34, No. 3, 2011. Doi: 10.2514/1.52133

[44]. Oberth, H. J. *Wege zur Raumschiffahrt ("Ways to Spaceflight")*, 1929.

[45]. Dusek, H. M. *Motion in the Vicinity of Libration Points of a Generlized Restricted Three-Body Model*, 1966.

[46]. McInnes, C., and Simmons, J. F. L. "Solar Sail Halo Orbits. Part I - Heliocentric Case," *Journal of Spacecraft and Rockets* Vol. 29, No. 4, 1992, pp. 466-471. Doi: 10.2514/3.25487

[47]. McInnes, C. R. "The Existence And Stability Of Families Of Displaced Two-Body Orbits," *Celestial Mechanics and Dynamical Astronomy* Vol. 67, No. 2, 1997, pp. 167-180. Doi: 10.1023/A:1008280609889

[48]. Biggs, J. D., McInnes, C. R., and Waters, T. "Control of Solar Sail Periodic Orbits in the Elliptic Three-Body Problem," *Journal of Guidance, Control, and Dynamics* Vol. 32, No. 1, 2009, pp. 318-320. Doi: 10.2514/1.38362

[49]. McInnes, C. R., and Simmons, J. F. L. "Solar Sail Halo Orbit. Part II - Geocentric Case," *Journal of Spacecraft and Rockets* Vol. 29, No. 4, 1992, pp. 472-479. Doi: 10.2514/3.55639

[50]. Macdonald, M., McInnes, C., Alexander, D., and Sandman, A. "GeoSail: Exploring the Magnetosphere Using a Low-cost Solar Sail," *Acta Astronautica* Vol. 59, 2006, pp. 757-767. Doi: 10.1016/j.actaastro.2005.07.023

[51]. Bookless, J., and McInnes, C. R. "Dynamics and Control of Displaced Periodic Orbits Using Solar-Sail Propulsion," *Journal of Guidance, Control, and Dynamics* Vol. 29, No. 3, 2006, pp. 527-537. Doi: 10.2514/1.15655

[52]. Nock, K. T. "Rendezvous with Saturn's rings," *CNES Planetary Rings*. 1984, pp. 743-759.

[53]. Spilker, T. R. "Saturn Ring Observer," *Acta Astronautica* Vol. 52, 2003, pp. 259-265. Doi: 10.1016/S0094-5765(02)00165-0

[54]. Lu, E. T., and Love, S. G. "Gravitational Tractor for Towing Asteroids," *Nature* Vol. 438, 2005, pp. 177-178. Doi: 10.1038/438177a

[55]. Wie, B. "Dynamics and Control of Gravity Tractor Spacecraft for Asteroid Deflection," *Journal of Guidance, Control, and Dynamics* Vol. 31, No. 5, 2008, pp. 1413-1426. Doi: 10.2514/1.32735

[56]. McInnes, C. R., McDonald, A. J., Simmons, J. F. L., and MacDonald, E. W. "Solar Sail Parking in Restricted Three-Body Systems," *Journal of Guidance, Control, and Dynamics* Vol. 17, No. 2, 1994, pp. 399-406. Doi: 10.2514/3.21211

[57]. Baoyin, H., and McInnes, C. "Solar Sail Halo Orbits at the Sun-Earth Artificial L1-point," *Celestial Mechanics and Dynamical Astronomy* Vol. 94, 2006, pp. 155-171. Doi: 10.1007/s10569-005-4626-3

[58]. Ceriotti, M., and McInnes, C. R. "An Earth Pole-Sitter Using Hybrid Propulsion," *AIAA/AAS Astrodynamics Specialists Conference*. Toronto, Canada, 2010.

[59]. West, J. L. "The GeoStorm Warning Mission: Enhanced Opportunities Based on New Technology," *14th AAS/AIAA Spaceflight Mechanics Conference*. AAS-04-102, Maui, Hawaii, 2004.

[60]. Grebow, D. J., Ozimek, M. T., and Howell, K. C. "Advanced Modeling of Optimal Low-Thrust Lunar Pole-Sitter Trajectories," *Acta Astronautica* Vol. 67, No. 7-8, 2010, pp. 991-1001. Doi: 10.1016/j.actaastro.2010.04.024

[61]. Simo, J., and McInnes, C. R. "Solar Sail Orbits at the Earth-Moon Libration Points," *Communications in Nonlinear Science and Numerical Simulation* Vol. 14, No. 12, 2009, pp. 4191-4196. Doi: 10.1016/j.cnsns.2009.03.032

[62]. Wertz, J. R., and Larson, W. J. *Space Mission Analysis and Design*. El Segundo, USA/London, UK: Space Technology Library, Microcosm Press/Kluwer Academic Publishers, 1999.

[63]. Choueiri, E. Y. "A Critical History of Electric Propulsion: The First 50 Years (1906-1956)," *Journal of Propulsion and Power* Vol. 20, No. 2, 2004, pp. 193-203. Doi: 10.2514/1.9245

[64]. Sovey, J. S., Rawlin, V. K., and Patterson, M. J. "A Synopsis of Ion Propulsion Development Projects in the United States: SERT I to Deep Space I," *35th AIAA/ASME/SAE/ASEE Joint Propulsion Conference and Exhibit*. Los Angeles, California, 1999.

[65]. Rayman, M. D., Chadbourne, P. A., Culwell, J. S., and Williams, S. N. "Mission Design for Deep Space 1: A Low-Thrust Technology Validation Mission," *Acta Astronautica* Vol. 45, 1999, pp. 381-388. Doi: 10.1016/S0094-5765(99)00157-5

[66]. Foing, B. H., Racca, G. D., Marini, A., Evrard, E., Stagnaro, L., Almeida, M., Koschny, D., Frew, D., Zender, J., Heather, J., Grande, M., Huovelin, J., Keller, H. U., Nathues, A., Josset, J. L., Malkki, A., Schmidt, W., Noci, G., Birkl, R., Iess, L., Sodnik, Z., and McManamon, P. "SMART-1 Mission to the Moon: Status, First Results and Goals," *Advances in Space Research* Vol. 37, No. 1, 2006, pp. 6-13. Doi: 10.1016/j.asr.2005.12.016

[67]. Kawaguchi, J. i., Fujiwara, A., and Uesugi, T. "Hayabusa - Its Technology and Science Accomplishment Summary and Hayabusa-2," *Acta Astronautica* Vol. 62, No. 10–11, 2008, pp. 639-647. Doi: 10.1016/j.actaastro.2008.01.028

[68]. Russell, C. T., Coradini, A., Christensen, U., De Sanctis, M. C., Feldman, W. C., Jaumann, R., Keller, H. U., Konopliv, A. S., McCord, T. B., McFadden, L. A., McSween, H. Y., Mottola, S., Neukum, G., Pieters, C. M., Prettyman, T. H., Raymond, C. A., Smith, D. E., Sykes, M. V., Williams, B. G., Wise, J., and Zuber, M. T. "Dawn: A Journey in Space and Time," *Planetary and Space Science* Vol. 52, No. 5–6, 2004, pp. 465-489. Doi: 10.1016/j.pss.2003.06.013

[69]. Muzi, D., and Allasio, A. "GOCE: The First Core Earth Explorer of ESA's Earth Observation Programme," *Acta Astronautica* Vol. 54, No. 3, 2004, pp. 167-175. Doi: 10.1016/s0094-5765(02)00296-5

[70]. Gray, H. L., and Kemble, S. "Using Electric Propulsion to Get to Mercury - The BepiColombo Mission," *43rd AIAA/ASME/SAE/ASEE Joint Propulsion Conference & Exhibit*. AIAA 2007-5229, Cincinnati, Ohio, 2007.

[71]. Ziemer, J. K., and Merkowitz, S. M. "Microthrust Propulsion for the LISA Mission," *40th AIAA/ASME/SAE/ASEE Joint Propulsion Conference and Exhibit*. Fort Lauderdale, Florida, 2004.

[72]. Schmidt, G. R., Patterson, M. J., and Benson, S. W. "The NASA Evolutionary Xenon Thruster (NEXT): The Next Step for U.S. Deep Space Propulsion," *59th International Astronautical Congress*. Glasgow, United Kingdom, 2008.

[73]. Scharlemann, C., Genovese, A., Buldrini, N., Schnitzer, R., and Tajmar, M. "In-FEEP Qualification Test Program for LISA Pathfinder," *44th AIAA/ASME/SAE/ASEE Joint Propulsion Conference & Exhibit*. AIAA 2008-4825, Hartford, Connecticut, 2008.

[74]. Bond, T. A., and Christensen, J. A. "NSTAR Ion Thrusters and Power Processors (NASA/CR-1999-209162)." 1999.

[75]. EADS Astrium. "EADS Astrium Ion Propulsion Systems." Retrieved from http://cs.astrium.eads.net/sp/spacecraft-propulsion/ion-propulsion/index.html, 10 June 2012.

[76]. Crofton, M. W., Pollard, J. E., Beiting, E. J., Spektor, R., Diamant, K. D., Eapen, X. L., Cohen, R. B., and Patterson, M. J. "Characterization of the NASA NEXT Thruster," *45th AIAA/ASME/SAE/ASEE Joint Propulsion Conference & Exhibit*. AIAA 2009-4815, Denver, Colorado, 2009.

[77]. QinetiQ. "T6 Gridded Ion Engine." Retrieved from http://www2.qinetiq.com/home/markets/related_markets/space/electric_propulsion/electric_propulsion0/t6_gridded_ion_engine.html, 20 December 2012.

[78]. Tsiolkovsky, K. E. "Extension of Man into Outer Space." 1921.

[79]. Tsander, F. A. *Problems of Flight by Jet Propulsion (Collection of articles, translated from Russian)*, 1964.

[80]. Tsuda, Y., Mori, O., Funase, R., Sawada, H., Yamamoto, T., Saiki, T., Endo, T., and Kawaguchi, J. "Flight Status of IKAROS Deep Space Solar Sail Demonstrator," *Acta Astronautica* Vol. 69, No. 9-10, 2011, pp. 833-840. Doi: 10.1016/j.actaastro.2011.06.005

[81]. Johnson, L., Whorton, M., Heaton, A., Pinson, R., Laue, G., and Adams, C. "NanoSail-D: A Solar Sail Demonstration Mission," *Acta Astronautica* Vol. 68, 2011, pp. 571-575. Doi: 10.1016/j.actaastro.2010.02.008

[82]. Dachwald, B., Mengali, G., Quarta, A. A., and Macdonald, M. "Parametric Model and Optimal Control of Solar Sails with Optical Degradation," *Journal of Guidance, Control, and Dynamics* Vol. 29, No. 5, 2006, pp. 1170-1178. Doi: 10.2514/1.20313

[83]. Murphy, D. M., Murphey, T. W., and Gierow, P. A. "Scalable Solar-sail Subsystem Design Considerations," *43rd Structures, Structural Dynamics, and Materials Conference*. AIAA-2002-1703, Denver, Colorado, 2002.

[84]. Dachwald, B. "Optimal Solar Sail Trajectories for Missions to the Outer Solar System," *AIAA/AAS Astrodynamics Specialist Conference and Exhibit*. AIAA-2004-5406, Providence, Rhode Island, 2004.

[85]. Baig, S., and McInnes, C. R. "Artificial Three-Body Equilibria for Hybrid Low-Thrust Propulsion," *Journal of Guidance, Control, and Dynamics* Vol. 31, No. 6, 2008, pp. 1644-1655. Doi: 10.2514/1.36125

[86]. Mengali, G., and Quarta, A. A. "Optimal Three-Dimensional Interplanetary Rendezvous Using Nonideal Solar Sail," *Journal of Guidance, Control, and Dynamics* Vol. 28, No. 1, 2005, pp. 173-177. Doi: 10.2514/1.8325

[87]. Macdonald, M., and McInnes, C. R. "Solar Sail Mission Applications and Future Advancement," *2nd International Symposium on Solar Sailing*. New York, New York, 2010.

[88]. Leipold, M., and Götz, M. "Hybrid Photonic/Electric Propulsion." Kayser-Threde GmbH, Technical Report SOL4-TR-KTH-001, ESA contract No. 15334/01/NL/PA, Munich, Germany, 2002.

[89]. Mengali, G., and Quarta, A. A. "Trajectory Design with Hybrid Low-Thrust Propulsion System," *Journal of Guidance, Control, and Dynamics* Vol. 30, No. 2, 2007, pp. 419-426. Doi: 10.2514/1.22433

[90]. Mengali, G., and Quarta, A. A. "Tradeoff Performance of Hybrid Low-Thrust Propulsion System," *Journal of Spacecraft and Rockets* Vol. 44, No. 6, 2007, pp. 1263-1270. Doi: 10.2514/1.30298

[91]. Simo, J., and McInnes, C. R. "Designing Displaced Lunar Orbits Using Low-thrust Propulsion," *Journal of Guidance, Control, and Dynamics* Vol. 33, No. 1, 2010, pp. 259-265. Doi: 10.2514/1.45305

[92]. Mori, O., Sawada, H., Funase, R., Endo, T., Morimoto, M., Yamamoto, T., Tsuda, Y., Kawakatsu, Y., and Kawaguchi, J. "Development of First Solar Power Sail Demonstrator - IKAROS," *21st International Symposium on Space Flight Dynamics*. Toulouse, France, 2009.

[93]. Kawaguchi, J., Mimasu, Y., Mori, O., Funase, R., Yamamoto, T., and Tsuda, Y. "IKAROS - Ready for Lift-Off as the World's First Solar Sail Demonstration in Interplanetary Space," *60th International Astronautical Congress*. Daejeon, South Korea, 2009.

[94]. Betts, J. T. "Survey of Numerical Methods for Trajectory Optimization," *Journal of Guidance, Control, and Dynamics* Vol. 21, No. 2, 1998, pp. 193-207. Doi: 10.2514/2.4231

[95]. Vincent, T. L., and Grantham, W. J. *Nonlinear and Optimal Control Systems*: John Wiley & Sons, Inc., Canada, 1997.

[96]. Fahroo, F., and Ross, M. "Costate Estimation by a Legendre Pseudospectral Method," *Journal of Guidance, Control, and Dynamics* Vol. 24, No. 2, 2001, pp. 270-277. Doi: 10.2514/2.4709

[97]. Bryson, A. E., and Ho, Y. C. *Applied Optimal Control: Optimization, Estimation, and Control (Revised printing)*: Taylor & Francis Group, New York, USA, 1975.

[98]. Pontryagin, L. S. *The Mathematical Theory of Optimal Processes*: Wiley-Interscience, New York, 1962.

[99]. Betts, J. T. *Practical Methods for Optimal Control Using Nonlinear Programming*: Society for Industrial and Applied Mathematics (SIAM), Philadelphia, USA, 2001.

[100]. Hargraves, C. R., and Paris, S. W. "Direct Trajectory Optimization Using Nonlinear Programming and Collocation," *Journal of Guidance, Control, and Dynamics* Vol. 10, No. 4, 1987, pp. 338-342. Doi: 10.2514/3.20223

[101]. Elnagar, G., Kazemi, M. A., and Razzaghi, M. "The Pseudospectral Legendre Method for Discretizing Optimal Control Problems," *IEEE Transactions on Automatic Control* Vol. 40, No. 10, 1995, pp. 1793-1796. Doi: 10.1109/9.467672

[102]. Fahroo, F., and Ross, I. M. "Advances in Pseudospectral Methods for Optimal Control," *AIAA Guidance, Navigation and Control Conference and Exhibit*. AIAA 2008-7309, Honolulu, Hawaii, 2008.

[103]. Huntington, G. T. "Advancement and Analysis of a Gauss Pseudospectral Transcription for Optimal Control Problems." PhD thesis, Department of Aeronautics and Astronautics, Massachusetts Institute of Technology, 2007.

[104]. Vlassenbroeck, J., and van Dooren, R. "A Chebyshev Technique for Solving Nonlinear Optimal Control Problems," *IEEE Transactions on Automatic Control* Vol. 33, No. 4, 1988, pp. 333-340. Doi: 10.1109/9.192187

[105]. Dahlquist, G., and Björck, Å. *Numerical Methods in Scientific Computing - Volume I*: Society for Industrial and Applied Mathematics (SIAM), 2008.

[106]. Becerra, V. M. "Solving Complex Optimal Control Problems at No Cost with PSOPT," *IEEE Multi-conference on Systems and Control*,Yokohama, Japan, 2010.

[107]. Benson, D. A., Huntington, G. T., Thorvaldsen, T. P., and Rao, A. V. "Direct Trajectory Optimization and Costate Estimation via an Orthogonal Collocation Method," *Journal of Guidance, Control, and Dynamics* Vol. 29, No. 6, 2006, pp. 1435-1440. Doi: 10.2514/1.20478

[108]. Becerra, V. M. "PSOPT Optimal Control Solver User Manual." 2009.

[109]. Wächter, A., and Biegler, L. T. "On the Implementation of an Interior-point Filter Line-search Algorithm for Large-scale Nonlinear Programming," *Mathematical Programming* Vol. 106, No. 1, 2006, pp. 25-57. Doi: 10.1007/s10107-004-0559-y

[110]. Gill, P. E., Murray, W., and Saunders, M. A. "SNOPT: An SQP Alghorithm for Large-Scale Constrained Optimization," *SIAM Journal on Optimization* Vol. 12, No. 4, 2002, pp. 979-1006. Doi: 10.1137/S1052623499350013

[111]. Griewank, A., Juedes, D., and Utke, J. "Algorithm 755: ADOL-C: A Package for the Automatic Differentiation of Algorithms Written in C/C++," *ACM Transactions on Mathematical Software* Vol. 22, No. 2, 1996, pp. 131-167. Doi: 10.1145/229473.229474

[112]. Rao, A. V., Benson, D. A., Darby, C. L., Patterson, M. A., Francolin, C., Sanders, I., and Huntington, G. T. "Algorithm 902: GPOPS, A MATLAB Software for Solving Multiple-Phase Optimal Control Problems Using The Gauss Pseudospectral Method," *ACM Transactions on Mathematical Software* Vol. 37, No. 2, 2010, pp. 1-39. Doi: 10.1145/1731022.1731032

[113]. Boltz, F. W. "Orbital Motion Under Continuous Tangential Thrust," *Journal of Guidance, Control, and Dynamics* Vol. 15, No. 6, 1992, pp. 1503-1507. Doi: 10.2514/3.56583

[114]. Boltz, F. W. "Orbital Motion Under Continuous Radial Thrust," *Journal of Guidance, Control, and Dynamics* Vol. 14, No. 3, 1989, pp. 667-670. Doi: 10.2514/3.20690

[115]. Prussing, J. E., and Coverstone-Carroll, V. "Constant Radial Thrust Acceleration Redux," *Journal of Guidance, Control, and Dynamics* Vol. 21, No. 3, 1998, pp. 516-518. Doi: 10.2514/2.7609

[116]. Markopoulos, N. "Explicit, Near-Optimal Guidance for Power-Limited Transfers Between Coplanar Circular Orbits," *Journal of Guidance, Control, and Dynamics* Vol. 19, No. 6, 1996, pp. 1317-1325. Doi: 10.2514/3.21788

[117]. Kechichian, J. A. "Reformulation of Edelbaum's Low-Thrust Transfer Problem Using Optimal Control Theory," *Journal of Guidance, Control, and Dynamics* Vol. 20, No. 5, 1997, pp. 988-994. Doi: 10.2514/2.4145

[118]. Petropoulos, A. E., Longuski, J. M., and Vinh, N. X. "Shape-Based Analytic Representations of Low-Thrust Trajectories for Gravity-Assist Applications," *AAS/AIAA Astrodynamics Specialists Conference*. AAS 99-337, Girdwood, Alaska, 1999.

[119]. Petropoulos, A. E., and Longuski, J. M. "Automated Design of Low-Thrust Gravity-Assist Trajectories," *AIAA/AAS Astrodynamics Specialist Conference*. AIAA-2000-4033, Denver, Colorado, 2000.

[120]. Petropoulos, A. E., and Longuski, J. M. "Shape-Based Algorithm for Automated Design of Low-Thrust, Gravity-Assist Trajectories," *Journal of Spacecraft and Rockets* Vol. 41, No. 5, 2004, pp. 787-796. Doi: 10.2514/1.13095

[121]. De Pascale, P., and Vasile, M. "Preliminary Design of Low-Thrust Multiple Gravity-Assist Trajectories," *Journal of Spacecraft and Rockets* Vol. 43, No. 5, 2006, pp. 1065-1076. Doi: 10.2514/1.19646

[122]. Wall, B. J. "Shape-Based Approximation Method for Low-Thrust Trajectory Optimization," *AIAA/AAS Astrodynamics Specialist Conference and Exhibit*. AIAA-2008-6616, Honolulu, Hawaii, 2008.

[123]. Wall, B. J., and Conway, B. A. "Shape-Based Approach to Low-Thrust Rendezvous Trajectory Design," *Journal of Guidance, Control, and Dynamics* Vol. 32, No. 1, 2009, pp. 95-101. Doi: 10.2514/1.36848

[124]. Novak, D., and Vasile, M. "Improved Shaping Approach to the Preliminary Design of Low-Thrust Trajectories," *Journal of Guidance, Control, and Dynamics* Vol. 34, No. 1, 2010, pp. 128-147. Doi: 10.2514/1.50434

[125]. Meserve, B. E. *Fundamental Concepts of Algebra*. New York: Dover Publications, 1982.

[126]. Vallado, D. A. *Fundamentals of Astrodynamics and Applications*. New York, USA: Space Technology Library, 2007.

[127]. Evans, B. G. *Satellite Communication Systems*. London, UK: The Institution of Engineering and Technology, 1999.

[128]. Yashko, G. J., and Hastings, D. E. "Analysis of Thruster Requirements and Capabilities for Local Satellite Clusters," *AIAA Small Satellite Conference*. Logan, West Virginia, 1996.

[129]. Schneider, A., Sun, W., and Schuff, H. "The European Platform LUXOR for Small Communications Satellites," *26th International Communications Satellite Systems Conference (ICSSC)*. AIAA-2008-5441, San Diego, California, 2008.

[130]. Sun, W., Ellmers, F., Winklers, A., Schuff, H., and Sansegundo Chamarro, M. J. "European Small Geostationary Communications Satellites," *Acta Astronautica* Vol. 68, 2010, pp. 802-810. Doi: 10.1016/j.actaastro.2010.07.002

[131]. Liddle, D., Davies, P., Jason, S., Paffett, J., Underwood, C., and Sweeting, M. "A Low-cost Geostationary Minisatellite Platform," *Acta Astronautica* Vol. 55, 2004, pp. 271-284. Doi: 10.1016/j.actaastro.2004.05.056

[132]. Powell, M. J. D. *A Fast Algorithm for Nonlinearly Constrained Optimization Calculations*: Springer Berlin / Heidelberg, 1978.

[133]. Ceriotti, M., and McInnes, C. R. "Systems Design of a Hybrid Sail Pole-sitter," *Advances in Space Research* Vol. 48, No. 11, 2011, pp. 1754-1762. Doi: 10.1016/j.asr.2011.02.010

[134]. Gershman, R., and Seybold, C. "Propulsion Trades for Space Science Missions," *Acta Astronautica* Vol. 45, 1999, pp. 541-548. Doi: 10.1016/S0094-5765(99)00174-5

[135]. Kitamura, S., Ohkawa, Y., Hayakawa, Y., Yoshida, H., and Miyazaki, K. "Overview and Research Status of the JAXA 150-mN Ion Engine," *Acta Astronautica* Vol. 61, 2007, pp. 360-366. Doi: 10.1016/j.actaastro.2007.01.010

[136]. Heiligers, J., Ceriotti, M., McInnes, C. R., and Biggs, J. D. "Mission Analysis and Systems Design of a Near-Term and Far-Term Pole-Sitter Mission," *Acta Astronautica*, In Press, 2012. Doi:

[137]. Herman, D. A. "NASA's Evolutionary Xenon Thruster (NEXT) Project Qualification Propellant Throughput Milestone: Performance, Ersion, and Thruster Service Life Prediction After 450 kg (Report: NASA/TM-2010-216816)." November 2010.

[138]. Arianespace. "Ariane 5 User's Manual - Issue 5 - Revision 0." 2008.

[139]. Starsem "The Soyuz Company". "Soyuz User's Manual (ST-GTD-SUM-01 - issue 3 - revision 0)." 2001.

[140]. Shampine, L. F., Kierzenka, J., and Reichelt, M. W. "Solving Boundary Value Problems for Ordinary Differential Equations in MATLAB with bvp4c." Retrieved from http://www.mathworks.co.uk/matlabcentral/fileexchange/3819, 12 May 2012.

[141]. Ceriotti, M., Heiligers, J., and McInnes, C. R. "Trajectory and Spacecraft Design for a Pole-Sitter Mission," *Journal of Spacecraft and Rockets*, 2012, Accepted subject to minor corrections. Doi:

[142]. Heiligers, J., Ceriotti, M., McInnes, C. R., and Biggs, J. D. "Mission Analysis and Systems Design of a Near-term and Far-term Pole-sitter Mission," *1st IAA Conference on Dynamics and Control of Space Systems*. Porto, Portugal, 2012.

[143]. Ceriotti, M., and McInnes, C. R. "Hybrid Solar Sail and Solar Electric Propulsion for Novel Earth Observation Missions," *Acta Astronautica* Vol. 69, No. 9-10, 2011, pp. 809-821. Doi: 10.1016/j.actaastro.2011.06.007

[144]. Ceriotti, M., and McInnes, C. "A Near Term Pole-Sitter Using Hybrid Solar Sail Propulsion," *2nd International Symposium on Solar Sailing*. New York, New York, 2010.

[145]. Kluever, C. A., and Oleson, S. R. "Direct Approach for Computing near-Optimal Low-Thrust Earth-Orbit Transfers," *Journal of Spacecraft and Rockets* Vol. 35, No. 4, 1998, pp. 509-515. Doi: 10.2514/2.3360

[146]. Meyer, K. R. "Jacobi Elliptic Functions from a Dynamical Systems Point of View," *The American Mathematical Monthly* Vol. 108, No. 8, 2001, pp. 729-737. Doi: 10.2307/2695616

[147]. Abramowitz, M., and Stegun, I. A. *Handbook of Mathematical Functions: with Formulas, Graphs and Mathematical Tables*. Mineola, New York: Dover Publications, Inc., 1972.

[148]. Chipperfield, A. J., and Fleming, P. J. "The MATLAB Genetic Algorithm Toolbox," *IEE Colloquium on Applied Control Techniques Using MATLAB*, 1995, pp. 10/1 - 10/4.

[149]. Benson, D. A. "A Gauss Pseudospectral Transcription for Optimal Control." PhD thesis, Department of Aeronautics and Astronautics, Massachusetts Institute of Technology, 2004.

[150]. Huntington, G. T., and Rao, A. V. "Optimal Spacecraft Formation Configuration Using a Gauss Pseudospectral Method," *AAS/AIAA Spaceflight Mechanics Meeting*. AAS 05-103, Copper Mountain, Colorado, 2005.

[151]. Gao, Y. "Near-Optimal Very Low-Thrust Earth-Orbit Transfers and Guidance Schemes," *Journal of Guidance, Control, and Dynamics* Vol. 30, No. 2, 2007, pp. 529-539. Doi: 10.2514/1.24836

[152]. Gao, Y., and Kluever, C. A. "Analytic Orbital Averaging Technique for Computing Tangential-Thrust Trajectories," *Journal of Guidance, Control, and Dynamics* Vol. 28, No. 6, 2005, pp. 1320-1323. Doi: 10.2514/1.14698

[153]. Geffroy, S., and Epenoy, R. "Optimal Low-Thrust Transfers with Constraints - Generalization of Averaging Techniques," *Acta Astronautica* Vol. 41, No. 3, 1997, pp. 133-149. Doi: 10.1016/S0094-5765(97)00208-7

[154]. Ely, T. A. "Mean Element Propagations using Numerical Averaging," *2009 AAS/AIAA Astrodynamics Specialist Conference*. AAS 09-440, Pittsburgh, Pennsylvania, 2009.

[155]. Prado, A. F. B. A. "Third-body Perturbation in Orbits Around Natural Satellites," *Journal of Guidance, Control, and Dynamics* Vol. 26, No. 1, 2003, pp. 34-40. Doi: 10.2514/2.5042

[156]. Domingos, R. C., Vilhena de Moraes, R., and Prado, A. F. B. A. "Third-Body Perturbation in the Case of Elliptic Orbits for the Disturbing Body (Article ID 763654)," *Mathematical Problems in Engineering*, 2008. Doi: 10.1155/2008/763654

[157]. Kechichian, J. A. "Orbit Raising with Low-Thrust Tangential Acceleration in Presence of Earth Shadow," *Journal of Spacecraft and Rockets* Vol. 35, No. 4, 1998, pp. 516-525. Doi: 10.2514/2.3361

[158]. Betts, J. T., and Erb, S. O. "Optimal Low Thrust Trajectories to the Moon," *SIAM J. Applied Dynamical Systems* Vol. 2, No. 2, 2003, pp. 144-170. Doi: 10.1137/S1111111102409080

[159]. Gao, Y. "Direct Optimization of Low-Thrust Many-Revolution Earth-Orbit Transfers," *Chinese Journal of Aeronautics* Vol. 22, 2009, pp. 426-433. Doi: 10.1016/S1000-9361(08)60121-1

[160]. Caltech. "Advanced Composition Explorer (ACE) Home Page." Retrieved from http://www.srl.caltech.edu/ACE/, 6 July 2012.

[161]. Izzo, D. "Lambert's Problem for Exponential Sinusoids," *Journal of Guidance, Control, and Dynamics* Vol. 29, No. 5, 2006, pp. 1242-1245. Doi: 10.2514/1.21796

[162]. Forsythe, G. E., Malcolm, M. A., and Moler, C. B. *Computer Methods for Mathematical Computations*: Prentice-Hall, 1977.

[163]. Dysli, P. "Analytical Ephemeris for Planets (MATLAB code uplanet.m)." 1977.

[164]. NASA Jet Propulsion Laboratory. "JPL Small-Body Database Browser." Retrieved from http://ssd.jpl.nasa.gov/, 5 June 2011.

Appendix A

Expo-elliptic shape-based approach

During the design of the optimal Earth to pole-sitter transfers in Chapter 5, the expo-elliptic shape-based approach has been used to generate suitable initial guesses for the optimisation of the transfer with a direct pseudospectral method. In this appendix, the performance of the expo-elliptic shape is validated through a comparison with the performance of the exponential sinusoidal shape for a range of test cases, including both time-free problems (i.e. orbital transfers) in Section A.1 and time-fixed problems (i.e. Lambert's problem) in Section A.2).

A.1   Orbital transfers

For an initial assessment of the performance of the expo-elliptic shape with respect to the exponential sinusoidal shape, a set of planar, two-body, time-free transfers are considered. The problem definition is equal to the description provided for the transfer from LEO to the pole-sitter orbit in Section 5.4.1 and is applied here to an orbital transfer from Earth to Mars and from Earth to comet Temple-1. The only difference with respect to the approach in Section 5.4.1 is the definition of the objective function, because a problem specific objective function was defined in Section 5.4.1. Instead, in this appendix the following weighted objective function will be considered:

$$J = \Delta V_{traj} + w\left(\Delta V_0 + \Delta V_f\right) \tag{A.1}$$

with ΔV_0 and ΔV_f the impulses required at the start and end of the transfer in order to match the velocities in the initial and final orbit. Furthermore, ΔV_{traj} is the total impulse required during the transfer, which can be computed according to:

$$\Delta V_{traj} = \int_{\theta_0}^{\theta_f} \frac{|a|}{\dot{\theta}} d\theta \qquad (A.2)$$

where the acceleration, a, and angular rate, $\dot{\theta}$, are defined in Eqs. (5.32) and (5.31), respectively. To compute the value of this impulse during the transfer, the polar angle along the transfer is discretised into $50(N+1)$ equally spaced nodes, similar to the approach used in Section 5.4.1 to determine the maximum acceleration. Subsequently, trapezoidal numerical integration is used to approximate the integral in Eq. (A.2). Note that tests showed that 50 nodes per full revolution in combination with the trapezoidal approximation are sufficient to accurately compute the low-thrust impulse along the transfer.

A.1.1 Earth to Mars orbit

The first test case considered is the planar transfer from Earth's orbit to the orbit of Mars. For this, the orbits of Earth and Mars are approximated by circular orbits with orbital radii of 1 AU and 1.52 AU, respectively, and the orbit of Mars is assumed to lie in the ecliptic plane.

For the LEO to pole-sitter transfer in Section 5.4.1, the decision vector for the optimisation problem was five-dimensional, see above Eq. (5.42). However, since for a circle-to-circle transfer (such as the Earth to Mars transfer) the value for the initial polar angle θ_0 is irrelevant, the decision vector can be reduced to $\mathbf{y} = \begin{bmatrix} k_2 & \phi & k & \psi_t \end{bmatrix}^T$, where the bounds are set as $\begin{bmatrix} 0.01 & 0 & 0 & 0 \end{bmatrix}^T \leq \mathbf{y} \leq \begin{bmatrix} 1 & 2\pi & 1 & 2\pi \end{bmatrix}^T$. To try to locate the global optimum of Eq. (A.1) for the Earth to Mars transfer, the same genetic algorithm[148] as used in Section 5.4.1 with suggested default settings is employed.

A selection of the results of the optimisations carried out is provided in Fig. A.1, which shows the components of the objective function (Fig. A.1a) and the resulting transfers (Fig. A.1b) and acceleration profiles (Fig. A.1c) for both the expo-elliptic and the exponential sinusoidal shapes and for the number of full revolutions, N, set to 1. Furthermore, in Table A.1 the optimal values for the modulus k are presented.

The graph in Fig. A.1 shows that the expo-elliptic shape is better capable of satisfying the boundary constraints on the velocity, while requiring a similar value for ΔV_{traj} if $N > 0$.
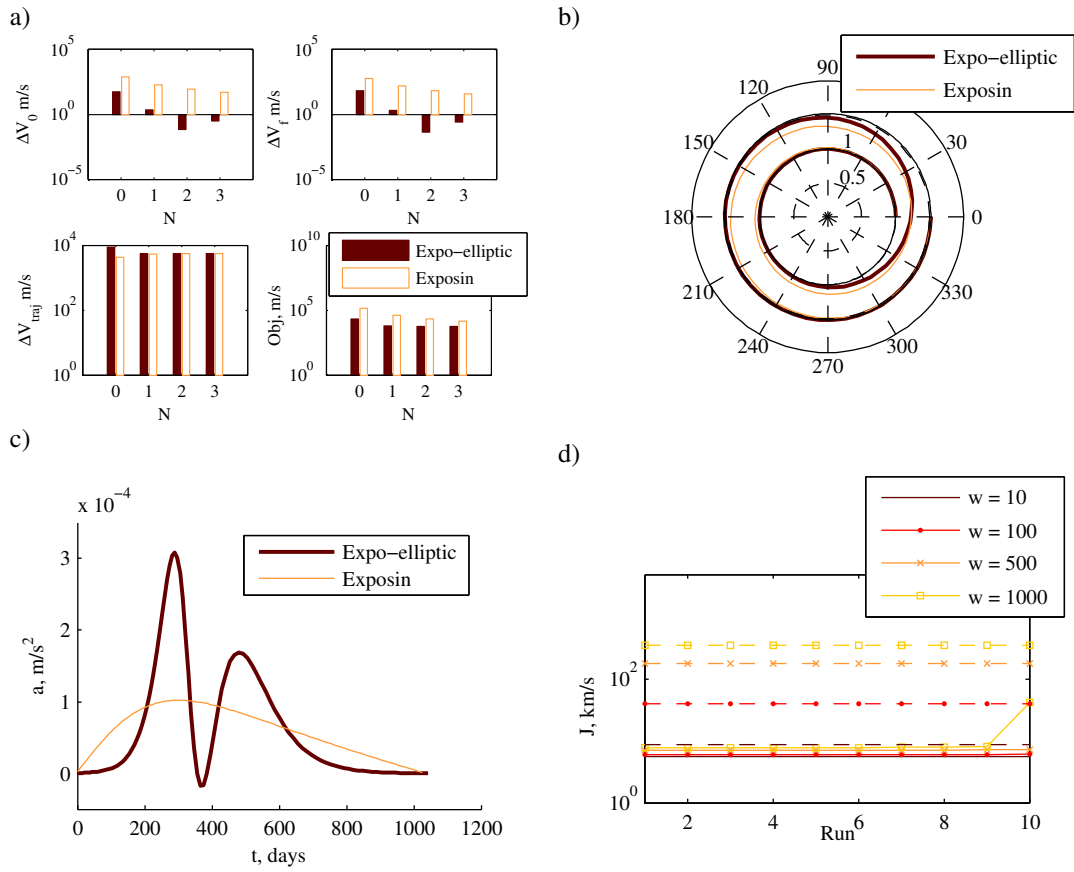
Fig. A.1 Optimal Earth to Mars orbital transfers for expo-elliptic and exponential sinusoidal (exposin) shapes. a) Required *ΔV*s and objective function value (*w* = 100) as a function of the number of full revolutions, *N*. Transfers with radius in AU (b) and acceleration profiles (c) for *w* = 100 and *N* = 1. d) Objective function values for all runs, *N* = 1 and for the expo-elliptic (solid lines) and exposin (dashed lines) shapes.

Table A.1 Optimal values for the modulus *k* for an Earth to Mars orbital transfer.

	w = 10	*w* = 100	*w* = 500	*w* = 1000
N = 0	0.97968	0.99890	0.99939	0.99903
N = 1	0.99930	0.99949	0.99984	0.99993
N = 2	0.99998	0.99998	0.99998	0.99998
N = 3	0.99908	0.99969	0.99999	0.99958

Furthermore, Fig. A.1d shows that the better performance of the expo-elliptic shape not only holds for the best solution found by the genetic algorithm, but for all ten runs that wer executed in order to account for the randomess inherent to the genetic algorithm.

Inspecting the optimal values for the modulus in Table A.1 shows that the better performance of the expo-elliptic shape is directly related to the modulus k as its values are significantly larger than zero, even very close to 1. This could raise the question whether the optimal value for the modulus should not be unity and that it is due to a premature convergence of the genetic algorithm that this value is not found. Therefore, additional optimisations have been carried out for which the value of the modulus has been set to a fixed value, i.e. the decision vector reduces to three dimensions, $\mathbf{y} = \begin{bmatrix} k_2 & \phi & \psi_t \end{bmatrix}^T$. The results are shown in Fig. A.2a and in Table A.2 for a value of 100 for the objective function weight, w. The results show that the objective function value decreases for increasing values of the modulus up to values close to unity where the objective function value suddenly sharply increases (see Table A.2). To demonstrate that the expo-elliptic shape is indeed sensitive to small changes in k especially at such large values, Fig. A.2b shows the Jacobi elliptic functions for these large values. The high precision numbers in Table A.1 are thus meaningful and are not due to a premature convergence of the optimiser. Table A.2 can furthermore be used to validate the results in Fig. A.1 and Table A.1. For example, for $N = 1$ and $w = 100$, Table A.2 shows that the optimal value for the modulus should be between 0.99 and 0.9999, which corresponds to the optimal value provided in Table A.1, namely 0.99949.

Finally, it must be noted that the better performance for the expo-elliptic shape comes at the cost of a larger required maximum acceleration as is shown in Fig. A.1c. When performing thrust constrained optimisations, this may cause problems when using the expo-elliptic shape as initial guess. However, as noted throughout this thesis, this can easily be overcome by first performing an optimisation in which the square of the thrust is minimised (without a limit on the thrust magnitude) which can serve as initial guess for the thrust-limited optimisation.
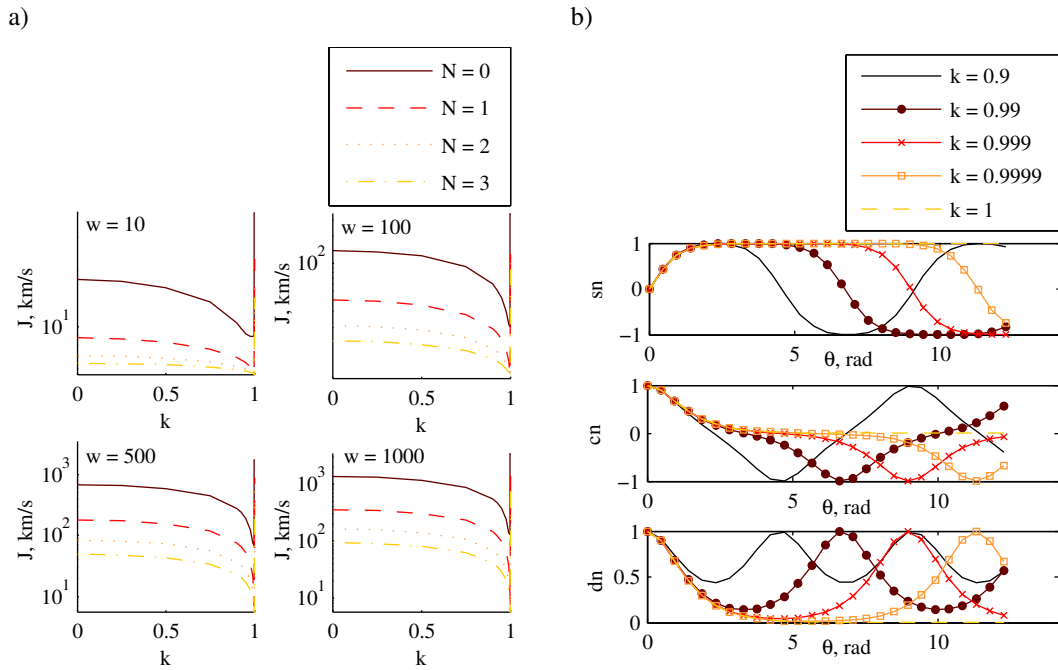
Fig. A.2 a) Optimal objective function values for an Earth to Mars orbital transfer for fixed value of the modulus k. b) Jacobi elliptic functions for large values for the modulus k.

Table A.2 Optimal objective function values for an Earth to Mars orbital transfer for fixed, large values of the modulus k and for $w = 100$.

	k				
	0.99	0.999	0.9999	0.99999	1
$N = 0$	21.82	20.55	352.7	352.7	352.7
$N = 1$	8.759	6.175	6.179	8.095	179.3
$N = 2$	7.026	5.871	5.652	5.625	121.5
$N = 3$	6.415	5.765	5.642	5.615	92.50

A.1.2   Earth to comet Tempel-1 orbit

The second test case concerns a transfer from the orbit of the Earth to the orbit of comet Tempel-1. The Earth's orbit is once again approximated by an orbit with constant radius of 1 AU and the orbit of Tempel-1 is assumed to lie in the ecliptic plane with periapsis and apoapsis radii of 1.509 AU and 4.739 AU, respectively. Contrary to the Earth to Mars transfer, the initial polar angle θ_0 plays an important role due to the non-zero eccentricity of

the orbit of Tempel-1, and is therefore included in the decision vector: $\mathbf{y} = \begin{bmatrix} k_2 & \phi & k & \psi_t & \theta_0 \end{bmatrix}^T$ with bounds $\begin{bmatrix} 0.01 & 0 & 0 & 0 & 0 \end{bmatrix}^T \leq \mathbf{y} \leq \begin{bmatrix} 1 & 2\pi & 1 & 2\pi & 2\pi \end{bmatrix}^T$.

The results in Fig. A.3 and Table A.3 show a similar performance as for the Earth to Mars transfer in Fig. A.1. Already from looking at the expo-elliptic and exponential sinusoidal trajectories in Fig. A.3b, the capability of the expo-elliptic shape to better satisfy the boundary constraints on the velocity vector becomes clear: the expo-elliptic trajectory nicely winds onto the elliptic orbit of Tempel-1, while the exposin trajectory intersects the orbit at an angle, causing a large mismatch in the final velocity. This better performance can again be attributed to large values for the modulus, see Table A.3. The figure furthermore shows that this performance comes with the additional advantage of a smaller value for ΔV_{traj} for $N > 0$, but again at the cost of a larger required maximum thrust acceleration.
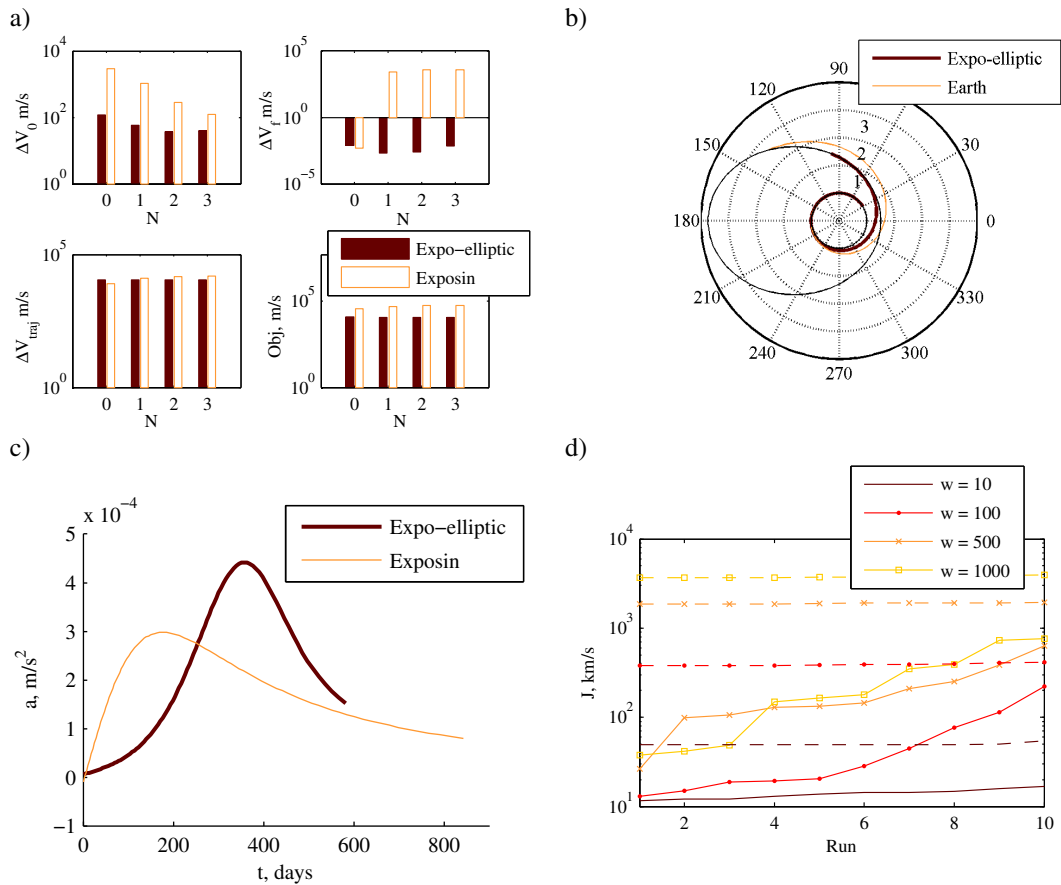
Fig. A.3 Optimal Earth to Tempel-1 transfers for expo-elliptic and exponential sinusoidal (exposin) shapes. a) Required ΔVs and objective function value ($w = 10$) as a function of the number of full revolutions, N. Transfers with radius in AU (b) and acceleration profiles (c) for $w = 10$ and $N = 1$. d) Objective function values for all runs, $N = 1$ and for the expo-elliptic (solid lines) and exposin (dashed lines) shapes.

Table A.3 Optimal values for the modulus k for an Earth to Tempel-1 transfer.

	$w = 10$	$w = 100$	$w = 500$	$w = 1000$
$N = 0$	0.99466	0.97674	0.99520	0.99367
$N = 1$	0.99506	0.99910	0.99849	0.99844
$N = 2$	0.99993	0.99852	0.99907	0.99987
$N = 3$	0.99999	0.99468	0.99504	0.99105

A.2   Lambert's problem

The previous section showed the improvements that the expo-elliptic shape can establish for time-free orbital transfers. This section will investigate whether the same holds for time-fixed transfers, i.e. when a rendezvous with a celestial body is considered. For the ballistic case, such problems are usually solved using Lambert's problem, which is concerned with finding a transfer that connects two points in space within a certain time of flight. This can, for example, be a transfer between two bodies with the time of flight given by the difference between the launch and arrival dates. For ballistic trajectories, Lambert's problem can easily be solved and is used extensively in space mission trajectory design.[38] In Reference 161 Izzo showed that a solution to Lambert's problem, as defined above, can also be derived for the exponential sinusoids by rewriting the feasibility condition, see Eq. (2.87), as a function of the initial flight path angle only. This provides bounds for the range of feasible time of flights and with that a solution to the time of flight constraint. Although less straightforward, Lambert's problem can also be solved for the use of the expo-elliptic shape.

Using polar coordinates, the three constraints involved in Lambert's problem are a constraint on the initial radius, final radius and the time of flight and are solved through the shape parameters k_0, ϕ and k_1, respectively, using the nested root-finding algorithm shown in Fig. A.4.

Starting with the time of flight constraint, the time of flight, T, can be computed through the angular rate as:

$$T = \int_{\theta_0}^{\theta_f} \frac{1}{\dot{\theta}} d\theta \qquad (A.3)$$

The shape parameter k_1 appeared to be very suitable for solving the time of flight constraint: plotting the time of flight as a function of k_1 results in Fig. A.5, which shows a smooth curve that is either monotonically increasing/decreasing or has a distinct minimum. Furthermore, the feasibility condition at periapsis and apoapsis can be satisfied by defining bounds on k_1 as follows:

$$k_{1,\min} = -\frac{1}{k_2^2 \, \mathrm{dn}(K,k)^2}$$

$$k_{1,\max} = \frac{1}{k_2^2 \, \mathrm{dn}(K,k)^2}$$

(A.4)

Genetic Algorithm

k_2, k

Solve constraint $r_f(\phi)$

- **If zero-crossing exists in $\left(r_f(\phi) - r_{f_L}\right)$-curve**
    - **Set $\phi = $ value**
        - **Solve constraint $T(k_1)$**
            - **If zero-crossing exists in $\left(T(k_1) - T_L\right)$-curve**
            - **Set $k_1 = $ value**
                - **Solve constraint $r_0(k_0)$**
                    - Compute k_0 through Eq. (5.38)
            - Compute $T(k_1)$ through Eq. (A.3)
            - Update k_1
            while $\mathrm{abs}(T - T_L) > \varepsilon$
        - Compute $r_f(\phi)$ through Eq. (5.29)
        - Update ϕ
        while $\mathrm{abs}\left(r_f - r_{f_L}\right) > \varepsilon$
        - Compute J through Eq. (A.1)
- **Else**
    - Set J to penalty value
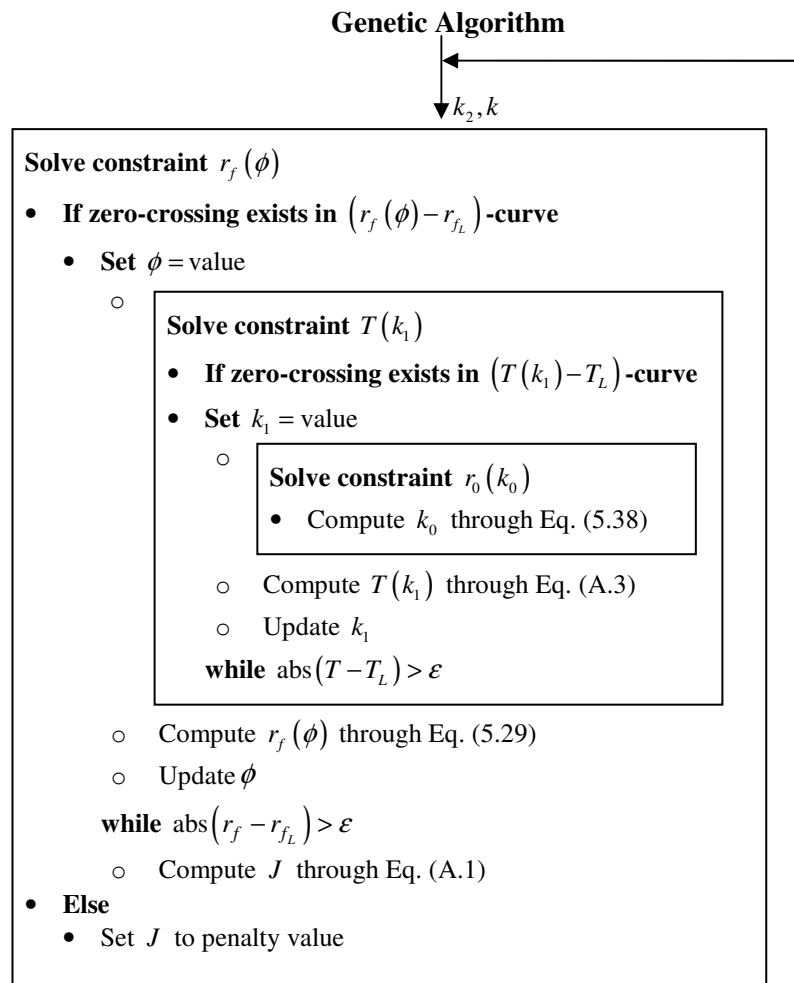
Fig. A.4 Nested root-finding algorithm, indicating the flow of expo-elliptic shape parameters with ε the tolerance of the root finder and the subscript 'L' indicating the value in Lambert's problem.

234
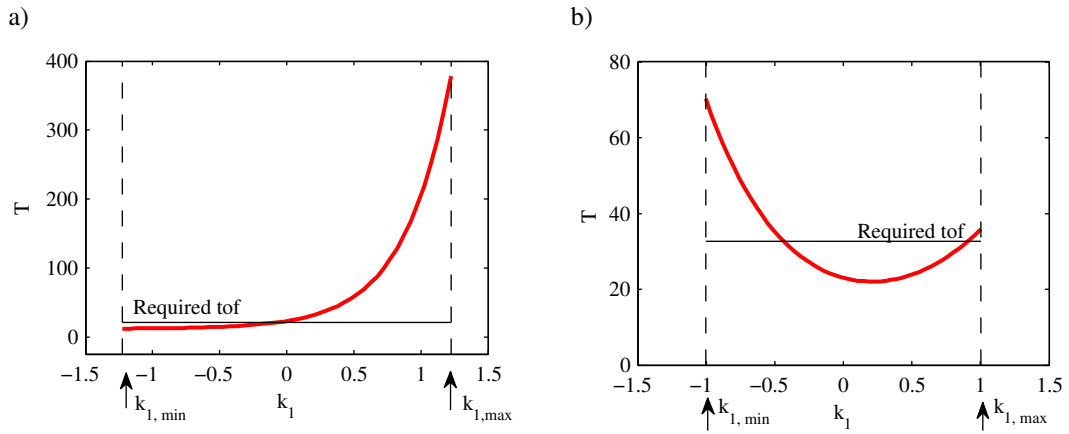
Fig. A.5 Illustration of trends of the dimensionless time of flight, T, versus k_1 curve.

Only, when the situation of Fig. 5.11 occurs, i.e. the minimum of the denominator in Eq. (5.31) does not coincide with periapsis or apoapsis, a quick root finder is employed to detect the values for k_1 for which the minimum of the denominator switches sign from negative to positive and to set the bounds for k_1 accordingly. By determining the intersection of the curve $T(k_1)$ with the required time of flight as set in Lambert's problem, T_L, for example by using the MATLAB® function *fzero*,[162] the time of flight constraint can be satisfied. Note that, in the case of Fig. A.5b where two intersections exist, both intersections are detected and the one that satisfies the constraint on the final radius best (see further on) is used for further calculations. Also note that the shape parameters k_2 and k could also have been used to satisfy the time of flight constraint and the feasibility condition. However, since previous work[161] used k_2 as design variable and the parameter k would require the computation of the inverse of the Jacobi elliptic function, preference was given to the shape parameter k_1.

As Fig. A.4 shows, inside the computations for the time of flight constraint, the constraint on the initial radius is satisfied by computing the shape parameter k_0, see Eq. (5.38), at each iteration step. The figure furthermore shows that the root finding algorithm for the time of flight constraint is nested inside another root finding algorithm that is used to satisfy the final radius constraint for which the shape parameter ϕ appeared most suitable. Figure A.6a shows an example of how the error on the final radius, Δr_f, changes for different values of ϕ. Note that the discontinuity arises from the evolution of the curve $T(k_1)$ for different values of ϕ, which is illustrated in Fig. A.6b. Applying a large, random search over the remaining free shape parameters k_2 and k, and the problem parameters r_0, r_f and the time

235

of flight, showed that the majority of the curves $\Delta r_f(\phi)$ satisfies the trend in Fig. A.6a. Also, note that, contrary to the exponential sinusoids, ϕ cannot be considered in the first two quadrants only, which is clear from Fig. A.6a as $\Delta r_f(\phi=0) \neq \Delta r_f(\phi=2\pi)$. Although more complex trends exist, among others when the time of flight constraint cannot be satisfied for certain values for ϕ, the roots of the curves can be determined by discretising the interval for ϕ and again applying the MATLAB® function *fzero* as soon as a change in sign is observed (excluding the sign changes arising from the discontinuity). In case of two roots, i.e. one in the interval $\phi[0,\pi]$ and one in the interval $\phi[\pi,2\pi]$, the root with the smallest objective function value is selected for further calculations, where the objective function is the same as the one used for the orbital transfers, see Eq. (A.1). Also the same genetic algorithm will be employed to locate the global minimum. For this, the polar angle along the transfer is once again discretised into $50(N+1)$ equally spaced nodes. The decision vector is changed, however, to include the launch date, t_L, time of flight, winding parameter and the modulus: $\mathbf{y} = \begin{bmatrix} t_L & T & k_2 & k \end{bmatrix}^T$. In case a particular decision vector does not provide an intersection for the curves $T(k_1)$ or $\Delta r_2(\phi)$, a penalty is introduced on the objective function value.

Hereafter, the same two test cases of Section A.1 will be considered, but this time including the actual ephemerides of Earth, Mars and Tempel-1.[163, 164] As for the orbital transfers, different values for the weight in the objective function and the number of full revolutions are considered and similar optimisations are carried out for the use of exponential sinusoids.

a)

b)
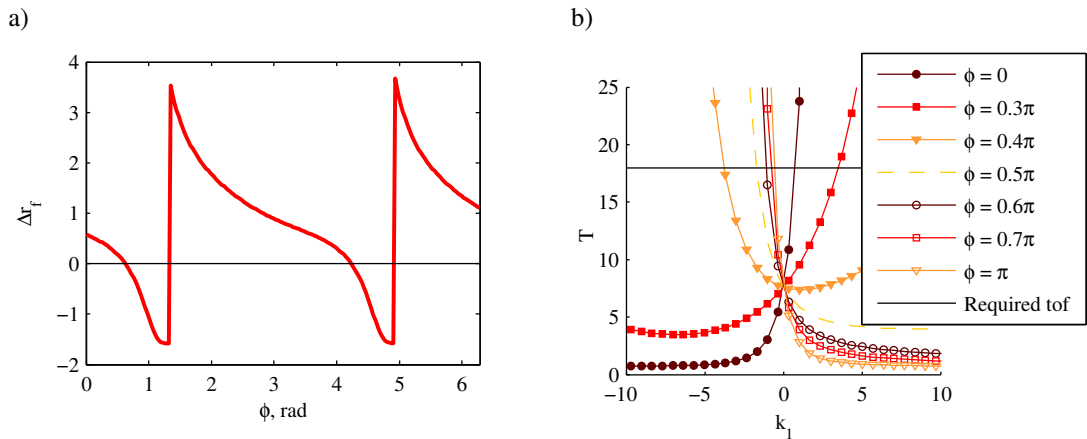
Fig. A.6 Illustration of trend of the error on the final radius as a function of ϕ (a) and explaining discontinuities that arise from the variation of the intersection of the dimensionless time of flight versus k_1 curve for different values for ϕ (b).

A.2.1 Earth to Mars rendezvous

This first test case considers a rendezvous mission from Earth to Mars. Since both the exponential sinusoids and the expo-elliptic shape can only consider planar transfers, the ephemeris of Mars is projected onto the ecliptic plane. The launch date covers the period between 1 January 2020 and 1 January 2025, while the time of flight is set to be between 500 and 2000 days. Finally, the bounds for the shape parameters k_2 and k are set to $0.01 \leq k_2 \leq 1$ and $0 \leq k \leq 1$, respectively. A selection of the results of the optimisations is shown in Fig. A.7 and Table A.4.

While the results for the orbital transfers in Section A.1 showed a clear, better performance for the expo-elliptic shape over the exponential sinusoids, Fig. A.7 shows that this better performance is less clear for the time-fixed Earth to Mars transfer. Inspecting the values for the modulus in Table A.4 also shows the influence of the additional time of flight constraint, as for some cases the optimal values for the modulus are much lower than for the time-free orbital transfers. Still, for all N, the objective function value for the expo-elliptic shape is smaller than for the exponential sinusoids, indicating a better match in initial and final orbital velocities, but again at the cost of a larger maximum acceleration.

Using the optimal results in Fig. A.7 as initial guess, the results using the exponential sinusoidal and expo-elliptic shapes have been re-optimised using a direct pseudospectral method implemented in PSOPT. This showed difficulties in terms of convergence for the exponential sinusoidal initial guess, which can be attributed to the large mismatch in boundary conditions, especially at the initial orbit. In that respect, the better match in boundary conditions for the expo-elliptic shape outweighs the larger maximum acceleration.
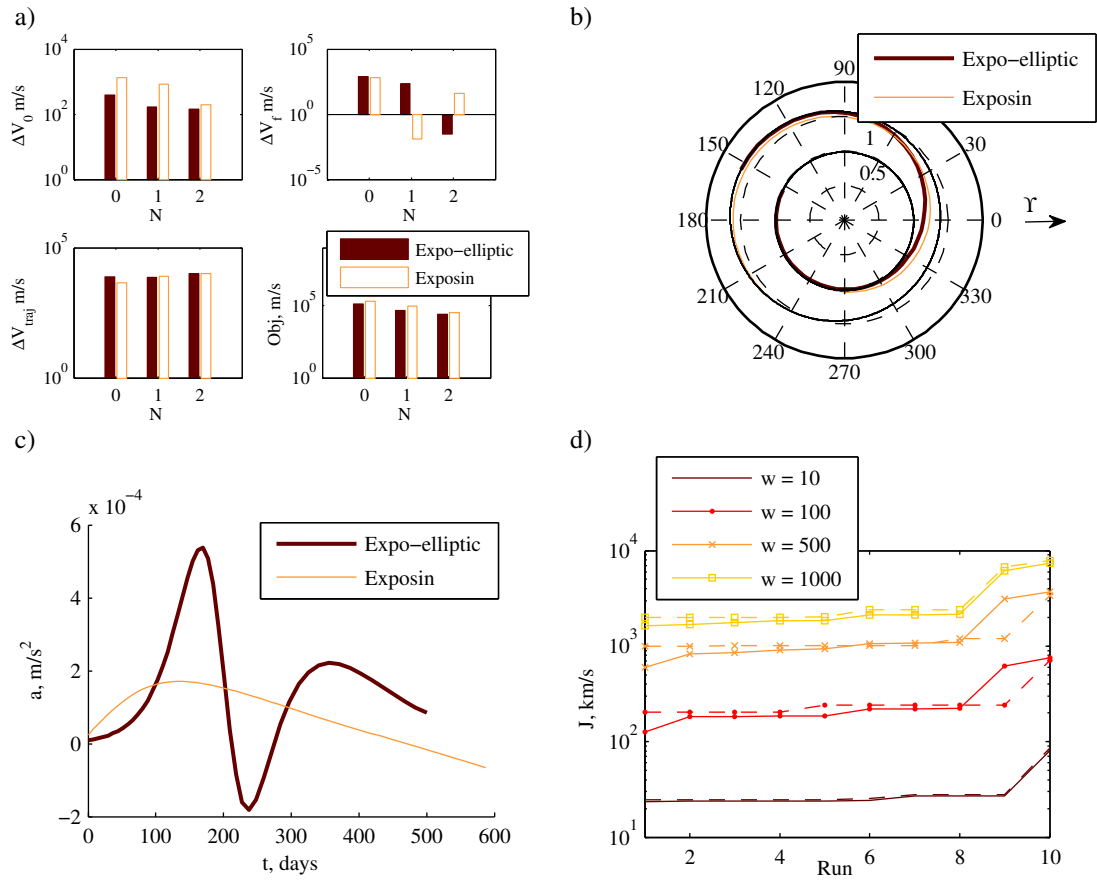
Fig. A.7 Optimal Earth to Mars rendezvous transfers for expo-elliptic and exponential sinusoidal (exposin) shapes. a) Required *ΔVs* and objective function value (*w* = 100) as a function of the number of full revolutions, *N*. Transfers with radius in AU (b) and acceleration profiles (c) for *w* = 100 and *N* = 0. d) Objective function values for all runs, *N* = 0 and for the expo-elliptic (solid lines) and exposin (dashed lines) shapes.

Table A.4 Optimal values for the modulus *k* for an Earth to Mars rendezvous transfer.

	w = 10	*w* = 100	*w* = 500	*w* = 1000
N = 0	0.77834	0.99953	0.99959	0.89496
N = 1	0.99027	0.99221	0.99228	0.99236
N = 2	0.32769	0.55652	0.98666	0.68425
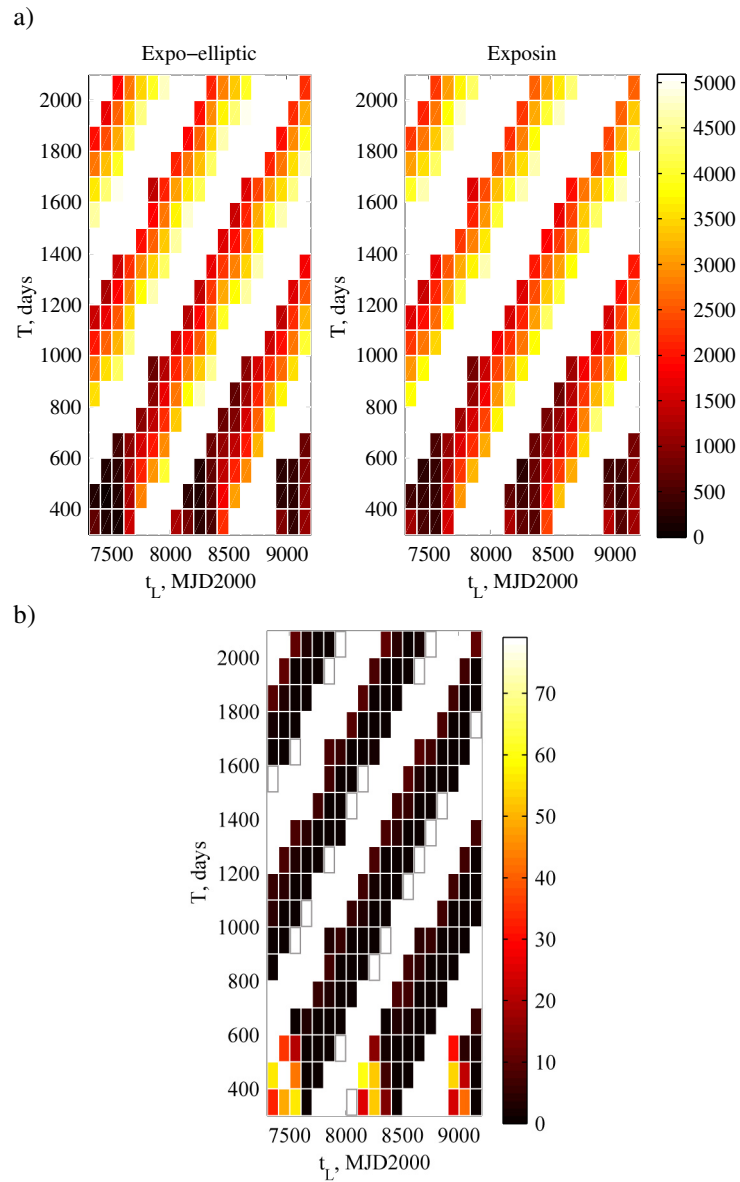
Fig. A.8 a) Minimised objective function value in km/s across the time of flight and launch date design space for an Earth to Mars rendezvous using the expo-elliptic and exponential sinusoidal (exposin) shapes and for $w = 100$ and $N = 0$. White areas indicate that no feasible solution exists. b) Percentage gain in objective function for the expo-elliptic shape over the exposin shape. White, stroked areas indicate that only the expo-elliptic shape generates a feasible solution.

Finally, to show that the expo-elliptic shape not only outperforms the exponential sinusoidal shape for the most optimal solution found in the (t_L, T) design space, additional optimisations have been carried out to show its performance across the entire design space. The results are shown in Fig. A.8, which are generated by fixing the launch date and time of flight, thereby reducing the decision vector to $\mathbf{y} = \begin{bmatrix} k_2 & k \end{bmatrix}^T$. Figure A.8a shows that for

certain combinations of launch date and time of flight no solution exists for the expo-elliptic and exponential sinusoidal shapes (white areas). However, also combinations exist where the exponential sinusoidal shape does not provide a solution, but the expo-elliptic shape does (white, stroked areas in Fig. A.8b). Furthermore, Fig. A.8b highlights the better performance of the expo-elliptic shape over the entire design space by providing the percentage gain in objective function that the expo-elliptic shape provides over the exponential sinusoidal shape. The figure shows that, either the expo-elliptic shape outperforms the exponential sinusoidal shape (up to a percentage gain of over 70 percent) or else the genetic algorithm converges to the exponential sinusoidal solution, i.e. the optimal value of the modulus k is zero.

A.2.2 Earth to comet Tempel-1 rendezvous

For this second and final test case, a similar approach is taken as for the Earth to Mars rendezvous. The ephemeris of Tempel-1 is projected onto the ecliptic plane, the launch date covers the period between 1 January 2020 and 1 January 2035, the time of flight is set between 700 and 1500 days and the bounds for k_2 and k are again defined as $0.01 \leq k_2 \leq 1$ and $0 \leq k \leq 1$, respectively.

Figure A.9 and Table A.5 provide the results of the optimisations. Contrary to the results in the previous section, the results in Fig. A.9 once again clearly show the better performance of the expo-elliptic shape over the exponential sinusoids. For all N, the objective function value is smaller and the initial and final orbital velocities are better matched, especially for $N = 0$ and 1, despite the fact that the transfers in Fig. A.9b suggest that the transfers are quite similar. Furthermore, Fig. A.9c shows that, contrary to the accelerations required for the orbital transfers and the Earth Mars rendezvous transfer, the level of acceleration required for the Earth to Tempel-1 rendezvous is smaller for the expo-elliptic shape than for the exponential sinusoids.

As for the Earth to Mars rendezvous, also the optimal results for the Earth to Tempel-1 rendezvous have been re-optimised using PSOPT. A similar behaviour could be observed, where the larger error on the initial boundary constraint for the exponential sinusoidal shape caused issues in terms of convergence.

Finally, Fig. A.10 provides the performance of the expo-elliptic and exponential sinusoidal shapes over the entire design space, similar to Fig. A.8 for the Earth to Mars rendezvous. In this case, both shapes provide feasible trajectories throughout the design space, but

Fig. A.10b indicates that, again, the expo-elliptic shape outperforms the exponential sinusoidal shape up to over 70 percent in the objective function value.
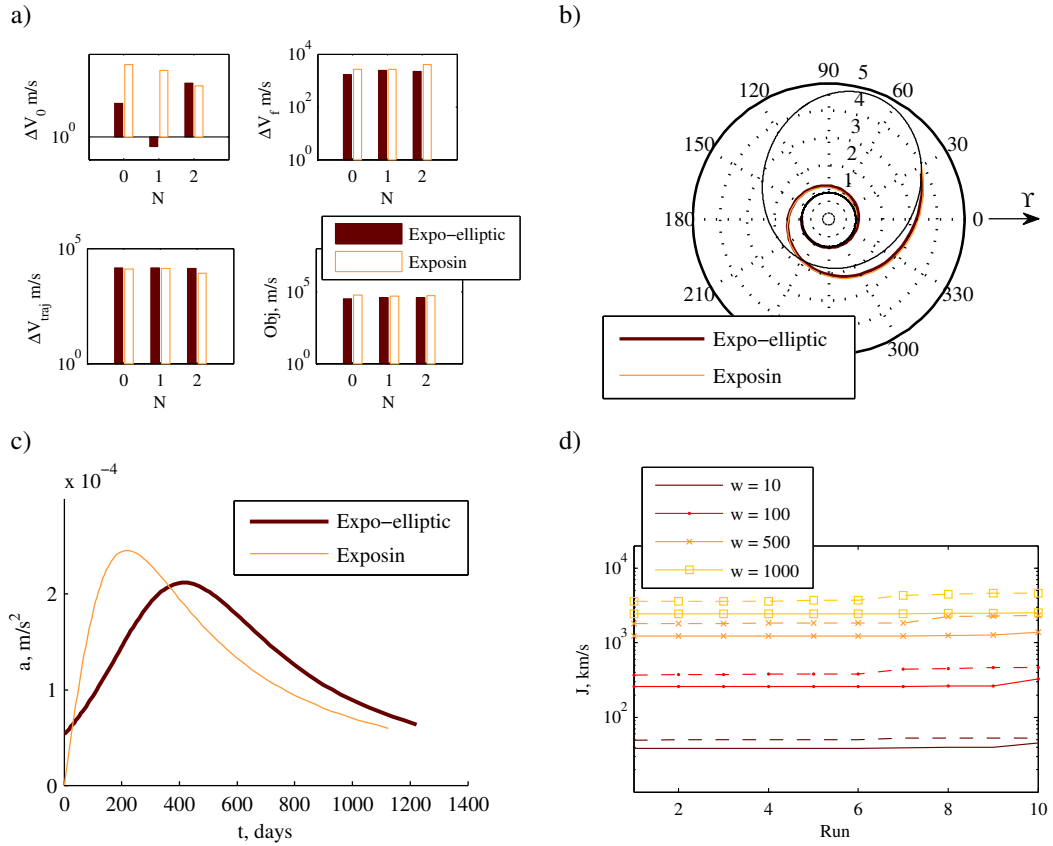
Fig. A.9 Optimal Earth to Tempel-1 rendezvous transfers for expo-elliptic and exponential sinusoidal (exposin) shapes. a) Required *ΔVs* and objective function value (*w* = 10) as a function of the number of full revolutions, *N*. Transfers with radius in AU (b) and acceleration profiles (c) for *w* = 10, *N* = 1. d) Objective function values for all runs, *N* = 1 and for the expo-elliptic (solid lines) and exposin (dashed lines) shapes.

Table A.5 Optimal values for the modulus *k* for an Earth to Tempel-1 rendezvous transfer.

	$w = 10$	$w = 100$	$w = 500$	$w = 1000$
$N = 0$	0.99915	0.99715	0.99713	0.99714
$N = 1$	0.99849	0.99019	0.99805	0.99829
$N = 2$	0.99974	0.99974	0.99974	0.99974

a)

b)
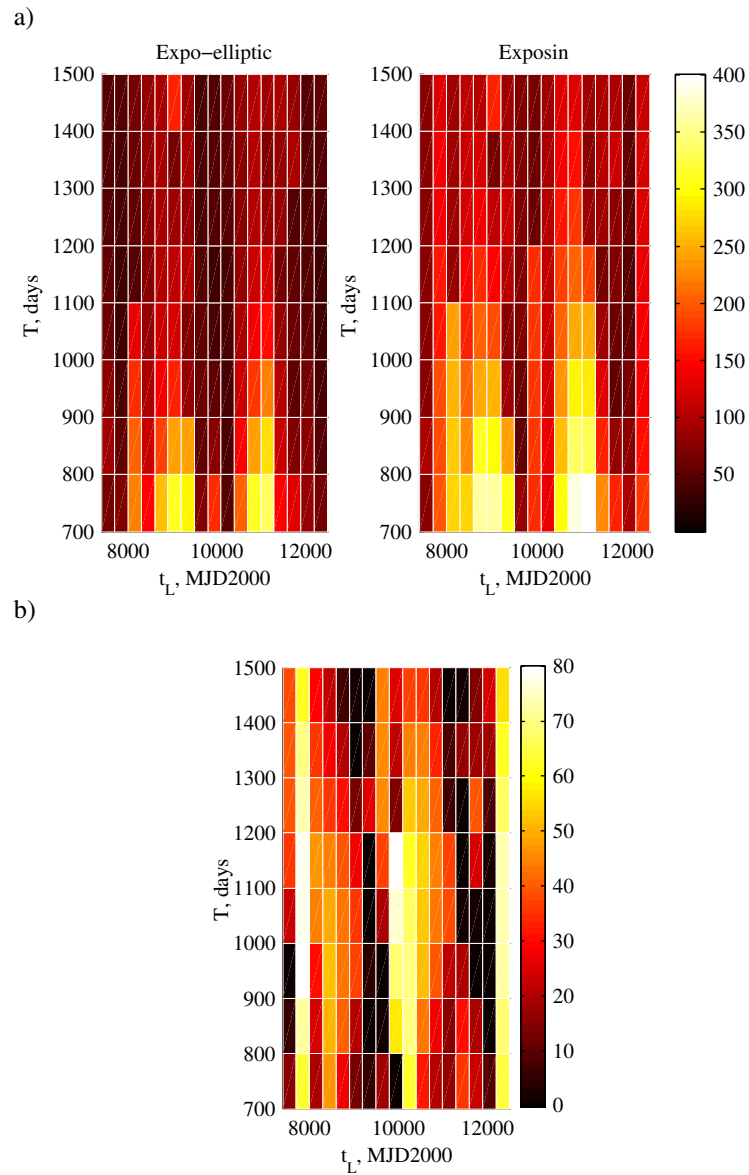
Fig. A.10 a) Minimised objective function in km/s value across the time of flight and launch date design space for an Earth to Tempel-1 rendezvous using the expo-elliptic and exponential sinusoidal (exposin) shapes and for *w* = 10 and *N* = 1. b) Percentage gain in objective function for the expo-elliptic shape over the exposin shape.